TRANSMISSION AND RADIATION CHARACTERISTICS OF CORRUGATED WAVEGUIDES

by

CLIVE GEORGE PARINI, B.Sc.(Eng.)

A thesis submitted to the University of London

for the Degree of Doctor of Philosophy

Department of Electrical and Electronic Engineering

Queen Mary College

University of London

October 1976

ABSTRACT

A theoretical and experimental investigation into the use of the corrugated circular waveguide as a feeder and radiator for microwave antennas is described. Because corrugated waveguide feeders are overmoded, the effects on the propagation and radiation characteristics of mode conversion due to bends are investigated. New methods of providing higher order mode suppression are described, and substantiated by experimental results using resonant cavity and transmission line methods. The cross-polarisation properties of corrugated waveguides are shown to be intrinsically superior to those of smooth wall waveguides when the waveguide wall suffers elliptical deformation. As an alternative to the problems involved in overmoded operation a design of corrugated circular waveguide for HE_{11} mono-mode operation, which still exhibits an attenuation advantage, is developed.

The radiated co-polar and cross-polar performance of corrugated circular waveguides and narrow flare-angle corrugated concial horns are studied both experimentally and theoretically using a more accurate analysis than attempted by previous authors. Design curves for optimum cross-polar radiation performance are presented and a new method of improving the cross-polarisation performance of these structures is theoretically predicted, and experimentally verified.

ACKNOWLEDGEMENTS

The author would like to express his most sincere thanks to:

- The Science Research Council who provided financial support throughout the duration of the project.
- Professor M.W. Humphrey Davies for his permission to undertake the research in the Department of Electrical and Electronic Engineering, Queen Mary College.
- His supervisors, Professor P.J.B. Clarricoats and Dr. A.D. Olver for their active interest and guidance throughout the project.
- Dr. G.T. Poulton who took an active interest in the work of chapter 6.
- Dr. G.A. Hockham for his many helpful discussions.
- The members of the Electromagnetics Group, Queen Mary College.
- Mr. N.J. Kolb, Mr. J. Ede and Mr. D. Field for their assistance with the experimental programme.
- The staff of the Electrical and Electronic Engineering Department, Queen Mary College.
- Mr. G.J. Bischak and Dr. K.R. Slinn of Andrew Antenna Systems.
- Last but not least, Mrs. Sylvia Reading for her excellent typing of this manuscript.

LIST OF PRINCIPAL SYMBOLS

A_N, B_N — electric and magnetic field coefficients of the N^{th} space-harmonic [$\bar{A}_N = A_N J_n(K_N r_1)$, $\bar{B}_N = B_N J_n(K_N r_1)$]

a_{mn} — amplitude coupling coefficient (from mode n to mode m) due to a waveguide tilt

b — ridge width

c — speed of light, 3×10^8 m/s

c_m, c_m' — electric field coefficients of m^{th} slot mode

C_{mn} — amplitude coupling coefficient from mode n to mode m

d — slot width or pattern deviation

d_m, d_m' — magnetic field coefficients of m^{th} slot mode

E_C, E_X — co-polar and cross-polar components of radiated electric field

$E\{x\}$ — expected value of x

f, f_c — frequency and mode low frequency cut-off

h — correlation length

$I_n(x)$ — modified Bessel function of the first kind, order n, argument x

$\underline{i}_x$ — unit vector of $\underline{x}$

j — $\sqrt{-1}$

$J_n(x)$ — Bessel function of the first kind, order n, argument x

$K_n(x)$	modified Bessel function of second kind, order n, argument x
K_N	transverse wavenumber of N^{th} space-harmonic
L, ℓ	resonant cavity length and waveguide length
n	azimuthal number
N	space-harmonic number
P_C, P_X	co-polar and cross-polar power
P_o	power flow for a waveguide mode
r, θ, z	cylindrical coordinates
R, θ, z	spherical coordinates
r_1, r_o	inner and outer radii of the corrugated circular waveguide
$\bar{r}_1$	normalised frequency: $\bar{r}_1 = \omega r_1/c$
R_n^D, R_n^N, S_n^D, S_n^N	Bessel function products of order n
v_g	mode group velocity
x, y, z	Cartesian coordinates
y_o	free-space wave admittance
z_o	free-space wave impedance or waveguide bend length
α, α_m	attenuation coefficient (of mode m)
β_N	propagation coefficient of N^{th} space-harmonic
β_m	propagation coefficient of the fundamental space-harmonic of mode m
β_e, β_o	propagation coefficients of the even and odd modes in elliptical waveguide

γ, γ_m	complex propagation coefficient (of mode m)
Γ_m, Γ_m'	longitudinal wavenumbers of m^{th} slot mode
Δf_L	3dB linewidth of a resonance
$2\Delta r$	waveguide ellipticity: major diameter - minor diameter
η_m, η_m'	longitudinal propagation coefficients of m^{th} slot mode
θ_o	semi flare-angle of a conical horn
λ	free-space wavelength
λ_g	guide wavelength
$\mu_{\Delta r}$	mean of Δr
$\sigma_{\Delta r}$	standard deviation of Δr
ϕ_o	polarisation tilt angle resulting from waveguide ellipticity
ω	angular frequency

CONTENTS

CHAPTER 1

INTRODUCTION

1.1 HISTORICAL DEVELOPMENT

The use of corrugated circular waveguides (figure 1.1) and narrow flare-angle conical corrugated horns as feeds for microwave reflector antennas has become well established during the last decade. Their desirable characteristics include nearly circularly symmetric co-polar radiation patterns with low sidelobes and low cross-polarisation lobes. These features are associated with the Gaussian like power distribution and linearly polarised transverse field of the HE_{11} hybrid mode. This occurs when, to a first approximation, the waveguide boundary conditions are such that both the E_θ and H_θ field components vanish at the corrugated walls.

In 1970, whilst engaged in a research programme on the propagation and radiation characteristics of corrugated waveguides and horns, Clarricoats and Saha < 1 > observed that the linearly polarised HE_{11} hybrid mode in a corrugated circular waveguide exhibited a low attenuation. This discovery resulted in Clarricoats and Olver initiating a general research programme at Queen Mary College into the low attenuation properties of corrugated waveguide structures. The research programme confirmed both experimentally and theoretically the low attenuation properties of the corrugated structure and led to the

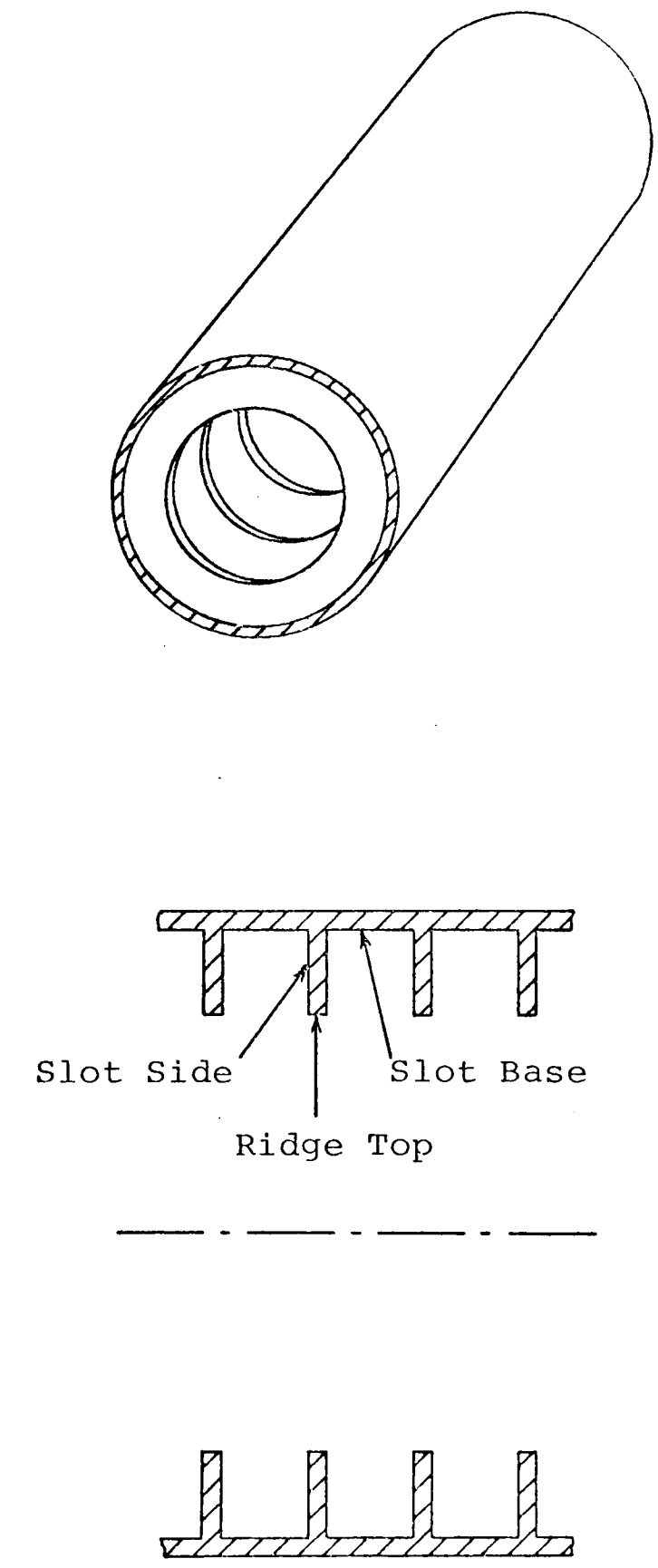

Fig. 1.1 The corrugated circular waveguide

publication of theses by Chong < 2 > and Al-Hariri < 3 > in 1974. This thesis is concerned with a continuation of both these programmes of research and earlier research into the radiation characteristics of corrugated waveguides and horns.

1.2 GENERAL CONSIDERATIONS

Future high capacity trunk telecommunications systems will probably be based on either the optical fibre waveguide or the TE^{o}_{01} metal waveguide. The optical fibre waveguide has seen a rapid development over the last decade and very low attenuation has been achieved. The use of a number of fibres each having bandwidths of up to 500MHz, coupled with ease of installation, makes the optical fibre waveguide an attractive proposition as the basis of a trunk waveguide communication system. In a relatively few cases, such as very high capacity links between major cities, the use of the TE^{o}_{01} metal trunk waveguide with its extremely large bandwidth (of order 50GHz) would appear to be a viable proposition. Considerable effort has been invested over the last two decades by the world's major telecommunications authorities into this TE^{o}_{01} mode smooth wall† circular trunk waveguide system.

†In order to achieve mode suppression and to break the degeneracy between the TE^{o}_{01} and TM^{o}_{11} modes, a practical system employs either helical or dielectric lined circular waveguide construction < 4 >.

It is probable that future applications for new low attenuation microwave waveguide structures will be as feeders for microwave antenna communications systems, rather than in trunk waveguide systems. Currently if low attenuation waveguide is required, (for example to feed 100m high microwave relay towers) designers have used over-moded smooth wall circular waveguides with the signal carried by the dominant TE_{11} mode. The lack of a preferred plane of polarisation for the low attenuation TE^{o}_{01} mode in this same waveguide precludes its use for an antenna feeder. However, the corrugated circular waveguide propagating the linearly polarised HE_{11} mode is ideally suited for this application, enabling low attenuation dual polarisation operation to be realised. In addition the mechanical structure of the corrugated waveguide permits the possibility of a flexible form of construction, an important factor in portable antenna communication systems. With the increasing congestion now occurring in the lower microwave frequency bands the move to the higher centimetric and millimetric wavelength bands will reinforce the need for a new low attenuation waveguide.

1.3 LOW ATTENUATION MICROWAVE WAVEGUIDES: A REVIEW

The initial analysis of the attenuation in the corrugated circular waveguide by Clarricoats and Saha < 1 > used a surface impedance model† to represent the corrugated

† frequently termed the simple impedance model.

region of the waveguide, the attenuation being calculated from the power losses on the metal surfaces using the well-known perturbation method. The predicted low attenuation phenomenon of the corrugated circular waveguide was subsequently confirmed, both experimentally and theoretically, by Clarricoats, Olver and Chong < 5 >. Experimental confirmation was achieved by: a) measuring the Q-factors of short lengths of corrugated waveguide made to form resonant cavities and b) measuring the attenuation directly over a long length of waveguide using the substitution and bridge methods. Good agreement was observed with a theory based on an exact space-harmonic representation for the waveguide fields. Because the corrugated circular waveguide is a periodic structure, the fields in the interior region were represented by a space-harmonic series, and those in the corrugation slots by a complete set of TE and TM standing waves. Clarricoats et al < 5 > found that for accurate computation of the propagation and attenuation coefficients it was sufficient to include only one pair of space-harmonics in addition to the fundamental, and one higher order TE-TM standing wave combination in addition to the lowest order TM field in the slots. The theoretical results predicted lower attenuation than the theoretical value for the TE^{o}_{01} mode in a comparable size of smooth wall circular waveguide, a mode which had long been regarded as the ultimate mode for low attenuation in metallic waveguides.

The reason for the low attenuation in the corrugated

waveguide is that the presence of the corrugation boundary acts to reduce the field intensity near the metal surfaces and thus lowers the power losses on these surfaces. The phenomenon can be understood physically by reference to figure 1.2. For the TE_{01} mode in a smooth wall circular waveguide only the longitudinal component of the magnetic field lies tangential to the wall, and this decreases indefinitely with frequency relative to the transverse fields which transport the power along the waveguide. Metal losses increase with frequency as $f^{\frac{1}{2}}$ but as the relative strength of the longitudinal magnetic field decreases as f^{-2}, the attenuation falls with frequency as $f^{-3/2}$. In the case of the TE_{11} mode both azimuthal and longitudinal magnetic fields lie tangential to the wave-guide wall and after an initial minimum the attenuation increases with frequency, the losses being dominated by the azimuthal magnetic field component. In the case of the corrugated waveguide when the corrugation depth is such that a *magnetic wall* is created this dominant azimuthal component is removed whilst the longitudinal component is maintained. The magnetic wall condition is only achieved at a specific frequency and so the low attenuation phenomenon constitutes a band pass effect. However, the 3dB bandwidth is typically of order half an octave and so is sufficiently large for most applications.

The low attenuation waveguide research programme at Queen Mary College also involved the study by Al-Hariri < 3 > of corrugated waveguides having both elliptical and

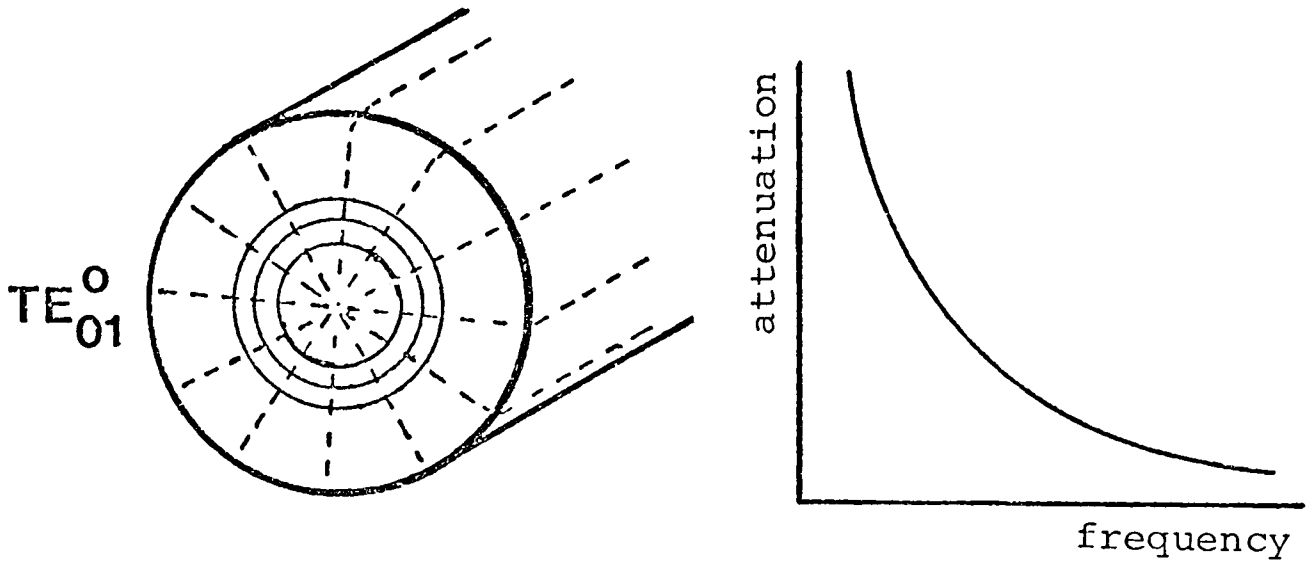

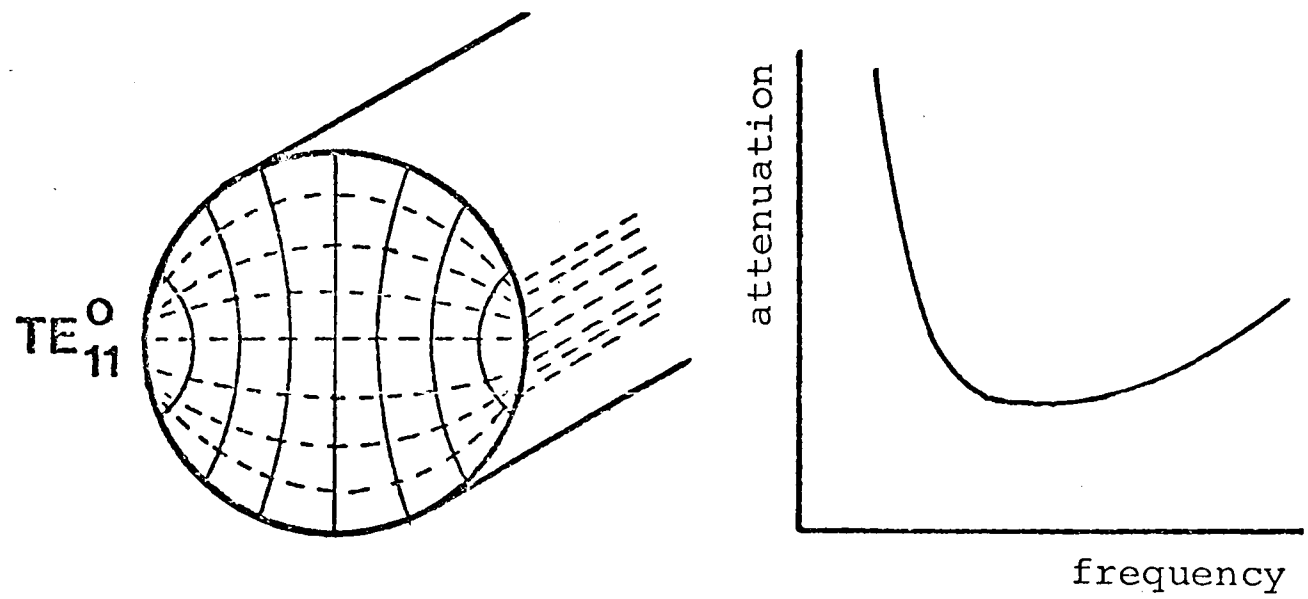

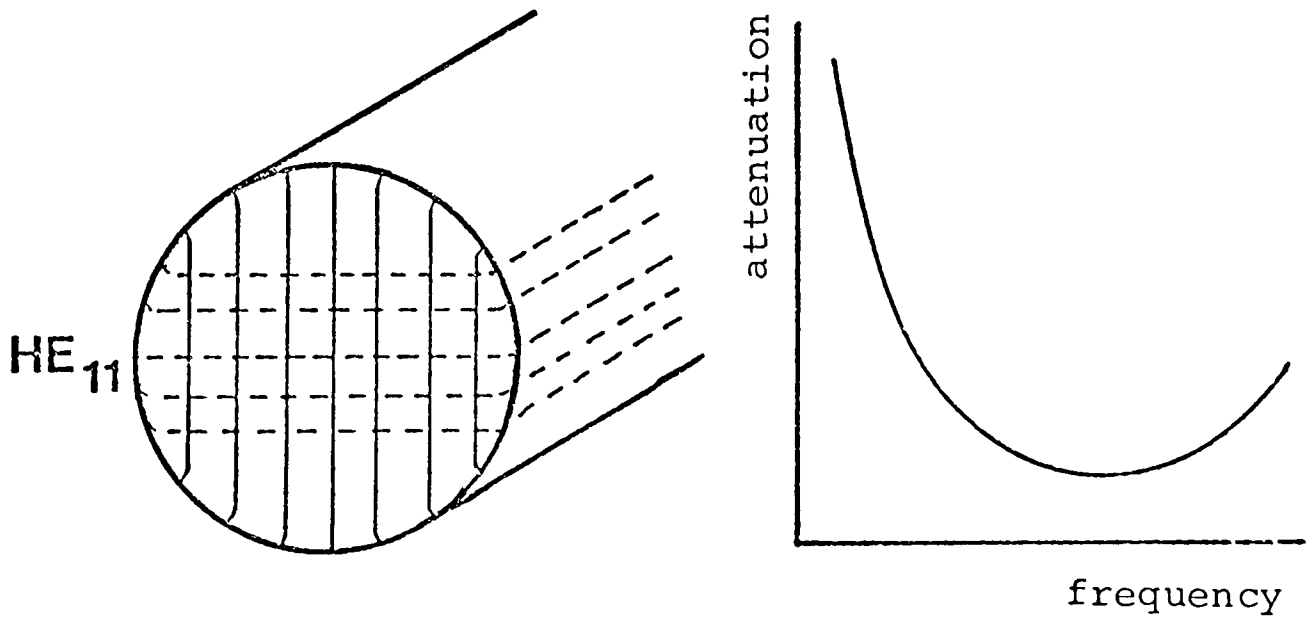

Fig. 1.2 Sketch of field pattern and attenuation characteristics in, respectively, smooth wall circular waveguide (TE^{o}_{01} mode), smooth wall circular waveguide (TE^{o}_{11} mode), and corrugated circular waveguide (HE_{11} mode)

rectangular cross-sections. It was concluded from this study that although these structures did exhibit some advantages over their smooth wall counterparts the corrugated circular waveguide remained the best waveguide for the low attenuation antenna feeder application.

Al-Hariri also studied the dielectric lined circular waveguide where a dielectric replaces the corrugations in producing the required anisotropic surface impedance. However, it was found that with currently available dielectrics the power loss in the dielectric resulted in the attenuation being only slightly better than that of the corresponding smooth wall waveguide.

Over the past few years several other alternative waveguide structures for achieving low attenuation transmission at microwave frequencies have emerged. Papiernik and Fray < 6 > have proposed the *open ring line* which is essentially a corrugated waveguide deprived of its outer shield, the remaining rings being held by a single longitudinal bar. These rings produce an anisotropic surface impedance enabling the EH_{11} *dipole mode* to propagate along the structure. Attenuations of 10dB/Km at 2GHz have been observed for this structure. Barlow < 7 > has proposed a similar type of structure, the *dipole mode waveguide*; in this case a series of lossy longitudinal wires produce the required anisotropic surface impedance. Both these waveguides propagate slow-waves and so are strictly unbounded structures making them unsuitable for use as antenna feeders. In addition, a brief experimental

study of the open ring line by the author (not reported in this thesis) indicated that it was unable to negotiate a bend without incurring considerable radiation leakage, a problem common to most forms of slow-wave structure.

The above review of low attenuation waveguides together with the general considerations of the previous section, suggest that the corrugated circular waveguide, used as a feeder and/or radiator, has the potential to improve the performance of an antenna communications system. However, to date, no practical realisation of this potential improvement has emerged. With the rapid growth in terrestrial and satellite antenna systems now occurring in both the developed and underdeveloped countries the potential performance improvement exhibited by the corrugated circular waveguide warrants a more detailed study. It is this study that forms the basis of this thesis.

1.4 DEVELOPMENT OF THE THESIS

In chapter 2 the performance requirements for antenna communications systems are reviewed with the purpose of identifying specific applications where the corrugated circular waveguide and conical horn, acting as a waveguide or primary feed, can be advantageously used. Two broad areas of study are suggested: a) The microwave link between the antenna and the transmitter/receiver; b) The cross-polarisation performance of high efficiency feeds for reflector antennas. The use of the corrugated

waveguide structure in these two areas are then considered in detail identifying the specific problems involved and so defining topics for further corrugated waveguide research. These topics are studied in the subsequent chapters of this thesis and in each chapter emphasis is given to the relevance of the results to the antenna feeder application.

Many of the studies involve experimental measurements and in chapters 3 and 4 the various experimental techniques employed throughout this thesis are described. Chapter 3 is concerned with antenna measurements and begins by describing the techniques used and errors involved in measuring the co-polar and cross-polar radiation patterns of antenna feeds. The remaining part of this chapter describes a new experimental technique for the determination of the levels of higher order modes present in the radiating aperture of a feed. Chapter 4 describes the techniques used and errors involved in measuring the attenuation and transmission characteristics of corrugated waveguides using both resonant cavity and transmission test methods.

If a flexible form of corrugated waveguide construction is to be used it is imperative to know the degree of mode conversion resulting from bends along the waveguide run. This problem is considered both theoretically and experimentally in chapter 5.

Practical waveguides will inevitably exhibit some manufacturing imperfections and in chapter 6 the problem of cross-polarisation induced by random ellipticity of the waveguide cross-section is studied theoretically. Results

for both smooth wall and corrugated circular waveguides are presented and compared.

Over a long length of corrugated waveguide it is inevitable that some degree of coupling to higher order modes will occur and to maintain this coupling to an acceptable level the use of mode filters may be necessary. Presently available designs of mode filter introduce too much loss to the HE_{11} mode and in chapter 7 the development of a new type of corrugated waveguide mode filter, exhibiting negligible HE_{11} mode loss, is described.

In some antenna feeder applications flexibility and dual polarisation operation, coupled with a fairly low attenuation, are the prime requirements. To overcome the many problems involved with overmoded operation chapter 8 describes a design of corrugated circular waveguide for HE_{11} mono-mode operation.

Chapters 9 and 10 are concerned with the radiation characteristics of corrugated circular waveguides and narrow flare-angle conical corrugated horns. In chapter 9 the theoretical prediction of the co-polar and cross-polar patterns of these structures is studied and a more accurate analysis than attempted by previous workers is derived. In chapter 10 experimental verification of this improved analysis is presented. Using this analysis, design curves for optimum cross-polar radiation performance are derived and a new method of improving the cross-polar performance of these structures is theoretically predicted and experimentally verified.

The thesis is concluded in chapter 11 by a summary of the main results, and suggestions for future study.

CHAPTER 2

APPLICATIONS FOR CORRUGATED WAVEGUIDING STRUCTURES IN ANTENNA COMMUNICATION SYSTEMS

2.1 INTRODUCTION

In this chapter the performance requirements for an antenna communication system such as would be used for a microwave radio link or satellite ground station are studied. The purpose of this investigation is to identify applications where the corrugated circular waveguide and conical horn, acting as waveguides or primary feeds, can be advantageously used. The performance requirements strongly depend on the *class* into which the antenna communication system fits, whether it be a high capacity satellite earth station or a low capacity portable microwave link. An antenna communication system can be divided up into a number of principal subsystems. To enable the varied performance requirements to be placed in perspective, section 2.2 briefly considers the dependence of antenna *class* on the performance requirements for each of the constituent subsystems. As a result of this study it becomes clear that there are two areas where corrugated waveguide structures can provide an improvement in system performance:

1) The microwave waveguide link between the antenna and the transmitter/receiver.

2) The cross-polarisation performance of high efficiency feeds for reflector antennas.

Sections 2.3 and 2.4 consider these two areas in detail, identifying the problems involved and defining areas where additional corrugated waveguide research is required. These areas form the basis of the work to be presented in this thesis.

2.2 SYSTEM PERFORMANCE REQUIREMENTS

Any microwave antenna communication system can be divided into four main subsystems as shown in figure 2.1. The performance requirements of these subsystems strongly depends into which *class* the antenna system under consideration falls. For the purposes of this study a general antenna communication system can be classified into one of the three classes defined in table 2.1. For the systems of classes 1 and 2 stringent international and national specifications exist to ensure uniformity of performance throughout the complete telecommunications system. The systems of class 3 are usually independent communication systems but can often, as in the case of a military system, have a very rigid specification. The remainder of this section will outline the performance requirements for the various subsystems making use of the system classification defined above.

2.2.1 The Encoder/Transmitter, Receiver/Decoder

Over the last few years this area has seen the most significant improvement in performance and increase

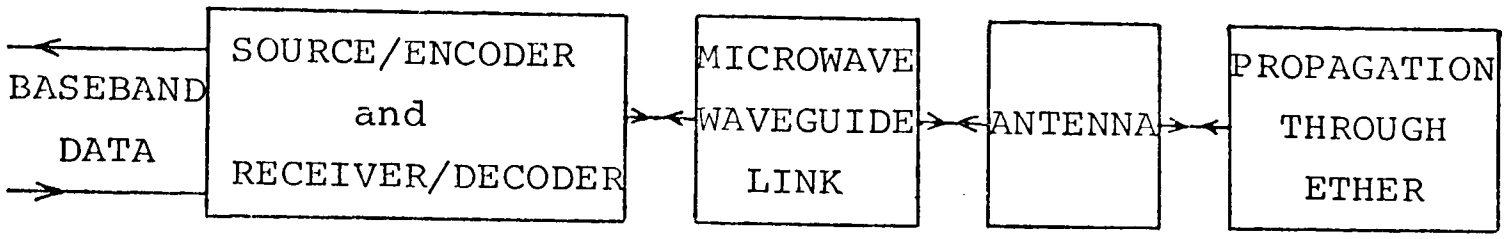

Fig. 2.1 Division of an antenna communication system into its main subsystems.

CLASS	TYPE OF SYSTEM	TYPICAL APPLICATION
1	Large and medium size satellite earth stations	High and medium capacity global, regional or domestic satellite communication
2	High and medium capacity terrestrial microwave radio relay systems	National trunk telecommunications
3	Small/portable radio relay or satellite ground stations	Low capacity private or military communications links, low capacity satellite ground stations

Table 2.1

in choice of system available. To date the most common modulation method used for all three classes of antenna is where the carrier is Frequency Modulated (F.M.) by base band signals made up from a number of Frequency Division Muliplexed (F.D.M.) telephone channels and/or one television channel. For classes 1 and 2 multiple carriers are transmitted but for class 3 systems a single carrier is normally used. However, digital systems using base band P.C.M. with Phase Shift Key (P.S.K.) modulation plus single channel per carrier or time division multiplex operation are beginning to be implemented in the class 1 and 2 systems < 8 > < 9 >.

For the satellite systems encompassing class 1, the available power at the receiving antenna is very weak, typically <-140dBm for a global satellite system. This is mainly because of the large bandwidth used and the fact that the satellite transmitter has a limited Gain Bandwidth product. In addition the satellite antenna gain is low because of the wide beamwidth required for global coverage. Consequently low noise, cooled, parametric amplifier receivers with noise temperatures between $10^{o}K$ and $20^{o}K$ are used <10>. For domestic or regional satellite systems, or for global systems employing spot beams, the bandwidth is smaller and the satellite power is concentrated over a much smaller area, resulting in a higher available power at the receiver. This means that an uncooled parametric amplifier can be used as the receiver, which has the advantage of being cheaper and simpler to operate. Typical

transmitters employ high power wide band Travelling Wave Tube (T.W.T.) amplifiers, or a number of high power Klystrons, one for each separate carrier. Transmitter powers generally lie between 500W and 5000W <11>.

The frequency band used for commercial satellite communication is the 4GHz/6GHz band (4GHz down from the satellite and 6GHz up to it). However, this band is becoming increasingly saturated and the next generation of satellite systems will employ dual polarisation frequency re-use and/or higher frequencies. The next higher band to be commercially used is the 11GHz/14GHz band, proposed for Intelsat V and the European O.T.S. and E.C.S. satellites <12>. Experiments at even higher frequencies are being undertaken, for example a 20GHz/30GHz link is presently under study in Japan <12>.

For the terrestrial systems of class 2 the available power at the receiver is typically -60dBm for an average transmission distance of 50Km < 9 >. This much higher available power allows the use of relatively cheap, low noise, solid state bipolar transistor amplifiers having noise figures <4dB for frequencies up to about 6GHz. Thin gate F.E.T. amplifiers also possess a low noise, plus a frequency of operation up to about 12GHz <12>. Typical transmitter powers lie between 1W and 20W and can be obtained using solid state bipolar transistors for frequencies below 6GHz. Above 6GHz T.W.T. amplifiers are, at present, used. It is now possible to construct radio relay repeaters using only R.F. amplification, but

unfortunately in many cases provision must be made to change carrier frequencies from repeater-to-repeater which requires conversion down to I.F. The present frequency ranges are becoming rapidly saturated, and to overcome this both higher frequency bands and dual polarisation frequency re-use operation is beginning to be implemented.

The systems comprising class 3 generally have a low data capacity and usually employ only a single carrier. Again uncooled, low noise, solid state receivers are generally used with frequencies varying from 2GHz to over 30GHz. Typical examples of systems included in this class are the worldwide maritime navigation and communication satellite systems Marisat and Marots, and the small portable microwave links used for television outside broadcast.

2.2.2 The Waveguide Link

In order to keep the overall system noise temperature down to a minimum high and medium capacity satellite earth stations have the low noise receiver mounted as near as possible to the primary feed of the antenna. By making the waveguide connection between feed and receiver as short as possible waveguide losses are kept to a minimum. To remain within the Intelsat specification for a G/T† of 40.7dB/K, the input circuit

†G/T is the earth station *figure of merit* = Gain(dB)-10logT, where T is the earth station effective noise temperature (^{o}K) <10>.

losses must typically be kept below 0.2dB <9>. For losses greater than 0.2dB the noise temperature resulting from these losses will begin to dominate the effective noise temperature of the system. An alternative method recently developed for feeding large earth stations is that of the beam waveguide feed <13>. This is shown diagramatically in figure 2.2 where a system of four reflecting *mirrors* is used to transfer the feed horn patterns onto the subreflector, and to provide the necessary rotational connections for antenna orientation. This system has the advantage that the transmitter/ receiver can be situated on the ground away from the antenna, facilitating easier equipment maintenance. An American built system using this technique, with a narrow flare-angle corrugated conical horn feed, has achieved overall input circuit losses of 0.15dB <13>. Here an application for the low loss corrugated waveguide becomes apparent. By coupling the corrugated feed horn to the low noise receiver using a length of corrugated waveguide an attenuation lower than conventional smooth wall waveguide would be achieved. For example, an overmoded smooth wall waveguide of length 10m, operating at 11GHz, would contribute $22^{o}K^{\dagger}$ to the overall system noise temperature, which is high compared to the typically required value of about $10^{o}K$. A corrugated waveguide similarly overmoded

†The noise temperature, T, induced by feeder losses can be obtained from the equation $T = -(10^{\frac{-\alpha}{10}}-1)T_{o}$, where α is the attenuation in dB and T_{o} is the ambient temperature (^{o}K) <10>.

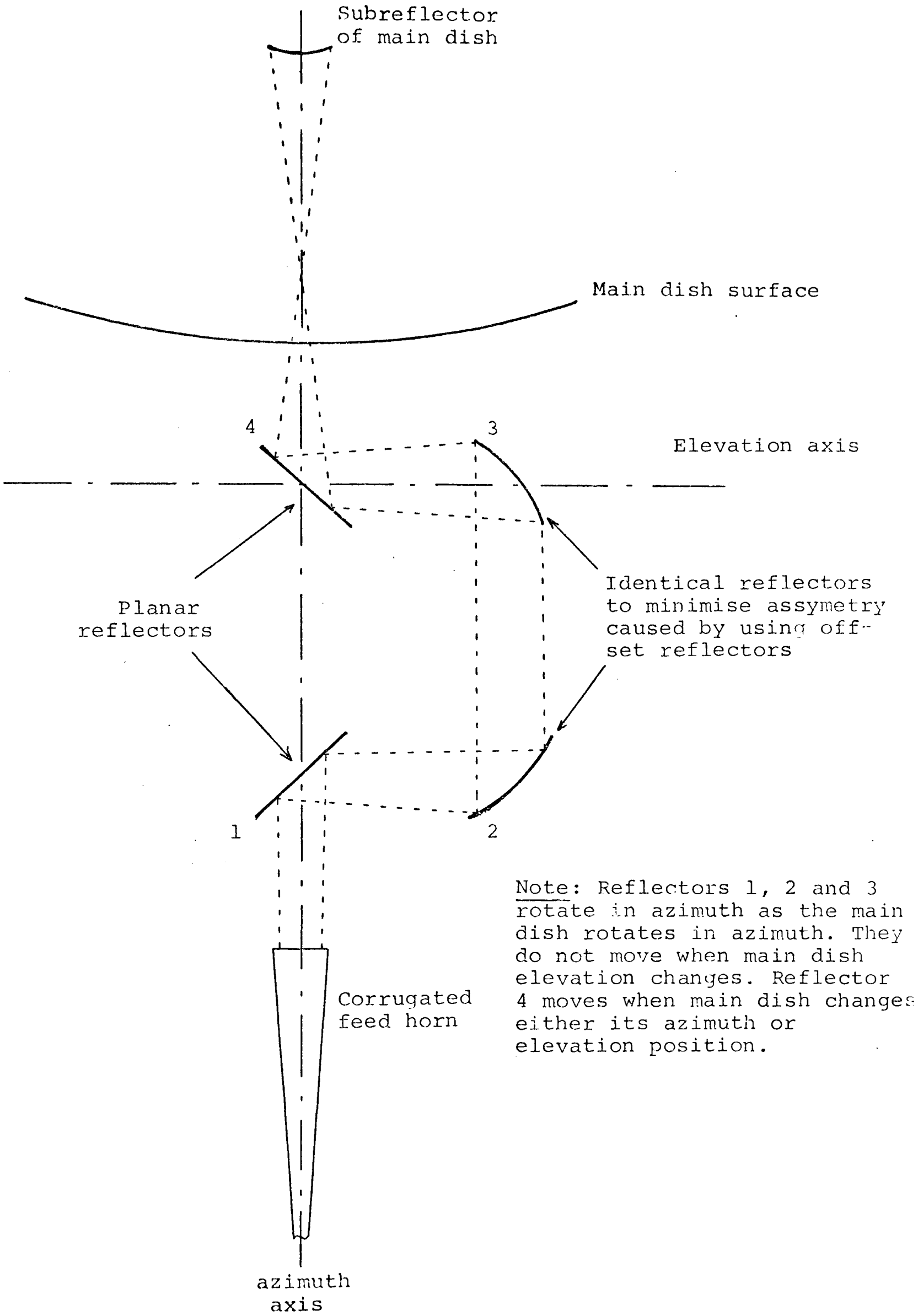

Fig. 2.2 Beam waveguide feed configuration

(figure 2.3), and of the same length, would contribute only $6^{o}K$, clearly indicating the improvement possible. The use of the corrugated waveguide also makes for a more efficient connection, because by using the HE_{11} hybrid mode in both the feed horn and waveguide the need for conversion between TE_{11} and HE_{11} modes at the feed throat is eliminated.

For high capacity microwave relay systems relatively long waveguide links between antenna and receiver/transmitter are generally used for frequencies below about 12GHz. This is because, in general, a number of antennas share a common tower and to mount the receiver/transmitter on the tower would increase tower costs and create maintenance difficulties. It is possible to use long waveguide lengths without degrading system performance because of the higher noise temperature receivers used. Consequently the input circuit loss can be much higher before their resulting noise temperatures begin to dominate the system. In a microwave relay link it is usually necessary to keep these feeder losses, including diplexers, filters, etc. below 3dB.

Tower heights normally vary from about 130m downwards, depending on the terrain. The type of microwave waveguide used to feed the tower largely depend on the allowable input circuit losses. For most applications coaxial cable or single mode waveguides of rigid rectangular, rigid circular, or flexible elliptical construction are used. However, for systems requiring

— — — Flexible elliptical waveguide, single mode

- - - - - - - - - Rigid rectangular waveguide, single mode

—— · —— Rigid circular waveguide, single mode

—— — —— Rigid circular waveguide, overmoded, $f/f_c = 2{\cdot}0$

———— Flexible or rigid corrugated circular waveguide, overmoded, $f/f_c = 1{\cdot}75$

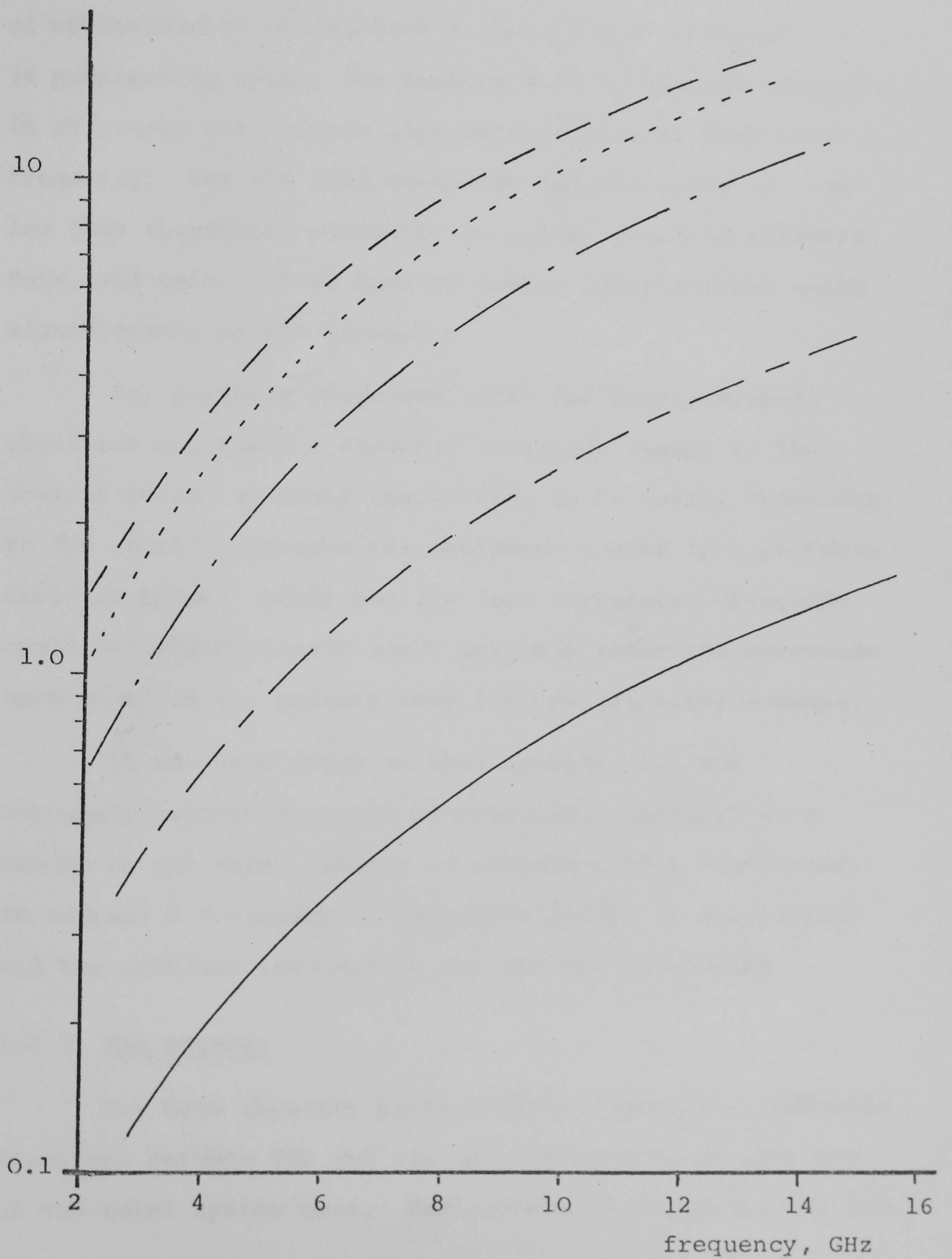

Fig. 2.3 Typical feeder losses for various types of copper waveguide

low feeder attenuation, rigid overmoded smooth wall circular waveguides are used. The latter is also used for dual polarisation operation. Figure 2.3 compares, as a function of frequency, the feeder losses for these types of waveguiding structure with those for the overmoded (4 propagating modes, see section 2.3) corrugated waveguide. In all cases the optimum size of waveguide is used at each frequency. For the long waveguide lengths involved, the low loss corrugated waveguide in either rigid or flexible form, and using either dual or single polarisation, would significantly reduce losses.

For portable microwave links and portable/small satellite receivers a flexible waveguide feeder is the obvious choice allowing the antenna to be easily connected to the receiver/transmitter equipment housed in a portable cabin or truck. Again the low loss corrugated waveguide could be advantageously used, possibly using the waveguide open-ended as the primary feed for the reflector antenna.

It has been shown in this section that the corrugated waveguide could be favourably employed as a feeder in all three classes of antenna system considered. In section 2.3 corrugated waveguide design is considered, and the problems involved in its use are identified.

2.2.3 The Antenna

The high capacity earth stations have main reflector diameters between 26m and 32m and they represent some 40% of the total system cost. Performance requirements for the

antenna are: high gain, low feed V.S.W.R., low sidelobes (to minimise terrestrial interference and reduce equivalent noise temperature), and a typical 3dB beamwidth of 0.2^{o}. Cassegrain or shaped dual reflector antennas are used because of their efficient illumination, low spillover in the direction of the earth, and reduced feeder losses due to favourable feed position. The medium capacity earth stations retain the Cassegrain configuration but have main reflector diameters of order 10m. For high efficiency the primary feed pattern must produce a good match to the focal region fields of the reflector antenna. The most important classes of feed producing such a match are the corrugated waveguide and corrugated horn (section 2.4). For this reason many earth stations use narrow flare-angle conical corrugated horns to produce the required narrow beam, and circularly symmetric pattern.

Dual polarisation frequency re-use operation is beginning to be introduced into satellite systems, resulting in an approximate doubling of available information capacity. Comstar 1<14>, the American domestic communications satellite system uses 12 channels with horizontal polarisation and another 12 channels, using the same frequencies, with vertical polarisation. However, frequency re-use imposes a stringent constraint on the cross-polarisation characteristics of both the satellite and earth station antennas to achieve adequate channel isolation. For the earth station, the radiated cross-polar power, in the vicinity of boresight, must be below

approximately -40dB relative to the co-polar boresight signal. For the satellite antenna this maximum cross-polar level of -40dB must be maintained over all the earth coverage. It is thus essential that the antenna, and in turn, the narrow flare-angle conical corrugated horn exhibit a low cross-polar radiation.

Antennas for microwave relay systems, class 2, are generally front feed paraboloids with: high gain, low feed V.S.W.R., low sidelobes, and low front-to-back ratio. Reflector diameters vary from about 4m downwards, depending on the frequency and the required gain. The smallest diameter possible is used to minimise tower wind loading, and so reduce tower structural costs. The 3dB beamwidth is typically about 1.5^{o} and the antenna gain is normally of order 40dB. The primary feed is often an open-ended smooth wall circular waveguide sometimes with the addition of choke ring to improve radiation pattern symmetry. The -10dB beamwidth of the feed can be as large as 180^{o} in the case of a focal plane reflector. For dual polarisation operation a maximum of about -40dB for the cross-polar power radiated from the feed and captured by the reflector is specified. Corrugated waveguide feeds, possessing low cross-polarisation over a wide bandwidth, are possible contenders for the primary feed in this case.

For low capacity portable satellite earth stations, with G/T's of 14 to 20, Cassegrain antennas with main reflector diameters of about 3m and beamwidths of order 1^{o} are used. For low capacity portable terrestrial microwave

links, small front feed paraboloid reflectors are used. For systems comprising, class 3, dual polarisation operation is unlikely to be used, but the antenna may, in some cases, have to possess sufficient isolation between orthogonal polarisations.

In this section it has been shown that a requirement exists for low cross-polarisation antennas. This, in turn, imposes a similar requirement on the antenna feed and in section 2.4 the cross-polarisation performance of corrugated feeds and their importance in determining the overall antenna performance is considered.

2.2.4 Propagation

As the lower frequency bands become congested the move to higher frequencies will involve extra problems concerned with propagation. Below 10GHz precipitation (rain, snow, fog) in the troposphere does not introduce any significant increase in path attenuation. However, above 10GHz scattering of the wave by raindrops can cause a significant increase in path attenuation which generally increases with increasing frequency <10>. Above 20GHz absorption by oxygen and water vapour molecules can greatly increase the path loss at certain frequencies making them unusable for communication purposes <10>. These increased path attenuations will result in the use of larger fade margins, shorter path lengths and possibly space diversity techniques. Design curves relating rainfall rate, path length, path attenuation and frequency have been presented

by several workers <15>. Cross-polarisation induced by precipitation for linear polarisation has been found to be insignificant for rain rates where the increased co-polar attenuation remains within an acceptable fade margin <16>. At the lower microwave frequencies (<4GHz) the phenomena of Faraday rotation <10>, occurring in the ionosphere, can cause a linearly polarised signal to suffer a polarisation rotation. For this reason circular polarisation, being resilient to this phenomena, is generally used at the lower frequencies.

2.3 THE CORRUGATED WAVEGUIDE AS A FEEDER FOR MICROWAVE ANTENNAS

In section 2.2.2 it was shown that a major application for the corrugated waveguide was as a low attenuation feeder for microwave antennas. In this section the design procedures for low attenuation corrugated waveguides are described, the problems involved in the waveguides use are considered and finally areas where performance is unknown, or where improved performance is required, are identified.

2.3.1 Corrugated Waveguide Design

The designs presented in this section, along with figures 2.5 to 2.9 are a brief extract from the extensive study of the propagation and attenuation characteristics of corrugated circular waveguides made by Clarricoats, Olver and Chong < 5 > < 2 >.

To achieve low attenuation the corrugated waveguide is operated overmoded and the attenuation obtained largely depends on the number of propagating modes that can be tolerated. The waveguide geometry is shown in figure 2.4. Figure 2.5 shows the mode chart for the corrugated waveguide, giving the approximate low frequency cut-off for the first 17 modes as a function of $\frac{r_1}{r_o}$. This chart allows a designer to determine the number of propagating modes for a specified normalised operating frequency, $\bar{r}_1$. Figure 2.6(a) shows, for a practical size of corrugated waveguide, the normalised phase change coefficient, βr_1, for the first 15 modes, as a function of normalised frequency. In figure 2.6(b) the corresponding attenuation coefficient obtained for this same waveguide is given and clearly shows the bandpass characteristics of the HE_{11} mode. Both these results were calculated using one pair of higher order space harmonics in the inner region and one pair of higher order slot modes.

To date, two principal corrugated waveguide designs are available < 2 >. The first of these designs assumes that there is no restriction on the number of propagating higher order modes and aims to achieve the lowest possible waveguide attenuation. In figure 2.7 the minimum attenuation of the HE_{11} mode in a brass corrugated waveguide is shown as a function of radius. Also shown for comparison are the corresponding curves for the TE_{11} and TE_{01} modes in smooth wall circular waveguide of internal radius equal to both inner and outer radii of the

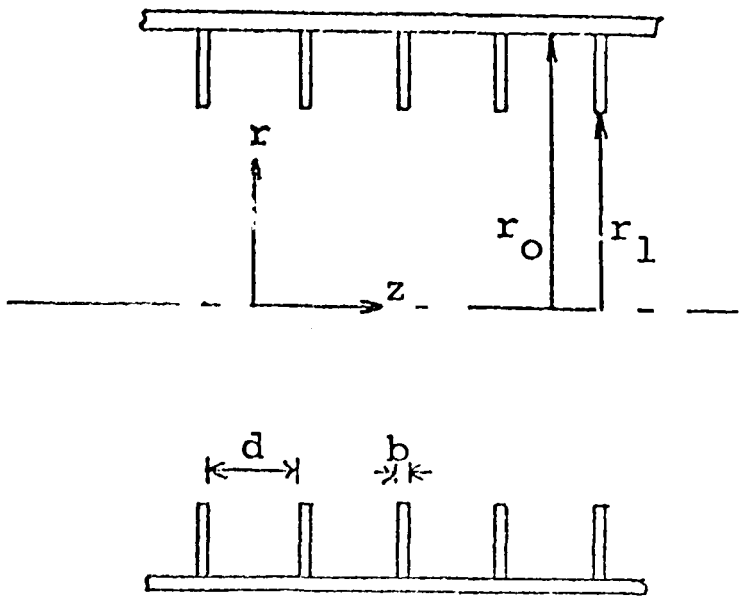

Fig. 2.4 Corrugated waveguide geometry

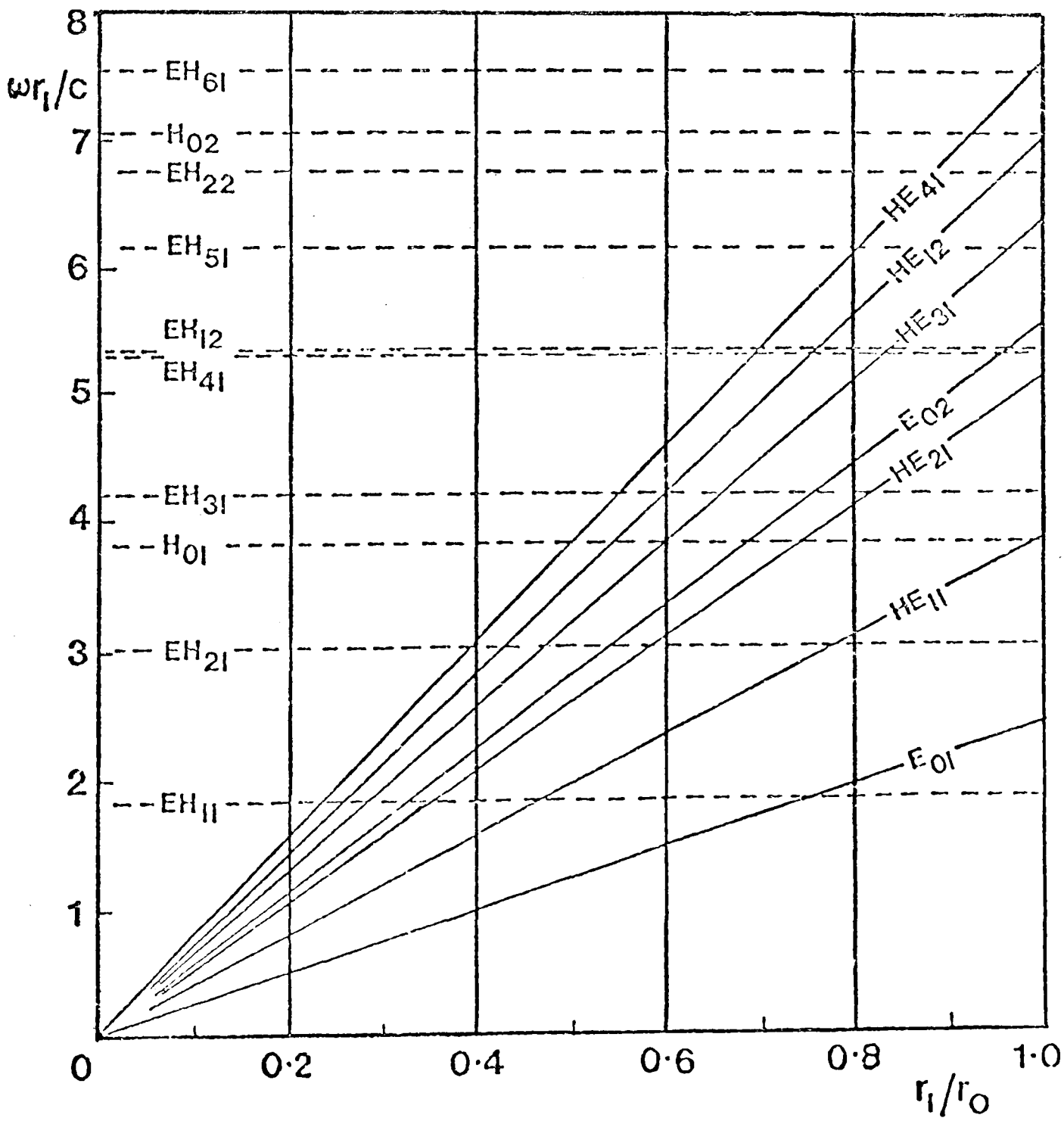

Fig. 2.5 Mode chart for corrugated circular waveguide

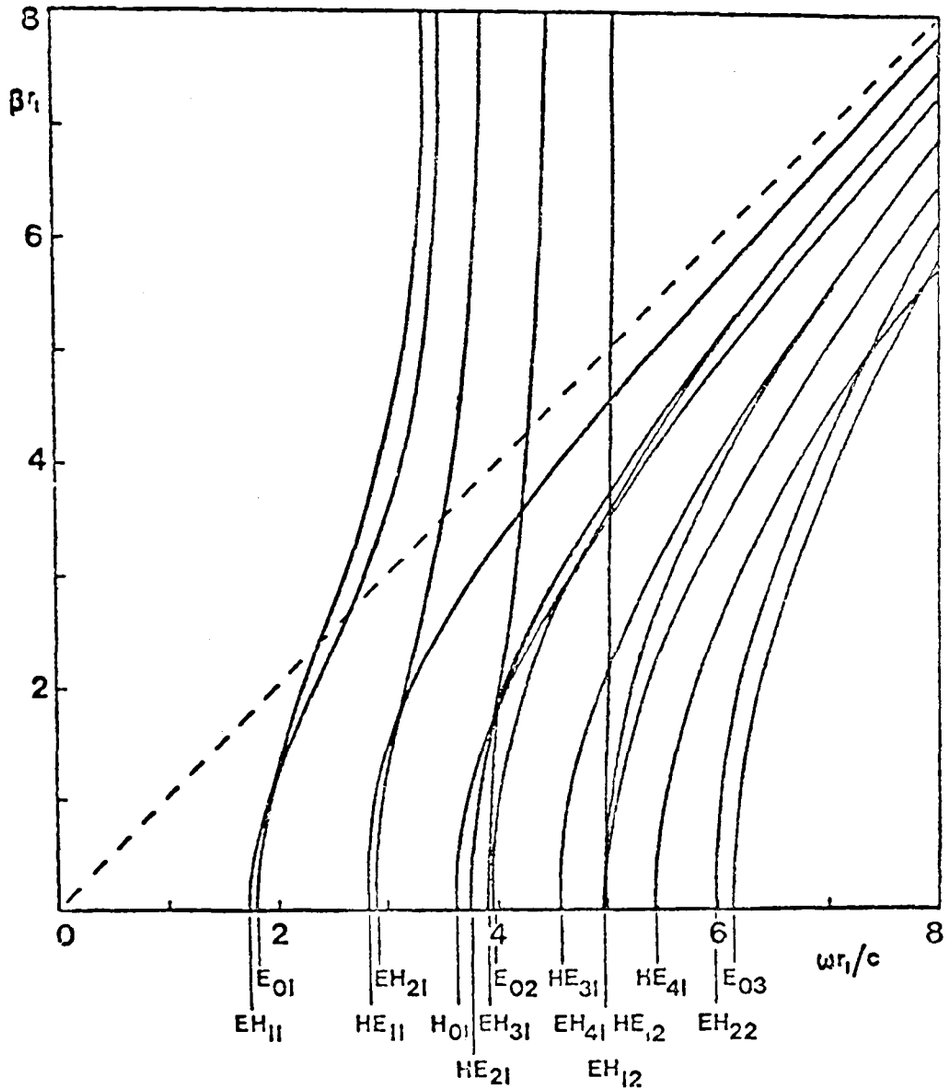

(a)

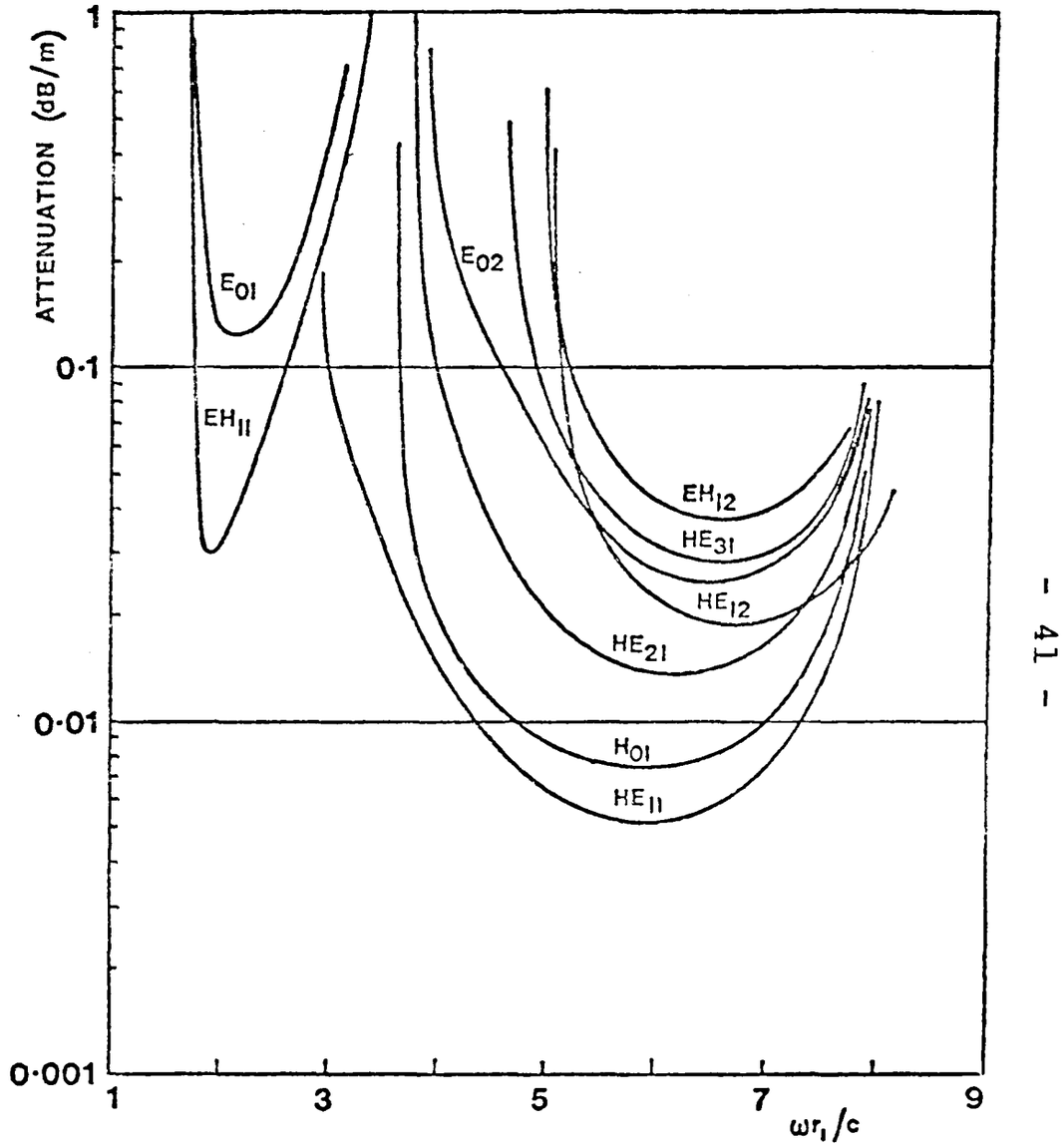

(b)

Fig. 2.6 Typical propagation and attenuation characteristics for a corrugated circular waveguide

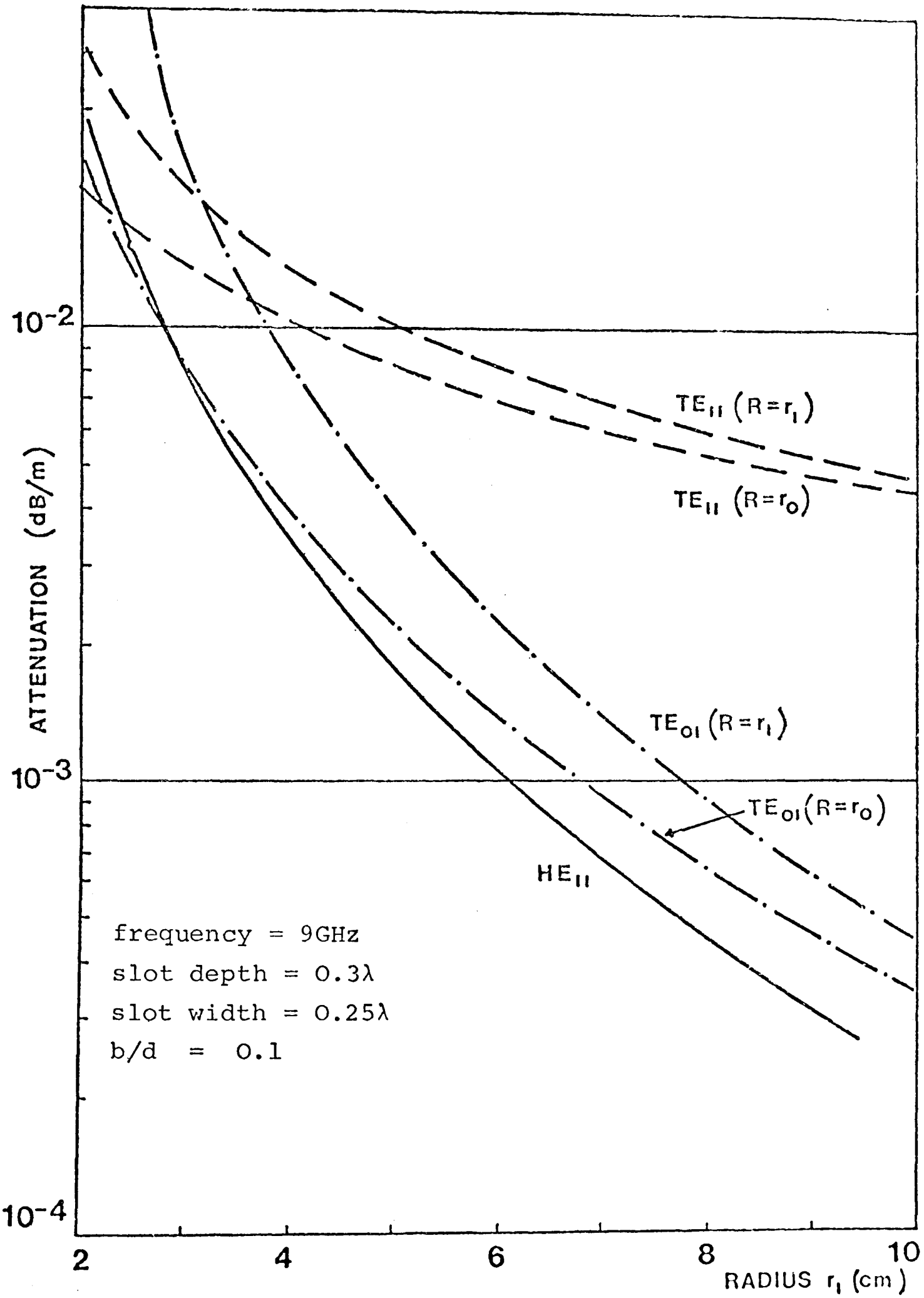

Fig. 2.7 Attenuation characteristic of corrugated circular waveguide as a function of radius, compared with various smooth wall waveguide modes of comparable diameters.

corrugated waveguide. Throughout most of the range the HE_{11} mode attenuation is lower than any of the smooth wall circular waveguide modes. Although the attenuation has a bandpass characteristic the variation between maximum and minimum attenuation over a half octave bandwidth is only approximately 50%. It should also be pointed out that the overmoding factor for the corrugated waveguide is less than that for the corresponding smooth wall waveguide.

The other, more practical design, is to restrict the waveguide operation so that only the HE_{11} mode, plus three higher order modes (H_{01}, E_{02}, HE_{21}) can propagate. This requires that the normalised operating frequency be given by $\bar{r}_1 = 4.7$, which ensures that the HE_{12} and EH_{12} modes, being difficult to suppress once coupled, remain below cut-off. A design chart < 2 > for this waveguide is shown in figure 2.8, and is used as follows. For a chosen operating frequency the waveguide parameters r_1, r_o and d are read from the left hand scale, while the attenuation at the operating frequency is read from the right hand scale, the other optimised parameters are shown on the figure. Comparison of the attenuation for the corrugated waveguide with its competitors, figure 2.9, shows it to be lower than for the TE_{11} mode in a comparable circular waveguide and significantly lower than for the dominant mode waveguides.

A higher overmoding factor creates many problems, especially due to HE_{1m} mode coupling, and therefore it is this latter restricted mode design that will be used in

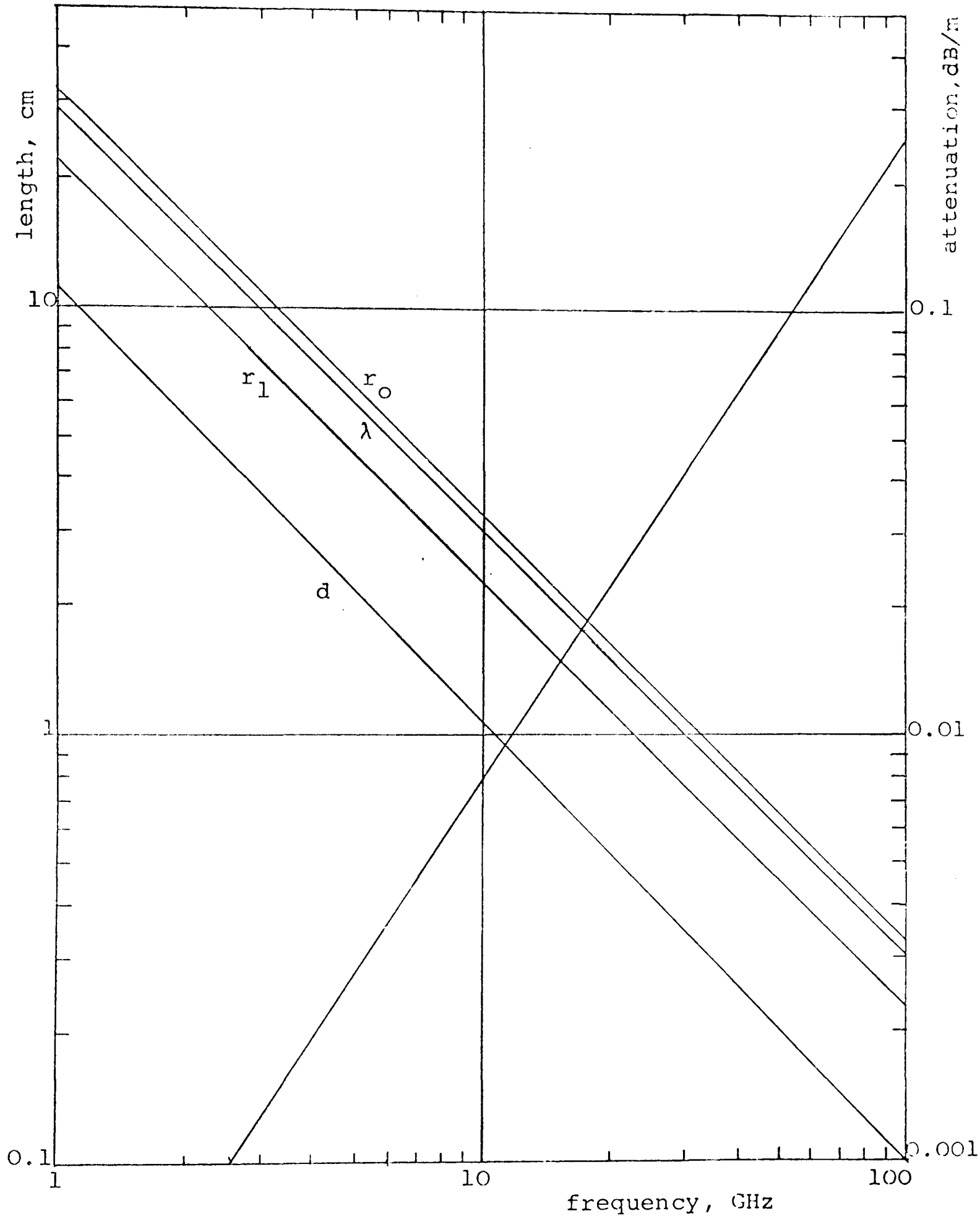

Fig. 2.8 Design chart for operation of HE_{11} mode with 4 propagating modes.

parameters: $\bar{r}_1 = 4.7$, $r_1/r_o = 0.694$, $(r_o - r_1) = 0.33\lambda$

$b/d = 0.1$, $d = 0.35\lambda$

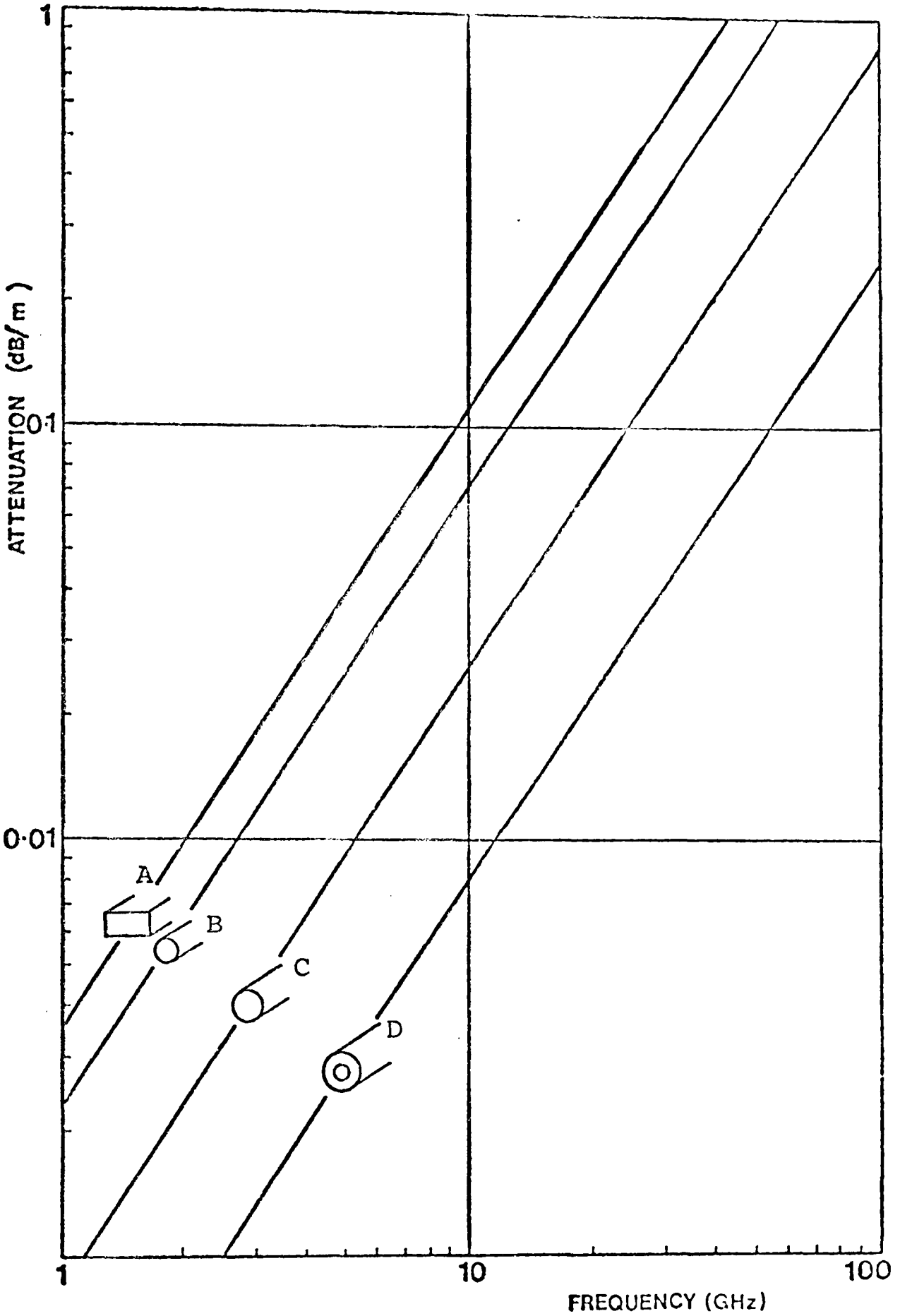

Fig. 2.9 Comparison of the attenuation of various copper waveguides.

A Rectangular waveguide, TE_{10} mode, $f/f_c = 1.5$, single mode

B Smooth wall circular, TE_{11} mode, $f/f_c = 1.35$, single mode

C Smooth wall circular, TE_{11} mode, $f/f_c = 2.0$, 3 propagating modes

D Corrugated circular, HE_{11} mode, $f/f_c = 1.75$, 4 propagating modes.

this antenna feeder application. However, in chapter 8 an HE_{11} single mode design is developed for use where low attenuation is not a prime requirement.

In general two possible mechanical configurations for the corrugated waveguide exist, one of which is a rigid construction, figure 2.10(a), having corrugations with thin ridges for low attenuation (generally the thinner the ridge width the lower the attenuation < 5 >). The other is a flexible structure having thicker ridge widths, figure 2.10(b), and consequently possessing a slightly higher attenuation. For the waveguide shown in figure 2.10(b) the increase in attenuation at $\bar{r}_1 = 4.7$, due purely to the larger ridge width, is approximately 6% over that of the rigid waveguide design, figure 2.10(a). Al-Hariri < 3 > has studied the effects of a rounded slot profile on the propagation and attenuation characteristics of corrugated circular waveguides. This was done by approximating the rounded groove by a step profile and using the simple impedance concept to calculate the propagation and attenuation characteristics. Using this technique the effect of the rounded slot profile, shown drawn to scale in figure 2.10(b), is to increase the attenuation by 9% over that of the rectangular slot profile. Therefore taking into account both effects the flexible waveguide design, figure 2.10(b), has a 15% higher attenuation than the rigid waveguide design, figure 2.10(a).

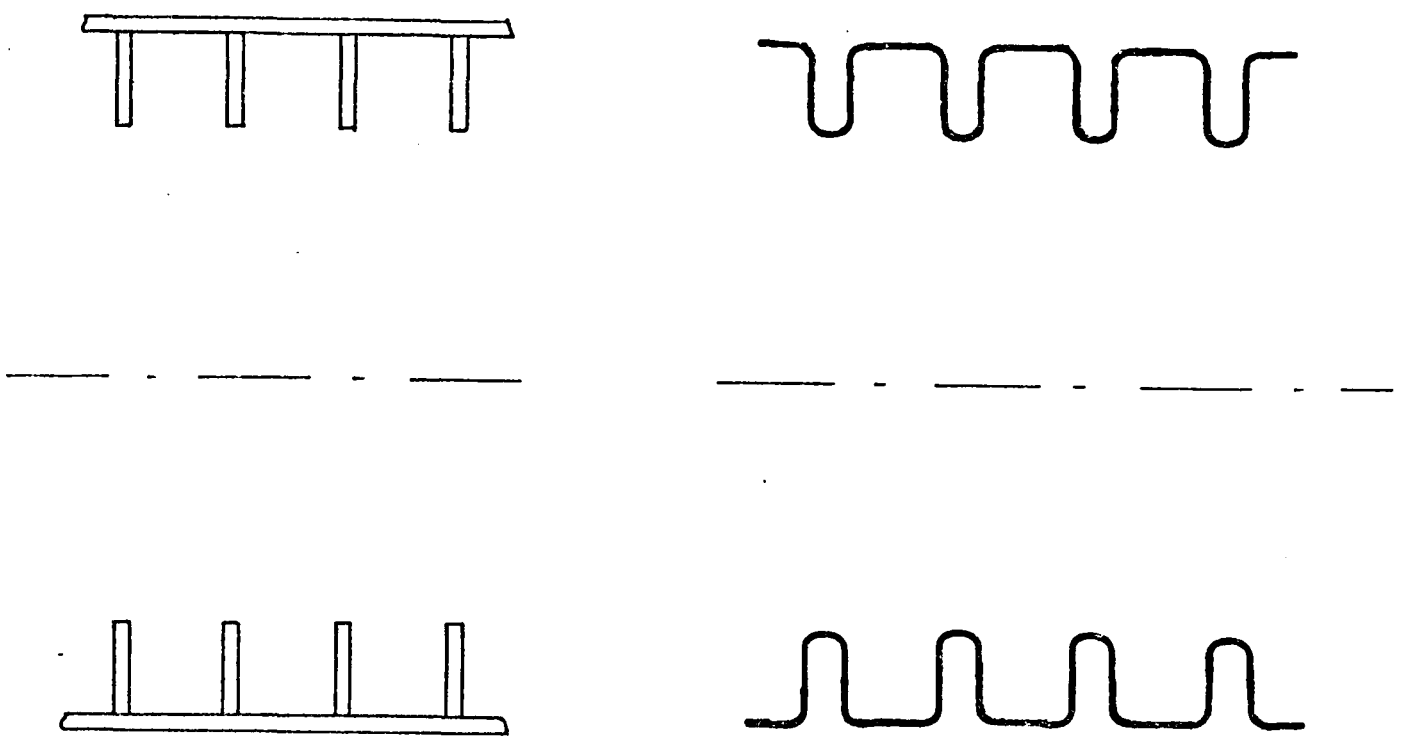

(a) Rigid Design (b) Flexible Design

Fig. 2.10 Scale drawings of rigid and flexible corrugated waveguide designs for 9GHz operation. (4 propagating modes)

2.3.2 Survey of the Problems Involved in the use of the Corrugated Waveguide as an Antenna Feeder

One of the major problems involved in the use of overmoded waveguides is avoiding the possible coupling of the dominant mode into higher order modes. For the corrugated circular waveguide design restricted to 4 propagating modes the dominant HE_{11} mode couples into all 3 higher order propagating modes (H_{01}, E_{02}, HE_{21}), due to various types of imperfection along the waveguide run. This higher order mode coupling can be caused by 3 principal mechanisms:

1) Bends along the waveguide run.

2) The increase in corrugated waveguide diameter required after the transition from smooth wall-to-corrugated waveguide.

3) Poor mechanical construction of the waveguide.

The effect on the performance of the corrugated waveguide due to the presence of higher order modes depends on how it is employed as an antenna feeder. When one end of the waveguide run is used open-ended, as the primary feed for a reflector or when it is directly connected to a corrugated horn primary feed, the presence of higher order modes produce two detremental effects on the antenna performance when no mode or polarisation filtering is used. Firstly the primary feed co-polar radiation pattern is distorted and secondly the primary feed pattern exhibits a high level of cross-polarisation in all planes. This distortion of the radiation pattern is undesirable because of (a) loss of antenna gain, (b) shifting in the main beam direction, and (c) loss of polarisation purity. It is therefore essential to determine in what way various higher order modes distort the co-polar and cross-polar patterns and this is studied in chapter 9.

When the corrugated waveguide is operated with single mode input-output, as in the case where it is used to replace the waveguide run in an existing antenna system, the undesirable *trapped mode effect* < 4 > occurs. The effect is shown diagramatically in figure 2.11, for the idealised case of only one higher order mode present. The

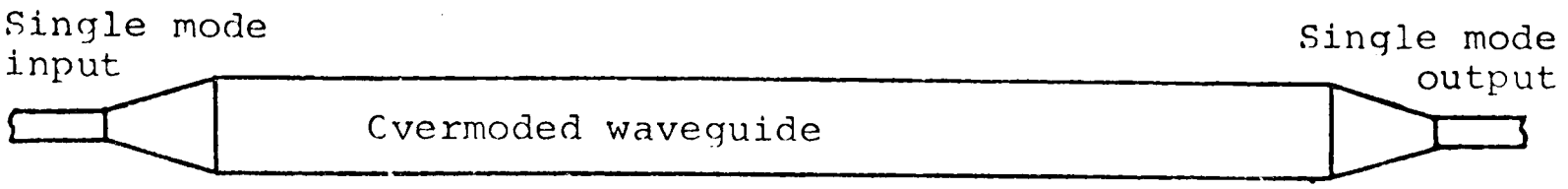

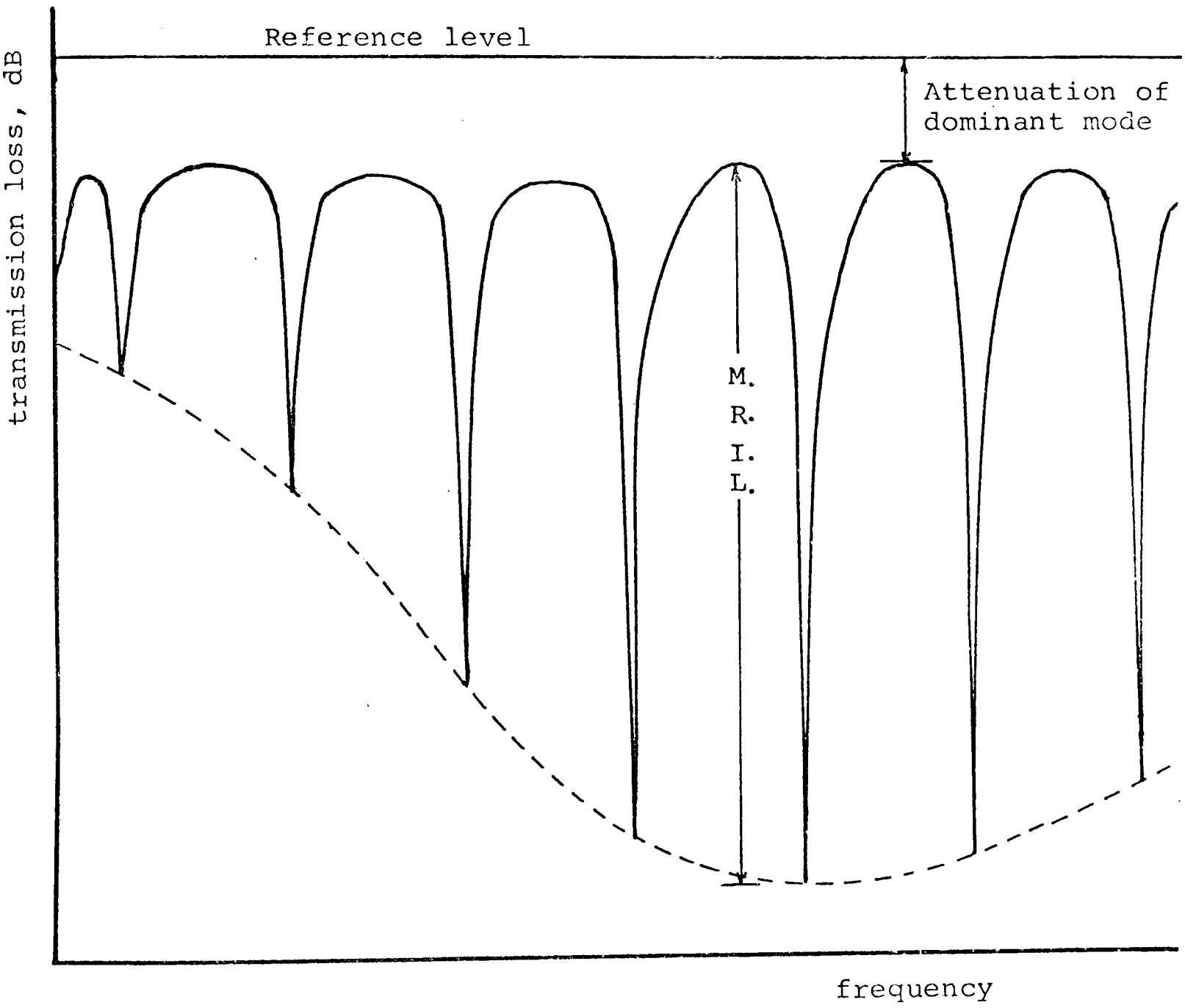

Fig. 2.11 Sketch of the transmission spectrum for an overmoded waveguide with single mode input and output

transitions in corrugated waveguide diameter occurring at each end of the waveguide run do not permit the higher order modes to propagate through them, these modes becoming cut-off in the throat region of the transition. This causes the incident higher order mode to be reflected back down the waveguide, the transition acting like an endplate of a resonant cavity to these modes. When the frequency is such that the forward and backward travelling waves of the higher order mode interfere constructively a resonance occurs. The level of coupling from HE_{11} mode to H_{01} mode varies periodically with frequency < 4 > as shown in figure 2.11. The amplitude of the largest resonance, the Maximum Relative Insertion Loss (M.R.I.L.) depends on the higher order mode attenuation. In the case of the corrugated waveguide the H_{01} mode has the lowest attenuation, figure 2.6(b), and consequently produces the most serious trapped mode loss. This trapped mode loss is totally unacceptable in a communications system, where a flat, or at worst monotonically changing,† transmission spectrum is essential for error free communication.

In view of the potentially serious effects of higher order modes on the antenna system performance the various mechanisms causing this coupling will now be considered, with a view to identifying the major mechanisms and

†A monotonically changing transmission spectrum is common in communication systems due to frequency dependence of diplexers, circulators, mixers, etc. and is corrected using electronic equalisation.

quantifying their contribution.

Mode conversion due to intentional or unintentional waveguide bends is most serious in a flexible waveguide design. As well as the 2 or 3 intentional bends likely to occur in a typical waveguide feeder there can exist a number of small bends or tilts which may significantly add to the level of higher order mode coupled. This latter effect can be overcome by using a mechanical construction that resists unintentional tilts. For example, the use of a rubberised coating on the outer wall, similar to that used in covering flexible rectangular waveguide. Chong < 2 > has briefly studied theoretically, the problem of coupling due to intentional bends, using the simple impedance corrugated waveguide model. However, no attempt was made to include the effect of the space-harmonics or to consider how the plane of the bend influenced the coupling level. As far as the author is aware, no experimental measurements to determine mode conversion due to bending in a corrugated waveguide have ever been made. In order to quantify this potentially detremental effect to the feeder performance, a theoretical and experimental investigation of mode conversion due to bends was undertaken and is presented in chapter 5.

Mode conversion due to the required transition from smooth wall circular to corrugated circular waveguide occurs because of the change in diameter and surface impedance seen by the HE_{11} mode. Chong < 2 > has studied the design of these transitions both theoretically and experimentally, and

designs exhibiting V.S.W.R.'s of 1.05 and H_{01}, E_{02}, HE_{21} mode conversion levels of better than -30dB† were measured. The low coupling is to be expected as Karbowiak < 4 > has shown that a *pure* diameter change will only couple modes of the same azimuthal number as the input modes. For the corrugated waveguide considered here, the HE_{12} is the first such mode to propagate, and was found by Chong to have a coupling level of ≈-25dB for his transition design. However, by limiting the waveguide design to only 4 propagating modes the HE_{12} mode is kept just below cut-off. Therefore it can be concluded that mode conversion due to the transitions can be considered negligible if care is taken in their design.

Mode conversion will also occur due to current flow discontinuities on the inner surface of the corrugated waveguide, resulting from poor mechanical construction. This effect is serious because the current discontinuity causes increased dominant mode attenuation. The effect occurs in both flexible and rigid waveguides and largely depends on the method of construction used. Chong < 2 > found that a helical welded seam running down the length of a flexible corrugated waveguide produced serious mode conversion problems. The author has found that poor contact between the corrugated side wall and base, of a rigid waveguide, resulted in a high attenuation and high

†This was the lowest coupling level that could be measured by Chong.

mode conversion levels. These and similar mechanisms should be avoided at all costs, and manufacturing methods designed to avoid such effects are considered in chapter 11.

It appears certain that some amount of higher order mode power will be present in a corrugated waveguide feeder, especially when a flexible construction is used. For this reason the use of mode filters to provide higher order mode suppression is considered in chapter 7 where a new type of mode filter providing continual mode suppression, with negligible insertion loss, is presented. However, where flexibility is a major requirement, as in the portable antennas of class 3, the use of these mode filters is a disadvantage, as it limits the waveguide to single linear polarisation operation. Therefore for this class of antenna, where very low attenuation is not a prime requirement and where dual linear or circular polarisation operation is desirable, the requirement exists for a monomode corrugated waveguide with an attenuation of <3dB/100m. By adjusting the corrugated waveguide geometric parameters HE_{11} single mode operation within this attenuation limit is possible. A complete design study of this single mode corrugated waveguide is presented in chapter 8.

Another major effect that can deteriorate the performance of waveguide feeders is the inevitable presence of random ellipticities resulting from manufacturing tolerances and handling deformations. Such imperfections cause coupling to the orthogonal polarisation of the dominant mode resulting in the presence of a cross-

polarised component at the waveguide output. This waveguide generated cross-polarisation adds to that radiated by the desired feed mode resulting in a deterioration of the overall antenna cross-polar performance. With the increased emphasis placed on dual polarisation frequency re-use operation it is important to assess the potential cross-polar performance of corrugated waveguides in the presence of random ellipticity. In chapter 6 this problem is examined theoretically and experimentally in order to quantify the ellipticity tolerance allowable in order to remain within a specified level of cross-polarisation. Results for both smooth wall and corrugated waveguides are presented.

In this section the problems involved in using the corrugated waveguide as an antenna feeder have been identified. In subsequent chapters these problems are considered in detail enabling the overall performance of corrugated waveguide feeders to be predicted. A summary of the performance requirements for corrugated waveguide feeders, in each of the three main antenna classes, is given in table 2.2.

2.4 THE CORRUGATED WAVEGUIDE AS A LOW CROSS-POLARISATION PRIMARY FEED

It was shown in section 2.2 that one of the major areas of antenna development now occurring in both satellite and terrestrial communication systems is that of dual polarisation frequency re-use operation. For the

TABLE 2.2

Antenna Class	1	2	3
Typical Application	Waveguide feeder for satellite earth station employing a beam waveguide feed	Waveguide feeder for micro-wave relay system	Flexible waveguide feeder for portable satellite or terrestrial antenna system
Corrugated Wave-guide Type	Overmoded, Rigid for minimum mode conversion, Thin ridge width for low attenuation, Sufficient circularity to produce less than -70dB cross-polarisation, Operated with one end open and feeding a narrow flare-angle corrugated conical horn	Overmoded or single mode, Rigid or flexible design, Attenuation less than overmoded smooth wall circular, Sufficient circularity to produce less than -50dB cross-polarisation, Operated with either one end open or single mode input-output	Single mode Flexible design Attenuation <3dB/100m Sufficient circularity to produce less than -50dB cross-polarisation, Operated with one end open
Typical Waveguide Length	10 metres or less	100 metres	100 metres
Polarisation	Dual linear or Dual Circular	Dual or single	Dual or single
Typical Operating Frequencies	4GHz to 6GHz; 11GHz to 14GHz	Generally below 10GHz	7GHz
Typical Bandwidth	40%; 24%	10%	5%

portion of the frequency spectrum at present employed, the bandwidth available using this technique can be approximately doubled over that available with single polarisation operation.

In any communication system where dual polarisation frequency re-use is to be achieved the characteristics of the antenna become a critical feature of the overall system performance. The antenna requires a high degree of polarisation purity because the channel isolation depends on the overall cross-polarisation purity achieved. This implies much stricter requirements than in the past where cross-polarisation was solely considered as one of the efficiency reducing factors. The various factors contributing to the total radiated cross-polar power of an antenna are listed below:

1) The primary feed radiation pattern.
2) Primary feed displacement and misalignment.
3) Subreflector misalignments (dual reflector configurations).
4) Blockage due to primary feed, struts and subreflector.
5) The main reflector curvature.
6) Reflector profile errors.
7) Reflector asymmetry (offset configurations).

Various workers have studied these individual effects in order to determine their relative importance, and a brief review of this work will now be given.

Thomas <17> has shown that for both front fed paraboloid and dual reflector antenna systems minimum cross-polarisation is achieved when the feed radiates a polarisation pure field, and in this case the front fed paraboloid is superior. In fact if a parabolic reflector is fed using a pure Huygens source, zero radiated cross-polar power is obtained. Rifai <18> has made an extensive study of the effects contributing to cross-polarisation in dual reflector antennas, and has found that, for a polarisation pure feed, misalignments of the subreflector and feed are the most dominant factors. Cross-polarisation due to blockage effects have been found to be a minor contributing factor. Miller <19> has studied the effect of reflector profile errors and has found that for errors less than $\frac{\lambda}{16}$ negligible cross-polarisation results, the feed cross-polarisation being the dominant factor. Miller has also shown that cross-polarisation produced by the main reflector curvature is generally less than -50dB, and therefore a minor effect. Reflector asymmetry, such as found in an offset reflector antenna, produces an inherent cross-polarisation in the plane of asymmetry when fed by a linearly polarised Huygens source <20>. However, Rudge <21> has shown that by using a multimode feed to match the focal region fields this cross-polarisation can be cancelled. When a circularly polarised primary feed illumination is employed offset reflectors do not generate a cross-polarised component, the only significant cross-polarisation occurring being due directly to the primary

feed <20>.

Brain <22> has studied the cross-polarisation efficiency of front fed parabolid reflector antennas, defining this efficiency as the ratio between the relative peak cross-polarisation from the overall antenna to that from the feed alone. Using theoretical and experimental data for typical corrugated waveguide feed patterns published by the author <23> he found that a typical parabolic reflector antenna (edge illumination around -10dB, F/D in range 0.3→0.5) will have a cross-polarisation efficiency of about -4 to -6dB. Therefore to obtain the generally specified <24> overall antenna peak cross-polarisation of -40dB the feed must possess a peak cross-polar level of about -36dB.

The results obtained by various workers and presented in this section strongly suggest that future studies should be aimed at improved feed systems <24>.

Over the past few years considerable effort has gone into the design of feeds to efficiently illuminate either main reflector or subreflector of the antenna. Fundamental to these designs has been the analysis of the fields in the focal region of the reflector antenna <25>. This has shown that a hybrid mode field is required in the feed if there is to be efficient coupling between the feed and the focal region field. The most important classes of feed producing a hybrid mode field are corrugated circular waveguides and horns. When operating in the dominant HE_{11} mode such feeds can produce a field at their aperture which very closely

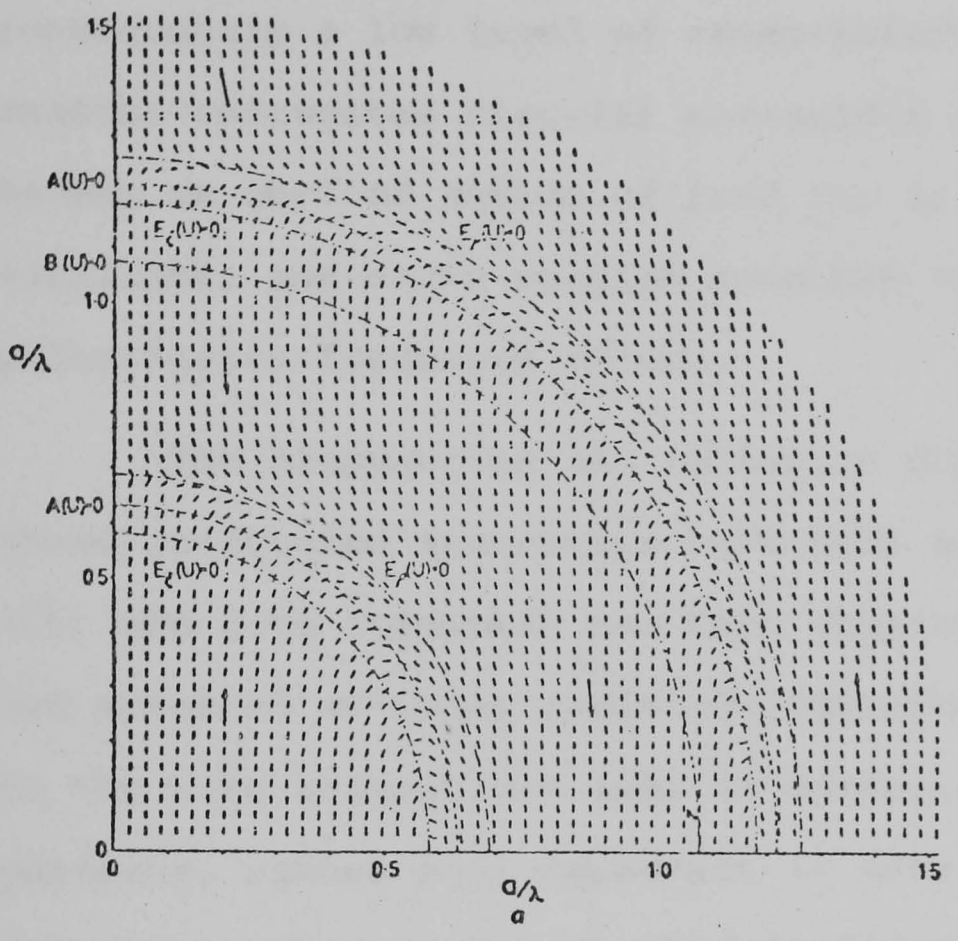

Typical electric field distribution in focal plane of a paraboloid

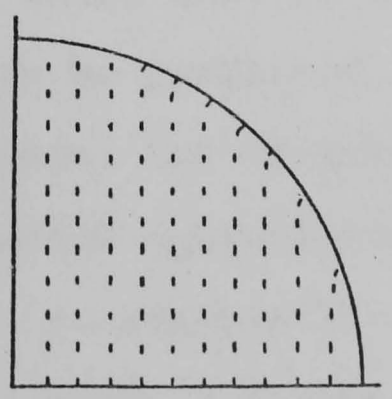

Aperture electric field of the HE_{11} mode in a corrugated waveguide

Fig. 2.12 Comparison of focal region field of a paraboloid reflector with the aperture field of a corrugated waveguide

resembles the focal region field of a reflector antenna, figure 2.12. Because of this match these feeds produce a near circularly symmetric radiation pattern and consequently a low level of cross-polarisation. For these reasons corrugated circular waveguides and conical horns become an obvious choice of feed for terrestrial, satellite, and earth station antennas operating with dual polarisation frequency re-use.

The propagation and radiation characteristics of these corrugated structures have been analysed extensively <26> and good agreement has been obtained between predicted and measured co-polar radiation patterns. However, subject to the same assumptions made in determining the co-polar patterns, rather poor agreement is obtained for the cross-polar patterns, as illustrated in figure 2.13. Because of the dominance of the feed cross-polarisation in determining the overall antenna cross-polar performance an accurate feed model must be used if accurate antenna performances are to be predicted. An accurate feed model is also essential for future antenna design if use is to be made of design optimisation techniques, now being developed <27>, to achieve an acceptable cross-polar performance. Accordingly a theoretical and experimental investigation has been conducted (chapters 9 and 10) for two types of feed, 1) a corrugated waveguide, of small diameter producing a wide beamwidth, as required at the prime focus of a reflector antenna; 2) a narrow flare-angle conical corrugated horn of large diameter producing a

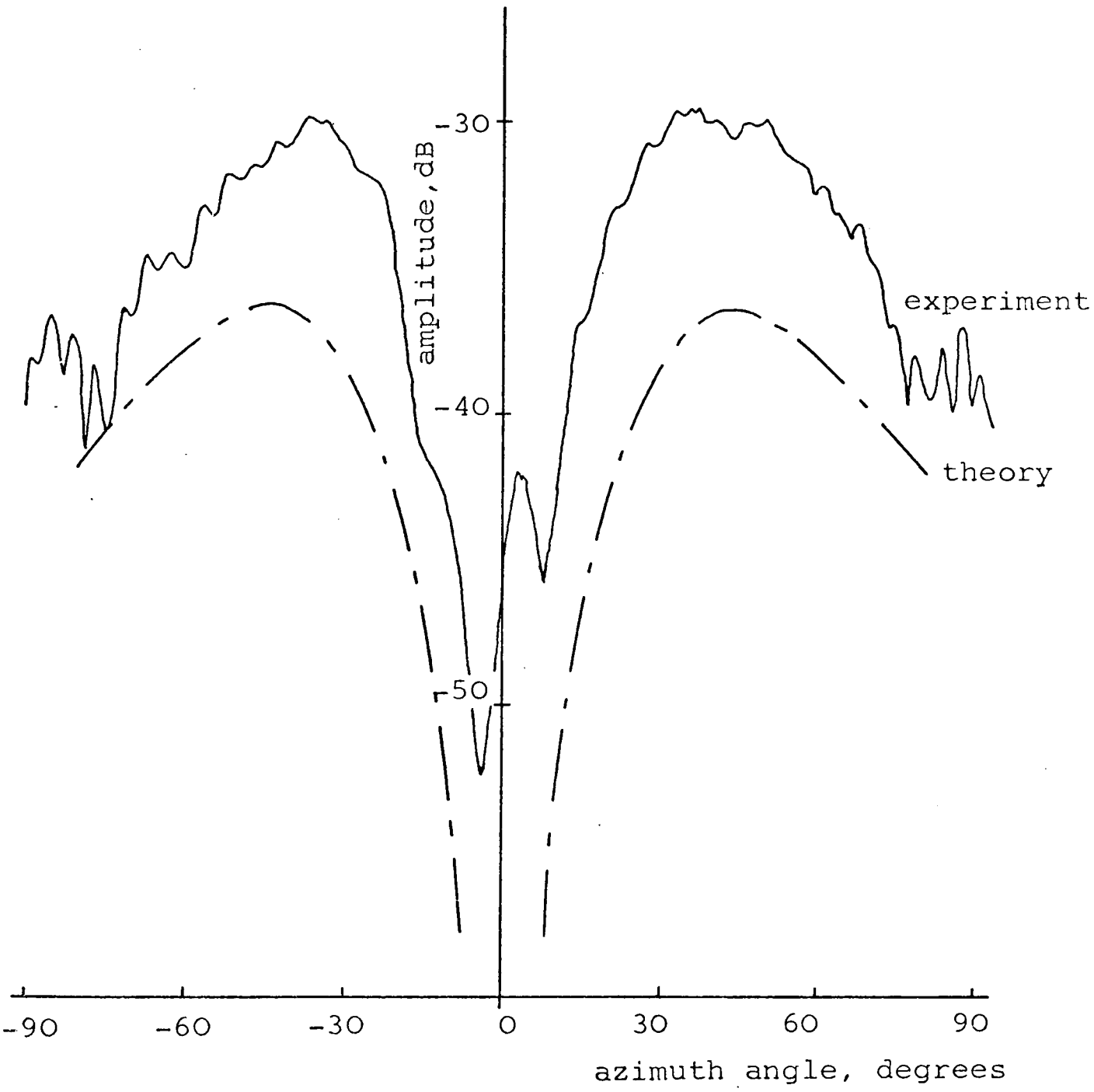

Fig. 2.13 Comparison of the measured and predicted cross-polar radiation pattern of a corrugated waveguide

narrow beamwidth as required in a Cassegrain reflector antenna. From these two cases general conclusions are reached concerning the phenomenon of cross-polar radiation from corrugated feeds. In chapter 10 these conclusions are used to obtain design curves for optimum feed cross-polar performance.

CHAPTER 3

ANTENNA FEED MEASUREMENTS

3.1 INTRODUCTION

Many of the experimental measurements made for this thesis involve the measurement of co-polar and cross-polar antenna feed radiation patterns. Therefore the first part of this chapter describes the techniques used and the errors involved in the measurement of these radiation patterns. In the final part of this chapter a new experimental technique for the determination of the level of higher order mode present in the radiating aperture of a feed is described.

The three basic antenna radiation pattern measurement techniques available are considered in section 3.2 and the two best suited for antenna feed measurements are identified. In section 3.3 the measurement of co-polar and cross-polar feed radiation patterns using an anechoic chamber are described and an experimental evaluation of the Queen Mary College Anechoic Chamber, enabling the accuracy of measured patterns to be determined, is presented. Finally, section 3.4 describes the technique developed for measuring the level of higher order mode in a feed aperture.

3.2 ANTENNA RADIATION PATTERN MEASUREMENTS

To measure the radiation pattern of any antenna or

feed, it is necessary to produce a region of pseudo plane electromagnetic waves within which the test antenna can be placed. There are four basic methods of creating this pseudo plane wave region:

1) Anechoic chamber
2) Far-field Range
3) Compact Antenna Range
4) Near-field measurements followed by computations to obtain far-field equivalent radiation patterns.

The last method is rather different from the first three and is currently only used where another method is impractical, for example the measurement of on-board satellite antennas prior to launch. This method will not be referred to again here.

The anechoic chamber and far-field range create the pseudo plane wave region by utilising a small portion of a spherical wavefront, figure 3.1(a). If the test antenna aperture diameter, D, is small compared to the length of the range the phase and amplitude of the electromagnetic wave at the test aperture will possess only a slight taper away from the axis. Usually the minimum length for this type of range is taken to be $\frac{2D^2}{\lambda}$ which gives a phase difference of 22.5^{o} between centre and edge of the test aperture. However, in practice it is necessary to employ some method of suppressing reflections from surrounding surfaces and objects in order that they do not interfere with the direct rays producing the pseudo plane wave test region. For small

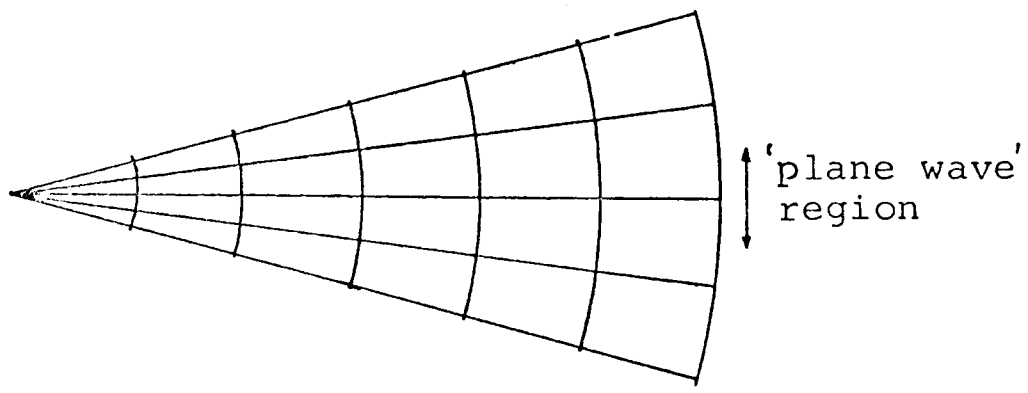

Fig. 3.1(a) Spherical wavefront used in far-field ranges

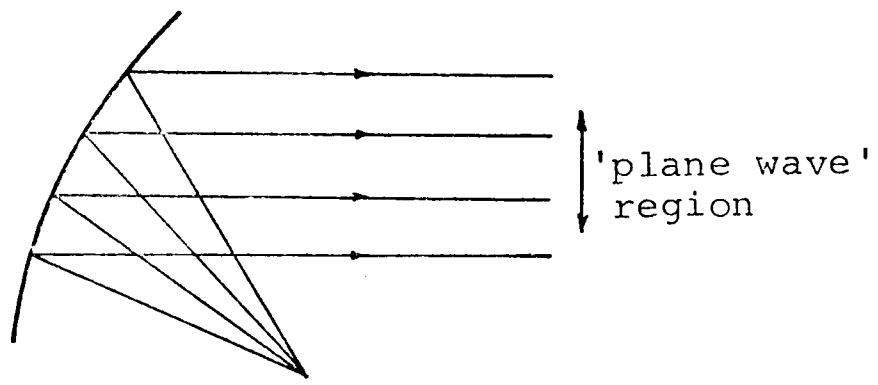

Fig. 3.1(b) Parabolic reflector used to produce offset Compact Range

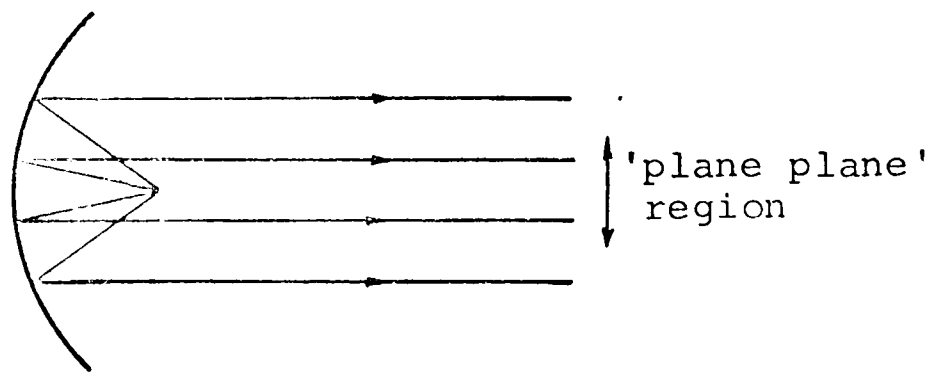

Fig. 3.1(c) Centre-fed Compact Range

diameter antennas, such as feeds, a relatively short length between source and test antennas can be used. In this case it is practical to enclose both the source and test antennas in an anechoic chamber. Therefore all reflected rays are partially absorbed, the degree of absorption depending essentially on the design of the chamber and the quality of the absorbent material used to line its walls. Alternatively large diameter antennas require large distances between source and test antennas, for example a 3 metre diameter antenna would require a range distance of >600 metres. It is clearly impractical in this case to use the anechoic chamber solution. Therefore the source and test antennas are mounted on high towers so that the only local reflecting surface is the ground. By ensuring that the source antenna radiates a null in the direction of the ground reflected ray an acceptable pseudo plane wave test region can be obtained. This latter method is termed the outdoor far-field antenna measurement range.

Where possible it is advantageous to use an anechoic chamber as it is (1) simpler and more convenient to use; (2) requires a less powerful source and less sensitive receiver; (3) has the added advantage of indoor operation. Because of the requirement here to only measure small feeds, the outdoor far-field range will not be referred to again.

The basic concept behind the compact antenna range is to achieve the pseudo plane wave region by collimating

the radiation from a point source using a parabolic reflector, which is either offset or centre fed, figure 3.1(b) and (c). A portion of the collimated beam, in the source antenna near-field, will be a plane wave with superimposed small amplitude ripples caused by radiation from the edges of the reflector and feed support (centre fed). It has been found <28> that these ripples can be made small enough so that test antennas occupying up to about one sixth of the area of the source reflector can be measured. Because of the beam collimation effect only a small amount of absorber is required to keep reflections down to an acceptable level. A brief comparison of compact antenna ranges with far-field ranges is shown in table 3.1, which is extracted from an extensive study performed by Olver <28>.

With the increasing use of dual polarisation frequency re-use antennas over the past few years has come the need for accurate antenna cross-polarisation measurements. Because of this requirement the inherent level of cross-polar power present in the pseudo plane wave test area of an antenna measuring range is an important factor in determining measurement accuracy. To date there has been little published work on the cross-polarisation performance of anechoic chambers and compact antenna ranges. The remainder of this section considers the factors determining the cross-polar performance of these two types of antenna measurement ranges.

TABLE 3.1

Comparison of Antenna Ranges

	Outdoor far-field	Indoor far-field (Anechoic Chamber)	Compact Antenna Range
Range length	$>2D^2/\lambda$	$>2D^2/\lambda$	5 - 10m
Usable frequencies	All	100MHz - 100GHz	1 - 40GHz
Reflectivity level	Depends on site could be -80dB	Depends on wall absorber (-50dB)	-30dB to -60dB
Test area electric field characteristic	Amplitude and phase taper	Amplitude and phase taper	Amplitude ripple and taper
Cross-polarisation performance	Good	Fairly good	Moderate
Source power	High	Low	Low
Antennas capable of being measured	All	Feeds Small antennas	Feeds Reflectors up to 2π Arrays
Weather effects operation	Yes	No	No
Interference from other sources and ranges	Yes	No	No
Security	No	Yes	Yes
Cost components	Land Towers Test equipment	Lined room Test equipment	Some absorber Reflector mounting Test equipment

The anechoic chamber has a potentially low level of cross-polarisation because the specular reflections giving rise to cross-polarised components are, to a degree, absorbed. This degree of absorption depends on the chamber design, of which there are two main types, either a rectangular box or a funnel shape. The latter tapers from the test end down to a point at the source end and has been favoured in recent years because of the reduction in absorber required over the equivalent box design. However, because most absorbent materials are poor absorbers at high angles of incidence from the normal the reflected power is higher for the funnel design than for the box design. In fact the walls of the tapered chamber cause it to act in a similar fashion to the walls of a waveguide horn, and consequently the wave propagating from the source at the apex of the funnel is not a plane wave but a waveguide mode <29>. Therefore the source antenna (usually a conical or pyramidal horn) needs to be accurately set at the phase centre of the tapered chamber if cross-polarisation rich modes are not to be excited in the funnel. On the other hand, the box design possesses none of these problems. In addition, because of the far-field nature of the pseudo plane wave test area the source antenna only requires a cross-polar null in the region of boresight to achieve a good performance over a sizeable test area, the cross-polar lobes being absorbed by the walls of the chamber. The Q.M.C. Anechoic Chamber, figure 3.2, is a compromise between the two main chamber

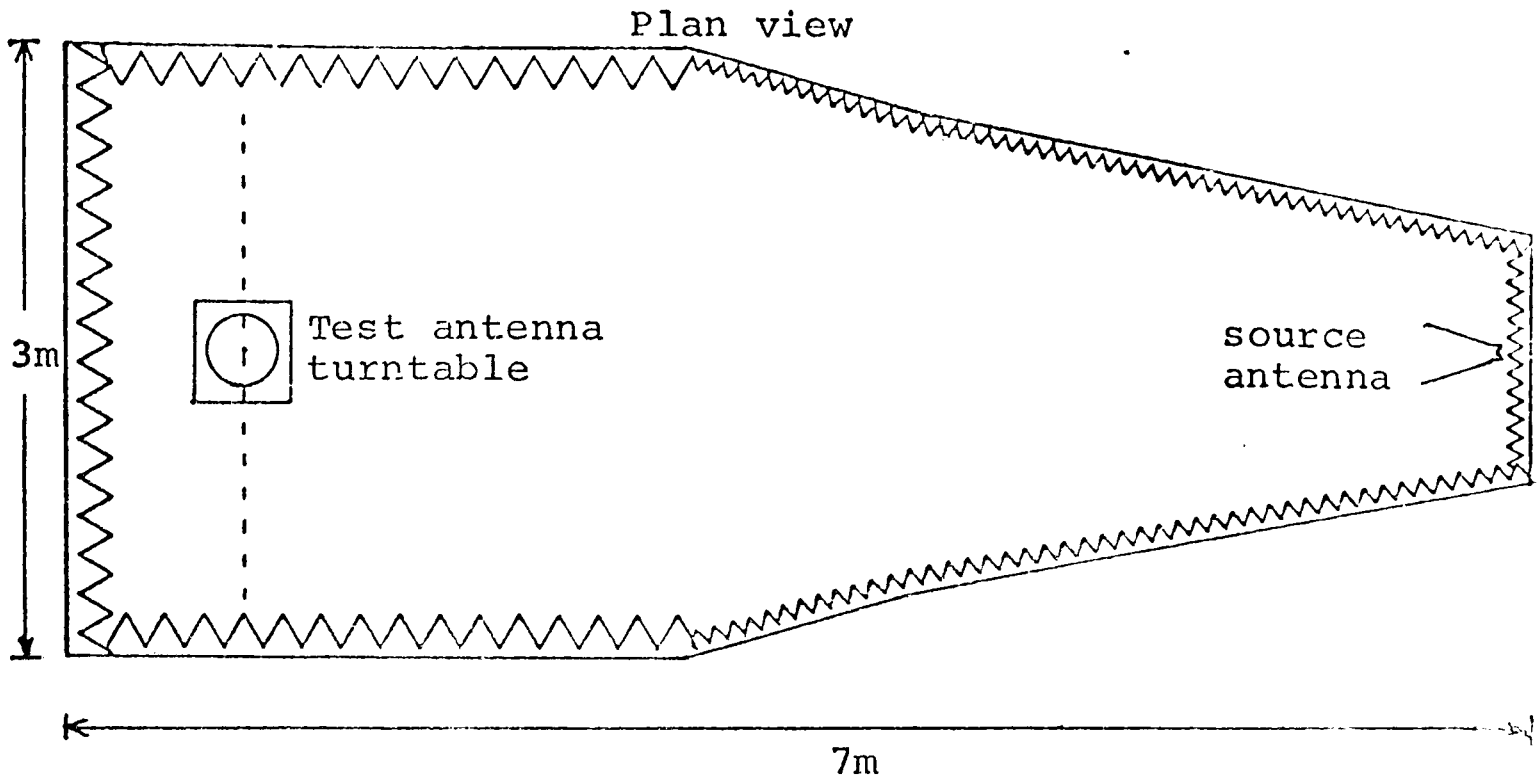

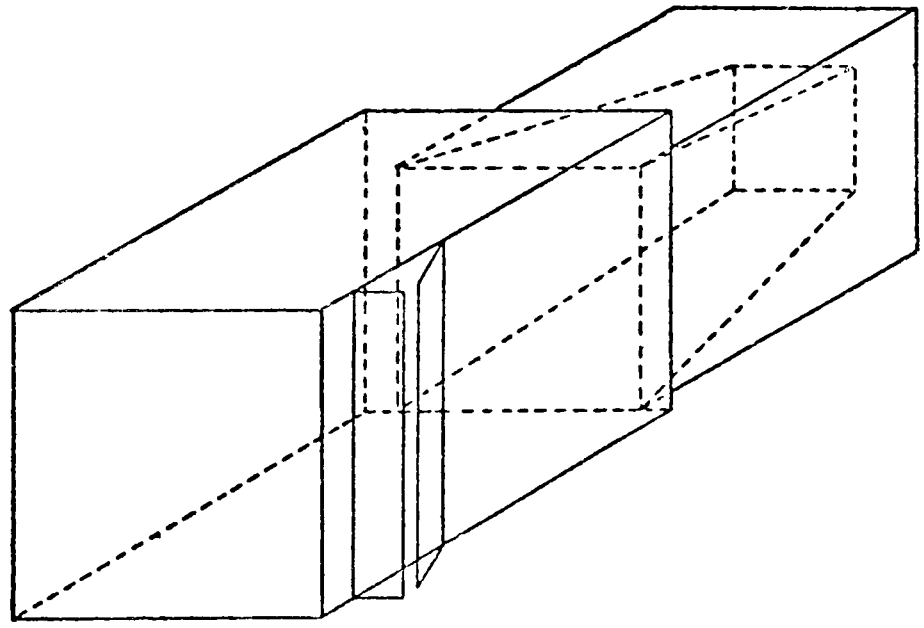

Schematic view

Fig. 3.2 The Q.M.C. Anechoic Chamber

designs <29> and exhibits a cross-polarisation level in the test region of approximately -55dB.

On the other hand, the compact antenna range can possess a high level of cross-polarisation which is principally caused by the depolarisation due to the reflector curvature. The smaller the F/D ratio of the reflector the higher the level of cross-polarisation generated. The other main contributing factors to cross-polarisation in compact antenna ranges are listed below.

1) The cross-polar lobes radiated by the feed are collimated by the reflector into the pseudo plane wave region.

2) Diffraction from the edge of the reflector, which can be reduced by reducing the edge illumination or by shaping the reflector edge so that the diffracted field components cancel <30>.

3) For a centre fed reflector additional cross-polarisation is generated by diffraction from the feed and feed support structures.

The Queen Mary College Compact Antenna Range consists of a centre fed parabolic reflector of F/D = 0.33 and has been found by the author to have a cross-polar level in the test region of order -20dB. This is principally caused by the reflector curvature and diffraction from the feed/feed support structure. For the case when an offset feed is used the cross-polarisation contributed by reflector curvature increases with increasing offset

angle. However, this configuration has the advantage that there is no diffracted cross-polar power from the feed/ feed support structure.

In view of all the above adverse effects occurring in a compact antenna range it would appear extremely difficult to achieve the -55dB cross-polarisation levels possible with an anechoic chamber. Therefore for feed cross-polarisation measurements the anechoic chamber is the obvious choice, and in section 3.3 a co-polar and cross-polar performance evaluation of the Q.M.C. Anechoic Chamber is presented. However, for co-polar pattern measurements the compact antenna range has the advantage that the experimental floor area is not confined, enabling it to accommodate large experimental rigs. For this reason the Q.M.C. Compact Antenna Range was used for measurement of the mode conversion due to bends in a flexible corrugated waveguide, where a large experimental platform is required to produce a constant radius of curvature waveguide bend.

3.3 CO-POLAR AND CROSS-POLAR FEED MEASUREMENTS USING AN ANECHOIC CHAMBER

Corrugated circular waveguides and narrow flare-angle conical corrugated horns have a characteristically low level of radiated cross-polar power, and patterns with peak levels <-40dB are possible. It is essential to know the accuracy to which these patterns can be measured if comparison with theoretical results is to be meaningful.

For this reason an experimental evaluation of the Q.M.C. Anechoic Chamber, shown in figure 3.2, was undertaken to determine this accuracy. The chamber was principally designed for X-band operation and all the feed measurements relating to this thesis were made within this band.

The measured radiation pattern of a feed will be distorted by receiving indirect rays which have been reflected from the walls of the chamber. The object of the experimental evaluation is to quantify the total signal arriving at the test area and hence specify the *reflectivity*, which is a measure of the strength of the spurious signals received by the test antenna. The reflectivity is specified in dB and indicates, for a given test antenna pattern, the level at which the recorded pattern will be distorted by signals of equal magnitude reflected from the chamber walls and arriving at the test antenna <31>. The test antenna used for the evaluation was a 17dB gain pyramidal horn, and whilst the reflectivity results obtained only strictly apply to this test antenna pattern, it is representative of the corrugated waveguide feed radiation patterns to be measured. A common technique used to measure the reflectivity is known as the *pattern comparison method* <31> <32>. The method basically consists of measuring the radiation patterns of the test antenna with the turntable centred on a number of points along a line transverse to the axis of the chamber. By choosing the spacing between the transverse measurements such that the direct and wall reflected rays differ in phase by 180^{o},

the chances of observing the interference is maximised. However, a reasonable number of points must be taken because the reflections from microwave absorber are non-specular. Figure 3.3 shows the super-position of a number of H-plane radiation patterns obtained for the Q.M.C. Anechoic Chamber. The peak-to-peak variation on the pattern due to reflections is obtained by plotting, for each recorded position in the chamber, the variation of received power at a chosen level on a reference pattern (usually centre chamber position). The results obtained for the Q.M.C. Anechoic Chamber are shown in figure 3.4 for both sides of the radiation pattern, and various pattern levels. These deviations are then translated into an equivalent reflectivity by means of the graph of figure 3.5† <28>. By repeating the procedure in the E-plane and averaging the results a mean value for the reflectivity of -56dB was obtained at a frequency of 9GHz. By using figure 3.5 the approximate accuracy of the measured radiation pattern, at any given pattern level, can be obtained. For example, at a point on a feed radiation pattern -20dB down the approximate accuracy, obtained from figure 3.5, is ±0.15dB, clearly indicating the good performance of the Q.M.C. Anechoic Chamber. Having determined that the anechoic chamber has a low reflectivity level the measurement of cross-polar

†This graph is simply a plot of $t = 20\log_{10}(\frac{I+R}{I-R})$, where t is the peak-to-peak deviation, I is the pattern level, and R the required reflectivity.

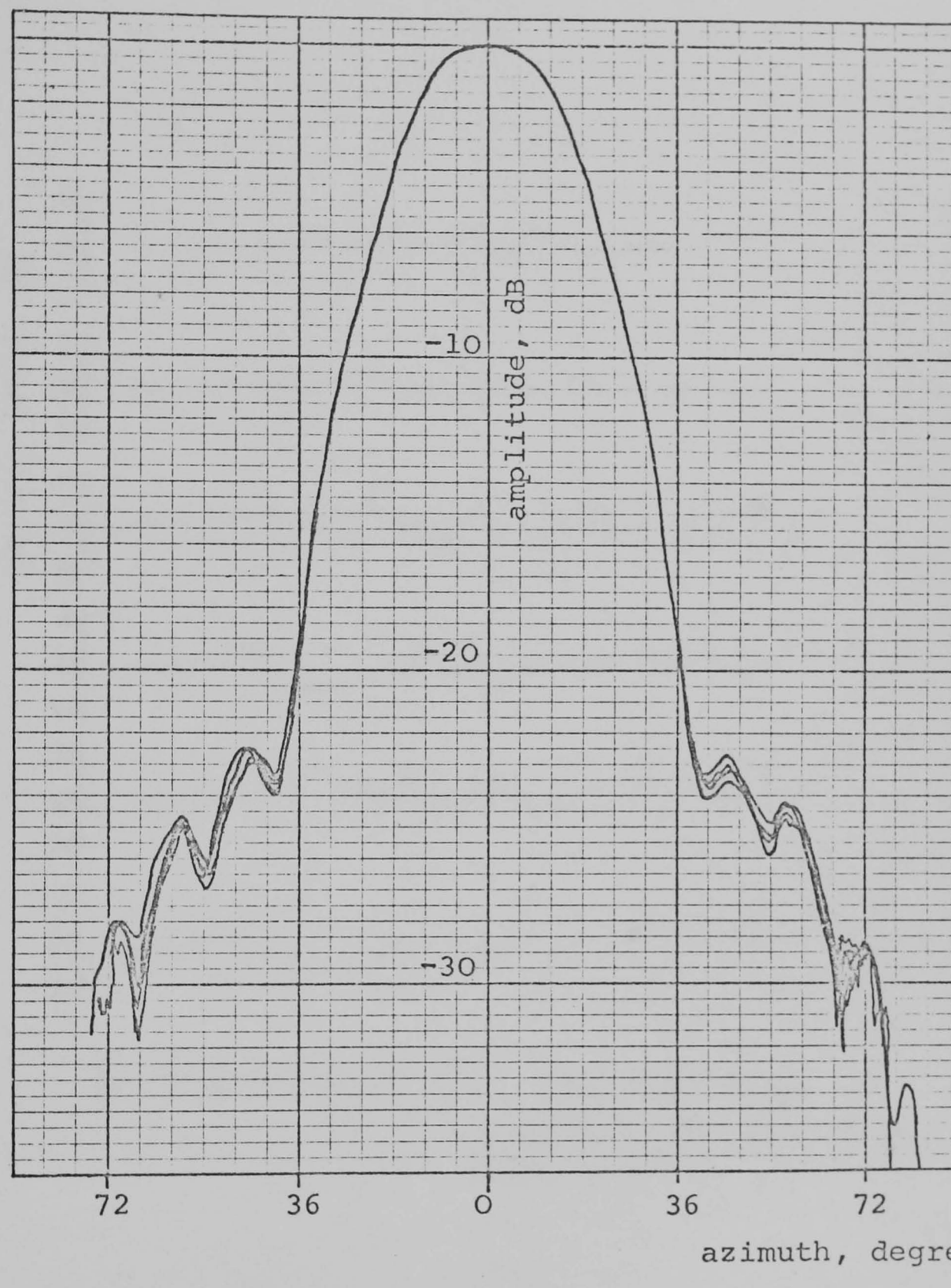

Fig. 3.3 Superposition of a number of H-plane patterns recorded at different points across the chamber.

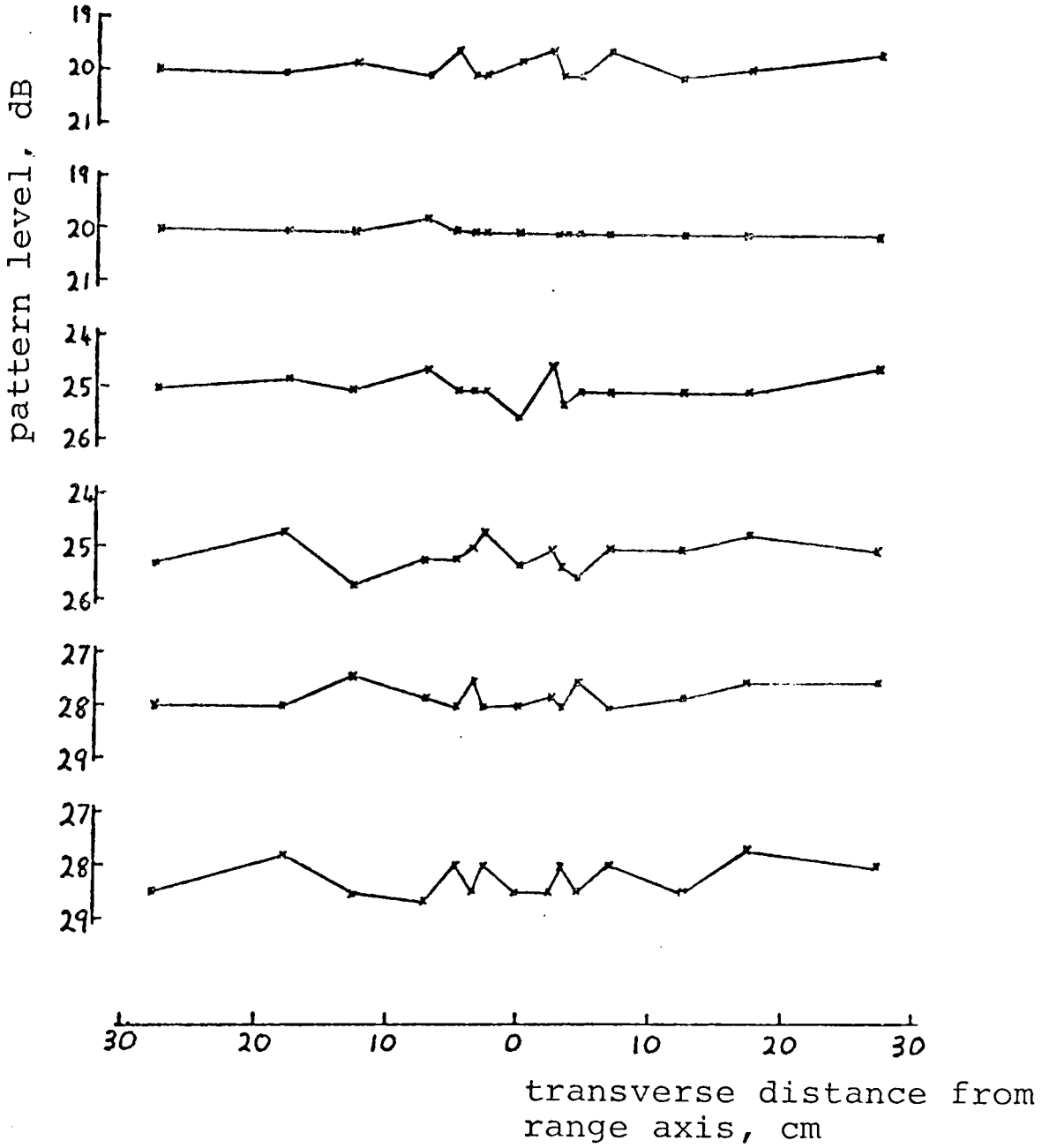

Fig. 3.4 Deviations of power level for the radiation patterns of figure 3.3 plotted as a function of transverse distance from the anechoic chamber axis

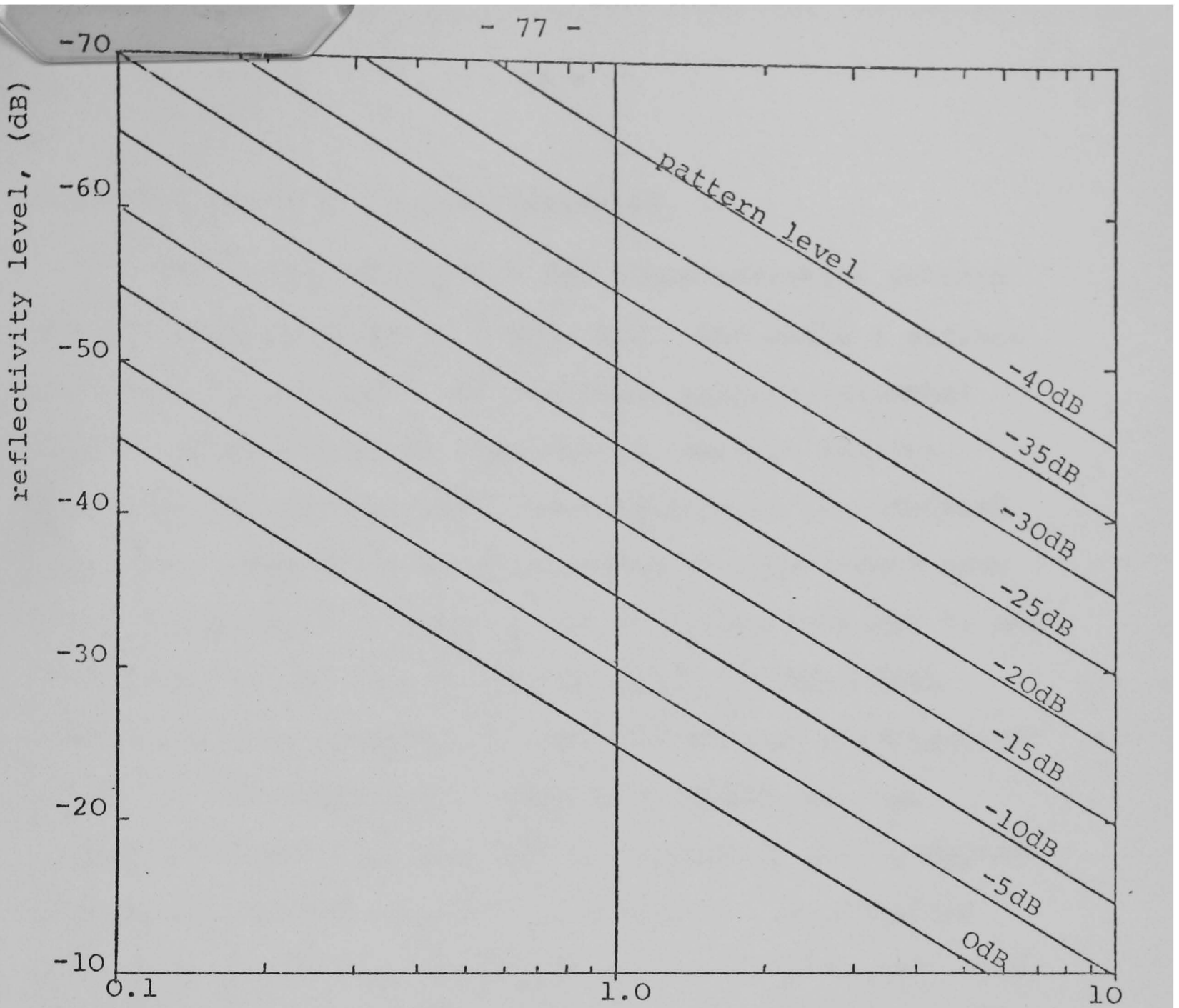

Fig. 3.5 Reflectivity level for use with Pattern Comparison method of assessing anechoic chambers or compact ranges

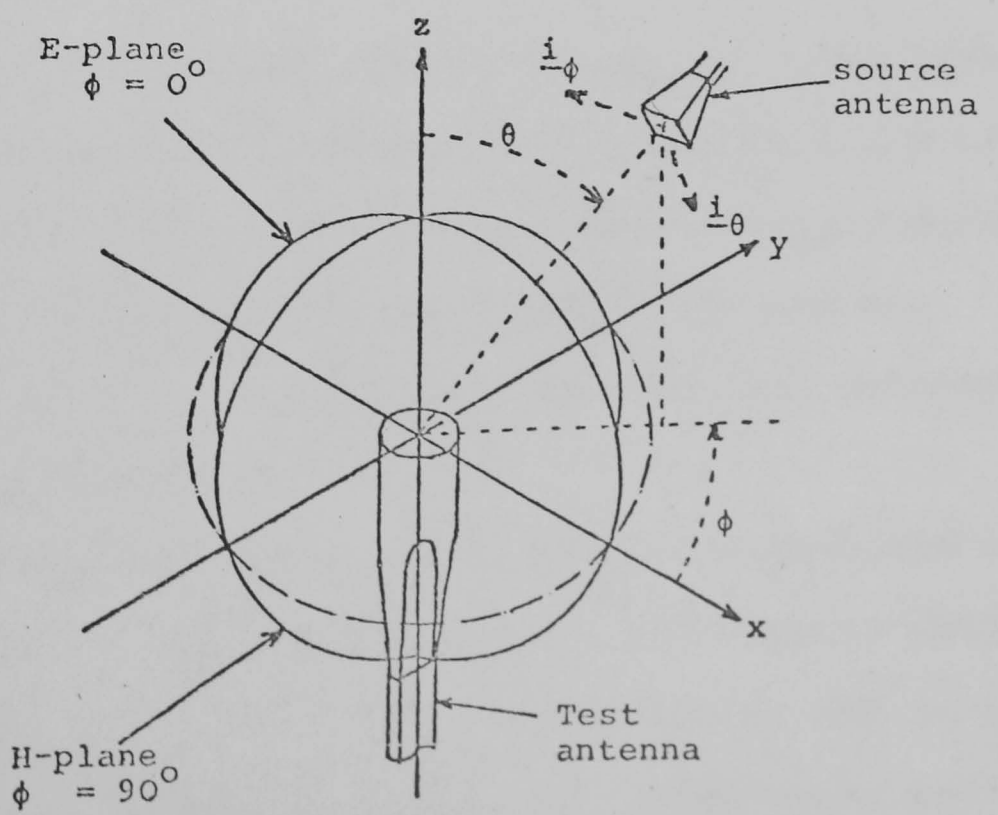

Fig. 3.6 Geometry for radiation pattern measurement

radiation patterns is now considered.

The coordinate system for these radiation pattern measurements is shown in figure 3.6, The angle ϕ defines the plane of cut and θ the radiation pattern azimuthal angle. In practice the transmitting antenna remains fixed and the antenna under test rotates on an azimuthal turntable. The feeds to be measured in this thesis have their cross-polar maximum in the 45^{o}-plane (chapter 9) and this plane of cut is achieved by first rotating both source and test antennas so that the E-field polarisation is 45^{o} to the horizontal. Then by turning the test antenna through a further 90^{o} (ϕ direction) and recording its pattern whilst rotating in azimuthal, the required 45^{o}-plane cross-polar radiation pattern is obtained. The method described above defines Ludwig's third definition of cross-polarisation <33>, and is considered in chapter 9 with reference to the calculation of cross-polar radiation patterns.

Accurate alignment of the source and test antennas is an important factor in determining the accuracy of measured cross-polar radiation patterns. Listed below are the various important alignments required, and the undesirable effects occurring if they are not executed sufficiently accurately.

1) Both source and test horns must be orientated so that the E-field polarisations are exactly orthogonal. If this is not so a small component of the co-polar pattern is introduced into the cross-polar pattern

(a)

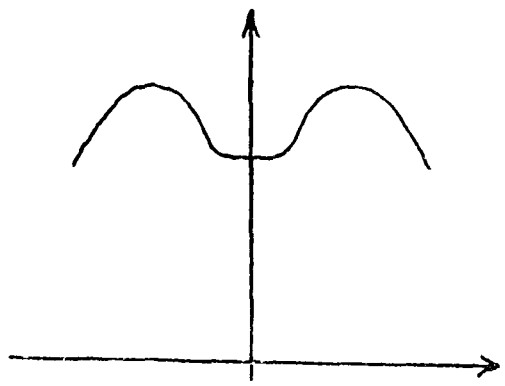

(b)

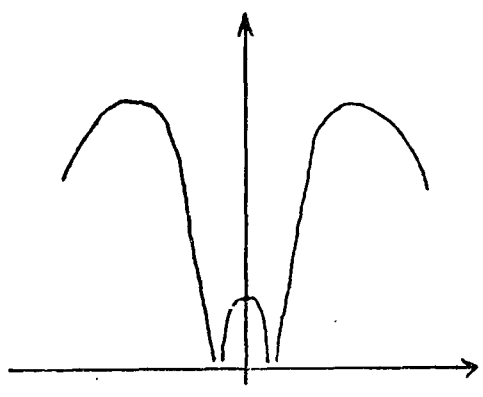

(c)

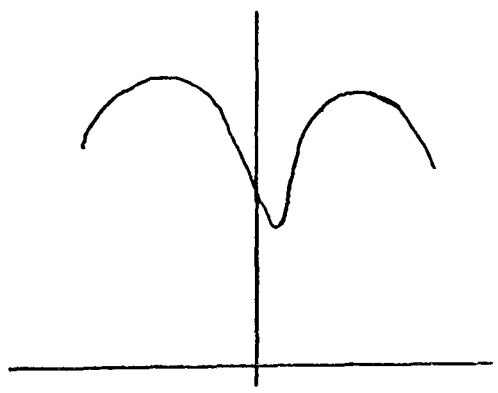

(d)

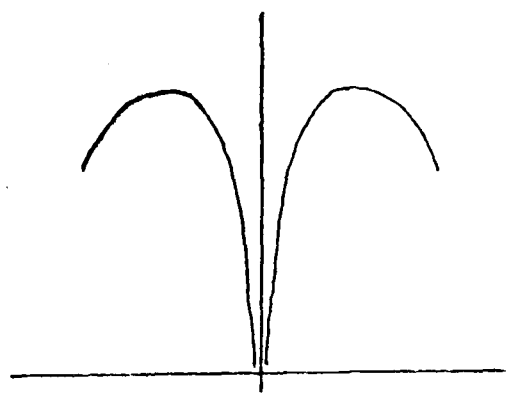

undistorted pattern

Fig. 3.7 Effect on a measured cross-polar radiation pattern due to various alignment errors (see text)

filling in the axial null, figure 3.7(a).

2) The test antenna polarisation must be maintained at a fixed orientation throughout its azimuthal rotation. If a change does occur a small co-polar component will distort the off-axis cross-polar pattern.

3) The axes of both source and test antennas must be horizontal and as near as possible identical. Several undesirable effects occur if this is not achieved, depending on the misalignment, these are:

   (a) The test antenna axis is not horizontal, resulting in the pattern cut not passing through boresight, figure 3.7(b).

   (b) The source and test antenna axes are not identical, resulting in the cross-polar null of the source antenna being no longer directed over the test antenna. This causes an amplitude taper of cross-polar power across the test area and consequently an asymmetrical distortion of the measured cross-polar pattern, figure 3.7(c).

To see if there was any deterioration over the co-polar pattern performance of the anechoic chamber, the pattern comparison technique was repeated for the 45^{o}-plane cross-polar pattern of the 17dB gain pyramidal test horn. This yielded a mean reflectivity of -54dB at 9GHz, an insignificant change from the co-polar result. Therefore, using figure 3.5, the accuracy for the measured co-polar and cross-polar feed radiation patterns, measured

using the Q.M.C. Anechoic Chamber, can be tabulated for various pattern levels, table 3.2.

Table 3.2

Pattern Level, dB	Approximate Pattern Accuracy, dB
-15	±0.1
-20	±0.15
-25	±0.3
-30	±0.5
-35	±0.9
-40	±1.5
-45	±2.7

Whilst all the reflectivity measurements presented here were made at 9GHz, Olver <29> has shown that there is little change in reflectivity over all of X-band, the value being controlled by the reflectivity/frequency characteristics of the absorber.

To conclude, the Q.M.C. Anechoic Chamber can be successfully used to measure the required -40dB peak cross-polar feed patterns, and for such a level the accuracy of the measured pattern will be approximately ±1.5dB.

3.4 A RADIATION METHOD FOR THE MEASUREMENT OF MODE CONVERSION LEVELS

In this section an experimental technique for measuring the level of higher order mode present in a feed aperture is described. To date the only measurement method available is a technique originally devised by Klinger <34>, which relies on the observation of the absorption spectrum due to trapped-mode resonances produced by placing a shorting plate across the feed aperture. From a knowledge of the resonant amplitude, resonant linewidth, and waveguide feeder length, the level of higher order mode generated in the waveguide feeder can be calculated <35>. However, for waveguide lengths typically used in antenna feeders the resonances become very closely spread and difficult, if not impossible, to identify and measure. The method to be described here relies on measuring the changes which occur in the radiation pattern of the dominant mode due to the presence of radiating higher order modes. The method has the advantage of directly measuring the dominant mode radiation pattern deviation at a chosen angle off bore-sight. For an antenna feed the important criteria in determining the allowable level of higher order is the amount of radiation pattern distortion caused and not the modes power coupling level. This is because by specifying a maximum allowable dominant mode pattern deviation the maximum loss in total antenna efficiency and change in main beam direction is set. In addition this method has

the advantage that the measurement is independent of the length of waveguide and that it is made with the waveguide feeder in its intended environment and not the artificial environment of a resonant cavity.

The basic concept behind the technique is best explained by an example. Consider an overmoded corrugated waveguide feeder excited principally in the dominant HE_{11} mode but supporting, in addition, the H_{01} mode which is present due to coupling between the HE_{11} mode and H_{01} mode at some waveguide imperfection. Figure 3.8 shows theoretically how the H-plane dominant mode radiation pattern is modified by the presence of the H_{01} mode in the two extreme cases where the patterns of the two modes are either in-phase or out-of-phase. The phase of the H_{01} mode differs on either side of boresight, producing the asymmetrical radiation pattern shown in figure 3.8. In practice this extreme pattern deviation is obtained by scanning over a sufficiently wide frequency range, which changes the relative phase between the dominant and higher order mode. It being assumed that the dominant mode pattern does not change substantially with frequency, a fact which is true for corrugated feeds. The peak-to-peak pattern deviation obtained for the feed can, if required, be used to assess the degradation in the overall feed plus reflector performance. Alternatively the pattern deviation can be theoretically related to the higher order mode power present at the feed aperture. This forms the basis of the measurement procedure which is

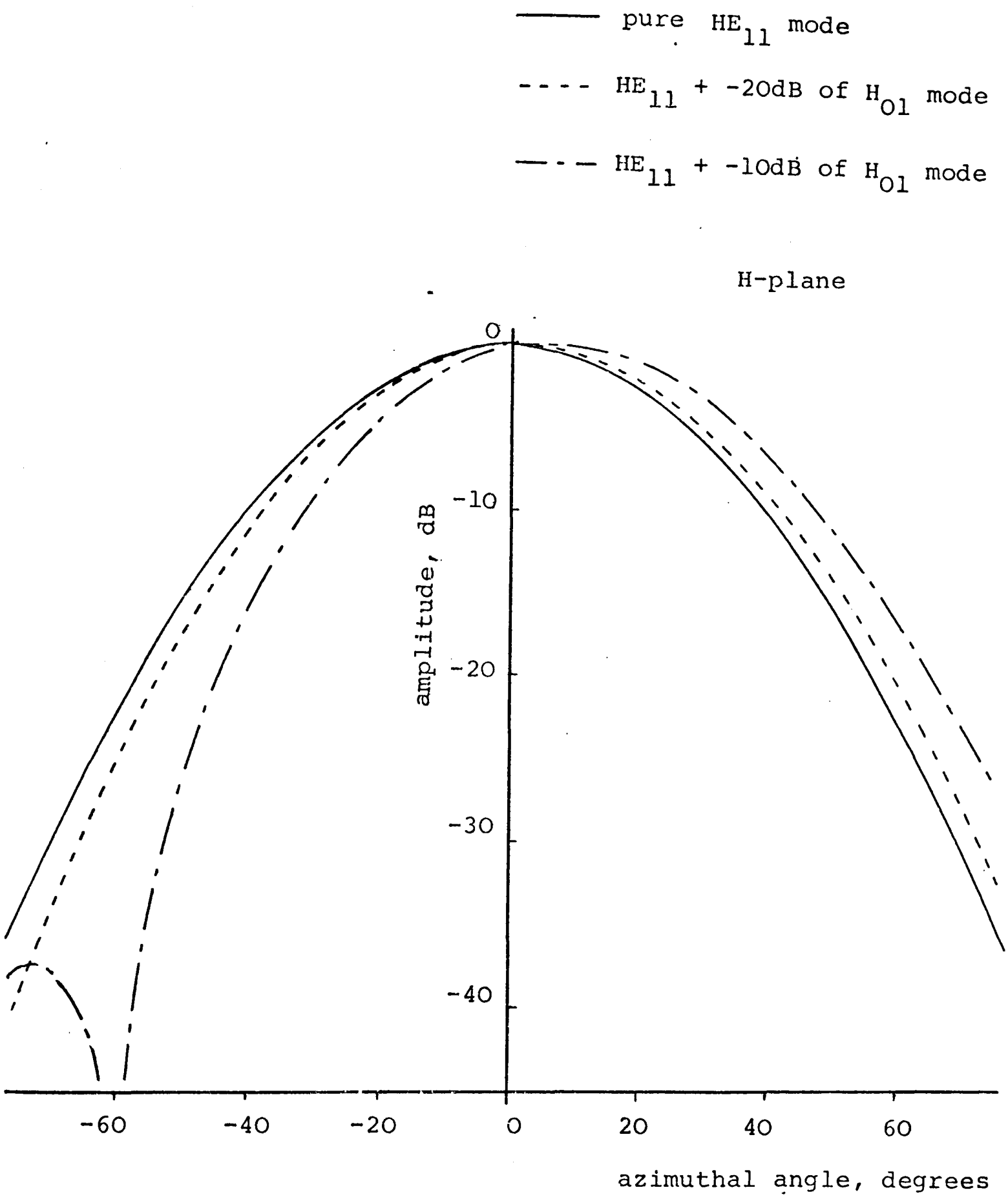

Figure 3.8 Effect of various relative powers of the H_{01} mode on the HE_{11} mode radiation pattern of a corrugated circular waveguide

$r_1 = 25.7\text{mm}$, $\frac{r_1}{r_o} = 0.718$, $\bar{r}_1 = 4.91$

now described.

Radiation from the feed is detected at an angle θ_o from boresight (figure 3.9(a)), in the appropriate plane, so that the presence of a particular higher order mode, or mode combination, perturbs the dominant mode pattern. The required plane can be easily determined for most common waveguide structures by considering the radiation properties of the higher order modes. For example table 3.3 (obtained from the study in chapter 9) shows the plane and polarisation in which the higher order modes of a corrugated circular waveguide perturb the HE_{11} mode radiation pattern, for the practical design supporting three higher order modes. Having chosen the required plane, the frequency of the source is swept over a sufficient range for the relative phase of the modes to pass through one cycle. The observation is repeated at the angle $-\theta_o$ so as to reverse the relative phase of the modes. A further swept frequency observation on boresight is made to normalise the two previous recordings so that changes in amplitude due to changes in the VSWR of the waveguide are eliminated. After normalisation a curve similar to that shown diagramatically in figure 3.9(b) for a single higher order mode is obtained, yielding the required dominant mode pattern deviation, d.

If the radiation patterns of the dominant mode with a specified relative power of higher order mode can be theoretically calculated, it is possible to relate d to the power coupling coefficient of the higher order mode, or mode combination. This has been done for the corrugated

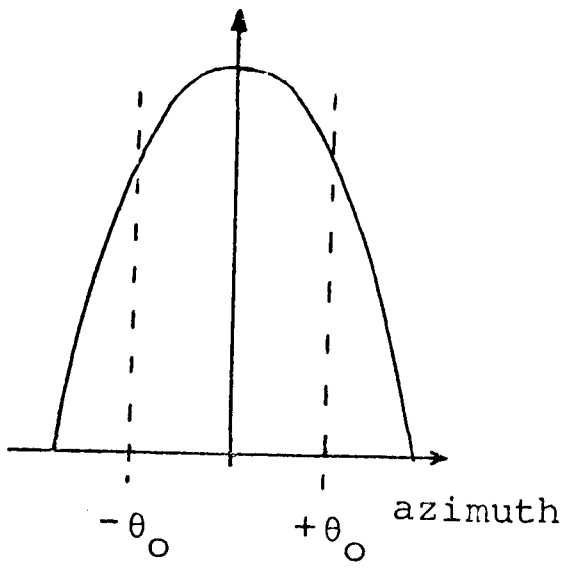

Fig. 3.9(a)

Typical radiation pattern showing position of swept frequency pattern cuts

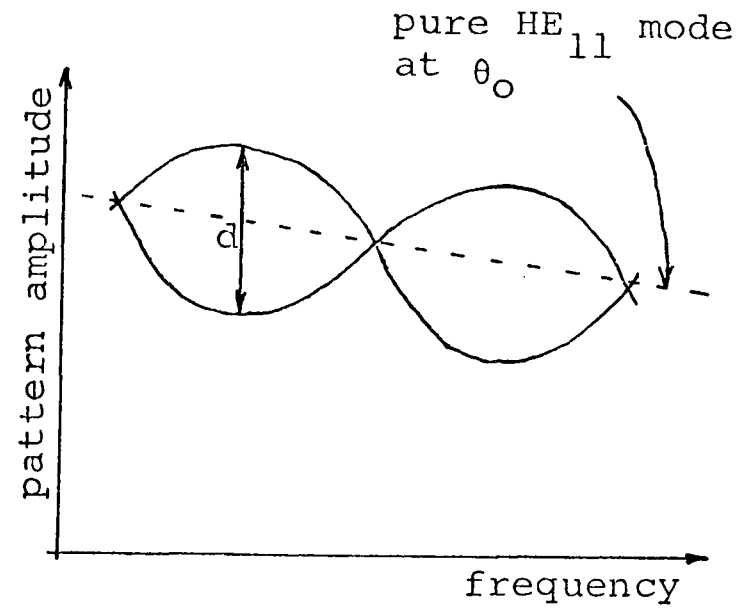

Fig. 3.9(b)

Swept frequency pattern for a waveguide with only the H_{01} coupled mode propagating

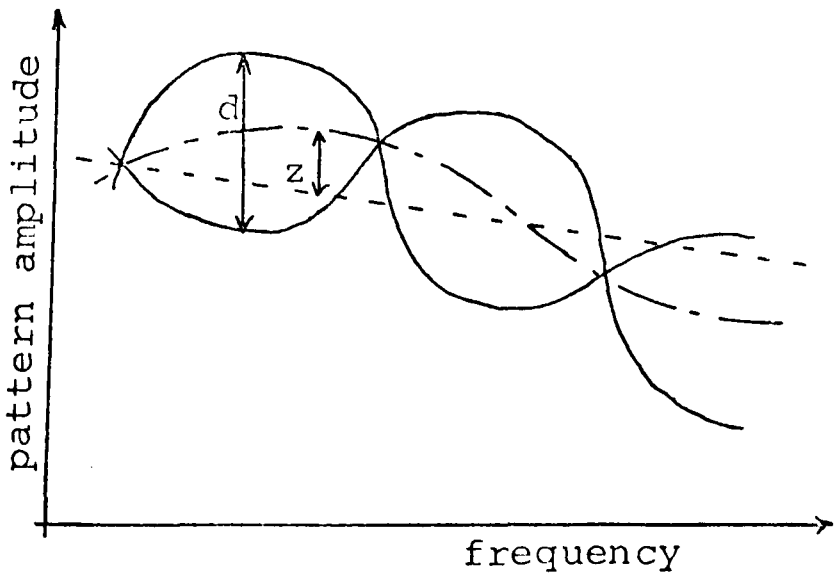

Fig. 3.9(c)

As (b) but with the HE_{12} mode also propagating

MODE	E-PLANE		H-PLANE	
	co-polar	cross-polar	co-polar	cross-polar
H_{01}		✓	✓	
E_{02}	✓			✓
HE_{21}	✓			✓
HE^{*}_{21} †		✓	✓	

Table 3.3

Plane and polarisation of higher order mode perturbing HE_{11} mode radiation pattern.

† The HE_{21} mode possesses two orthogonal polarisations, designated HE_{21} and HE^{*}_{21}, and separated by 45^{o}.

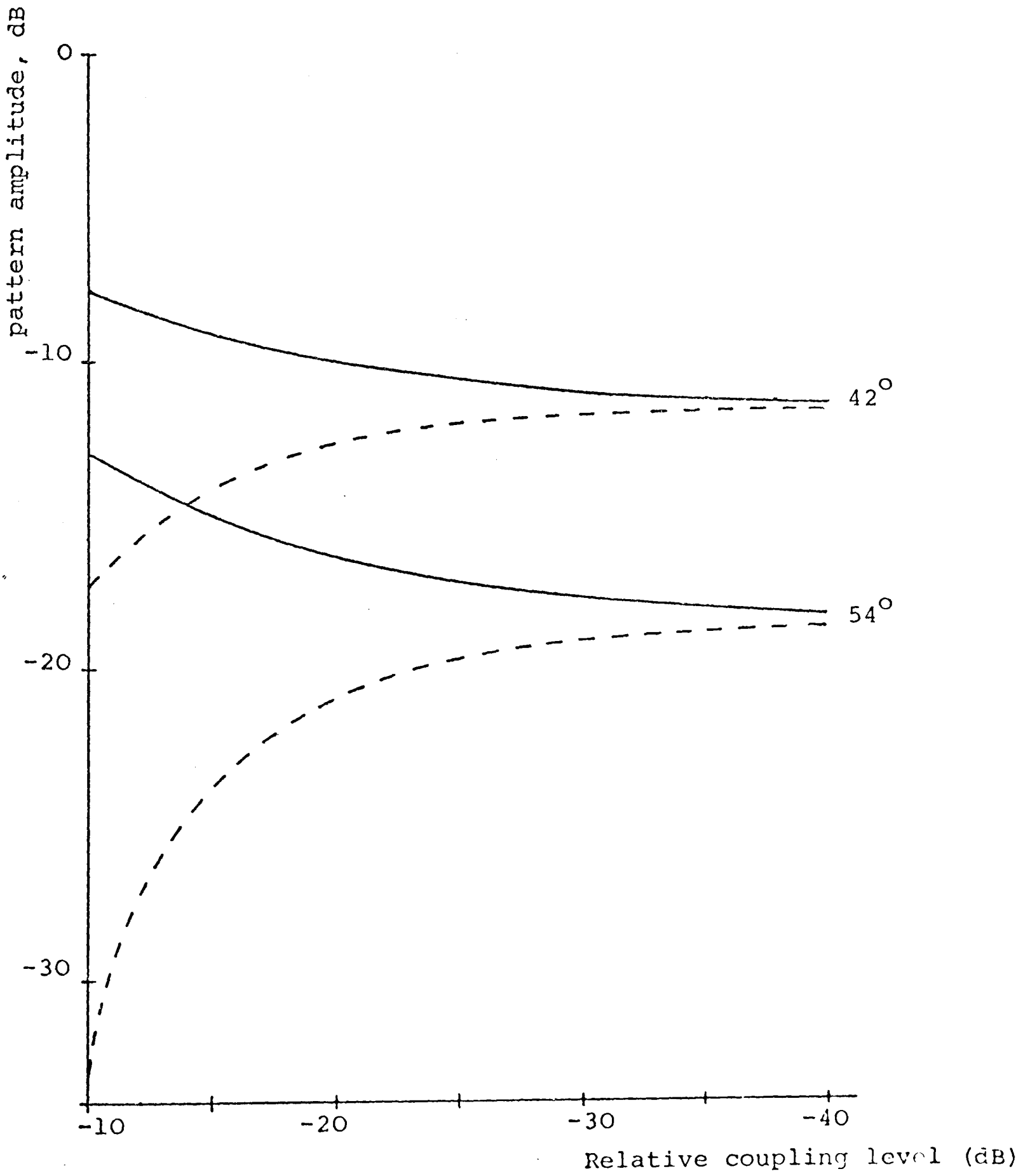

Fig. 3.10 Swept frequency pattern deviation as a function of mode coupling level for rigid corrugated waveguide; 8.8GHz; H-plane.

circular waveguide and a typical curve relating d to the power coupling coefficient of the H_{01} mode is shown in figure 3.10 for two angles off boresight. Because of the fact that the H_{01} and HE^{*}_{21} modes in the corrugated waveguide have near identical radiation patterns (see chapter 9), figure 3.10 can be used to determine the power coupling level of the $H_{01}+HE^{*}_{21}$ mode combination. A similar property exists for the $E_{02}+HE_{21}$ modes in a corrugated waveguide and the $TM_{01}+TE_{21}$ modes in a smooth wall circular waveguide.

The swept frequency radiation pattern technique described above was tested using a rigid length of corrugated circular waveguide known to couple mainly to the H_{01} mode. A block diagram of the experimental system used for these measurements is shown in figure 3.11. The large support table was specifically designed to produce a controlled bend in a length of flexible waveguide enabling the mode conversion caused by the bend to be measured (the results of this study are presented in chapter 5). The Q.M.C. Compact Antenna Range was used to provide the pseudo plane wave test region. By using a small dipole to probe the transverse field in the centre of this region and adjusting the transverse position of the source antenna feed, a constant amplitude field (to within 0.1dB) covering the test waveguides aperture, was achieved. This corresponds to a range *reflectivity* of about -45dB (figure 3.5) and means that a measured pattern at a level -20dB down from the boresight level might have a 1dB peak-to-peak ripple. Assuming the worst case of an asymmetrical

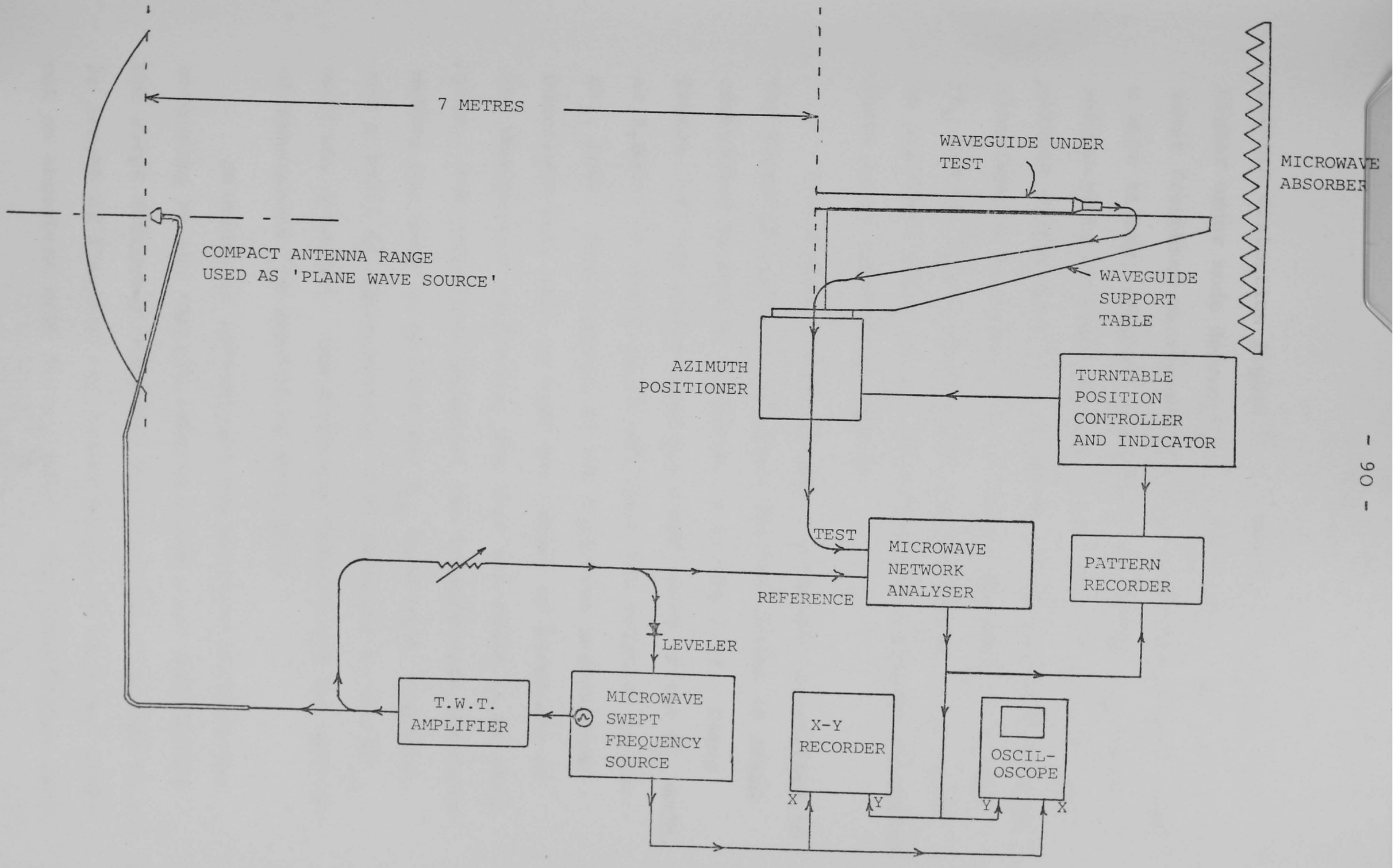

Fig. 3.11 Schematic of mode conversion measurement apparatus

pattern distortion figure 3.10 then sets the level of higher order mode detectable to about -35dB. However, swept frequency measurements to be described later, using a mode filter, indicate that the compact antenna range reflectivity does not produce this order of *asymmetrical* pattern distortion. The accuracy of the measured results also depends on being able to obtain patterns at θ_o and $-\theta_o$ and <u>not</u> $\theta_o+\delta\theta_o$ and $-\theta_o+\delta\theta_o$ as the latter would yield an incorrect value of d. Therefore the boresight direction needs to be accurately defined.

The H-plane swept frequency patterns, normalised to the boresight pattern, obtained for the length of rigid corrugated waveguide are shown in figure 3.12. Using figure 3.10 the power coupling coefficient of the H_{01} mode, at 8.8GHz, is found to be -26.5dB±0.5dB relative to the HE_{11} mode. Measurements at two different angles from boresight were made to test the extent of agreement of the measurement technique, and this was found to be very good. For comparison purposes the trapped-mode resonance method was used to measure the H_{01} mode power coupling, and a level of approximately -26dB relative to the HE_{11} mode was obtained. The agreement between the two methods of measurement is seen to be very good.

In order to investigate how spurious reflections occurring in the compact antenna range were influencing the swept frequency patterns, measurements were made on a 2m length of flexible corrugated waveguide with and without an absorbent mode filter added. The mode filter used

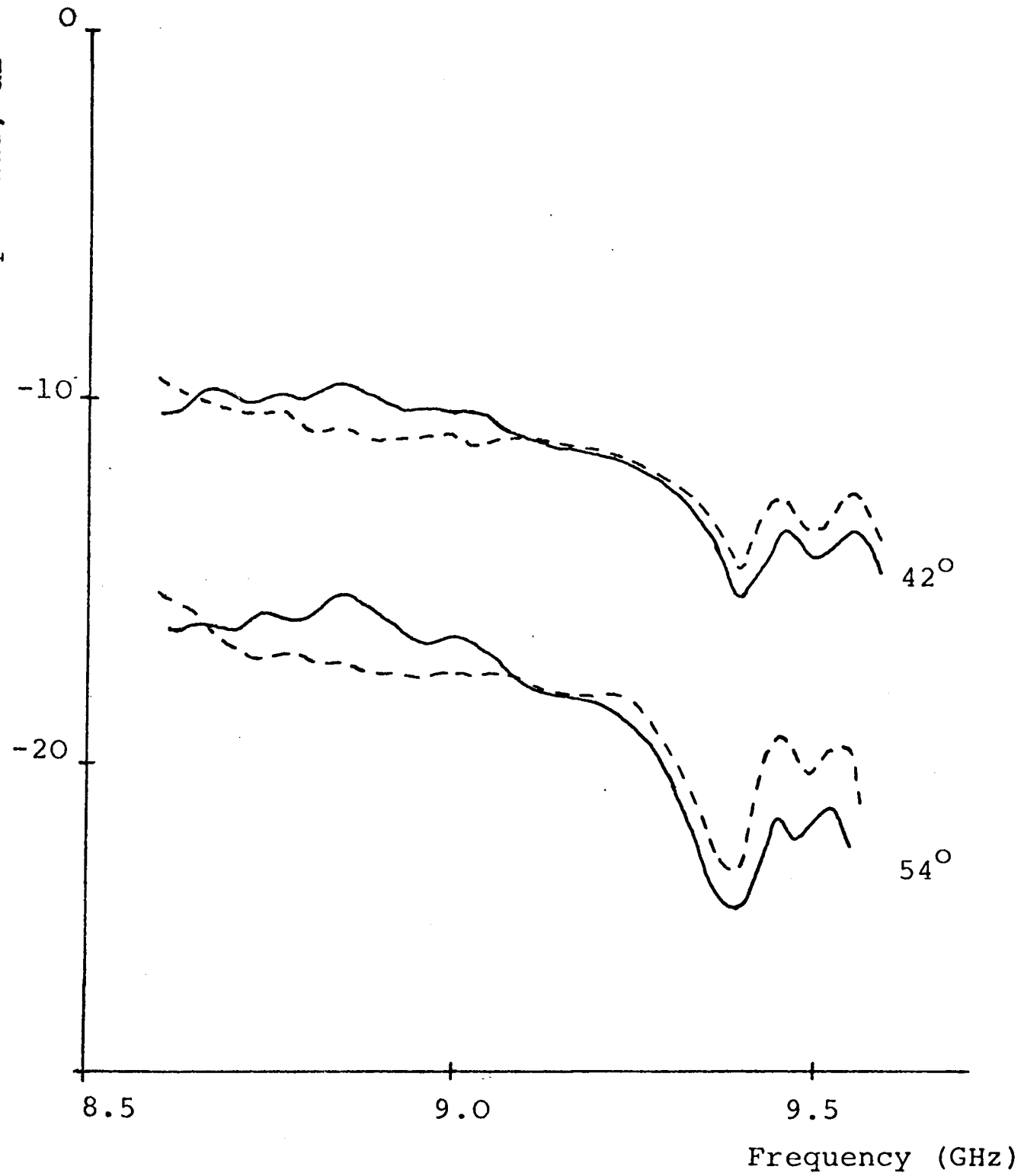

Fig. 3.12 Swept frequency radiation pattern, normalised to the boresight pattern, for a length of rigid corrugated waveguide.
parameter: angle off boresight

is shown in figure 3.13, and is designed to attenuate modes with relatively high electric field strengths at the corrugation boundary < 2 >. Since the HE_{11} mode has a low field strength in this region, relative to the higher order modes, it is only slightly attenuated. The swept frequency patterns obtained with an without the mode filter in the waveguide are shown in figure 3.14. The negligible pattern deviation obtained with the mode filter present in the waveguide clearly indicates that reflection effects give a negligible contribution to the pattern deviation. It should be pointed out in passing that whilst this design of mode filter successfully suppresses the higher order modes, it has an unacceptably high HE_{11} mode insertion loss.

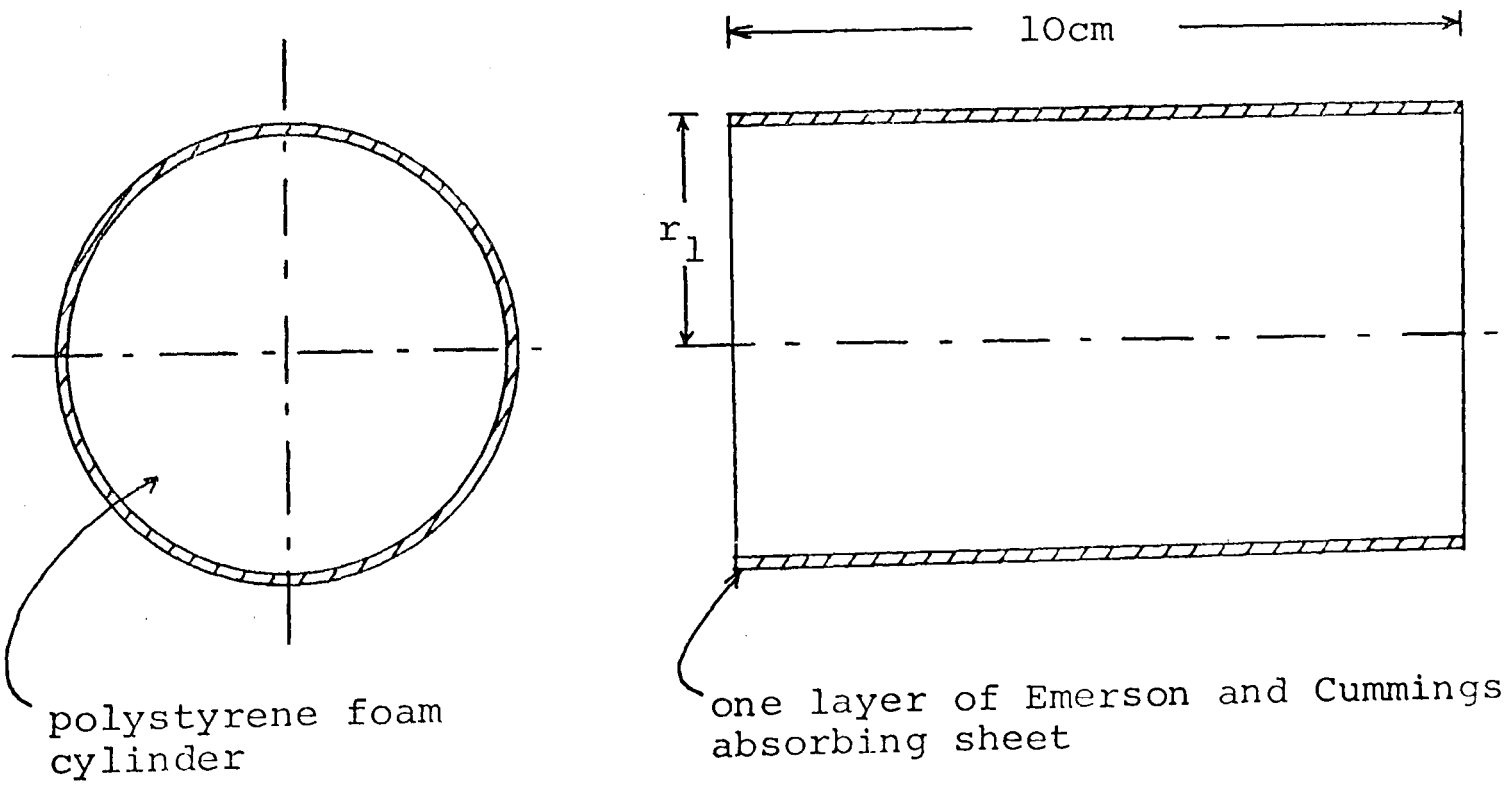

Fig. 3.13 Absorbent Mode Filter

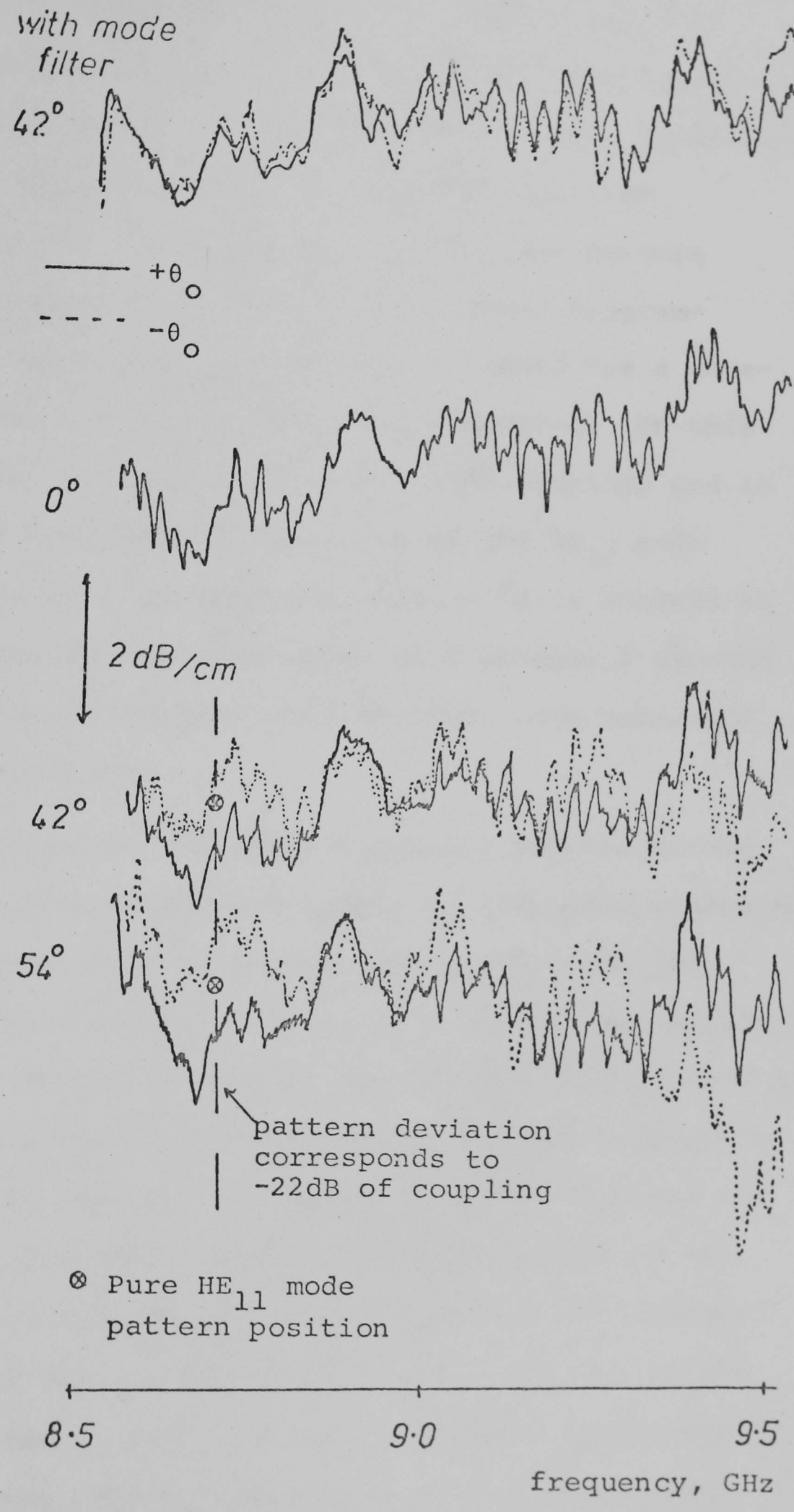

Fig. 3.14 Typical swept frequency radiation pattern for flexible corrugated waveguide with and without the mode filter of figure 3.13.

The above swept frequency measurement technique can be extended to measure the level of HE_{12} mode present in a corrugated waveguide. Because of the unity azimuthal number of the HE_{12} its effect on the dominant mode radiation pattern is to produce a symmetrical pattern distortion (chapter 9). Figure 3.9(c) shows diagrammatically the swept frequency pattern obtained for a waveguide with both the H_{01} and HE_{12} modes coupled. In this case d is still a measure of the H_{01} mode coupling and in addition z is a measure of the level of the HE_{12} mode coupling. However, the measured value of z is subject to more error than the measured value of d because z depends on the accuracy of the predicted dominant mode radiation pattern, figure 3.9(c).

In conclusion, the swept frequency pattern method for measuring mode conversion levels in overmoded waveguide feeders has been shown to compare favourably with the trapped resonance method. It is, in a sense, complementary to the latter method in that it can be used when one end of the overmoded waveguide is open and no trapped resonances are formed. In addition the method directly measures the dominant mode radiation pattern distortion which is the major factor of interest in the antenna feed application. The method has been explained here with reference to the corrugated circular waveguide but is equally applicable to overmoded smooth wall waveguides as well as other overmoded feed/feeder geometries, so long as their radiation characteristics do not change substantially over the required frequency sweep.

CHAPTER 4

WAVEGUIDE MEASUREMENTS

4.1 INTRODUCTION

In this chapter methods of measuring the attenuation and transmission characteristics of corrugated circular waveguides are described. In subsequent chapters these measurement techniques are employed to determine the performance of modified types of corrugated waveguide structure designed for mode filtering (chapter 7), and to measure the attenuation in a corrugated waveguide designed for single mode operation (chapter 8).

Two principal methods of measuring the performance of a waveguide exist, these are:

1) Resonant Cavity Measurements

2) Transmission Test Measurements

and both these methods will be used in this study. The resonant cavity method enables the propagation and attenuation characteristics of any propagating mode to be determined from a relatively short length of waveguide made to form a resonant cavity. When measuring various configurations of low attenuation prototype waveguide this method has a cost and time advantage over measuring the waveguide performance directly over a long length, as in the case of the transmission test method. However, the resonant cavity method does suffer from the need for accurate cavity construction and accurate measurement of

the very high Q-factors involved. The measurement technique employed and the errors involved in using the resonant cavity method are described in section 4.2.

The transmission test method of waveguide measurement enables the transmission characteristics of the dominant waveguide mode to be investigated under the conditions encountered in practical operation. It has the advantage that the *trapped mode resonances* (chapter 2) can be studied, enabling the degree of suppression of these resonances obtainable with mode filters to be directly measured. However, for a low-loss waveguide it suffers the disadvantage of requiring a very long length of waveguide if the dominant mode attenuation is to be measured accurately. The transmission test method and its use in measuring the performance of mode filters is described in section 4.3.

4.2 RESONANT CAVITY MEASUREMENTS

In this section the resonant cavity method for determining the attenuation of the propagating modes in a corrugated circular waveguide is described. Firstly the relationship between waveguide attenuation and the 3dB linewidth of a mode resonance is presented in section 4.2.1. A simple method of measuring the change in attenuation of the corrugated waveguide modes, resulting from a modification of the structure for mode filtering purposes, is also developed in this section. Section 4.2.2 considers the constructional problems involved in manufacturing a

corrugated waveguide resonant cavity and describes the method used to couple into the desired waveguide modes. The experimental system used for measuring the 3dB linewidth of a mode resonance is described in section 4.2.3. In section 4.2.4 the measurement accuracy is considered and results of several experimental reliability studies are presented. In addition measured results obtained using a resonant cavity for the attenuation of the HE_{11} and HE_{12} modes in a corrugated circular waveguide are presented and are compared with those previously measured by Chong < 2 >. Finally the conclusions resulting from this study of cavity measurements are presented in section 4.2.5.

4.2.1 Measurement of the attenuation of a waveguide mode using a resonant cavity

The resonant cavity is formed by a short length of corrugated circular waveguide terminated at both ends by a flat metallic end plate, this termination being in the middle of a corrugation slot to achieve image symmetry with the end plate <36>. Power is injected or extracted from the cavity by introducing small coupling holes into the end plates, the position of these coupling holes determines the group of modes excited and this is considered in the next section. When the length of the waveguide is an integer multiple of half guide wavelengths for any of the excited modes, a resonance occurs. If the resonant cavity is of the transmission type, figure 4.1, then a peak of energy is detected at resonance. The 3dB

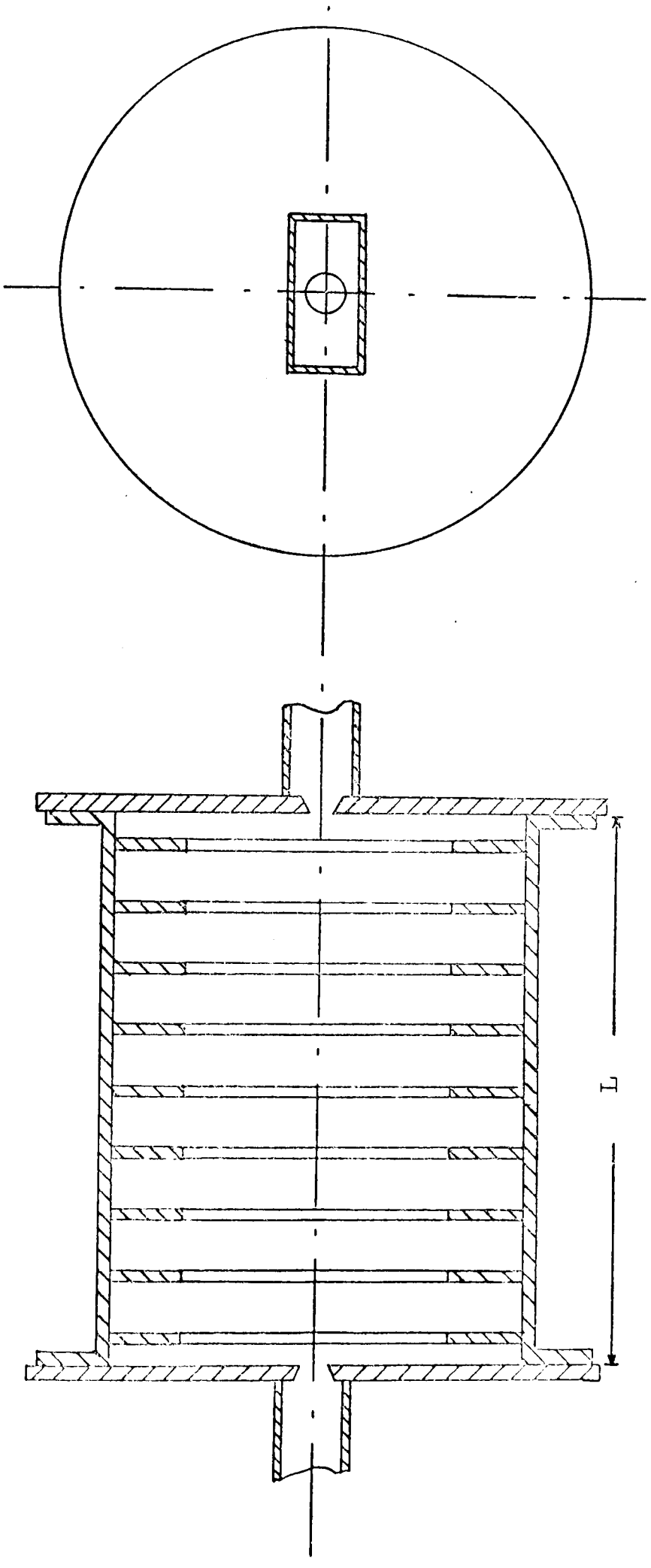

Fig. 4.1 Transmission type resonant cavity

linewidth, Δf_L, of the mode resonance is a measure of the total power loss in the resonant cavity, this power loss comprising of three separate components:

1) The intrinsic waveguide loss, which depends on the waveguide length, L.
2) The loss in the metal end plates, which for a given mode is fixed and independent of waveguide length.
3) The loss due to the small coupling holes, which, for practical waveguide lengths, where mutual coupling between the input and output coupling holes is negligible, is independent of L.

It can be shown < 2 > that the 3dB linewidth, Δf_L, can be related to the mode attenuation coefficient, α, by the following equation

$$\Delta f_L = \frac{v_g \alpha}{\pi} + \frac{C}{L} \qquad (4.1)$$

where: v_g is the mode group velocity; α is the mode attenuation in N/m; and C is a constant depending on the coupling and end plates losses for the mode. Since equation 4.1 is a linear relationship in $\frac{1}{L}$, measurement of Δf_L for a number of different waveguide lengths having the *same* resonant frequency allows the required mode attenuation, α, to be extracted from the results. This is done by plotting Δf_L against $\frac{1}{L}$ and using a regression line method to obtain the *unloaded linewidth* ($\frac{v_g \alpha}{\pi}$), which is the linewidth that would be obtained from an infinitely long resonant cavity. The required mode attenuation, α, is then obtained from this unloaded linewidth. This method

has been extensively used by Clarricoats, Olver and Chong <5> <2> to measure the attenuation of the HE_{11} and HE_{12} modes in corrugated circular waveguides.

For the measurement of mode filters where it is required to determine the increase in attenuation of the various waveguide modes due to modification of the waveguide structure, it is unnecessary to manufacture or measure a large number of different resonant cavity lengths. By comparing the measured 3dB linewidth for the unmodified structure, Δf_L, with that measured for the modified (mode filtering) structure, $\Delta f_L'$, having the *same* resonant cavity length it is possible to determine the change in mode attenuation caused by the modified structure. From equation 4.1, the proportional increase in linewidth is equal to the proportional increase in *total* cavity loss, this increased total loss being due only to the increased waveguide loss. Therefore neglecting coupling hole losses and with a knowledge of the ratio of total cavity power loss to waveguide wall loss the required change in mode attenuation is obtained as:-

$$\frac{\text{attenuation of modified waveguide}}{\text{attenuation of unmodified waveguide}} = 1 + \frac{(\Delta f_L' - \Delta f_L)}{\Delta f_L} \left(\frac{\text{total cavity loss}}{\text{waveguide wall loss}} \right) \qquad (4.2)$$

This method assumes that there is no appreciable change in mode resonant frequency due to the modified structure which for the mode filters to be investigated in this thesis has been found to be a valid assumption. The formulation of the ratio of total cavity power loss to waveguide wall loss

for the corrugated waveguide is presented in appendix 4.1. Therefore by measuring only a single resonant cavity length and using equation 4.2 the change in attenuation of the waveguide modes, due to the mode filtering structure, can be assessed.

4.2.2 The mechanical construction of corrugated waveguide resonant cavities

The mechanical construction of a corrugated waveguide resonant cavity depends on the type of measurement to be made. To measure the attenuation of a corrugated waveguide mode using a number of different resonant cavity lengths it is easier to construct the waveguide from a large number of removable sections which enable the required length to be built up. Section lengths equal to the corrugation periodicity is an obvious choice and this form of construction was used by Clarricoats, Olver and Chong < 5 > to measure the attenuation of the HE_{11} and HE_{12} modes for the waveguide shown in figure 4.2. This waveguide has been used by the author to repeat these attenuation measurements using a more accurate measurement system, and the results obtained are presented in section 4.2.4. The main disadvantage of this form of construction is the large number of joints involved, each requiring good contact in order not to distort the current flow on the waveguide walls. If poor contact in the resonant cavity does exist a double resonance, or widening of the resonance, occurs for some polarisations, this resulting

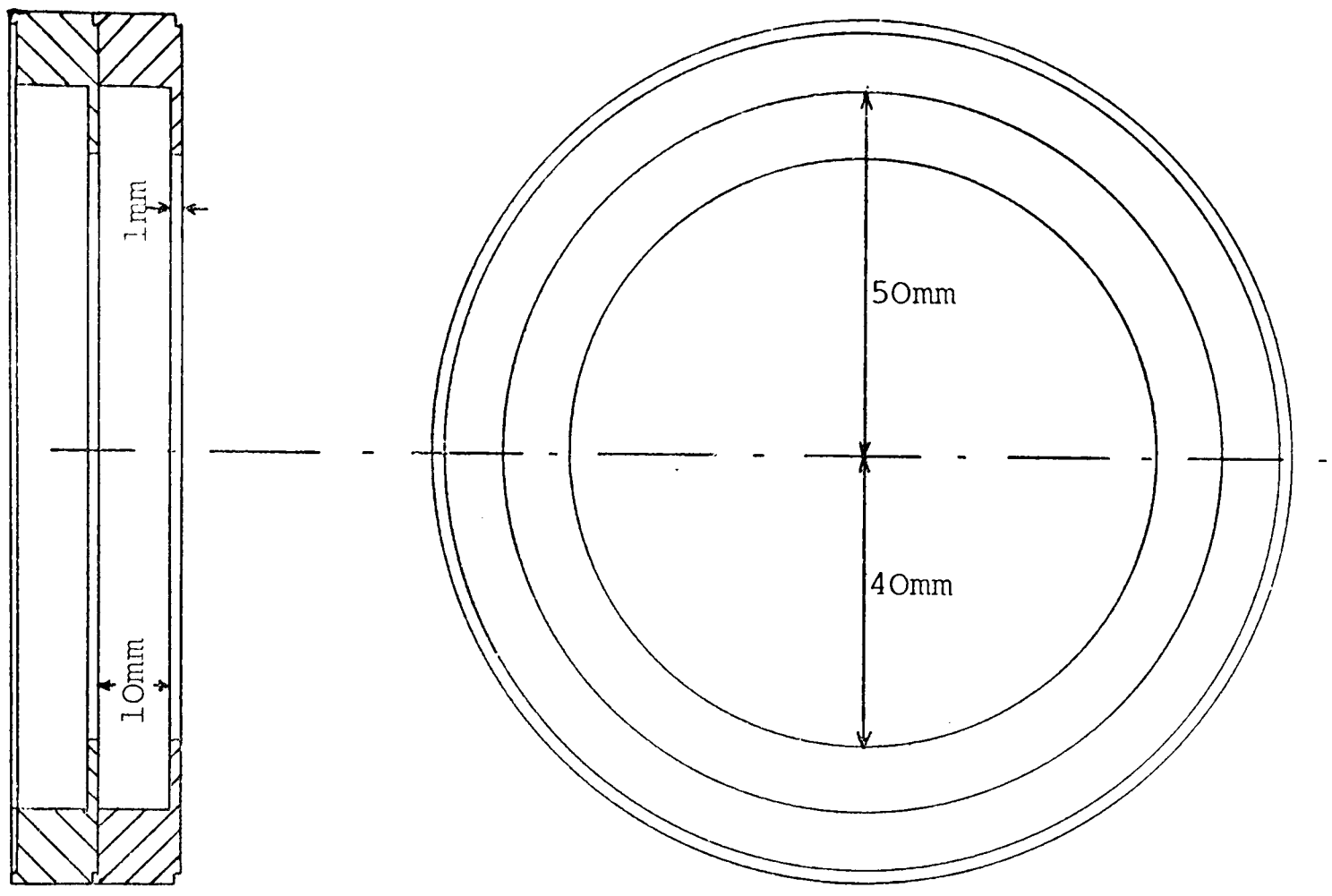

Fig. 4.2 Sectional method of waveguide construction

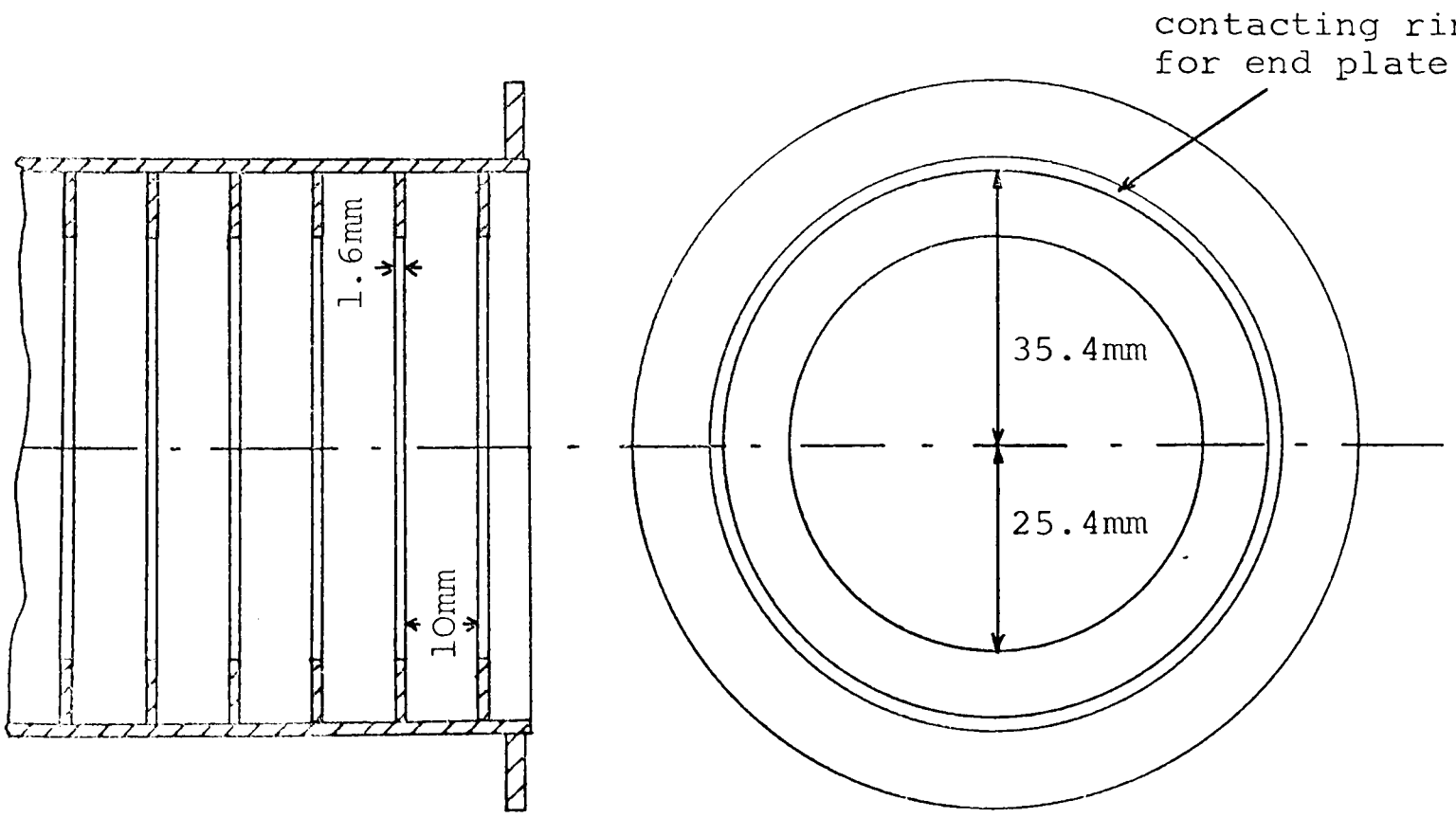

Fig. 4.3 Thermal contraction method of waveguide construction

from the splitting of the degeneracy between the two orthogonal polarisations of the mode. In addition the overall Q-factor of the resonant cavity is reduced because of the increased loss due to current interruption. For modes with zero azimuthal number, having no orthogonal polarisation, only this latter effect occurs. To achieve reliable and repeatable results it was found necessary to carefully clean and paint the contacting surfaces with highly conducting silver paint.

For the single length resonant cavity measurements used in the mode filter measurements a simpler method of construction was used. This method, developed by Olver <37> and termed the *thermal contraction method*, uses a length of smooth wall circular pipe to form the outer wall of the corrugated waveguide and metal irises secured inside the pipe to form the corrugations. These metal irises, which are made slightly larger than the internal diameter of the pipe, are cooled in liquid nitrogen then positioned inside the pipe and on returning to room temperature they expand, gripping the walls of the pipe thus forming a rigid fixing. The dimensions of the waveguide used are shown in figure 4.3. Whilst this method of construction does not involve the large number of moveable contacting surfaces of the previous method, it has been found in practice that a very high degree of circularity for the pipe is required in order to obtain good electrical contact between the iris and the pipe walls. For the waveguide shown in figure 4.3 it has been

found that a pipe ellipticity (the difference between major and minor diameters) of less than about 25μm is required to ensure good contact. As in the case of the previous construction poor contact results in the undesirable double resonance effects. To ensure good contact silver paint was run around the joints between the iris and pipe wall, but it was found that for pipe ellipticities greater than about 50μm this technique was *not* sufficient to cure the contact problem.

In both forms of resonant cavity constructions described here the inner surface of the cavity was left unpolished, the consequences of this on the value of attenuation measured is discussed in section 4.2.4.

A problem common to both forms of resonant cavity construction is that of end plate contact and alignment. If the end plates are not exactly aligned at 90^{o} to the waveguide axis a pure mode cannot be reflected and energy is lost by coupling to evanescent modes. This loss of energy results in an increase in the 3dB linewidth and hence an incorrect value of attenuation. As in the case of the waveguide sections, good contact between the end plate and the waveguide is essential and again silver paint was used between the contacting surfaces. The most reliable results were obtained if only a small contacting ring on the waveguide flange was present (see figure 4.3), this eliminating any current discontinuities associated with a large surface area of contact.

Coupling power into and out of the cavity was achieved by using a tapered coupling hole in the end plates of the resonant cavity, the coupling hole being fed by a rectangular waveguide which is terminated by the end plate and is shown in figure 4.1. The optimum diameter for the coupling hole to achieve a suitable level of coupling and to minimise any perturbation of the mode resonance has been determined experimentally by Chong < 2 >. The position of the coupling hole and the polarisation of the electric field at the hole will determine which group of modes are coupled. The centre positioned coupling hole of figure 4.1 , used by Chong, will couple to modes with a strong linearly polarised electric field in the centre of the waveguide. The HE_{1m} modes satisfy this requirement having a linear transverse electric field on axis and a radial power distribution which is a maximum on axis, consequently these modes will be the most strongly coupled. The H_{01}, E_{02}, and HE_{21} modes have a radial power distribution with a null on axis and a maximum in the region of $\frac{r_1}{2}$, and therefore are not coupled by axially positioned coupling holes. Figure 4.4 shows the transverse electric field pattern for the H_{01} mode and the position of the coupling holes required to efficiently couple into this mode. The radial distance from the waveguide axis of the coupling hole being in the region of maximum power, $\frac{r_1}{2}$. Rotating the output coupling hole by 90^{o} ensures that the HE_{1m} and EH_{1m} modes which are coupled into the resonant cavity with vertically polarised electric field are not coupled out.

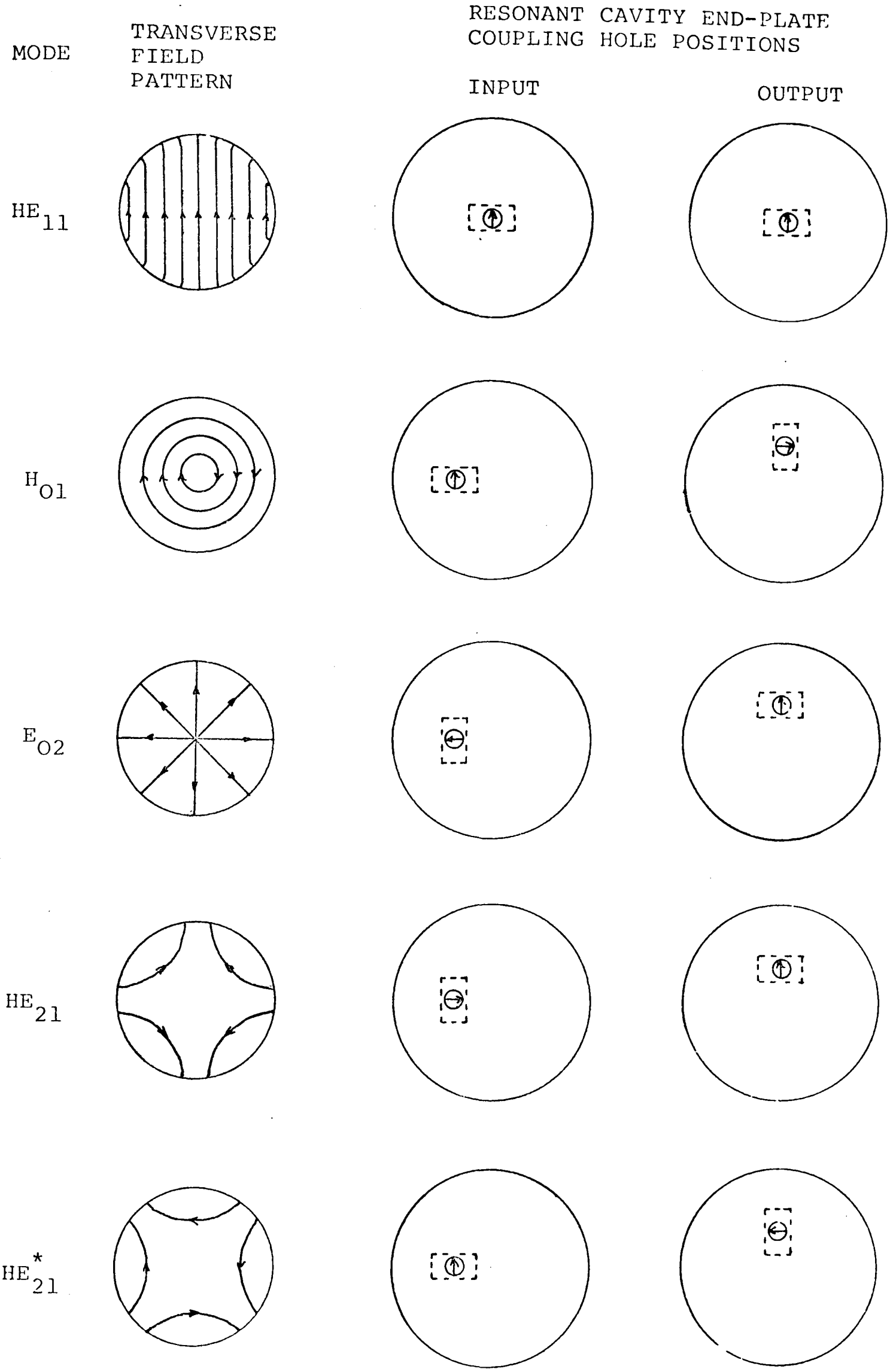

Fig. 4.4 Resonant cavity end plate coupling hole positions for various corrugated waveguide modes

This reduction in the number of modes coupled makes the mode resonance identification process, described in the next section, considerably easier. The transverse electric field patterns of the E_{02}, HE_{21}, and HE^{*}_{21} modes and the coupling hole positions required to excite these modes in the resonant cavity are also shown in figure 4.4.

4.2.3 The resonant cavity measurement system

A schematic of the experimental apparatus used in the resonant cavity measurements is shown in figure 4.5. Since most of the power is reflected by the input end plate of the resonant cavity, figure 4.1, isolators are used in conjunction with padding attenuators to suppress the resultant standing waves in the measuring system. In the output arm an isolator and matched rectangular waveguide crystal detector are used. These precautions ensure that no subsidiary low Q cavities exist in the input or output arms of the resonant cavity under test, which if present would cause frequency pulling of the main high Q cavity resonance.

Resonance identification was carried out using a computer program which predicts the resonant frequencies of the desired mode for a specified resonant cavity length. This computer program, developed by Chong < 2 >, takes the space-harmonic calculated dispersion curve for the desired mode and uses a numerical interpolation technique to obtain the resonant frequencies. Excellent agreement has been obtained between the measured and

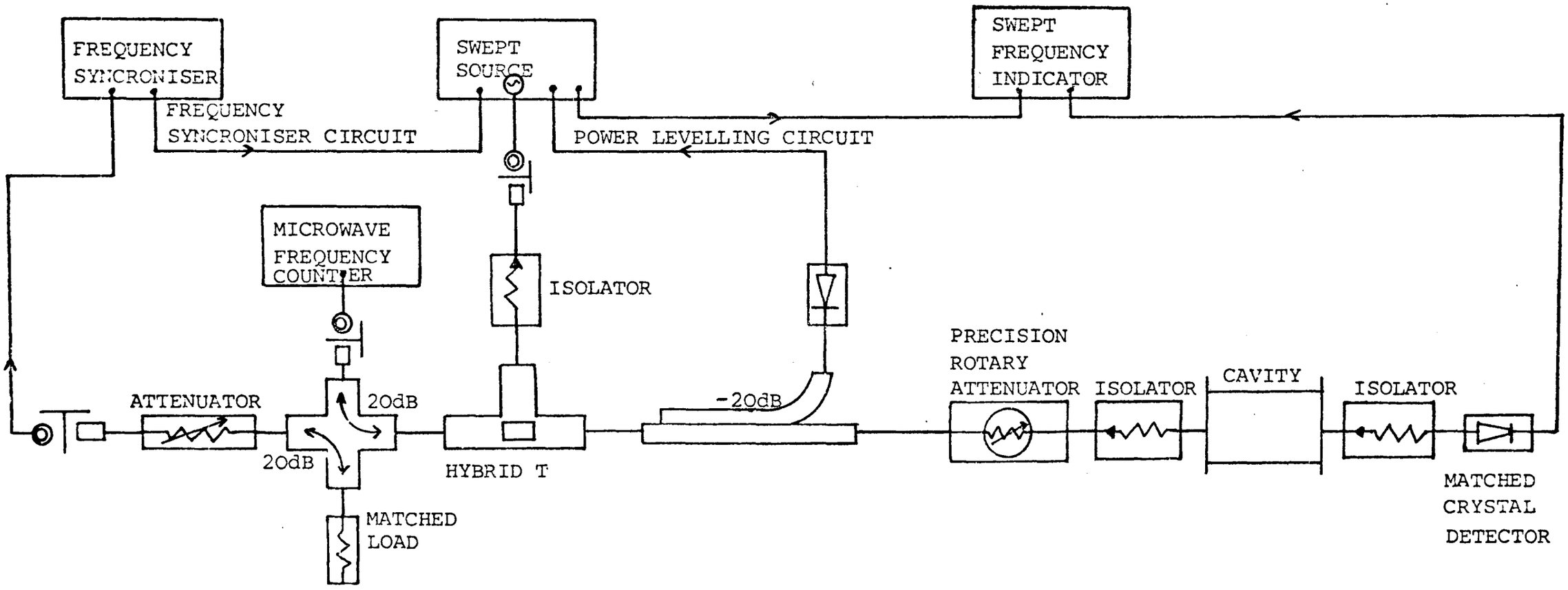

Fig. 4.5 Schematic of resonant cavity measurement apparatus

predicted resonant frequencies for the HE_{11} mode, a consistent error of ≈0.17% being obtained which was largely due to errors in measurement of the resonant cavity length.

The measurement method to be described here differs from that previously used by Clarricoats, Olver and Chong < 5 > as it employs a *microwave frequency synchroniser* to phase lock the backward wave oscillator source. This eliminates the considerable frequency measurement error resulting from the residual F.M. present in the swept frequency source, the error being estimated by these workers to be 4% or 20KHz whichever is the greater. The corrugated waveguide resonant cavities to be measured in this study generally have 3dB linewidths lying in the range 200KHz to 1MHz.

The microwave frequency synchroniser enables the frequency of the microwave source to be held stable to within 1 part in 10^8 <38>, and when locked in is manually tunable over approximately 1MHz. The following procedure, using the system of figure 4.5, was developed for measuring the 3dB linewidth of a mode resonance in a resonant cavity:

1) With the frequency synchroniser switched out the source is swept over a sufficient band to locate the required resonance, the power transmitted through the resonant cavity being viewed on the oscilloscope. The source centre frequency is then adjusted to align with the resonance peak.
2) The source is then switched to C.W. operation, the

synchroniser switched in and the frequency slightly readjusted to obtain a peak output signal. The frequency indicated on the direct read-out digital frequency counter is then the resonance centre frequency, f_o.

3) The received signal level displayed on the oscilloscope is then centred on a convenient horizontal reference and 3dB's of attenuation is taken out of the input arm using the precision rotary attenuator.

4) The synchronised C.W. signal is then tuned so that the received signal returns to the horizontal reference and the frequency, f_1, noted. This frequency represents one of the 3dB points on the resonance, figure 4.1.

5) The source is then retuned through the resonance to the other 3dB point and the frequency, f_2, noted. The required 3dB linewidth, Δf_L, is then given by $f_2 - f_1$.

The above method is simple and quick enabling the measurement to be repeated several times and the average taken. It does not suffer any of the problems and inaccuracies encountered with the swept frequency method previously used which were: a) frequency drift during recording of the resonance; b) frequency pulling of the resonance due to an unleveled source; c) frequency calibration error; d) the absolute error due to the residual F.M. of the swept source. The measurement accuracy for this improved measurement system is

considered in the following section.

4.2.4 Measurement accuracy

To determine the accuracy of the 3dB linewidths measured using the technique described in the previous section a series of 24 measurements for the 3dB linewidth of an HE_{11} mode resonance were made over several hours using the waveguide of figure 4.1 and a resonant cavity length of 13.28cm. The average measured linewidth of 316KHz was found to have a standard deviation of only 0.8%; and the resonant frequency of 9.415GHz a standard deviation of only 0.002%. Calculations showed that these variations were of the order consistent with thermal effects in the resonant cavity due to laboratory temperature changes.

Measurements were made with the thermal contraction waveguide to determine the repeatability of a good contact between the waveguide and the resonant cavity end plates. This is an important factor in the mode filter measurements where the measured linewidths of identical length resonant cavities are directly compared. Linewidth measurements were initially made several times and the average taken, then the end plates were: removed; the contact areas cleaned with wire wool; the contacting surfaces recoated with silver paint; the cavity reassembled and the linewidth measurements repeated. The above procedure was repeated 4 times for all 4 modes of interest and the results for the maximum 3dB linewidth variation are presented below.

MODE	MAXIMUM CHANGE IN MEASURED LINEWIDTH
HE_{11}	2%
H_{01}	1%
HE_{21}	8%
E_{02}	10%

The quite good results obtained for the HE_{11} and H_{01} modes reflect the low current flow present at the bottom of the corrugation slots where the end plate joins the waveguide (current flow patterns on the walls of a corrugated waveguide are presented in chapter 7). The poorer results for the E_{02} and HE_{21} modes are in agreement with the higher slot currents present for these modes.

The regression line method of attenuation measurement, described in section 4.2.1, has been used to determine the attenuation of the HE_{11} and HE_{12} modes for the waveguide of figure 4.2, allowing direct comparison with the earlier results obtained by Clarricoats, Olver and Chong < 5 > < 2 >. For the HE_{11} mode the experimental attenuation (at 10.5GHz) was found to be a factor of 2.1 times higher than predicted theoretically and for the HE_{12} mode the measured attenuation (at 10.9GHz) was found to be a factor of 3.0 times higher than theory. The HE_{11} mode attenuation is about 50% higher than measured by Chong < 2 > whilst the HE_{12} mode attenuation is consistent with the high value previously obtained. Chong's results are more comprehensive than those measured by the author as they

were obtained from a mean attenuation curve derived from measured results at 5 different frequencies.

An important factor, not previously considered, which increases the measured linewidth of a high Q-factor resonant cavity is that of slight random ellipticity in the cross-section of the waveguide forming the cavity. The ellipticity causes a slight split in the degeneracy between the two orthogonal polarisations of a resonant cavity mode, and for a mode with unity azimuthal number this results in the occurrence of a double resonance. For practical ellipticities the centre frequencies of the two resonances are very close and consequently they merge to form a single resonance with a lower Q-factor than that displayed by the single resonance of the perfectly circular resonant cavity. A theoretical analysis of this effect of random ellipticity on the resonant linewidth, and results relating to the waveguide of figure 4.2, are presented in chapter 6. The results of this study indicate that the measured ellipticity of the waveguide of figure 4.2 would have a negligible effect on the HE_{11} mode linewidth but a significant effect on the HE_{12} mode linewidth. When the linewidth widening effect of the HE_{12} mode resonance is taken into account the measured attenuation becomes approximately 2.1 times higher than theory, the same factor obtained for the HE_{11} mode.

The major contributing factor to the large difference between the measured and theoretical attenuations of the HE_{11} and HE_{12} modes comes from surface roughness

effects. Morgan <39> has shown that for surface scratches transverse to the direction of the surface current flow the increase in loss over that of a smooth surface is approximately 60% when the r.m.s. surface roughness is comparable to the skin depth and over 100% when the roughness is increased to twice the skin depth. For surface currents parallel to the grooves the increase in loss was found to be approximately one third of the above values. The skin depth in brass at 10GHz is 1.3μm and the surface of the waveguide sections used in the resonant cavity measurements were machined on a lathe and *not* polished, consequently the surface could easily exhibit surface scratches of order twice the skin depth. On the corrugation side walls and ridge top the surface scratches due to machining will be azimuthal and for the HE_{1m} modes the direction of the strongest current flow on these surfaces is radial,therefore resulting in a considerably increased loss. Consequently measured attenuations for the HE_{1m} modes twice those theoretically predicted can be expected due to surface roughness effects alone.

An additional contributing factor to the high value of measured attenuation results from the large number of contacting surfaces involved in the resonant cavity construction, it being inevitable that some imperfect contact will occur.

There are two main reasons for the discrepancy between the attenuation measurements made by Chong and those presented here. One concerns the measurement error

involved in Chong's measurement system and has already been discussed; the other concerns the contamination of the waveguide surface. A period of two years separates these two sets of measurements and over that time it is probable that the surface has become contaminated resulting in an increase in the surface resistivity of the brass over that of the bulk material. Measurements of this ageing effect have been made by Benson <40> at Q-band frequencies, where an increase in attenuation due to laboratory ageing of between 20% and 60% has been observed over a period of 15 months.

4.2.5 Conclusions

In this section a simple and quick method of measuring the 3dB linewidth of a cavity resonance has been described and shown experimentally to have a high degree of accuracy. A measurement technique has been developed to determine the change in attenuation of the propagating modes in a modified corrugated waveguide structure designed for mode filtering, and the probable error involved in the measurement has been experimentally studied for all four modes of interest. It has been found that this method is limited to measuring higher order mode attenuation increases of below about 100 times, the limiting factor being the lowest signal level that can be received from the output of the now *low Q-factor* resonant cavity.

The measurement of the attenuation of the HE_{11} and HE_{12} modes using a resonant cavity has been considered

and it can be concluded that unless a highly accurate form of cavity construction is employed the method cannot give an accurate assessment of mode attenuation. However, the relatively simple form of resonant cavity construction used here has enabled a general assessment of the attenuation of a prototype waveguide to be made quickly and cheaply, and herein lies the main use of the resonant cavity method of attenuation measurement.

4.3 TRANSMISSION TEST MEASUREMENTS

The resonant cavity technique, described in the previous section, is an indirect method of measuring the performance of modified corrugated waveguide structures for mode filtering, and is limited to measuring higher order mode attenuation increases of less than about 100 times. The transmission test method to be described in this section uses a long length of corrugated waveguide and compares the swept frequency signal transmitted through this waveguide with the input signal, thus yielding the frequency response of the corrugated waveguide. By using a corrugated waveguide known to exhibit a high trapped mode resonance loss the performance of a mode filter can be directly determined from its ability to suppress these trapped mode resonances.

In section 4.3.1 the trapped mode phenomenon is described and a method of mode filter measurement is developed. The measurement technique employed to implement this method is described in section 4.3.2 along

with a brief experimental investigation of its accuracy. Finally in section 4.3.3 the transmission test and resonant cavity methods for measuring mode filter performance are compared and shown to be complementary.

4.3.1 The trapped mode phenomenon

The mechanism resulting in the presence of a trapped mode resonance in the transmission spectrum of an overmoded waveguide, terminated in single mode input and output waveguides, has already been described in chapter 2. In a practical design of corrugated circular waveguide there are three propagating higher order modes and each of these modes exhibits a series of trapped mode resonances similar to that shown in figure 2.11 of chapter 2. As in the case of the resonant cavity a resonance occurs when the length of the waveguide, which in this case includes the portion of the corrugated waveguide transition in which the higher order mode propagates, is an integer multiple of half guide wavelengths. For each higher order mode the amplitude of the peak trapped mode resonance, the M.R.I.L. (maximum relative insertion loss), has been shown by Chong < 2 > to closely approximate the following formulae:

$$\text{M.R.I.L. (dB)} = \frac{150 \times 10^{-\left(\frac{C_{mn}}{20}\right)}}{\alpha_m L} \qquad (4.3)$$

where: C_{mn} is the amplitude coupling coefficient between the main and coupled modes, in dB;

α_m is the attenuation of the coupled mode, in dB/m;

L is the waveguide length, in metres.

From equation 4.3 it is clear that for a given coupling level the higher order mode with the lowest attenuation will produce the largest trapped mode loss. In the case of the corrugated waveguide the H_{01} mode has the lowest attenuation, its value being comparable to that of the dominant HE_{11} mode. The other two propagating modes (E_{02} and HE_{21}) have attenuations nearly an order of magnitude higher than the H_{01} mode and consequently produce a much smaller trapped mode loss.

The introduction of a mode filter into the waveguide increases the value of the higher order mode attenuation, α_m, and from equation 4.3 reduces the trapped mode resonance loss. Therefore by comparing the M.R.I.L.'s for each of the higher order modes with and without the mode filter present, *but with the total waveguide length kept constant* , the increase in higher order mode attenuation can be determined. It is necessary to maintain the waveguide length constant in order to maintain the resonances at the same frequency and the mode coupling levels constant. This method of measuring the performance of a mode filter has the advantage that it directly shows the degree by which the transmission characteristic is *smoothed out* an important performance criteria for corrugated waveguide feeders.

4.3.2 The transmission test measurement system

A 2 metre length of flexible corrugated circular waveguide, figure 4.6, known to exhibit a considerable

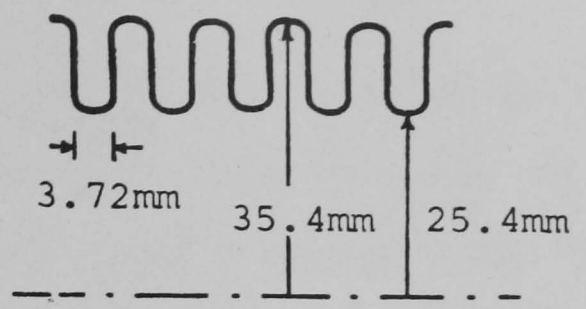

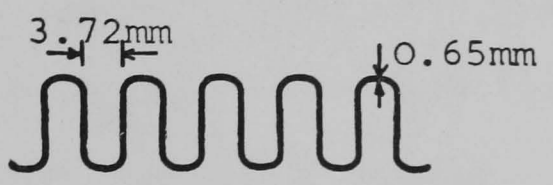

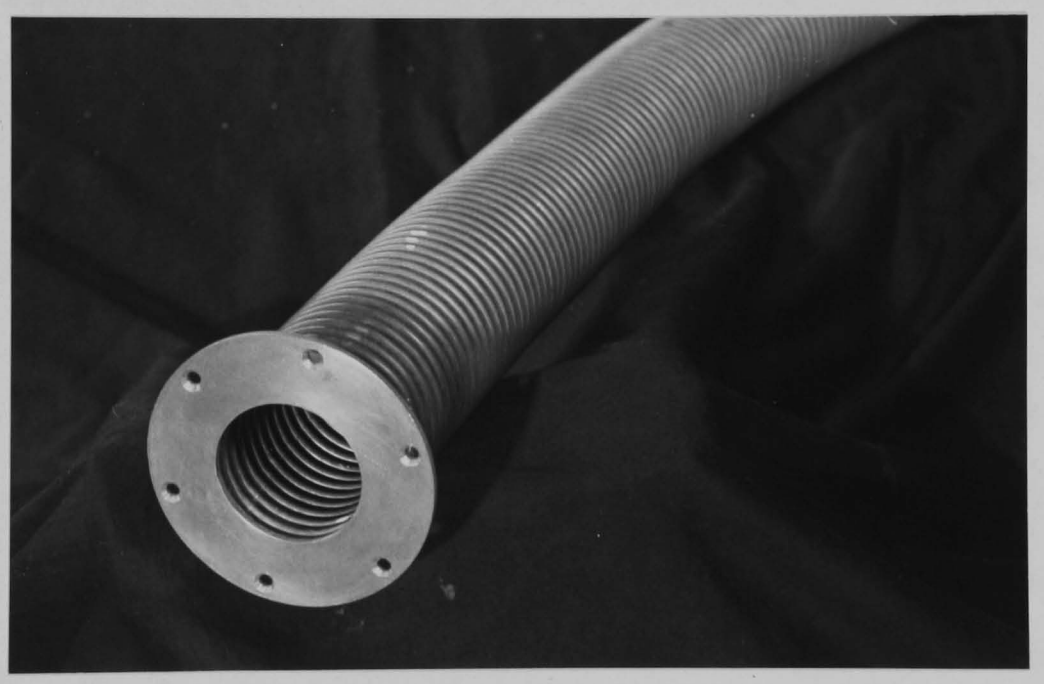

Fig. 4.6 The flexible corrugated bronze pipe

trapped mode loss was used for these transmission measurements. The mode filters to be measured using this method were manufactured from the same flexible pipe with a fixed length of 3.7cm. Unmodified lengths of this waveguide, also of length 3.7cm, were used to enable the measurement with and without the mode filter to be made with a constant total waveguide length. The flexible corrugated waveguide was held rigidly straight with fixed azimuthal orientation throughout the experimental programme to ensure no change in the mode coupling levels occurred.

A schematic of the experimental apparatus used for these transmission measurements is shown in figure 4.7. Details of the rectangular to smooth wall circular and smooth wall circular to corrugated circular waveguide transitions have been previously given by Chong < 2 > and will not be repeated here. To avoid the complication of multimode propagation in the smooth wall circular waveguide part of the transitions, the frequency of operation was kept below 10GHz. As in the case of the cavity measurements it is essential to minimise the level of multiple reflections in the measuring system and again isolators and padding attenuators were used to minimise these reflections. A Network Analyser was used to overcome the problem of microwave power fluctuations which can occur over the period of about 30 seconds required to record the transmission characteristic. To maintain a low VSWR in the system it was necessary to construct the reference and test channels in rectangular waveguide, as

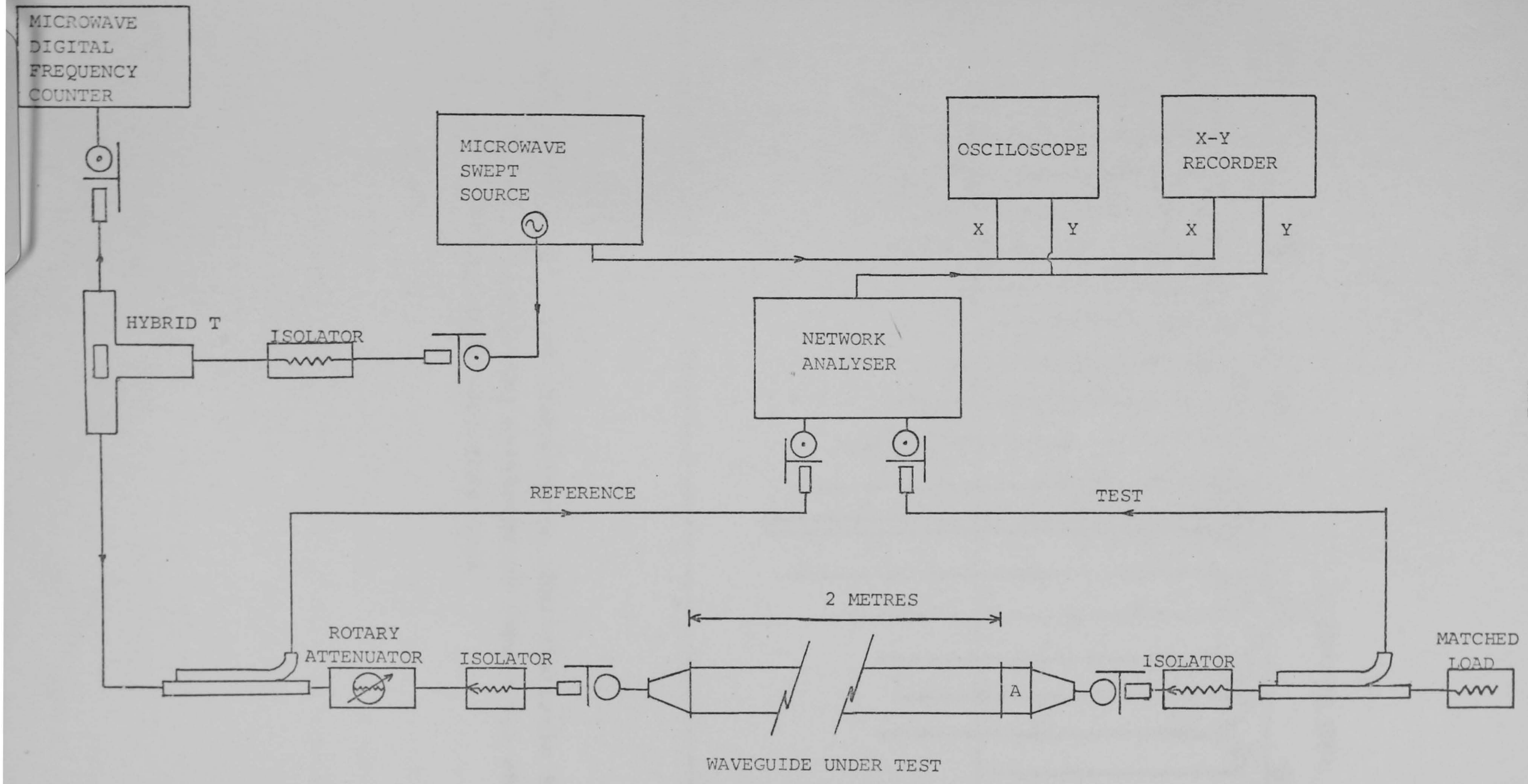

Fig. 4.7 Schematic of transmission test measurement apparatus

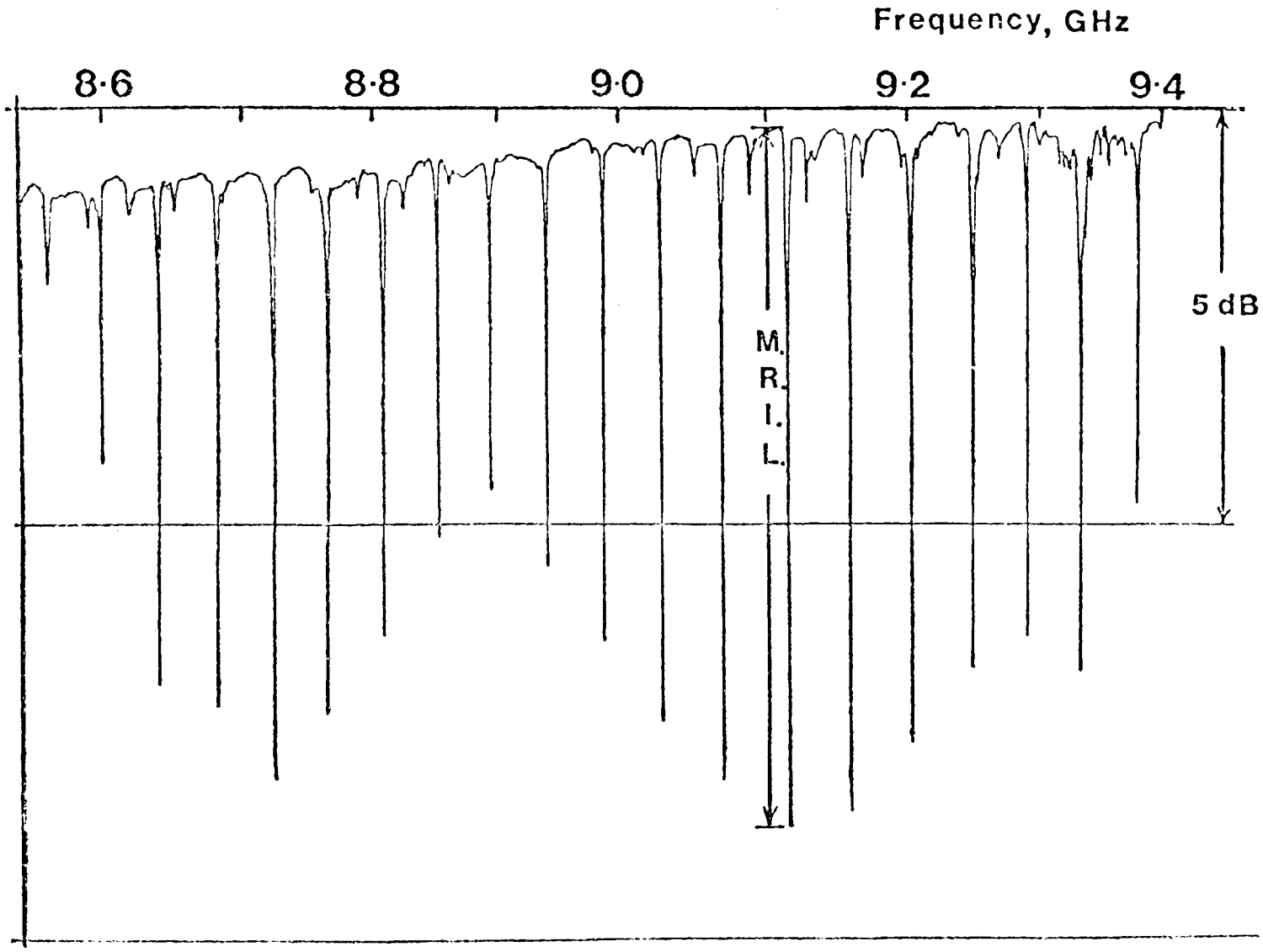

Fig. 4.8 Typical measured transmission characteristic for the flexible corrugated waveguide of figure 4.6 showing the trapped mode resonance loss

microwave coaxial cable was found to introduce a considerable ripple on the transmission pattern.

Figure 4.8 shows a typical transmission characteristic for the corrugated waveguide and transitions, the largest trapped mode resonances all being due to the H_{01} mode because of its low attenuation. Because of the inability of the chart recorder to accurately track these deep resonances, their amplitudes were measured using an oscilloscope and then added manually to the recorded pattern.

In order to estimate the experimental accuracy of the comparison between the trapped mode loss obtained with and without a mode filter in the corrugated waveguide, the following test was made. The trapped mode loss of several of the largest resonances were first measured, then the test section A, (figure 4.7) of the waveguide was removed, then replaced, and the measurement repeated. This test was repeated several times and the largest variation in the resonant amplitudes was found to be of order 10%. This is most certainly due to the slight change in coupling resulting from, 1) axial misalignment of test waveguide and 2) slight movement of the main corrugated waveguide run. In the mode filter designs to be considered in this thesis, order of magnitude changes in resonant amplitudes are of interest and so this small error is insignificant.

4.3.3 Conclusions

In this section a transmission test method for

measuring the performance of corrugated waveguide mode filters has been described. This method has the advantage over the resonant cavity method in that it directly measures the performance of the mode filter in one of its intended environments. In addition it allows increases in higher order mode attenuation of greater than 100 times to be measured. However the method cannot be used to give any accurate assessment of the small increase in HE_{11} mode attenuation due to the mode filter, this parameter being termed the filter *insertion loss*. A very low insertion loss is an important factor in the design of mode filters for low attenuation waveguides and so an accurate measurement of this parameter is required. The resonant cavity method is ideally suited to this measurement, the resonant cavity Q-factor being very sensitive to small increases in mode attenuation. In fact the resonant cavity method represents a relatively quick and simple technique for generally assessing the performance of a prototype mode filter.

To conclude, it is evident that the resonant cavity and transmission test methods are complementary in determining the performance of a corrugated waveguide mode filter. Both these measurement methods are used in the development of low insertion loss corrugated waveguide mode filters described in chapter 7. The resonant cavity method is also a convenient technique for assessing the dominant mode attenuation of new waveguide designs and is used in the study of the monomode corrugated waveguide presented in chapter 8.

CHAPTER 5

MODE CONVERSION DUE TO BENDS IN FLEXIBLE CORRUGATED CIRCULAR WAVEGUIDE

5.1 INTRODUCTION

The presence of a bend occurring along the length of an overmoded flexible waveguide causes coupling to the higher order propagating modes. In the attenna feeder application it is important to maintain the total level of higher order mode present in the waveguide below a specific level to ensure that the antenna system performance is not significantly degraded. A knowledge of the *power coupling coefficient* for these higher order modes allows the specification of the largest number of bends and the smallest bend radii that can occur along the feeder run in order to remain below this specified level of total coupling. In this chapter the problem of mode conversion resulting from a bend in a flexible corrugated circular waveguide is studied both theoretically and experimentally enabling these power coupling coefficients to be calculated.

In section 5.2 the theoretical analysis of the mode conversion process is presented and formulae for the power coupling coefficients of the three higher order modes propagating in the circular corrugated waveguide are derived. A physical interpretation of the mode coupling process is also presented in this section. Numerical

results for the coupling coefficients in a practical size of flexible corrugated waveguide are given in section 5.3, and the effect of the waveguide slot depth on their value is considered. Experimental results for the mode conversion levels due to a single bend in a corrugated waveguide are compared with the predicted results in section 5.4 and quite good agreement is seen to be obtained. Using these theoretical results for mode coupling, section 5.5 considers the effect of bends along a corrugated waveguide feeder on the performance of an antenna system employing either single or dual polarisation operation. The use of mode filters to improve the feeder performance is also considered.

5.2 THEORETICAL ANALYSIS OF MODE COUPLING DUE TO A WAVEGUIDE BEND

5.2.1 Formulation of the coupling coefficient

In this section the formulation of the mode conversion process due to a waveguide bend is described. The simplified problem of calculating the coupling due to a waveguide tilt is first considered, as any desired bend can be constructed from a succession of infinitesimal tilts and straight sections. The coordinate system for the tilt is shown in figure 5.1. By using a modal matching technique the amplitudes of the various modes constituting the field in waveguide 2 (figure 5.1) are obtained from the distorted version of the incident mode present at the input aperture to waveguide 2. This describes the coupling

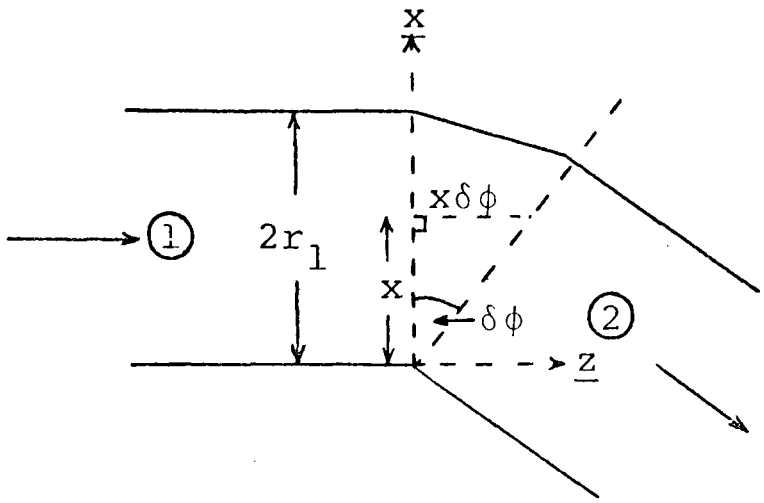

Fig. 5.1 Waveguide tilt geometry

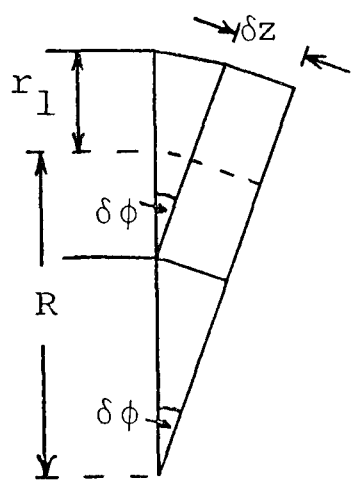

Fig. 5.2 Elemental section of a waveguide bend

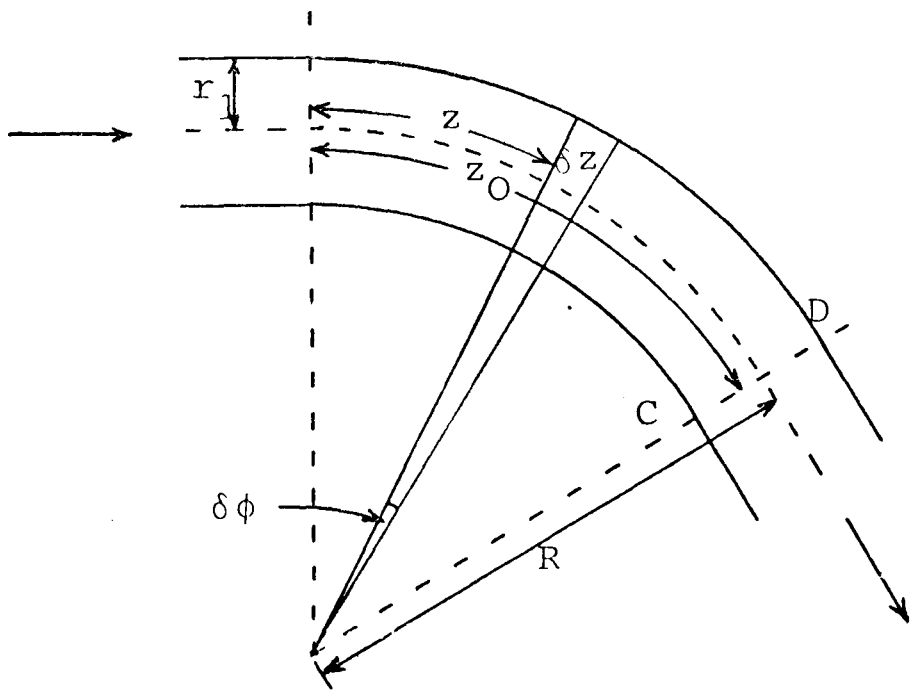

Fig. 5.3 Waveguide bend geometry

process correct to the first order, the second order process of coupling from the coupled modes already present in waveguide 1 back into the main mode (reconversion) is neglected.

The coupling coefficient amplitude per degree of tilt, a_{mn}, which represents the level of coupled mode, m, in waveguide 2 resulting from the incident mode, n, in waveguide 1, is derived for a general circular waveguide in appendix 5.2 following a method previously used by Poulton <42>. This formulation shows that the coefficient a_{mn} is zero unless the azimuthal number of the coupled mode differs by unity from that of the incident mode.

The coupling due to the more general waveguide bend is calculated by constructing the bend from elementary sections comprising a waveguide tilt, $\delta\phi$, followed by a straight length of waveguide, δz, figure 5.2. Considering the finite bend shown in figure 5.3, at each point z on the bend a small amount of energy will be scattered from the main mode, n, into the coupled mode, m. This coupled energy will travel around the bend a distance $z_o - z$ where the contributions from every point z on the bend may be summed. At point z the phase of the main mode is $e^{-\gamma_n z}$ and the phase of the coupled mode, m, coupled at z and travelling a distance $z_o - z$, is $e^{-\gamma_m (z_o - z)}$. The contribution to the total coupled field, $C_{mn}(z_o)$, due to the segment of the bend δz, at z, is thus

$$C_{mn}(\delta z) = (e^{-\gamma_n z} a_{mn} \delta\phi) e^{-\gamma_m (z_o - z)}$$

where $a_{mn}\delta\phi$ is the amplitude coupling coefficient due to the tilt $\delta\phi$.

This equation can be simplified for $R >> r_1$ to:-

$$C_{mn}(\delta z) = e^{-\gamma_m z_o} \frac{a_{mn}}{R} e^{-(\gamma_n-\gamma_m)z} \delta z \qquad (5.1)$$

The total amplitude of the coupled field is obtained from this equation by integrating over the bend length z_o. This yields

$$C_{mn}(z_o) = e^{-\gamma_m z_o} \int_o^{z_o} \frac{a_{mn}}{R(z)} e^{-(\gamma_n-\gamma_m)z} dz \qquad (5.2)$$

noting that the bend radius R need not be constant with z. However, for a constant bend radius the integral of equation 5.2 may be evaluated giving:-

$$C_{mn}(z_o) = \frac{a_{mn}}{R(\gamma_n-\gamma_m)} (e^{-\gamma_m z_o} - e^{-\gamma_n z_o}) \qquad (5.3)$$

Assuming a loss-less waveguide, $\gamma_m = j\beta_m$ and $\gamma_n = j\beta_n$, and after some manipulation the amplitude coupling coefficient for a waveguide bend of radius R and length z_o is obtained as:-

$$C_{mn}(z_o) = \frac{2a_{mn}}{R(\beta_n-\beta_m)} \sin\left[\frac{(\beta_n-\beta_m)z_o}{2}\right] e^{\frac{-j(\beta_n+\beta_m)z_o}{2}} \qquad (5.4)$$

From equation 5.4 it is evident that the *power* coupling coefficient varies as $\sin^2 \frac{(\beta_n-\beta_m)z_o}{2}$ and does *not* continually increase as the bend length increases, but oscillates with a period of $\frac{2\pi}{(\beta_n-\beta_m)}$. Therefore bend lengths that are integer multiples of $\frac{2\pi}{(\beta_n-\beta_m)}$ have zero

coupling to mode m, the power coupled from any one point on the bend being cancelled by an anti-phase contribution, distance $\frac{\pi}{(\beta_n - \beta_m)}$ away. The maximum amplitude of the coupled mode is independent of the bend length and is given by

$$\left|C_{mn}\right|_{max} = \frac{2|a_{mn}|}{R(\beta_n - \beta_m)} \qquad (5.5)$$

For the corrugated waveguide the main mode is the HE_{11} mode and consequently the coupled modes will have azimuthal numbers of either 0 or 2. In this case the evaluation of the θ integrals for a_{mn}, given in appendix 5.2, leads to the following results for mode conversion due to bending in a corrugated circular waveguide propagating 3 higher order modes.

1) An E-plane bend only couples into the E_{02} and HE_{21} modes.
2) An H-plane bend only couples into the H_{01} and HE^{*}_{21} modes.
3) The magnitude of the HE_{21} mode coupling coefficient is not dependent on the plane of the bend, although its polarisation is.

These concepts are shown diagramatically in figure 5.4 where the transverse field patterns of the modes are shown.

The space-harmonic field components in the inner region of the corrugated waveguide are presented in appendix 5.1, and normalising the space-harmonic coefficients

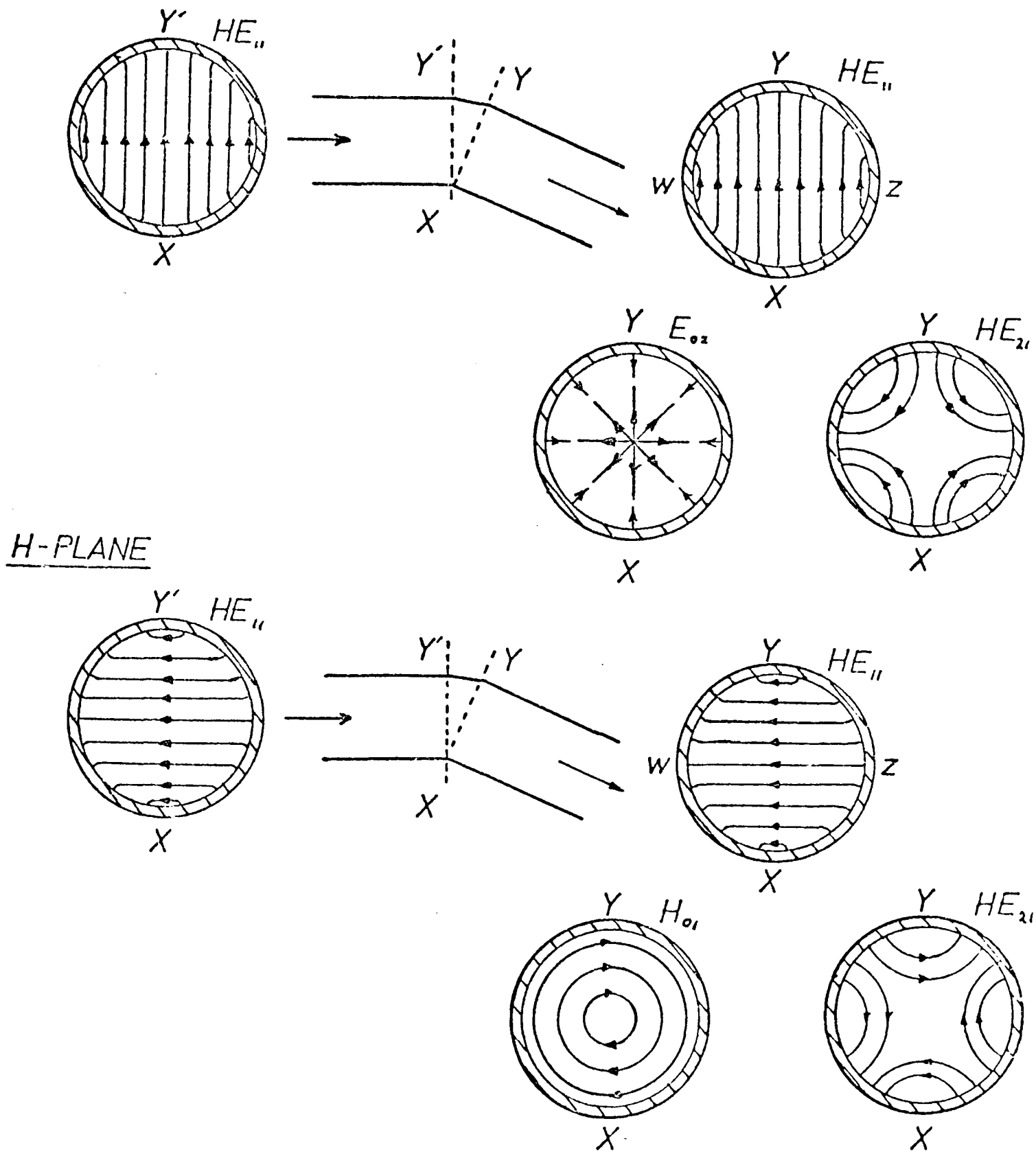

Fig. 5.4 Transverse electric field pattern for the main and coupled modes resulting from a tilt in a corrugated circular waveguide

for unit power modes allows the evaluation of the equations for a_{mn} in terms of the waveguide parameters. In this analysis the slot region of the waveguide has not been considered because the slot modes are non-propagating in the z direction. The amplitude coefficients of these slot modes will in practice be slightly modified by the bend causing a minor modification to the waveguide attenuation but having a negligible effect on the propagation coefficient.

5.2.2 Physical interpretation of mode coupling

A study of the transverse field patterns of figure 5.4 can lead to a physical understanding of the coupling process. The field present at xy will be a distorted version of the incident HE_{11} mode field and the region of maximum distortion will occur at the edge of the waveguide, in the xy regions. This is because at the exit aperture of the tilt, xy, the HE_{11} field has a phase error across it caused by the difference in path-length, and taking the centre of the guide as the phase zero, region x will have phase lead, region y phase lag and regions w and z will be in-phase. To obtain this field pattern at xy from an orthogonal set of modes it is necessary to include the fields of modes with azimuthal numbers of 0 and 2 as well as that of the HE_{11} mode. Hence the process of mode coupling.

Consider the case, shown in figure 5.4, when the HE_{11} field amplitude is a maximum at the aperture xy', the field amplitude of the perturbed HE_{11} mode will be smaller

in region y, greater in region x and unchanged in the w, z, and central regions from that of the pure HE_{11} mode. By visually summing the two field patterns of the E_{02} and HE_{21} modes shown in figure 5.4, this requirement is seen to be obtained for the E-plane polarisation, thus:

1) In regions x and y both modes have the same field direction and would respectfully increase and decrease the field amplitude of the HE_{11} mode in their regions.
2) In regions w and z the fields cancel each other producing little effect on the HE_{11} mode pattern.

The resultant field of the $H_{01} + HE^{*}_{21}$ mode combination is the opposite of that required of the coupled modes for an E-plane tilt and hence are not coupled. A similar result applies to the H_{01} and HE^{*}_{21} modes in an H-plane bend.

5.3 NUMERICAL RESULTS FOR MODE COUPLING DUE TO BENDING IN A FLEXIBLE CORRUGATED CIRCULAR WAVEGUIDE

The numerical results presented in this section are for the flexible corrugated waveguide shown in figure 5.5 which is used in the experimental investigation, described in the next section. The dimensions of this waveguide are close to the optimum for low attenuation and therefore the results are representative of a practical flexible antenna feeder. Figure 5.6 shows the maximum relative power of the coupled mode, equation 5.5, for this waveguide plotted as a function of frequency for a bend radius, R, of one metre. The three modes shown are the only coupled modes propagating over the frequency band covered. Results for

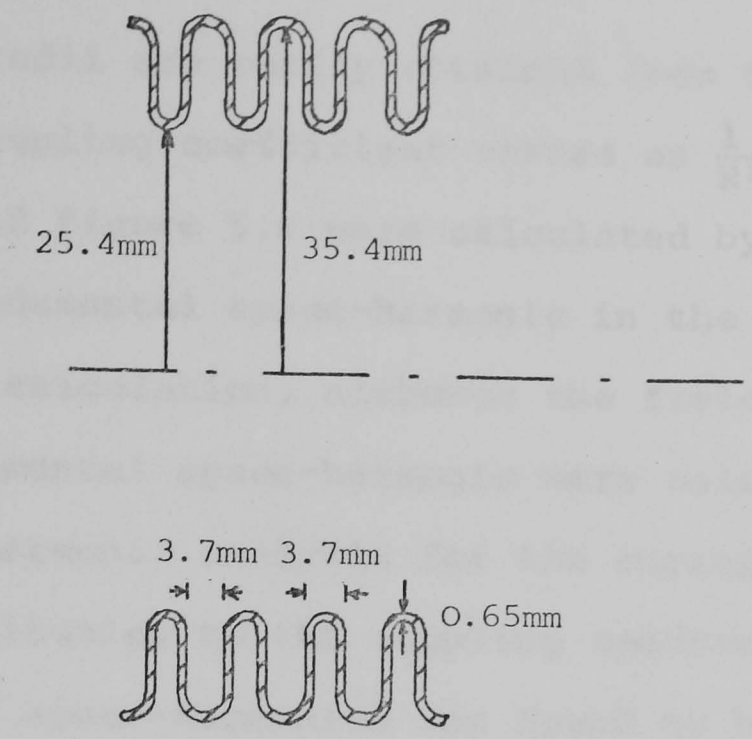

Fig. 5.5 Flexible corrugated bronze waveguide

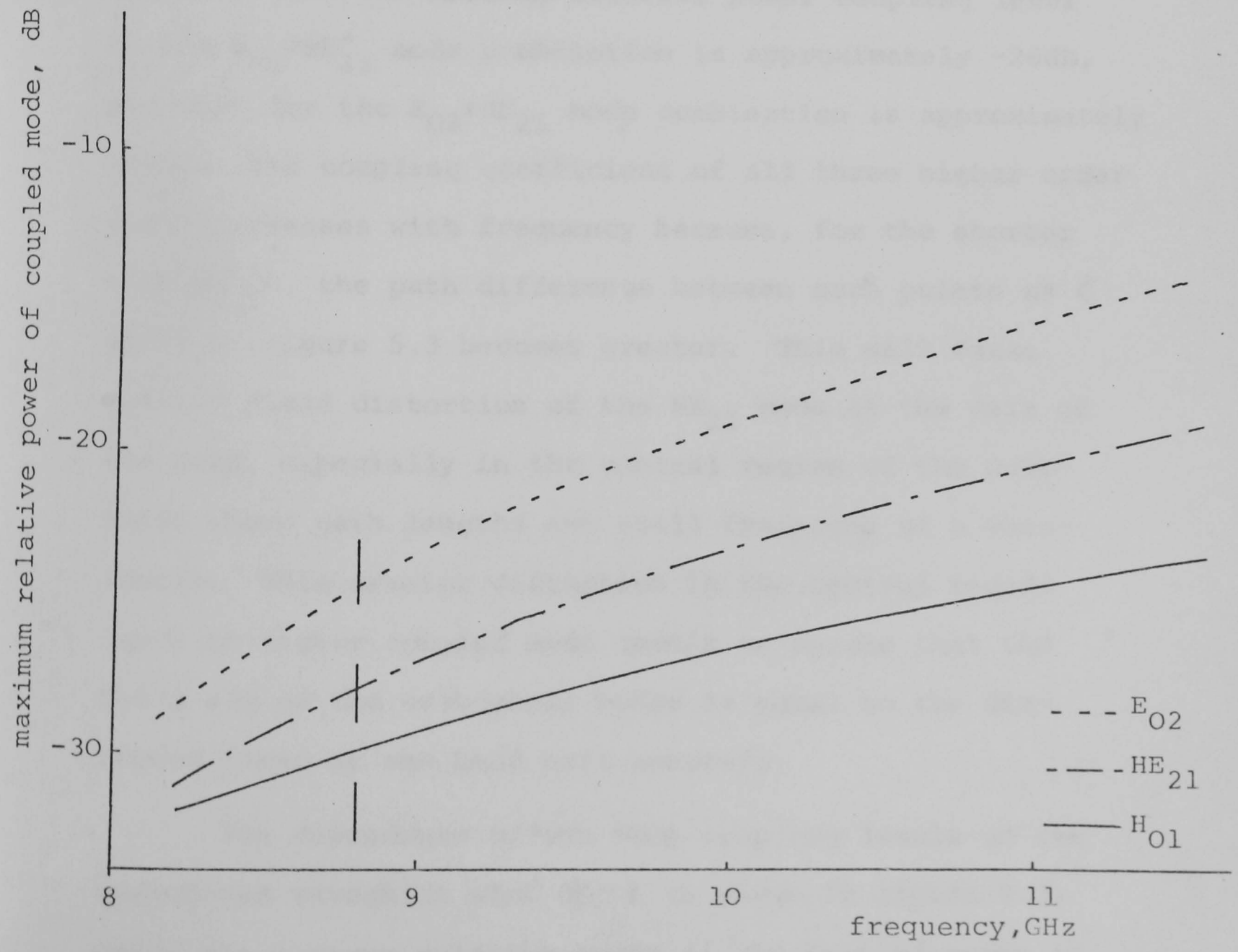

Fig. 5.6 Theoretical variation with frequency of mode coupling due to a 1 metre radius bend in a corrugated waveguide.

Waveguide dimensions are shown in figure 5.5

other bend radii are easily obtained from this figure as the power coupling coefficient varies as $\frac{1}{R^2}$, equation 5.5. The curves of figure 5.6 were calculated by considering only the fundamental space-harmonic in the coupling coefficient calculation, although the field coefficients of the fundamental space-harmonic were calculated from the full space-harmonic analysis for the corrugated waveguide. Direct contribution to the coupling coefficients from the higher order space-harmonics was found to be negligible.

At the design frequency for the flexible corrugated waveguide, 8.8GHz, the results of figure 5.6 indicate that the maximum relative power coupling level to the $H_{01}+HE^{*}_{21}$ mode combination is approximately -26dB, and that for the $E_{02}+HE_{21}$ mode combination is approximately -23dB. The coupling coefficient of all three higher order modes increases with frequency because, for the shorter wavelength, the path difference between such points as C and D of figure 5.3 becomes greater. This will cause greater field distortion of the HE_{11} mode at the exit of the bend, especially in the central region of the waveguide where path lengths are still fractions of a wavelength. This greater distortion in the central region leads to higher coupled mode levels to ensure that the field sum of the orthogonal modes is equal to the distorted field at the bend exit aperture.

The dependence of the mode coupling levels on the corrugated waveguide slot depth is shown in figure 5.7, where the maximum relative power of the coupled modes is

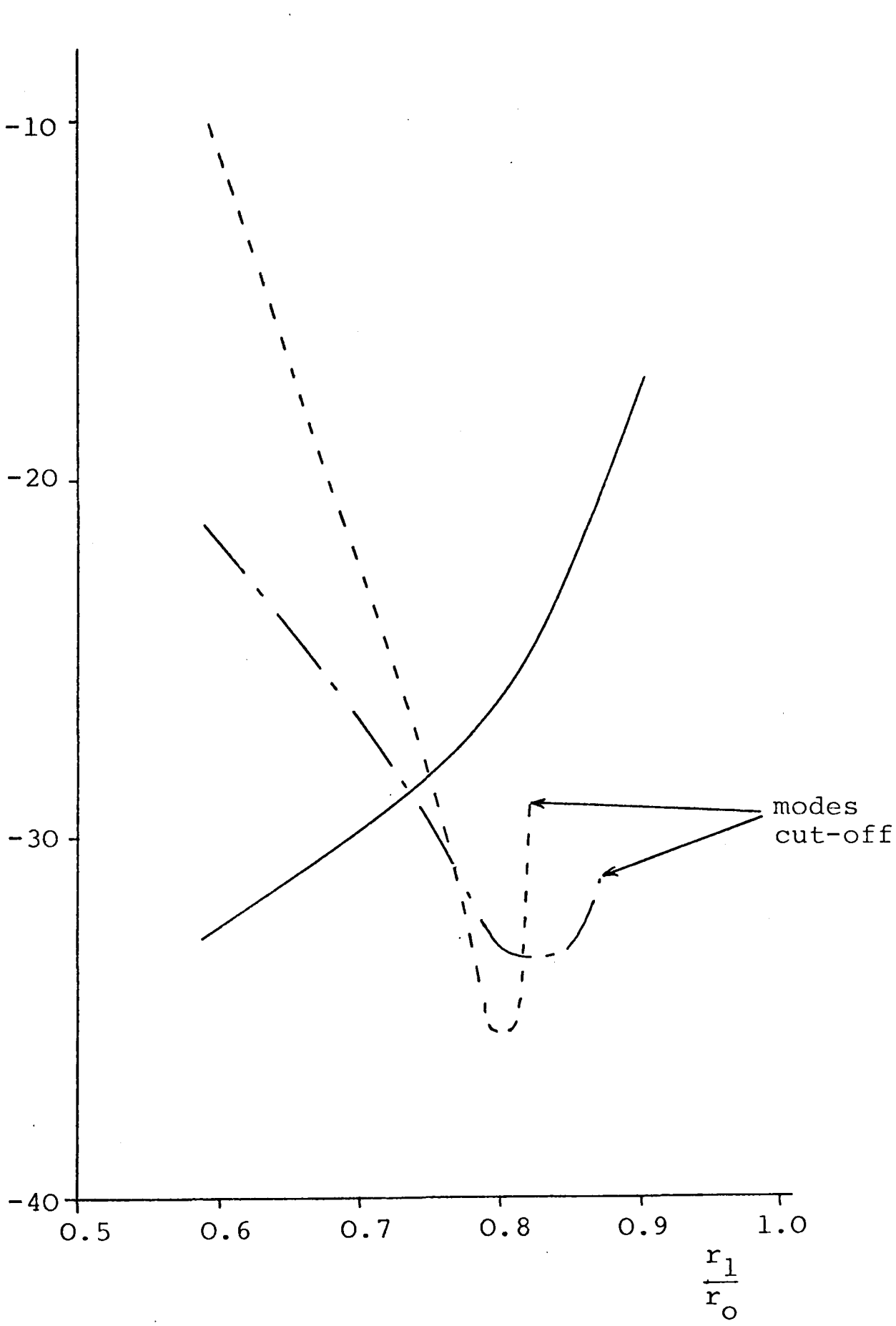

Fig. 5.7 Mode coupling levels due to a 1 metre radius bend as a function of r_1/r_o

Parameters: frequency = 8.8GHz, r_1 = 25.4mm

- - - E_{02}

- —— - HE_{21}

—— H_{01}

shown plotted as a function of $\frac{r_1}{r_o}$ for a fixed inner radius, r_1. From this figure it is found that the maximum power coupling level to the $H_{01}+HE^*_{21}$ mode combination remains nearly constant at a level of -26dB over the $\frac{r_1}{r_o}$ range 0.7 to 0.8. On the other hand the maximum power coupling level to the $E_{02}+HE_{21}$ mode combination has a definite minimum in the region $\frac{r_1}{r_o} = 0.8$. The results for the $H_{01}+HE^*_{21}$ mode combination suggest that there is no advantage in modifying the slot depth of the waveguide to improve the power coupling level.

Much of the shape of the curves of figure 5.7 can be attributed to the change in degeneracy between the HE_{11} and the coupled modes as the slot depth is varied. The power coupling coefficient is inversely proportional to the difference between the propagation coefficients of the main and coupled modes, equation 5.5. Figure 5.8(a) shows the dispersion curves for the HE_{11} and H_{01} modes for two values of $\frac{r_1}{r_o}$. The cut-off frequency for the H_{01} mode remains practically constant as $\frac{r_1}{r_o}$ is reduced, in contrast to the HE_{11} mode cut-off frequency which decreases with decreasing $\frac{r_1}{r_o}$. Therefore as $\frac{r_1}{r_o}$ is reduced the degeneracy between these two modes reduces and consequently the coupling level also reduces. Figure 5.8(b) shows the dispersion curves for the HE_{11} and E_{02} modes and in this case as $\frac{r_1}{r_o}$ is reduced the modes become more degenerate and consequently the coupling level of the E_{02} mode will increase as $\frac{r_1}{r_o}$ increases. The HE_{21} mode shows a similar variation with $\frac{r_1}{r_o}$. Figure 5.9 shows a plot of

a) H_{01} mode

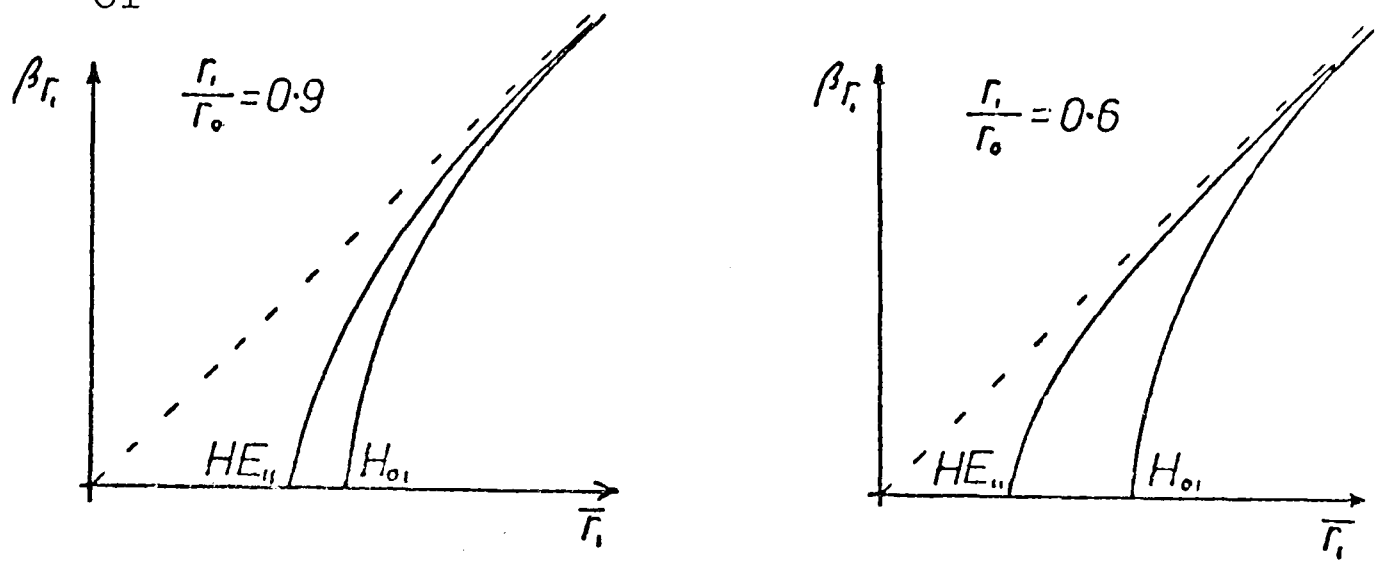

b) E_{02} mode

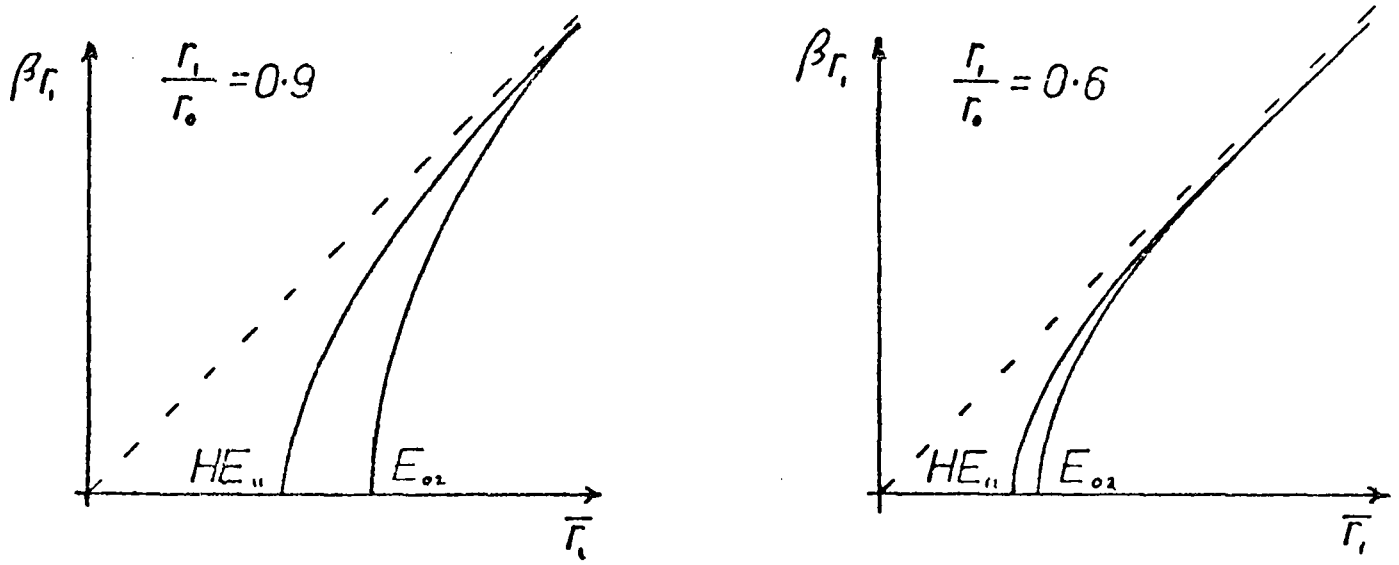

Fig. 5.8 Typical dispersion curves for several coupled modes at two r_1/r_0 values

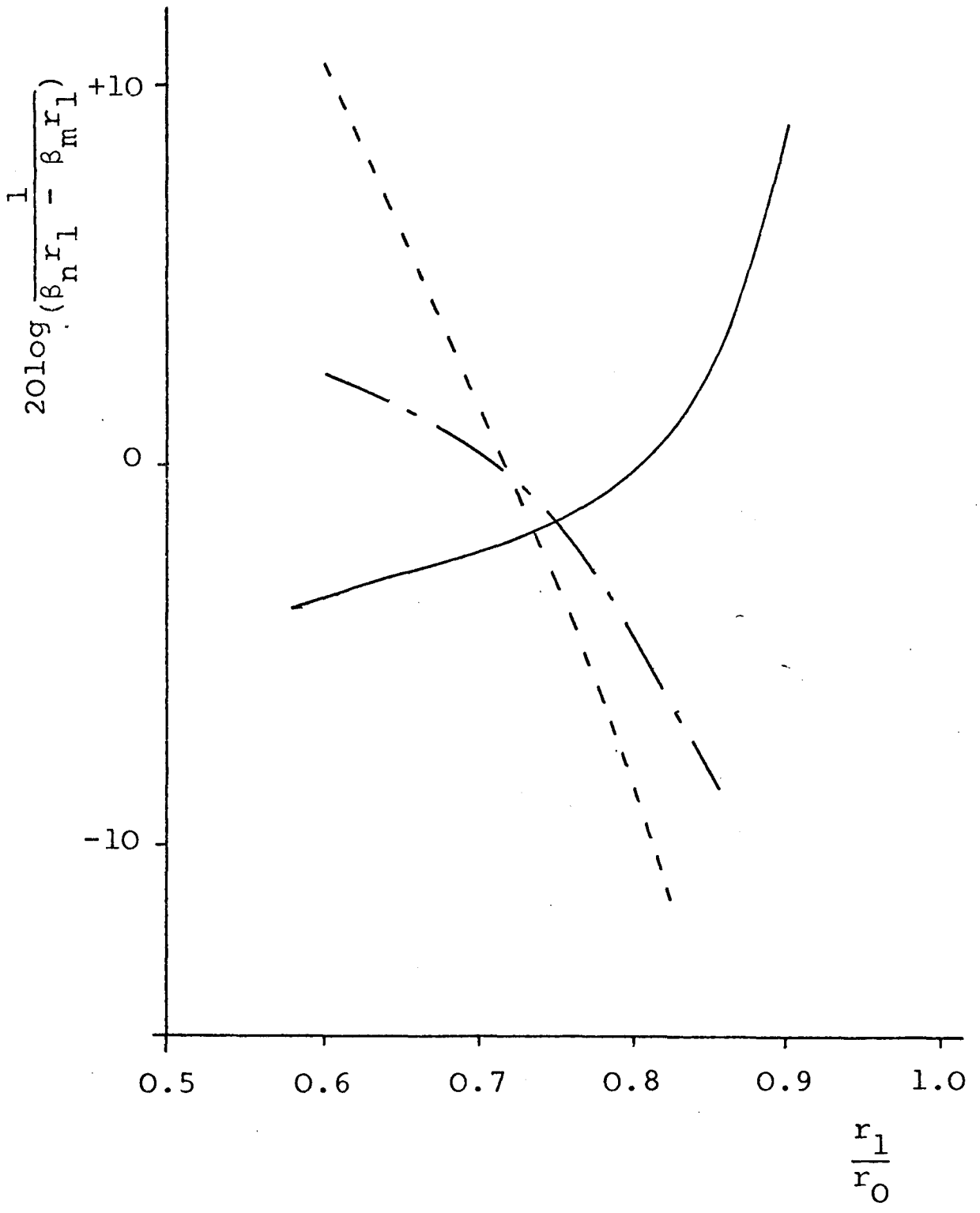

Fig. 5.9 Reciprocal of the degeneracy between the HE_{11} mode and the coupled modes as a function of r_1/r_o, waveguide parameters as figure 5.7

- - - - E_{02}

· —— · HE_{21}

——— H_{01}

$20 \log \frac{1}{(\beta_n r_1 - \beta_m r_1)}$ as a function of $\frac{r_1}{r_o}$ corresponding to the results of figure 5.7; clearly the shape of the $C_{mn_{max}}$ versus $\frac{r_1}{r_o}$ curve can be largely obtained by considering only the mode degeneracy.

The actual power coupling level for a given mode with fixed bend radius depends on the amplitude coupling coefficient for a waveguide tilt, a_{mn}, which in turn depends on the field amplitude of the HE_{11} mode in the neighbourhood of $r=r_1$. For a small tilt the maximum HE_{11} mode distortion at the tilt occurs in the region of the corrugations and consequently a high level of field there will require high coupled mode levels to synthesise the distorted field from the orthogonal waveguide modes. This suggests that low coupling due to bends and low attenuation have *similar* HE_{11} mode field requirements; low coupling requires low fields in the *neighbourhood* of the surface created by the corrugation walls and low attenuation requires a low field *at* this surface.

5.4 EXPERIMENTAL MEASUREMENTS OF THE MODE COUPLING COEFFICIENTS DUE TO A BEND IN A FLEXIBLE CORRUGATED CIRCULAR WAVEGUIDE

In this section measurements of the mode conversion levels due to a bend in a 2 metre length of flexible corrugated circular waveguide, figure 5.5, are described and comparison with the theoretically predicted values are made.

The measurement of the mode coupling levels was

made with one end of the waveguide open-ended using the swept frequency radiation pattern measurement technique described in chapter 3. The experimental measurement system is shown in figure 3.11 of chapter 3, the large waveguide support table containing a jig allowing the 2 metre length of waveguide to be held straight or with a single bend having a radius of curvature of 60cm. The flexible corrugated pipe used in these measurements was originally manufactured for fluid handling purposes and therefore did not have the manufacturing tolerances usually associated with microwave waveguide. The principal imperfection in the construction was the presence of a welded seam of poor finish which ran helically down the pipe.

The level of mode conversion measured in this waveguide when laid straight was found to depend on the polarisation of the HE_{11} mode. In the worst case, mode conversion levels as high as -11dB for the $E_{02}+HE_{21}$ mode combination and -12dB for the $H_{01}+HE^{*}_{21}$ mode combination were measured. Imperfections in the welded seam causing truncation of the current flow, and a series of random tilts along the waveguide run were found to be the main contributors to this high level of coupling. Imperfections in the welded seam would lead to a variation of coupling with polarisation, because the coupling level would depend on the current strength and direction at the weld imperfection. In addition, calculations show that a 6^{o} waveguide bend of 60cm radius of curvature would prcduce

coupling levels of order -20dB in both the radiation measurement planes. The total coupling due to several of these small bends could be cumulative depending on the phase of each individual contribution. Examination of the pipe when *straight* showed that several small bends of this order were present along the waveguide length. The lowest coupling level measured for the *straight* waveguide was found to be -20dB for both the $H_{01}+HE^{*}_{21}$ and $E_{02}+HE_{21}$ mode combinations.

When the incident HE_{11} mode polarisation was orientated so as to produce minimum mode conversion with the waveguide *straight*, the following mode coupling levels were measured when a 60cm radius of curvature bend was introduced:

An E-plane bend coupling to the $E_{02}+HE_{21}$ mode combination gave a measured coupling level of -18dB at 9.6GHz (theoretical prediction -15dB).

An H-plane bend coupling to the $H_{01}+HE^{*}_{21}$ mode combination gave a measured coupling level of -20dB at 9.2GHz (theoretical prediction -20dB).

With the waveguide in the minimum coupling position it can be assumed that the weld imperfections cause little coupling and that most of the coupling results from the several small bends present in the *straight* waveguide. However, when the waveguide is bent these small bends are removed due to the bending stress present in the pipe.

Therefore it can be assumed that the measured coupling levels for the bent waveguide are due to the bend and not the imperfections present in the waveguide. In view of this assumption the experimentally measured coupling levels obtained give quite a good agreement with the theoretically predicted results.

The normalised swept frequency radiation patterns measured were found to be approximately centred about the theoretical HE_{11} mode pattern level, indicating little coupling to the HE_{12} or EH_{12} modes (see chapter 3). This is in agreement with the theoretical study of section 5.2, which found that a bend would not cause direct coupling into unity azimuthal number modes.

5.5 THE EFFECT ON ANTENNA SYSTEM PERFORMANCE OF BENDS IN THE FLEXIBLE CORRUGATED WAVEGUIDE ANTENNA FEEDER

In this section the theoretical calculation of mode conversion levels, developed in section 5.2 and verified experimentally in the previous section, are used to estimate the effect on the performance of an antenna system.

It will be shown in chapter 10 of this thesis that a coupling level of order -35dB for both the $H_{01}+HE_{21}^{*}$ and $E_{02}+HE_{21}$ mode combinations is required in order not to significantly degrade the cross-polar pattern of the antenna feed. It is practical to assume that the $H_{01}+HE_{21}^{*}$ mode combination coupling level of -26dB for a 1 metre radius bend (figure 5.6) to be the highest coupling level,

as some reduction in the power level of the $E_{02}+HE_{21}$ modes would be expected because of their higher attenuation when compared to the HE_{11} and H_{01} modes. Therefore a feeder having the waveguide dimensions of figure 5.5 and comprising of *2 bends* having radii of curvature no smaller than about *3 metres* would approximately achieve the required -35dB coupling level specified. The bend requirements for any desired operating frequency can be obtained from these results by scaling, and a table of normalised results for several bend combinations is given in table 5.1. The specification for the radius and number of bends given above assumes that there is no mode coupling due to small tilts, or *microbends*, along the waveguide run. However, a method of construction is envisaged where the outer surface of the flexible corrugated waveguide would be covered in some form of rubber or plastic compound to reduce this microbending effect to a minimum. In passing it is worth noting that this problem is similar to that of microbends in optical fibre waveguide and consequently the plastic coating used for this application could also be used to cover the flexible corrugated waveguide.

By using a mode filter, a waveguide feeder with more bends and/or smaller bend radii can be made to achieve the required mode coupling levels. For dual polarisation operation the mode filters required, are based on the *optical fibre principle* < 3 > and a typical design is shown in figure 5.10. However they have a relatively high HE_{11} mode insertion loss (for the waveguide

Number of constant radius bends	Approximate minimum bend radii, wavelengths
1	6Oλ
2	9Oλ
3	12Oλ
4	15Oλ

Table 5.1 Minimum bend radii for specified number of bends required to achieve a mode coupling level of order -35dB

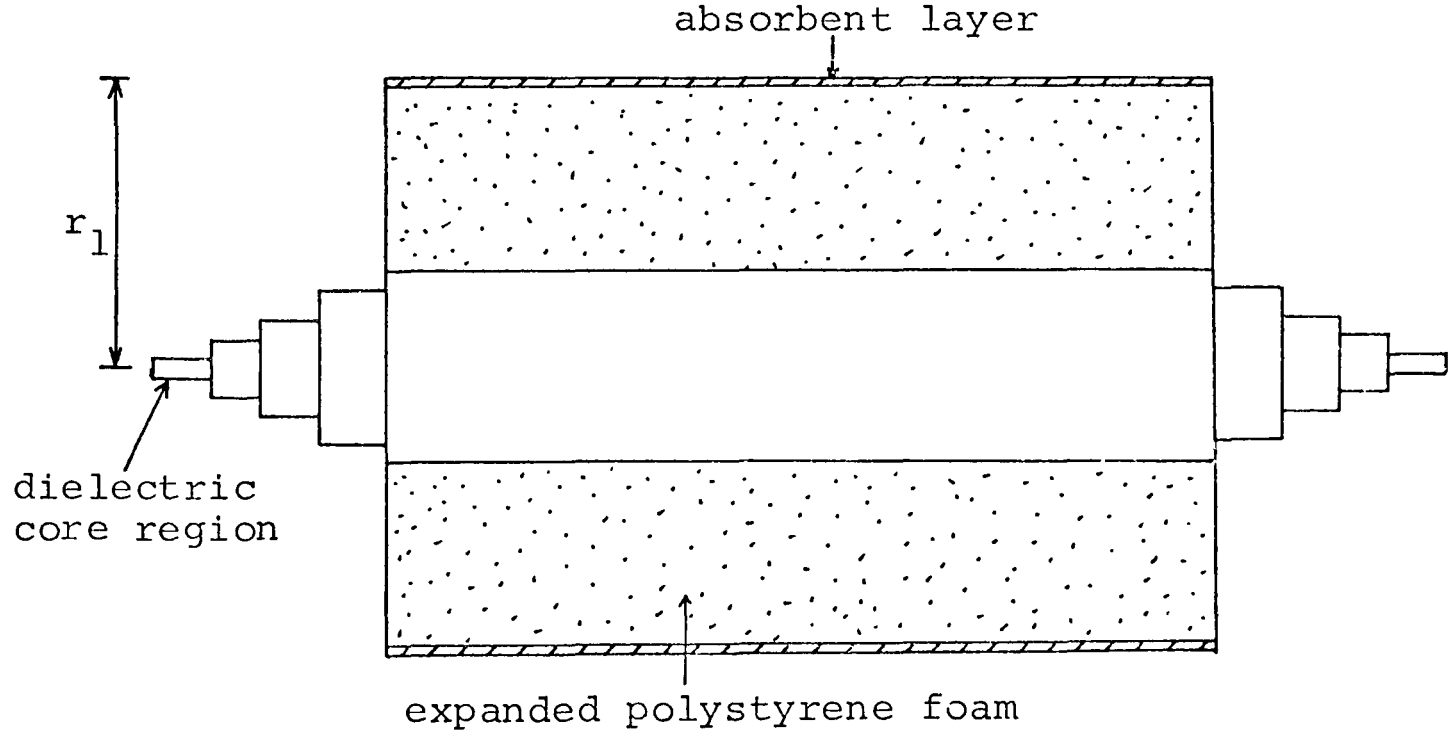

Fig. 5.10 Absorbent mode filter for dual polarisation operation

of figure 5.5, with an HE_{11} mode attenuation of 0.06dB/m, a typical mode filter would have a 0.2dB insertion loss < 2 >) which offsets much of the low attenuation advantage gained by using the corrugated waveguide. However, in some applications the slight increase in attenuation may be an acceptable trade-off for waveguide flexibility.

An additional factor that occurs when using a flexible corrugated waveguide for dual polarisation operation is that for small bend radii the waveguide cross-section in the region of the bend becomes slightly elliptical. This results in the generation of a cross-polarised component of the HE_{11} mode. Therefore bends of small radii of curvature should be avoided for this reason, in addition to the high mode coupling they produce. If the elliptical deformation for a given waveguide bend is known or can be measured the level of cross-polarisation produced can be estimated from the results of the investigation into cross-polarisation due to random ellipticity, presented in chapter 6.

For single polarisation operation the use of mode filters appears a much more attractive solution. Designs for H_{01}, HE_{21} and E_{02} mode filters having negligible insertion loss to a single polarisation of the HE_{11} mode have been developed by the author and are described in chapter 7. A typical corrugated waveguide feeder run, containing several bends each having radii of curvature of order one metre and employing these mode filters, can be made to exhibit an acceptably low level of higher order mode coupling.

CHAPTER 6

CROSS-POLARISATION COUPLING IN CIRCULAR WAVEGUIDE RUNS WITH RANDOMLY ORIENTATED ELLIPTICAL DEFORMATIONS IN CROSS-SECTION

6.1 INTRODUCTION

The analysis to be described in this chapter considers the problem of smooth wall circular or corrugated waveguides with slight ellipticity in cross-section. Such an ellipticity is likely to be present in a practical length of waveguide feeder due to manufacturing tolerances and handling deformations. This ellipticity is assumed to vary randomly in magnitude and orientation along the waveguide length. For a linearly polarised input mode the random ellipticity causes a cross-polarised component to be received at the output of the waveguide. In this chapter, results applicable to the antenna tower feeder application are presented, relating the cross-polarisation to the magnitude of the ellipticity for various circular waveguide types. It is shown that the corrugated circular waveguide is both mechanically and electrically less susceptible to cross-polarisation generation than its smooth wall waveguide competitors.

When a length of randomly elliptic waveguide forms a resonant cavity, slight splitting of the mode resonance occurs. For small ellipticities this resonant frequency splitting manifests itself as a widening or *spreading* of

the resonant linewidth. The effect is important when using a resonant cavity to determine waveguide attenuation. In section 6.5 it is shown that this effect is the cause for a previously unaccountably high measured attenuation for the HE_{12} mode in a corrugated waveguide.

There has been little published work on the problem of random waveguide ellipticity. Karbowiak < 4 > has studied the effect of random imperfections on mode conversion in overmoded waveguides. King <43> has measured the cross-polarisation resulting from random ellipticity in a smooth wall circular waveguide. In section 6.4 King's results are compared with those predicted using the theory developed in section 6.2 and quite good agreement is obtained. As far as the author is aware this chapter represents the first theoretical analysis on the generation of cross-polarisation and resonant cavity linewidth spreading, resulting from random waveguide ellipticity.

In section 6.2 the theoretical analysis for determination of the cross-polar power due to random ellipticities in a length of circular waveguide is described. An experimental method, employing a resonant cavity, is developed in section 6.3, to measure the change in propagation coefficient with waveguide ellipticity, allowing a comparison with the theoretically predicted results. In section 6.4 results relating the cross-polarisation to the magnitude of the waveguide ellipticity are presented. Comparison is made between results obtained for the smooth wall circular waveguide designs, at present

used for antenna feeders, with results for both the mono-mode and overmoded corrugated waveguides. The results allow a designer to estimate the cross-polar power resulting from a specified tolerance for waveguide ellipticity. Finally, section 6.5 describes an extension to the theoretical analysis of earlier sections to determine the resonant cavity linewidth spreading resulting from random waveguide ellipticity. Results are presented for the level of resonant linewidth spreading occurring in a practical resonant cavity used by the author for attenuation measurements.

6.2 THEORETICAL DETERMINATION OF THE CROSS-POLAR POWER DUE TO RANDOM WAVEGUIDE ELLIPTICITY

Random ellipticities in cross-section occur along any practical length of circular waveguide run because of manufacturing tolerances and handling deformations. In this section *ellipticity* is defined as the difference between the major and minor axis of the elliptic cross-section, $2\Delta r$ in figure 6.1(a). In such an elliptical waveguide, propagating a unity azimuthal number mode, a difference in propagation coefficient results for E-field polarisations orientated along the major and minor axis of the ellipse. These are the so-called *odd* and *even* elliptical waveguide modes respectively < 3 >. However, in practice this ellipticity varies randomly in orientation down the waveguide run and results in a splitting of the degeneracy between *any* two orthogonal polarisations. It

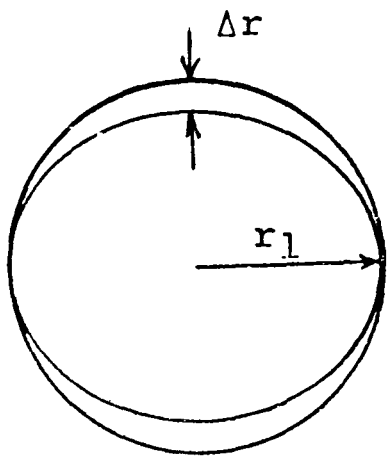

Fig. 6.1(a)

Deformation of a circular waveguide to an elliptical waveguide

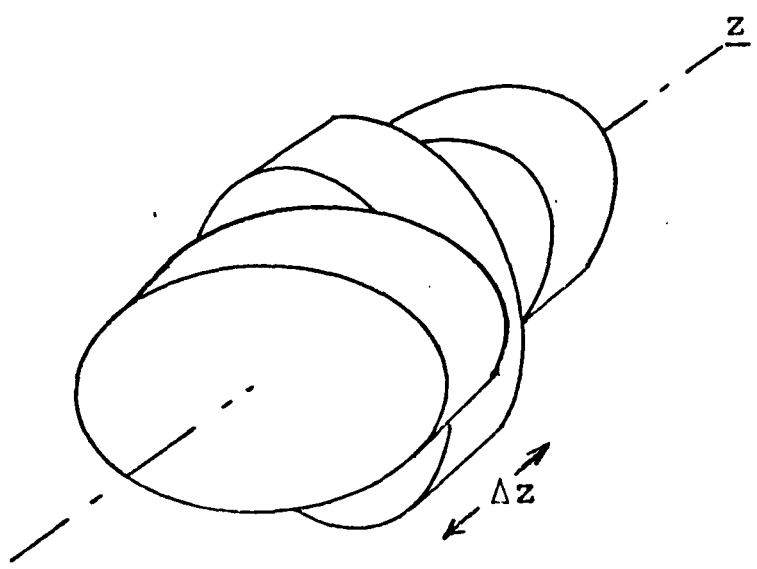

Fig. 6.1(b)

Elemental elliptic waveguide sections

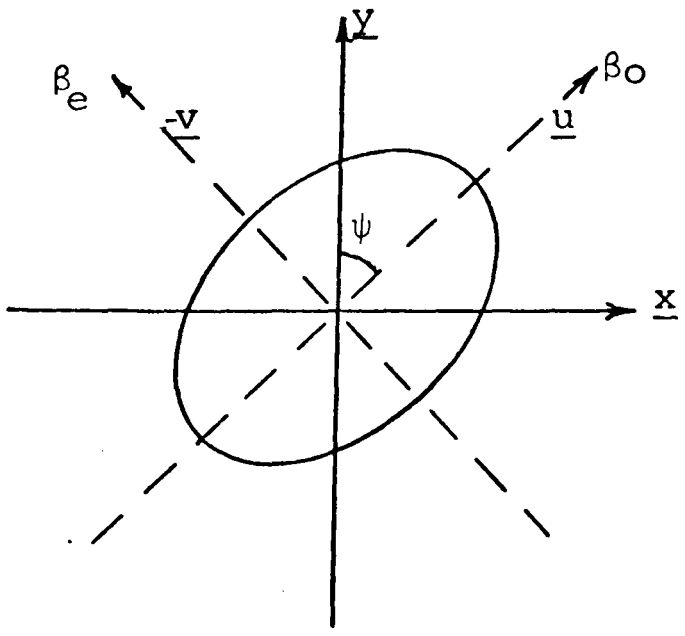

Fig. 6.1(c)

$\beta_e = \beta - \delta\beta_e$

$\beta_o = \beta - \delta\beta_o$

where:

β is the propagation coefficient for the circular waveguide

β_e and β_o are the propagation coefficients for the even and odd modes respectively

Hence:

$\Delta\beta = \beta_e - \beta_o$

$= \delta\beta_o - \delta\beta_e$

is this difference in propagation coefficients that leads to the cross-polarisation and cavity resonance spreading. Modes with azimuthal number greater than unity also produce such differences in propagation coefficient between orthogonal polarisations, but no mutual coupling occurs for an elliptic deformation < 4 >.

The analysis to be described in this section takes the following course. In section 6.2.1 the powers received at the output of the randomly elliptical waveguide which are parallel and orthogonal to the input polarisation are first formulated. The resultant phase difference between these two received powers is then derived in section 6.2.2. Finally, in section 6.2.3, these results are used to obtain the resultant co-polar direction. The power orthogonal to this direction then defines the required cross-polar power received at the output of the waveguide.

6.2.1 The Received Parallel and Orthogonal Polarised Powers

A linearly polarised mode of unity azimuthal number, propagating in a loss-less waveguide is assumed throughout this analysis. The waveguide is considered to be composed of a large number of small elemental elliptic sections. Both the ellipticity and the major axis orientation, ψ, varies randomly from section to section, figure 6.1(b). For a single section with incident $\underline{x}$ polarisation, the field can be resolved into the directions $\underline{u}$ and $\underline{v}$, figure 6.1(c), each having different propagation coefficients,

β_o (odd mode) and β_e (even mode). These two polarisations propagate the length Δz, and because of the different phasing, resolve back into the $\underline{x}$ direction, with electric field a_x, plus a small $\underline{y}$ component, with electric field a_y. A transmission matrix $\underline{A}'$ for the length Δz is derived, equation 6.1, whose elements depend on $\delta\beta_o$, $\delta\beta_e$ and the angle ψ. (Figure 6.1(c)).

$$\begin{bmatrix} a_x(z+\Delta z) \\ a_y(z+\Delta z) \end{bmatrix} = e^{+j\beta\Delta z} \underset{\sim}{A}' \begin{bmatrix} a_x(z) \\ a_y(z) \end{bmatrix} \qquad (6.1)$$

where: β is the propagation coefficient for the circular waveguide,

$$\underset{\sim}{A}' = \underset{\sim}{T}^{-1} \begin{bmatrix} 1 - j\delta\beta_e\Delta z & 0 \\ 0 & 1 - j\delta\beta_o\Delta z \end{bmatrix} \underset{\sim}{T} \qquad \text{and}$$

$$\underset{\sim}{T} = \begin{bmatrix} \cos\psi & -\sin\psi \\ \sin\psi & \cos\psi \end{bmatrix}$$

The properties of the entire waveguide, length ℓ, may then be obtained by cascading the elemental sections and proceeding to the limit. A matrix integral equation results and this is solved, using Picard's method <44>, to give a transmission matrix A relating the input field $\begin{bmatrix} a_x(0) \\ a_y(0) \end{bmatrix}$ to the output field $\begin{bmatrix} a_x(\ell) \\ a_y(\ell) \end{bmatrix}$:-

$$\begin{bmatrix} a_x(\ell) \\ a_y(\ell) \end{bmatrix} = \underset{\sim}{A} \begin{bmatrix} a_x(0) \\ a_y(0) \end{bmatrix} e^{+j\beta\ell} \qquad (6.2)$$

$$\underset{\sim}{A} = \begin{bmatrix} a_{11} & a_{12} \\ a_{21} & a_{22} \end{bmatrix}$$

$$= \begin{bmatrix} 1-j\int_0^{\ell}(\delta\beta_e\cos^2\psi+\delta\beta_o\sin^2\psi)\,dz & \frac{-j}{2}\int_0^{\ell}\sin 2\psi(\delta\beta_o-\delta\beta_e)\,dz \\ \frac{-j}{2}\int_0^{\ell}\sin 2\psi(\delta\beta_o-\delta\beta_e)\,dz & 1-j\int_0^{\ell}(\delta\beta_e\sin^2\psi+\delta\beta_o\cos^2\psi)\,dz \end{bmatrix}$$

The elements of $\underset{\sim}{A}$ contain integrals over z of $\delta\beta_e$, $\delta\beta_o$ and ψ, all of which vary randomly with z. For an input polarisation in the $\underline{x}$ direction the element a_{21} yields the orthogonally polarised field, $a_y(\ell)$, occurring at the waveguide output. Thus:

$$b_y(\ell) = \frac{-j\ b_x(0)}{2}\int_0^{\ell}\Delta\beta(z)\sin 2\psi(z)\,dz \qquad (6.3)$$

where, for convenience, $\begin{bmatrix} b_x(z) \\ b_y(z) \end{bmatrix} = e^{-j\beta z}\begin{bmatrix} a_x(z) \\ a_y(z) \end{bmatrix}$ has been used. For small ellipticities the received power parallel to the input polarisation, P_x, can be approximated to the input power, and from equation 6.2 is

$$P_x = b_x^2(0) \qquad (6.3A)$$

In general $\psi(z)$ and $\Delta\beta(z)$ are random functions of z, but if they have an analytical z dependence, then the required orthogonal power can be obtained from equation 6.3, so long as $\Delta\beta$ can be related to the ellipticity, Δr. The derivation of this relationship is now described.

As the deformations are likely to be small for any practical waveguide, perturbation theory <45> may be used to relate the small change in propagation coefficient

between orthogonal polarisations, $\Delta\beta$, to the ellipticity, $2\Delta r$, figure 6.1(c). However, Al-Hariri < 3 > has obtained, by direct analysis, the propagation coefficients of elliptical waveguide with both smooth and corrugated walls. Modification of his computer programs for small ellipticities permitted comparison with results obtained using perturbation theory (see section 6.3).

The derivation of the perturbation formulae for the case of the smooth wall waveguide follows closely that of Harrington <45>, allowing $\Delta\beta$ to be simply related to Δr by the factor F, equation 6.4.

$$\Delta\beta = F\Delta r \qquad (6.4)$$

The resulting perturbation formulae for both TE and TM modes is presented in appendix 6.2. The application of this perturbation method to the corrugated waveguide, however, is more complex. This is because at the waveguide boundary only the E_θ component of electric field vanishes (simple impedance approximation) <26>. A brief outline of the method used and the resulting perturbation formulae is presented in appendix 6.1. In general, the factor F depends on the total electromagnetic energy perturbed by the elliptical deformation, which consequently depends on the field distribution of the particular mode under consideration.

With $\Delta\beta$ related to Δr by equation 6.4, the required orthogonally polarised field, equation 6.3, becomes

$$b_y(\ell) = \frac{-j}{2} b_x(0) F \int_0^{\ell} \Delta r(z) \sin 2\psi(z) dz \qquad (6.5)$$

When $\psi(z)$ and $\Delta r(z)$ vary randomly with z the *expected value*† for the orthogonal power $E\{b_y(\ell) b_y^*(\ell)\}$ must be found. This leads to a formulation (appendix 6.5) in terms of an *autocorrelation function*, $R_\Delta(\tau)$, which depends on the statistical nature of the ellipticity. In the present context, the autocorrelation function is a measure of the dependence of the magnitude (Δr) and orientation (ψ) of the ellipticity at position $\tau = z$ on the magnitude and orientation of the ellipticity at position $\tau = 0$, <46>. For example, if the ellipticity measured at two points, distance τ apart, were found to be completely uncorrelated the value of the autocorrelation function $R_\Delta(\tau)$ would be zero. It is only possible to calculate $R_\Delta(\tau)$ for simple z dependences <46>, <47>. One such simple dependence is that the waveguide ellipticity and its orientation are constant over a fixed length h, where $h \ll \ell$. For waveguide lengths greater than the *correlation length*, h, the ellipticity and its orientation are completely uncorrelated. For completely random orientation of the elliptic waveguide sections $R_\Delta(\tau)$ is found to depend on the *mean* and *standard deviation* of Δr (appendix 6.5). The received orthogonal power P_y is then obtained as (appendix 6.5)

$$P_y = E\{b_y(\ell) b_y^*(\ell)\} = \frac{b_x^2(0)}{8} h\ell(\sigma_{\Delta r}^2 + \mu_{\Delta r}^2) F^2 \qquad (6.6)$$

† The expected value is the statistical average of a random variable <46>.

An alternative assumption for the autocorrelation function, making h the <u>average</u> correlation length yields a similar expression for the received orthogonal power:

$$P_y = \frac{b_x^2(0)}{4} h\ell(\sigma_{\Delta r}^2+\mu_{\Delta r}^2)F^2 \qquad (6.6A)$$

Experimental measurements on the circularity of a 1.5" diameter smooth wall waveguide indicate that the above assumptions used to determine the autocorrelation functions are practically valid. With some methods of fabrication the correlation length for the corrugated waveguide would be constant and equal to the corrugation periodicity.

The ratio of the orthogonally polarised power, P_y, to that of the power received parallel to the input polarisation P_x, is given, using equations 6.6 and 6.3A, by:-

$$\frac{P_y}{P_x} = \frac{F^2}{8} h\ell(\sigma_{\Delta r}^2+\mu_{\Delta r}^2) \qquad (6.7)$$

For the case where h is the average correlation length equation 6.7 is multiplied by 2.

6.2.2 <u>The Phase Difference Between Received Orthogonal Powers</u>

In this section the resultant phase difference between the received parallel and orthogonal polarisation is determined. When a length, ℓ, of the pseudo randomly elliptical waveguide is enclosed to form a resonant cavity, each mode will have two resonances associated with it due to the resultant difference in propagation coefficient,

$\Delta\beta_s$, between the two orthogonal polarisations. By determining $\Delta\beta_s$ the required phase difference, θ_d, is simply given by

$$\theta_d = \Delta\beta_s \ell \tag{6.8}$$

From the transmission matrix of the cavity and the boundary conditions, the cavity resonance condition is derived (appendix 6.3). The condition for resonance over length ℓ is shown to be

$$(\beta-\beta')\ell \pm \beta''\ell = n\pi \tag{6.9}$$

where:

β is the propagation coefficient for the circular waveguide

β' is the mean offset in propagation coefficient caused by ellipticity

$2\beta''$ is the difference in propagation coefficient between orthogonal polarisations.

The *expected value* of $(\beta'')^2$ can be formulated (appendix 6.3) in terms of the autocorrelation function defined in the previous section. After substitution of the autocorrelation function the required expected value for the difference in propagation coefficient $\Delta\beta_s$ is given, from appendix 6.3, by

$$\Delta\beta_s = F(\sigma_{\Delta r}^2+\mu_{\Delta r}^2)^{\frac{1}{2}} \sqrt{\frac{h}{\ell}} \tag{6.10}$$

where h is the fixed correlation length. The required phase difference between the orthogonal polarisations is then given, from equation 6.8, by

$$\theta_d = F(\sigma_{\Delta r}^2 + \mu_{\Delta r}^2)^{\frac{1}{2}} \sqrt{h\ell} \qquad (6.11)$$

When h is the average correlation length equation 6.11 is multiplied by $\sqrt{2}$.

6.2.3 The Received Cross-polar Power

In this section the required cross-polar power is determined using the results of the last two sections. Equation 6.7 defines the orthogonally polarised power, P_y, and not the required cross-polar power. This is because when measuring the co-polar power in this situation, the output polarisation is rotated for maximum received signal. The angle of rotation, ϕ_o termed the *polarisation tilt*, is typically of order a degree, and defines the received co-polar direction (with co-polar power P_C), shown in figure 6.2. The power received in the direction $\phi_o + 90^o$ defines

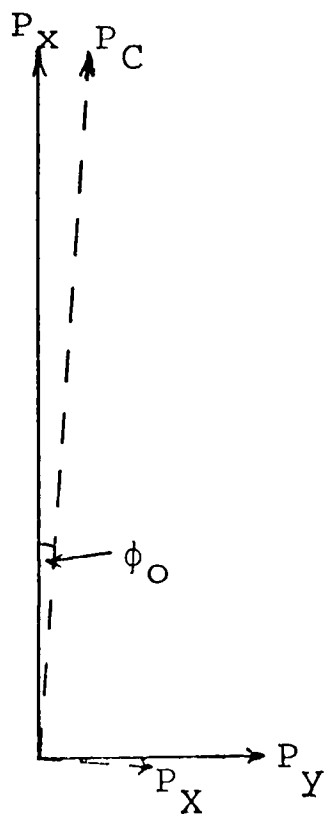

Fig. 6.2 Directions of received power from randomly elliptical waveguide, x polarised input.

the required cross-polar power, P_X. It is the phase difference θ_d, between P_x and P_y that leads to the existence of *both* the P_C and P_X components. At any instant in time the resultant field makes an angle ϕ with the $\underline{x}$ direction such that:

$$\phi = \tan^{-1}\left[\sqrt{\frac{P_y}{P_x}} \quad \frac{\cos(\omega t + \theta_d)}{\cos\omega t}\right]$$

where a $\cos\omega t$ time dependence has been assumed. The angle ϕ_o, where the magnitude of the time average resultant power is a maximum, defines the output co-polar direction. After some manipulation the polarisation tilt angle ϕ_o is obtained, to first order in Δr, as

$$\phi_o = \tan^{-1}\left[\sqrt{\frac{P_y}{P_x}} \quad \cos\theta_d\right] \qquad (6.12)$$

Resolving the fields in the $\phi_o + 90^o$ direction and finding the time average power yields the required cross-polar power, P_X. The ratio of this cross-polar power to the co-polar power, P_C, is then given as

$$\frac{P_X}{P_C} = \left(\frac{P_y}{P_x}\right) \sin^2\theta_d \qquad (6.13)$$

where $\left(\frac{P_y}{P_x}\right)$ is obtained from equation 6.7 and θ_d from equation 6.11.

6.2.4 Formulae for a Waveguide with Constant Ellipticity

For a waveguide with constant ellipticity, $2\Delta r$, and fixed orientation, ψ, the following equations for $\left(\frac{P_y}{P_x}\right)$ and θ_d can be easily derived from the above analysis.

$$\frac{P_y}{P_x} = \frac{\Delta r^2 F^2 \ell^2}{4} \sin^2 2\psi \qquad (6.14)$$

$$\theta_d \equiv \Delta\beta\ell = F\Delta r\ell \qquad (6.15)$$

The polarisation tilt angle and cross-polar power are then obtained from equations 6.12 and 6.13.

It can be simply shown, using the analysis of appendix 6.5, that if Δr remains fixed and ψ, the ellipticity orientation, varies randomly with z, equations 6.7 and 6.11 still apply, but with $(\sigma_{\Delta r}^2+\mu_{\Delta r}^2)$ replaced by Δr^2. It is thus interesting to note that for the case of constant ellipticity orientation the cross-polar power is proportional to ℓ^2, but for statistical orientation it is proportional to ℓ. Furthermore, it can also be shown (using appendix 6.5) that if ψ varies in a periodic fashion down the waveguide the cross-polar power will also vary periodically and be proportional to ℓ^2. Clearly for low cross-polarisation, any periodic elliptic deformation must be avoided.

6.3 RESULTS RELATING THE CHANGE IN PROPAGATION COEFFICIENT TO THE ELLIPTICITY OF A WAVEGUIDE

The magnitude of the cross-polar power in a randomly elliptical waveguide strongly depends on the factor F ($\Delta\beta=F\Delta r$). In this section comparison is made between values of F obtained using perturbation theory with those obtained by direct solution (Al-Hariri), henceforth termed the numerical solution. In view of the strong F dependence of the desired cross-polarisation results, experimental

verification of the predicted F value was considered necessary.

The experiment consisted of measuring the split, Δf, in the resonant frequency of small lengths ($\tilde{}$12cm) of waveguide, with known ellipticity, made to form a resonant cavity. A constant ellipticity with fixed orientation ($\psi = 45^{o}$ to input polarisation) was created by application of controlled transverse pressure to the waveguide. The experiment was repeated for several values of ellipticity. A simple relationship between Δf and the split in propagation coefficient between even and odd modes, $\Delta\beta$, is derived in appendix 6.4 as:

$$\Delta f = \frac{v_g \Delta\beta}{2\pi} \qquad (6.16)$$

where v_g is the mode group velocity. For this case of constant ellipticity $\Delta\beta = F\Delta r$ (equation 6.4) and so equation 6.16 becomes

$$\Delta f = \frac{v_g F \Delta r}{2\pi} \qquad (6.17)$$

This equation relates the applied ellipticity, $2\Delta r$, to the resulting split in resonant frequency, Δf. Thus from the slope of the measured Δf, Δr, curve the value of F can be obtained and compared with the theoretically predicted values. When the ellipticity applied to the cavity is small, the 3dB linewidth becomes widened by a factor x, figure 6.3(b). For example, when $\Delta f = \frac{\delta f}{2}$ and assuming the resonance to be Gaussian in shape, x can be shown to be approximately 1.2. When a larger ellipticity is applied

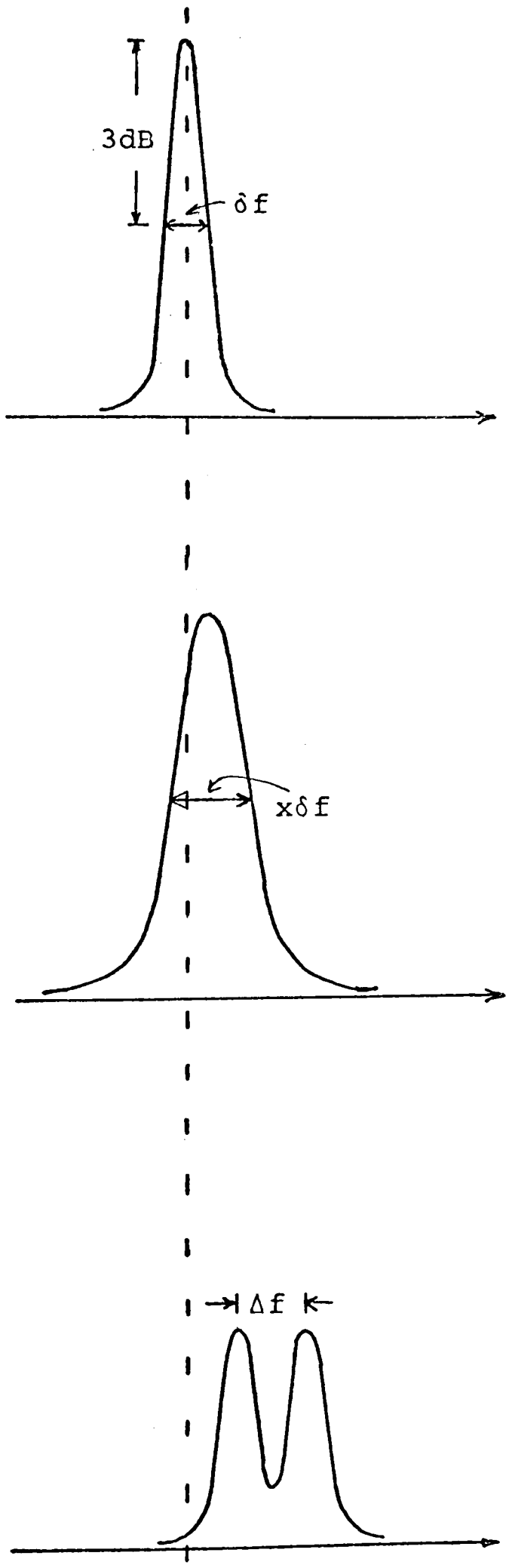

a) perfectly circular cavity

b) elliptical cavity with small resonant frequency spread

c) elliptical cavity with large resonant frequency spread

Fig. 6.3 Effect of cavity ellipticity on a mode resonance

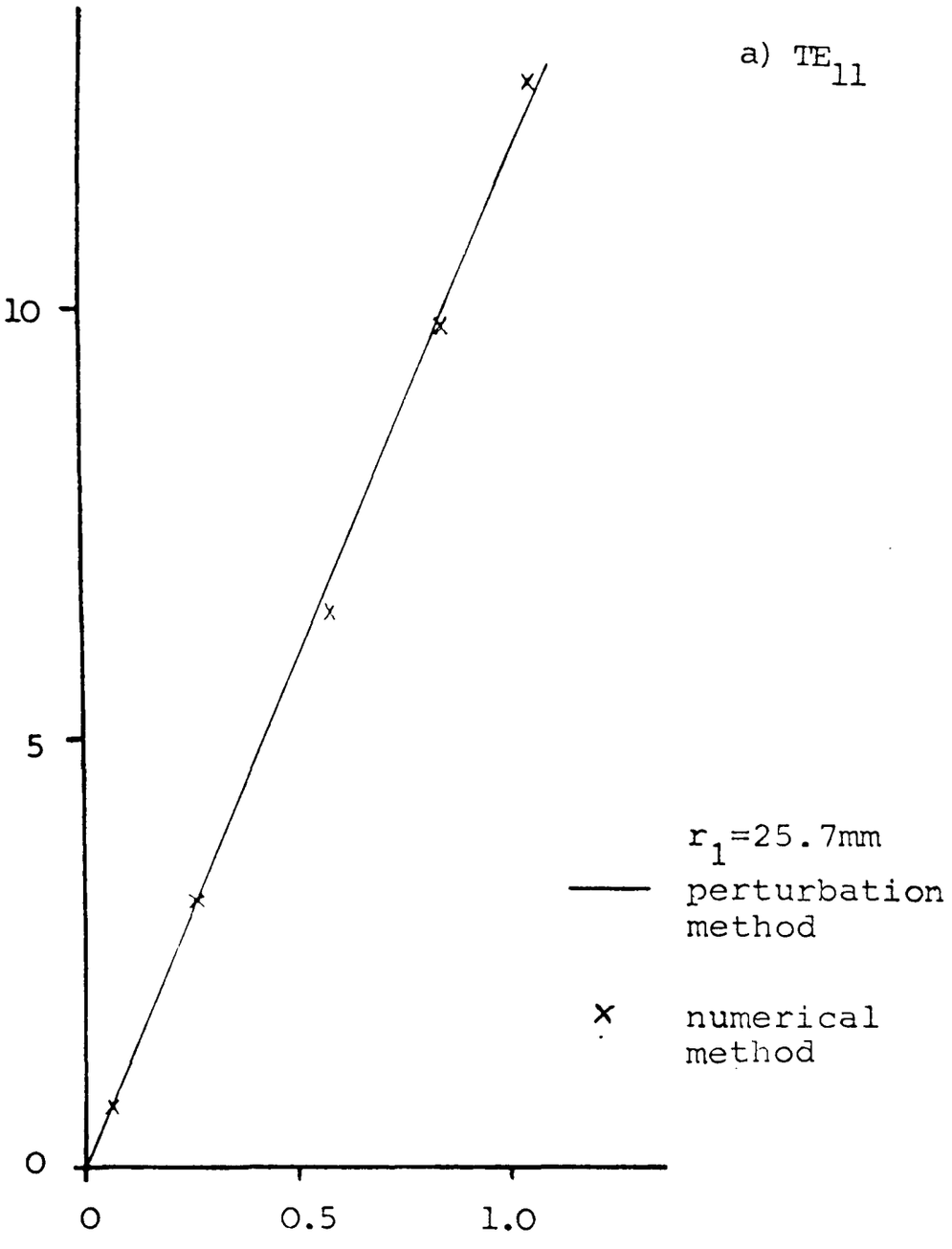

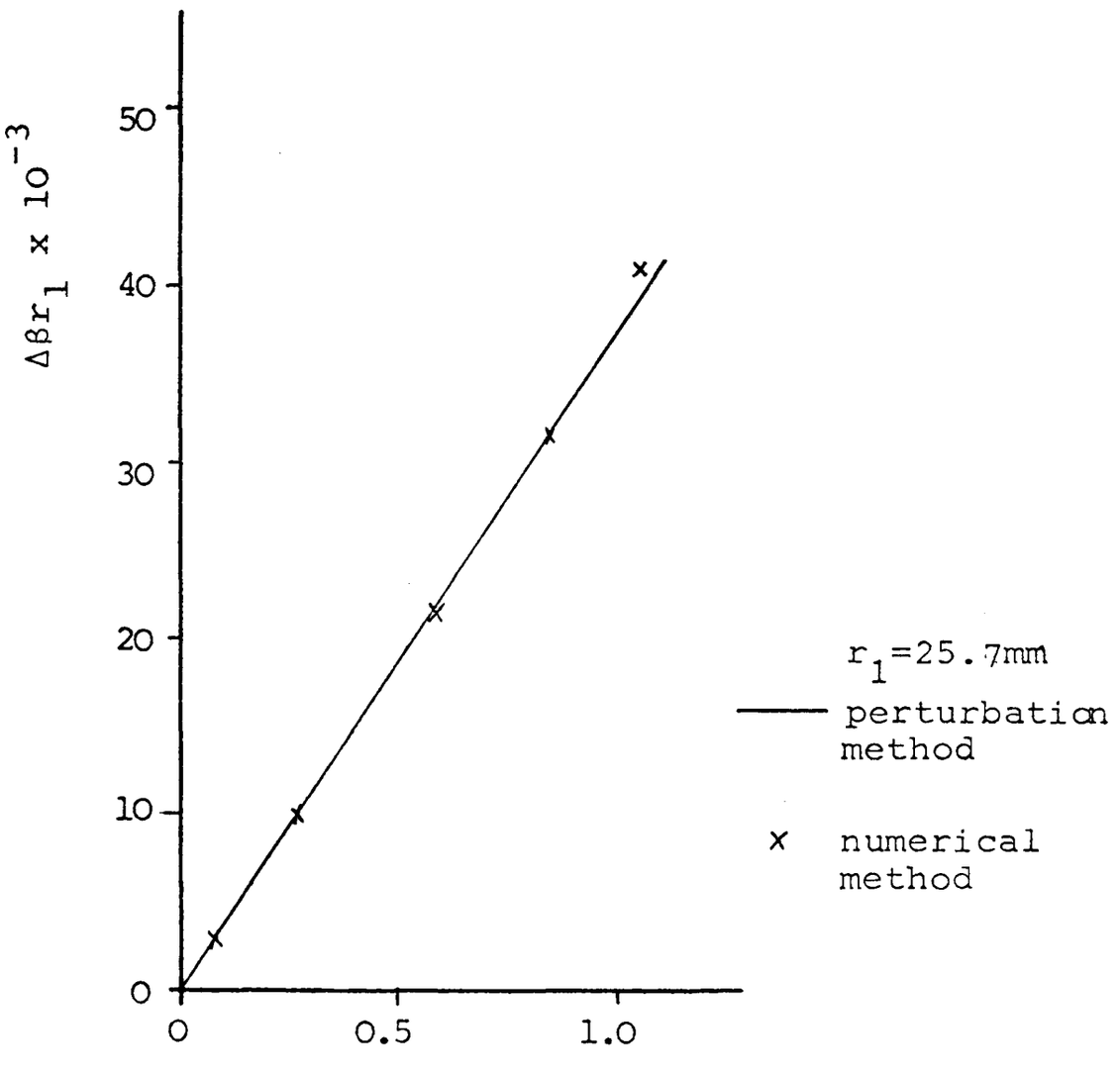

Fig. 6.4 Comparison of perturbation and numerical methods of calculating $\Delta\beta r_1$ as a function of Δr for a smooth wall circular waveguide

the dual resonance effect, shown diagramatically in figure 6.3(c), occurs. It is this latter effect that is used to determine the value of F. The earlier mentioned effect is considered in section 6.5 where linewidth widening, caused by random ellipticities in a resonant cavity used for attenuation measurements, is considered.

Figure 6.4(a) shows $\Delta\beta$ as a function of Δr obtained for the TE_{11} mode in a smooth wall circular waveguide, using the perturbation method, compared with the result obtained by numerical solution. Figure 6.4(b) shows a similar result for the TM_{11} mode. In both cases excellent agreement is obtained between the two methods. Figure 6.5 shows the

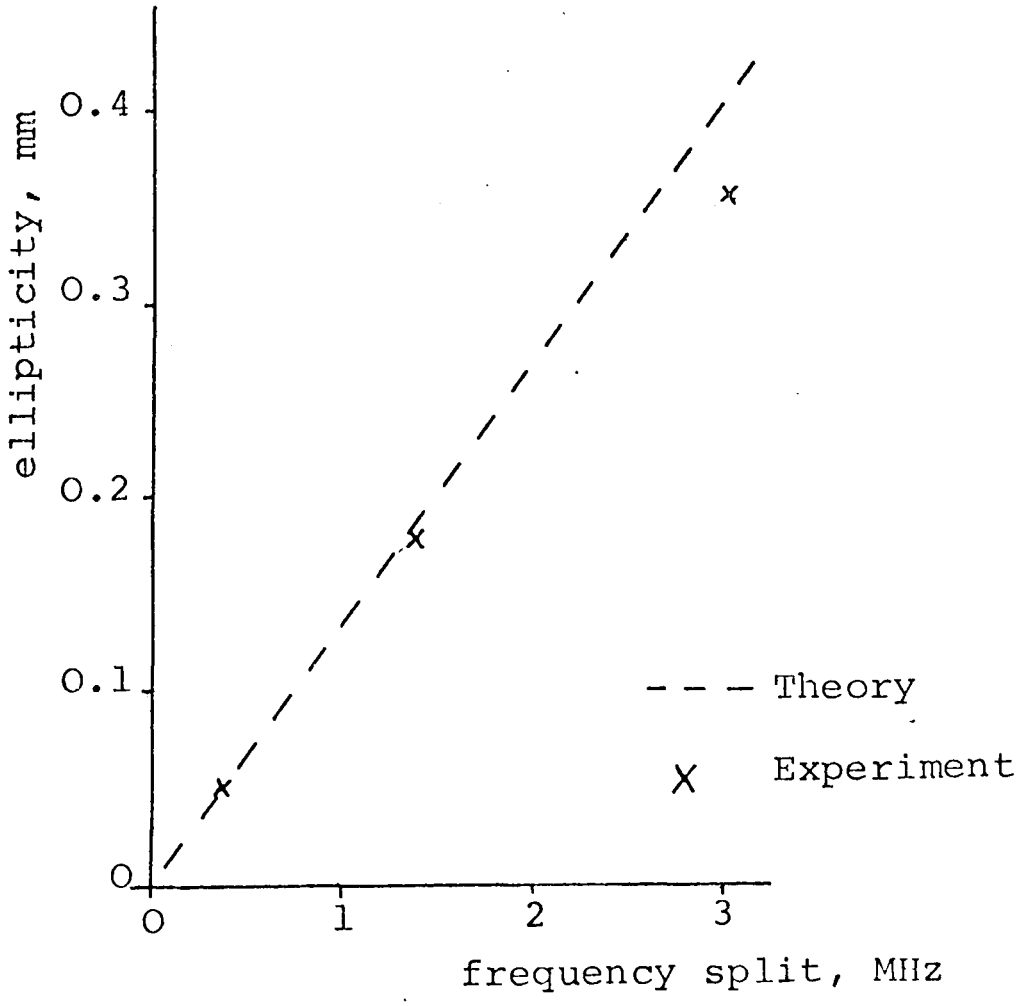

Fig. 6.5 Comparison of experimental and theoretical results for resonant cavity frequency spreading in a smooth wall waveguide, TE_{11} mode.
Diameter 70mm ; Frequency 10.9GHz

theoretical variation of resonant frequency split, Δf, with ellipticity, $2\Delta r$, for the TE_{11} mode in the same smooth wall waveguide. Excellent agreement between this theoretical result and the experimentally measured points is obtained. These results for the smooth wall waveguide lead to a high degree of confidence in the value of F obtained using the simple, and computationally fast, perturbation formulae.

Experimental results for the HE_{11} mode in a corrugated waveguide were, however, more difficult to obtain and subject to a high degree of error. The waveguide cavity used for this experiment was made up from a number of sections, with section length equal to the periodicity of the corrugations. To obtain the smallest measurable frequency split (0.4MHz in this case), an order of magnitude larger ellipticity is required compared to that required for the previously measured TE_{11} smooth wall waveguide. In addition, mechanical construction of the corrugated waveguide is such that it resists elliptic deformation, the corrugations acting as strengthening ribs. Thus the result of applying a deforming pressure to the cavity not only produces a poor approximation to an elliptical deformation but also causes each of the sections to slightly buckle. The buckling results in poor contact between sections and consequently an azimuthally varying current discontinuity. This discontinuity itself causes a double resonance effect which will partially cancel the effect caused by ellipticity. In an attempt to verify this supposition, experimental results of resonance splitting were also taken for the HE_{12} mode in the same waveguide

cavity. For this mode nearly an order of magnitude larger split, Δf, occurs for a given ellipticity, and consequently the effect of current discontinuity will be less dominant. Added to these effects is the fact that the perturbation method used in the theoretical prediction is subject to more error than in the smooth wall waveguide case. This is because the matching of the slot and inner region fields at the boundary inevitably results in some discontinuity < 2 >. Numerical solution predictions are also subject to error because the problem analysed is that for a corrugated waveguide with inner and outer boundaries that are ellipses of *concentric focii*. This means that the slot depth changes around the waveguide and leads to a reduction of the value of $\Delta\beta$.

Figure 6.6 (a) shows the experimentally obtained variation of resonant frequency split, Δf, with ellipticity, $2\Delta r$, for the HE_{11} mode in a corrugated waveguide cavity. The value of F obtained is compared, in table 6.1, with the theoretically computed values.

Method	$F = \frac{\Delta\beta}{\Delta r}$
Experimental	0.7
Numerical solution	3.0
Perturbation method	4.5

Table 6.1 HE_{11} mode, $\frac{r_1}{r_o} = 0.8$

$r_1 = 4cm$, frequency = 10.5GHz

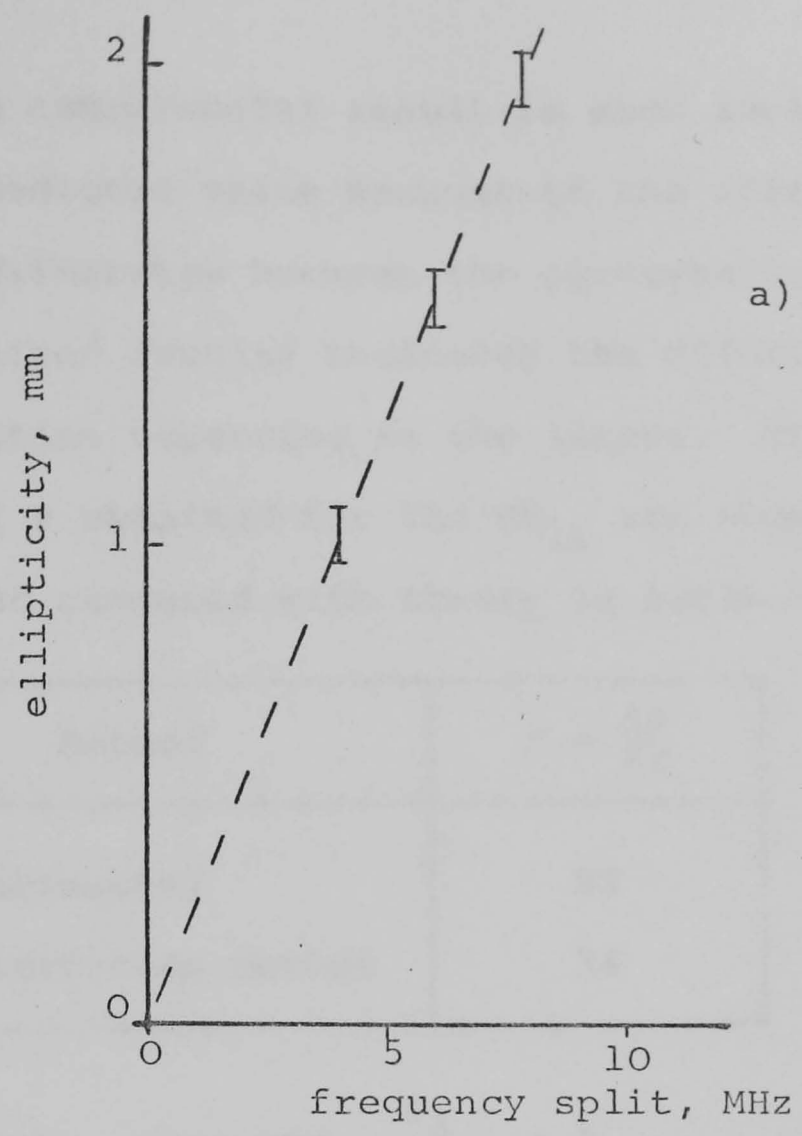

a) HE_{11} mode,
r_1 = 40mm,
10.5GHz

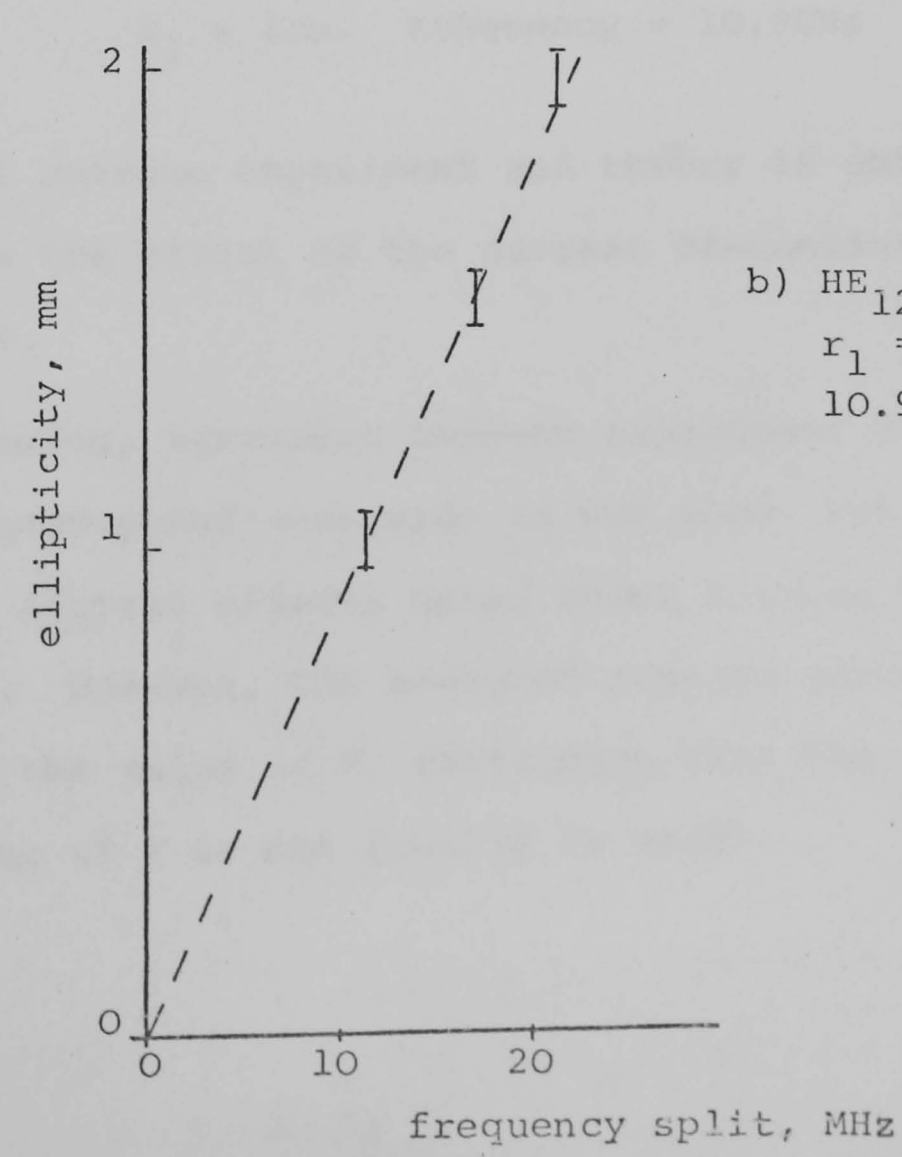

b) HE_{12} mode,
r_1 = 40mm
10.9GHz

Fig. 6.6 Experimental results for resonant cavity frequency spreading in a corrugated waveguide

As expected, the experimental result is much lower than the theoretically predicted value because of the effect of buckling. The difference between the perturbation and numerically obtained results indicates the effect of the slot depth variation occurring in the latter. The results for the value of F obtained for the HE_{12} are shown in figure 6.6(b) and compared with theory in table 6.2.

Method	$F = \frac{\Delta\beta}{\Delta r}$
Experimental	23
Perturbation method	34

Table 6.2 HE_{12} mode, $\frac{r_1}{r_o} = 0.8$

$r_1 = 4cm$, frequency = 10.9GHz

Better agreement between experiment and theory is obtained in this case, as the effect of the current discontinuity is less dominant.

In conclusion, agreement between experiment and theory for the corrugated waveguide is not good, but in view of all the adverse effects noted above nothing better can be expected. However, the measured results serve as a useful guide to the value of F, confirming that the theoretical value of F is not greatly in error.

6.4 PREDICTED CROSS-POLARISATION AND POLARISATION TILTING DUE TO RANDOM ELLIPTICITIES IN ANTENNA FEEDER WAVEGUIDES

The analysis of section 6.2, part of which has been verified in the previous section, is now used to predict the polarisation tilting and cross-polar power resulting from random ellipticities in smooth wall and corrugated circular waveguide runs. In this section, *ellipticity* is defined as $2(\sigma_{\Delta r}^2+\mu_{\Delta r}^2)^{\frac{1}{2}}$, where $\mu_{\Delta r}$ and $\sigma_{\Delta r}$ are the mean and standard deviation of the difference between semi-major and semi-minor axes of the waveguide.

Comparison of the theoretical results of cross-polarisation, using the above theory, in a smooth wall waveguide of length 150ft is made in figure 6.7, with the measured results obtained by King <43>. The high measured level in the region of 4.2GHz is most certainly due to some periodic deformation effect. King found the frequency characteristics to be dominated by the high levels of cross-polarisation at one orientation, for other orientations the levels showed dissimilar variations with frequency. Remembering that we are dealing here with statistical effects the agreement between measured and predicted results is quite good. The polarisation twist angle was also measured by King and estimated to be between 1^{o} and 2^{o}, comparing well with the predicted value of about 2.5^{o}.

The cross-polarisation generated over a 100 metre length of corrugated waveguide is compared with that produced by its smooth wall waveguide competitors in figure 6.8(a).

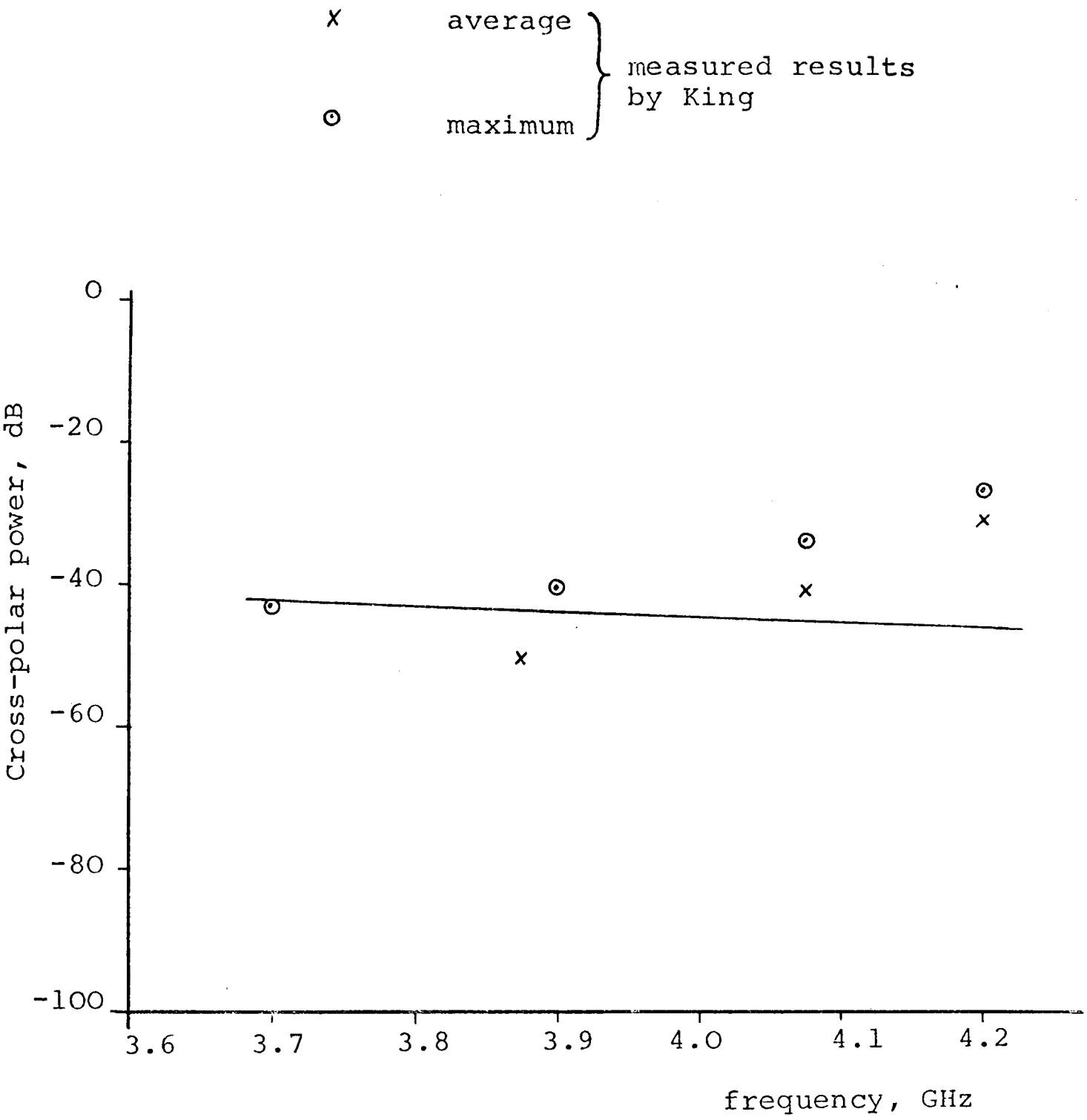

Fig. 6.7 Measured and predicted results for cross-polar power resulting from random ellipticity in a smooth wall circular waveguide

Parameters: waveguide length = 150ft
average ellipticity = 50μm
correlation length = 50cm

For Key see figure 6.8(b)

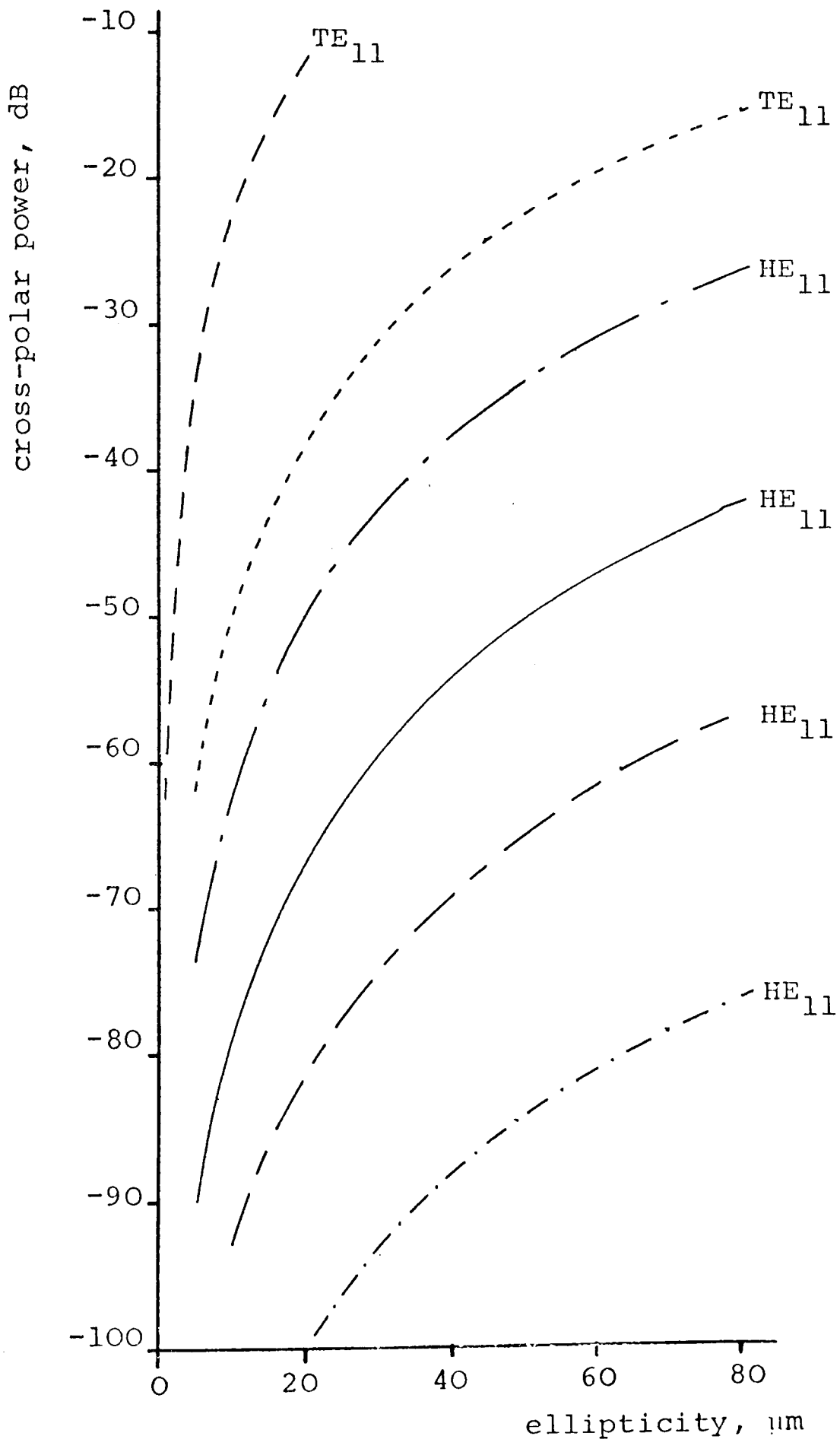

Fig. 6.8(a) Cross-polar power as a functicn of random ellipticity for various circular waveguide types

Parameters: Design frequency 8.7GHz, waveguide length = 100m

Results for both the overmoded and mono-mode (chapter 8) corrugated waveguides are presented. A waveguide feeder length of 100 metres was chosen as being typical of the requirements for linking the source at the base of a tower to the antenna. The smooth wall waveguide correlation length of 0.3m (average) was estimated from measured results <48> of circularity for a 1.5" diameter waveguide. The results of figure 6.8(a) show the corrugated waveguides to have a superior cross-polar performance to that of the smooth wall waveguides, even when the same correlation length for all waveguides is taken. However, for some commercial methods of manufacture envisaged for the corrugated waveguide (chapter 11), the correlation length would be equal to the corrugation periodicity, giving an added improvement in performance. The extremely low levels of cross-polarisation for the overmoded corrugated waveguide would be unlikely to be achieved in practice. This is because second order mode conversion effects (higher order mode coupling to HE_{11} mode) would dominate. However, this does not apply to the mono-mode corrugated waveguide. When single mode operation is desirable, the mono-mode corrugated waveguide shows a drastic improvement in cross-polar performance, due to random ellipticities, over the smooth wall TE_{11} mode waveguide.

A typical practical ellipticity for the mono-mode smooth wall waveguide is 20μm, yielding a cross-polar level of -23dB over 100 metres. This high level is due to the relatively high fields present at the deformed boundary.

Key

1. — — TE_{11} mode, smooth wall waveguide, single mode, $\frac{f}{fc} = 1.5$

2. - - - - TE_{11} mode, smooth wall waveguide, 3 propagating modes, $\frac{f}{fc} = 2.0$

3. — · — HE_{11} mode, corrugated mono-mode waveguide

4. ——— HE_{11} mode, corrugated waveguide, 4 propagating modes $\frac{f}{fc} = 1.6$

5. — — — HE_{11} mode, as 3 but with correlation length equal to corrugation periodicity

6. · — · · HE_{11} mode, as 4 but with correlation length equal to corrugation periodicity

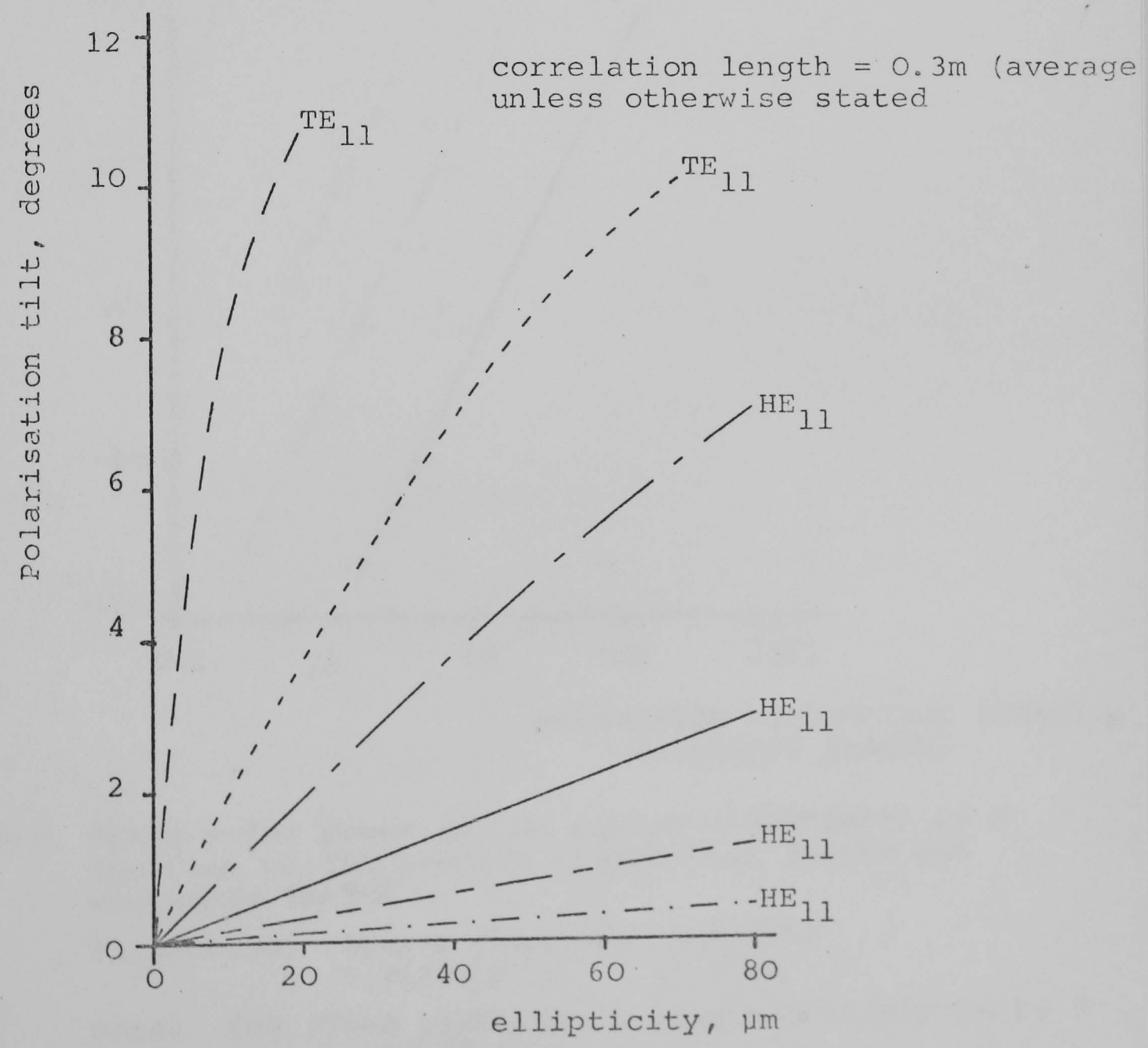

Fig. 6.8(b) Polarisation tilt as a function of random ellipticity corresponding to Fig. 6.8(a)

For Key see figure 6.8(b)

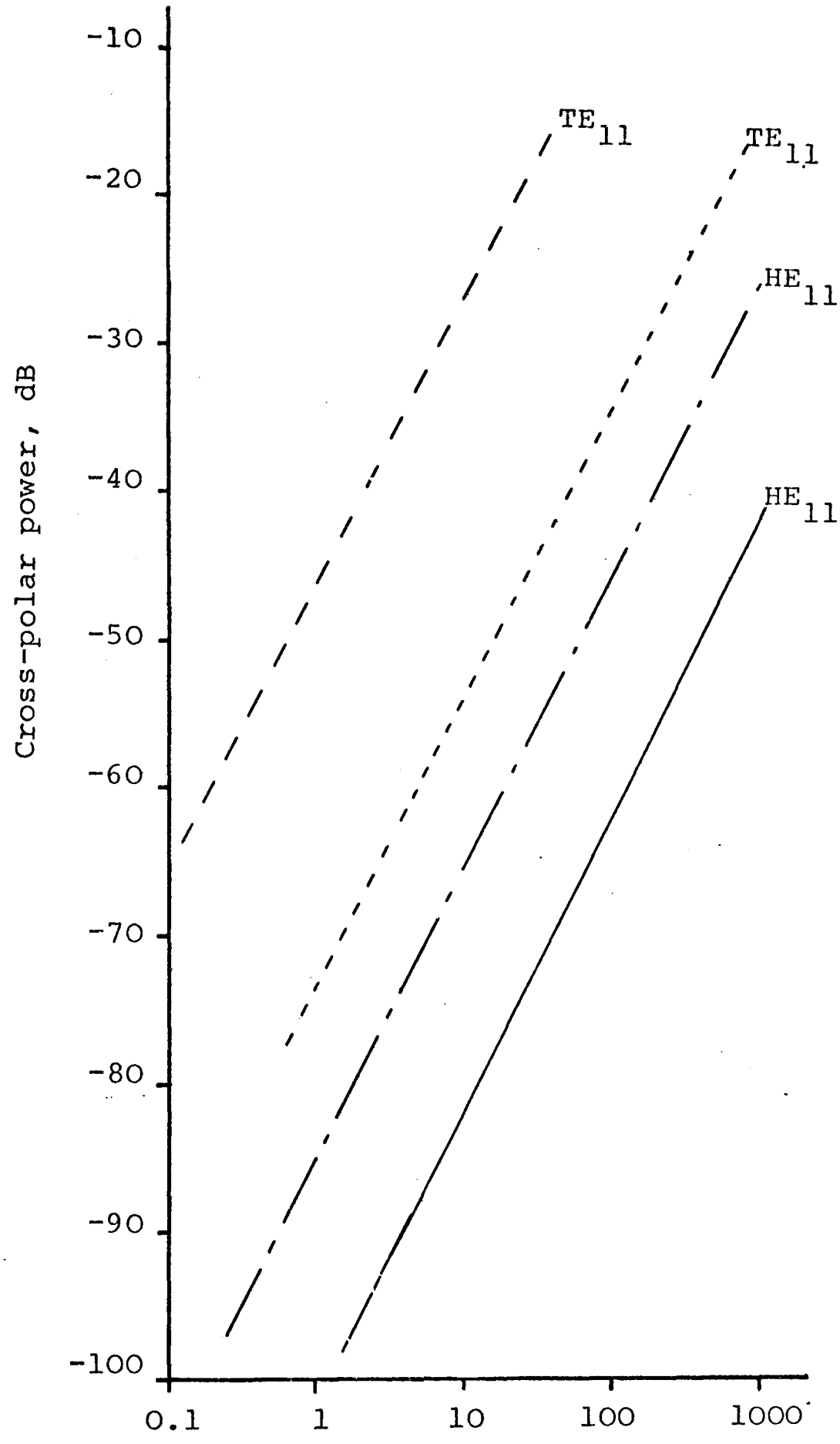

Fig. 6.9 Cross-polar power due to random ellipticity as a function of the product correlation length and waveguide length

Parameters: Design frequency = 8.7GHz
Ellipticity = 20μm

Note: for fixed correlation length multiply hℓ by 2

In the corrugated waveguide, the corrugations act to cushion the fields away from the walls, resulting in very low fields in the region of the perturbation, and hence a low cross-polarisation. Figure 6.8(b) compares the degree of polarisation twist occurring between the input and output polarisations, corresponding to the results of figure 6.8(a). Figure 6.9 shows the cross-polarisation as a function of the product $h\ell$ (correlation length x waveguide length) for the waveguides considered in figure 6.8; the waveguide ellipticity is taken to be 20 μm. The effect of a change in correlation length or waveguide length is clearly shown in this figure.

In the design of waveguide feeders for microwave antennas, figures 6.8 and 6.9 enable the designer to determine the allowable waveguide ellipticity for a required cross-polar performance. Results for any desired operating frequency can be obtained from these figures by scaling.

6.5 RESONANT CAVITY LINEWIDTH SPREADING

It has already been shown in section 6.3 that the effect of slight ellipticity in a resonant cavity is to produce an increase in the measured resonant linewidth. Much of the attenuation measurements on the corrugated waveguide, and its modified versions, have been performed using resonant cavity techniques, chapter 4, <5>, <49>. In order to accurately predict attenuation from Q-factor measurements it is essential to know the split in resonance

which arises from random elliptical deformation of the cavity cross-section.

In this case the resultant difference between the propagation coefficients ($\Delta\beta_s$) in the two orthogonal polarisations is given in section 6.2, equation 6.10, as

$$\Delta\beta_s = F(\sigma_{\Delta r}^2+\mu_{\Delta r}^2)^{\frac{1}{2}} \sqrt{\frac{h}{\ell}}$$

Using the result derived in appendix 6.3, the *expected* split in resonant frequency due to random ellipticity in a resonant cavity is

$$\Delta f = \frac{v_g \Delta\beta_s}{2\pi}$$

and thus:

$$\Delta f = \frac{v_g F}{2\pi} (\sigma_{\Delta r}^2+\mu_{\Delta r}^2)^{\frac{1}{2}} \sqrt{\frac{h}{\ell}} \qquad (6.18)$$

where h is the fixed correlation length. By measuring the ellipticity of the corrugated sections forming the resonant cavity it is possible, using equation 6.18, to estimate the degree of linewidth widening. For a 4cm radius corrugated waveguide cavity an ellipticity $\{2(\sigma_{\Delta r}^2+\mu_{\Delta r}^2)^{\frac{1}{2}}\}$ of 30μm was obtained, resulting in a resonant linewidth spreading of 20KHz for the HE_{11} mode. This is negligible when compared to the loaded 3dB linewidth of 340KHz. However, for the HE_{12} mode a Δf of 130KHz is obtained compared with the loaded linewidth of 570KHz. Although the cavity is not long enough to consider the ellipticity to be *random*, this widening does appear to account for the high HE_{12} mode attenuation first measured by Chong < 2 > and later confirmed by the author. If account of the linewidth widening is taken,

the experimental attenuation drops from a value 3 times higher than theory to a value 2.1 times higher than theory. This compares well with the experimental attenuation for the HE_{11} mode measured by the author, which was also 2.1 times higher than theory. The rather large difference between experiment and theory is quite consistent with observations made by other workers using high Q-factor cavities <40>.

CHAPTER 7

LOW INSERTION LOSS MODE FILTERS FOR CORRUGATED CIRCULAR WAVEGUIDES

7.1 INTRODUCTION

The use of a mode filter in the overmoded corrugated circular waveguide has already been briefly discussed in chapter 5 with reference to reducing the level of higher order modes resulting from waveguide bends. The use of a mode filter can also enable a cheaply manufactured flexible corrugated waveguide structure of poor mechanical tolerances to exhibit a level of higher order mode generation acceptable for use as an antenna feeder. A typical example of such a structure is the flexible corrugated waveguide described in chapters 4 and 5 which was originally manufactured for fluid handling purposes. To allow the low attenuation properties of the corrugated waveguide to be practically exploited the mode filter must have an extremely small insertion loss to the dominant HE_{11} mode. To date, the corrugated waveguide mode filters available (shown in chapter 5) exhibit an unacceptably high insertion loss which is typically equivalent to the attenuation loss of an extra 5 metres of X-band corrugated waveguide. In this chapter a new type of corrugated waveguide mode filter possessing negligible HE_{11} mode insertion loss is presented.

The basic concept behind this design of mode filter

is the introduction of slits into the corrugated waveguide structure to interrupt the wall current flow of the unwanted higher order mode whilst leaving the HE_{11} mode current flow essentially unperturbed.† In section 7.2 the general performance requirements for a corrugated waveguide mode filter are considered. From a study of the theoretical current flow patterns on the waveguide walls for both the main and higher order modes, the positions in the waveguide structure for the mode filtering slits are proposed in section 7.3. The effectiveness of the proposed slit positions in increasing the higher order mode attenuation is considered experimentally in section 7.4 using a resonant cavity measurement technique. From this initial experimental investigation a combination of two basic slit configurations are found to exhibit a degree of suppression to all three higher order modes with negligible extra HE_{11} mode loss; both these slits being positioned in the corrugation side walls. To increase the higher order mode loss to the level required for effective mode filtering, loading of the slits with resistive material is proposed and experimentally verified in section 7.5.

Having obtained a basic design of mode filter the transmission test method is used in an experimental

†This method of modifying the waveguide structure to achieve mode filtering is analogous to the insulated helical wire form of construction used for the H_{01}^{o} mode trunk waveguide.

parametric study to determine the optimum slit dimensions for maximum mode suppression. The results of this study are presented in section 7.6. Use of the mode filter in a corrugated waveguide antenna feeder is considered in section 7.7, where formulae for calculating the filter length required to maintain a specified degree of higher order mode suppression is presented. In addition, a method of corrugated waveguide manufacture exhibiting continual H_{01} mode suppression is proposed.

Finally the main conclusions resulting from this study are presented in section 7.8.

7.2 MODE FILTER PERFORMANCE REQUIREMENTS

In the restricted mode design of overmoded corrugated circular waveguide (chapter 2) there are three higher order modes propagating; the H_{01}, E_{02} and HE_{21} modes. Because of its low attenuation the H_{01} mode exhibits the most serious trapped mode resonance loss when the waveguide is operated with single mode input and output waveguides. Calculations show that the increase in attenuation of the H_{01} mode in the mode filtering section of the waveguide would need to be between 2 and 3 orders of magnitude to achieve an acceptable trapped mode resonance loss. Consider for example an X-band corrugated waveguide of poor mechanical tolerance exhibiting an H_{01} mode coupling level of -15dB and an attenuation of 3dB/100m. Application of equation 4.3 indicates that a total H_{01} mode attenuation over the waveguide run of 33dB is required to

maintain the maximum relative insertion loss (M.R.I.L.) to below 0.15dB. To achieve this in a waveguide having a total length of 100m and a mode filter length of 2m would require an increase in H_{01} mode attenuation in the mode filter section of about 500 times. For the HE_{21} and E_{02} modes, whose attenuation in the corrugated waveguide is nearly an order of magnitude larger than that of the H_{01} mode, much shorter lengths of mode filter exhibiting this degree of attenuation increase would be sufficient to maintain the desired degree of suppression. Because the mode filters to be considered here are an integral part of the corrugated waveguide structure filter lengths of order several metres are not unrealistic so long as the additional HE_{11} mode attenuation introduced by the slits is negligible. In this case it would be possible to use the modified waveguide structure over the complete waveguide length, enabling continuous mode suppression to be achieved.

A mode filter should ideally operate with both orthogonal polarisations of the HE_{11} mode, however in the next section it will be shown that mode filtering using slits in the waveguide structure fundamentally limits the waveguide to single linear polarisation operation.

7.3 DETERMINATION OF POSSIBLE POSITIONS FOR MODE FILTERING SLITS

The main criteria for the positioning of a mode filtering slit in the waveguide structure is that it

causes maximum interruption to the highest current flow of the unwanted mode(s) whilst causing a negligible perturbation to the current flow of the HE_{11} mode. In order to achieve this criteria a knowledge of the current flow on the inner walls of the corrugated waveguide, for both the main and higher order modes, is required. Chong < 2 > has formulated the current flow on the walls of the corrugated waveguide and using this analysis a computer graphics program was developed to plot out these current flow patterns. This computer program tracks the vector direction of the current flow over the waveguide surface at a specified instant in time. Two methods of graphically presenting the results are used. The first shows a *developed* view of the current flow in a quadrant of the corrugated waveguide and by covering a sufficient length of waveguide the full variation of current direction and magnitude can be obtained from a single time plot. The results obtained for both the HE_{11} and HE_{21} modes are shown in figures 7.1(a) and 7.1(b) respectively. The method of *development* is shown in figure 7.2. Results for the H_{01} mode, where the current flow direction is purely azimuthal, and the E_{02} mode, where the current flow direction is radial and longitudinal, are omitted.

The alternative method for presenting the results shows the current flow directions on the side walls of the corrugations and these results are shown in figure 7.3 for all four propagating modes.

From examination of these current flow patterns, and

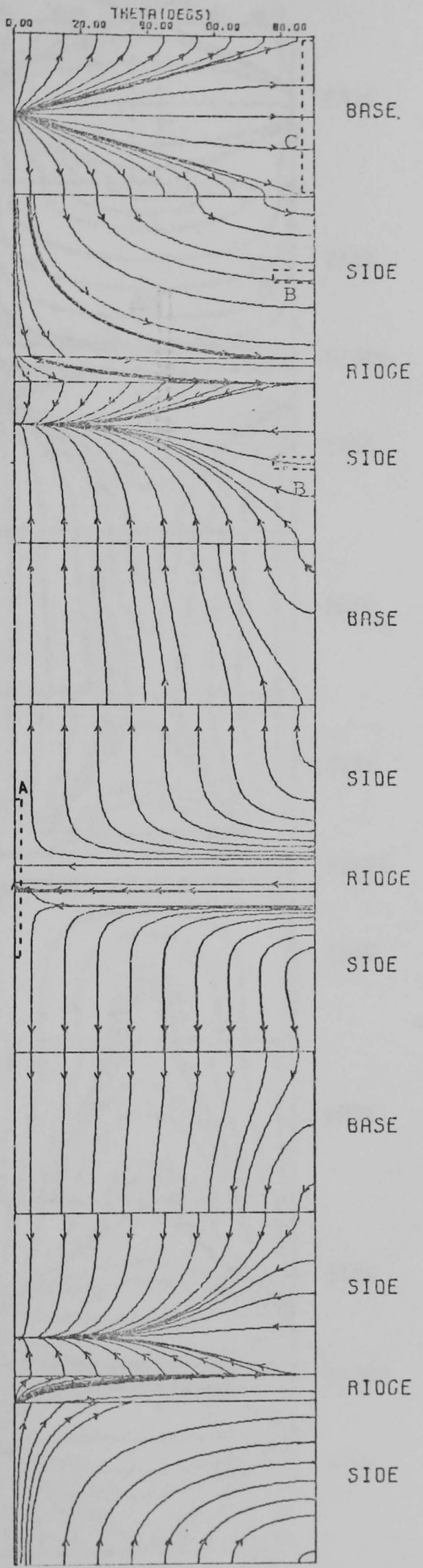

Fig. 7.1(a) 'Developed' current flow pattern for the HE_{11} mode in the waveguide of figure 4.3, frequency 9.7 GHz

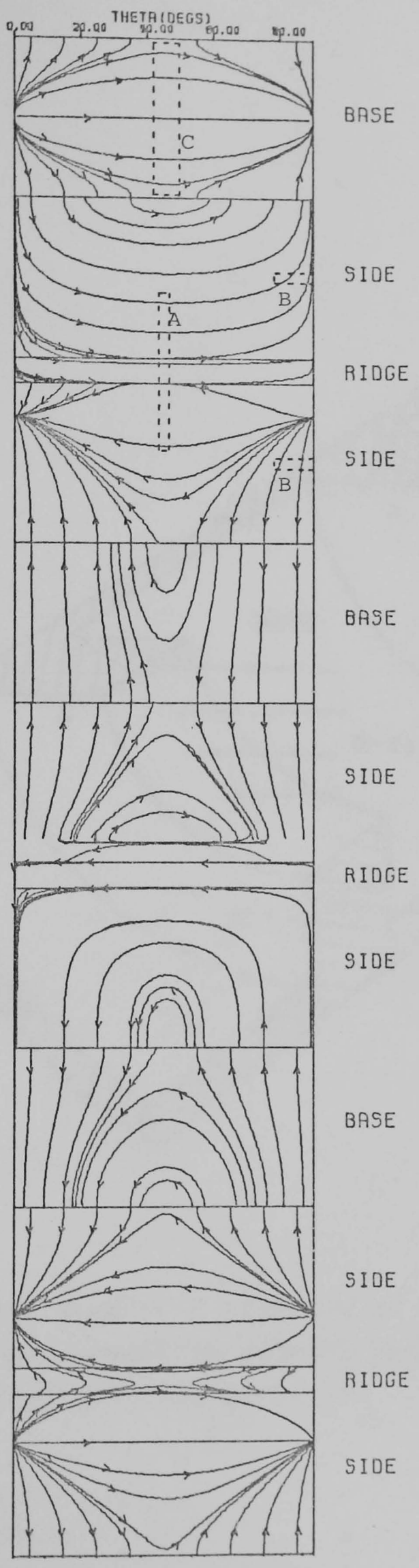

Fig. 7.1(b) 'Developed' current flow pattern for the HE_{21} mode corresponding to figure 7.1(a); the slits being shown in the position for maximum mode suppression

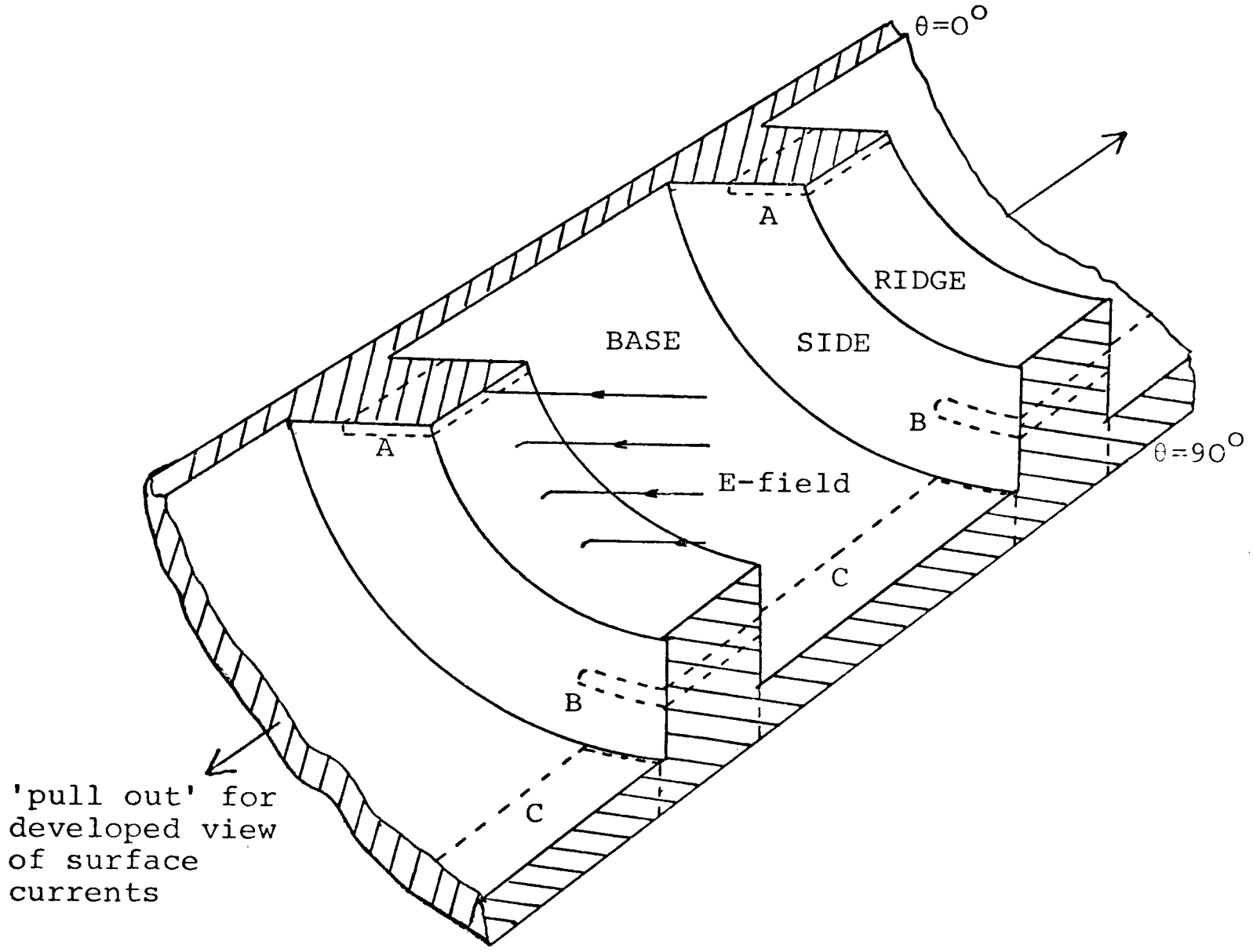

Fig. 7.2 Oblique view of a quadrant of the corrugated circular waveguide showing method of 'development' and proposed slit positions

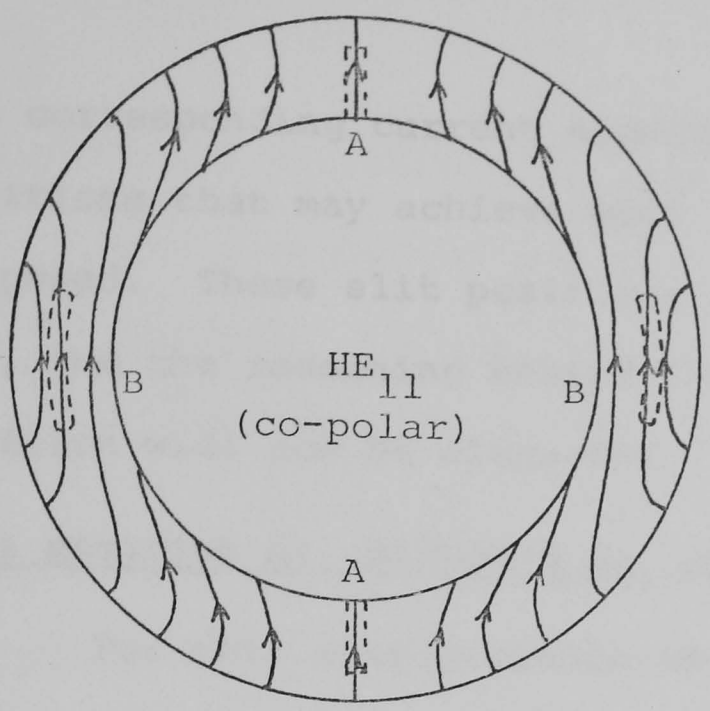

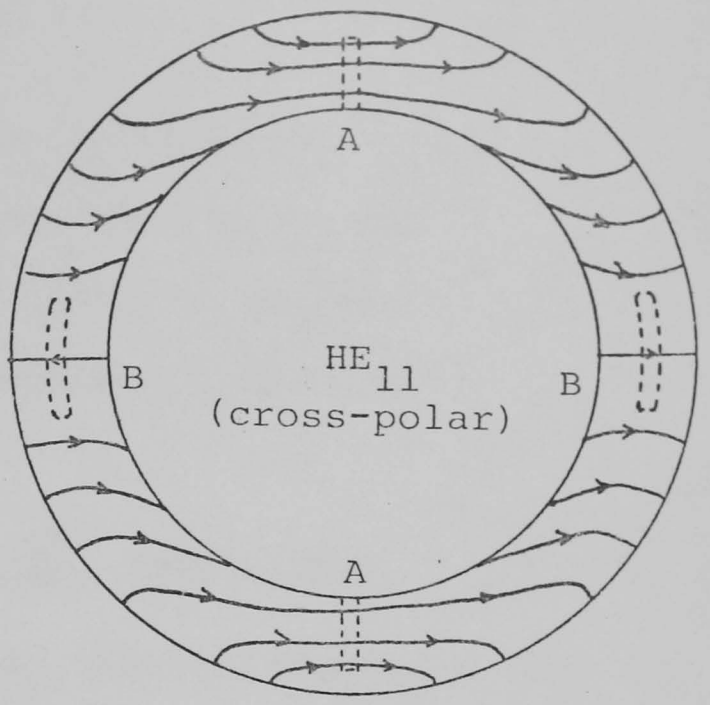

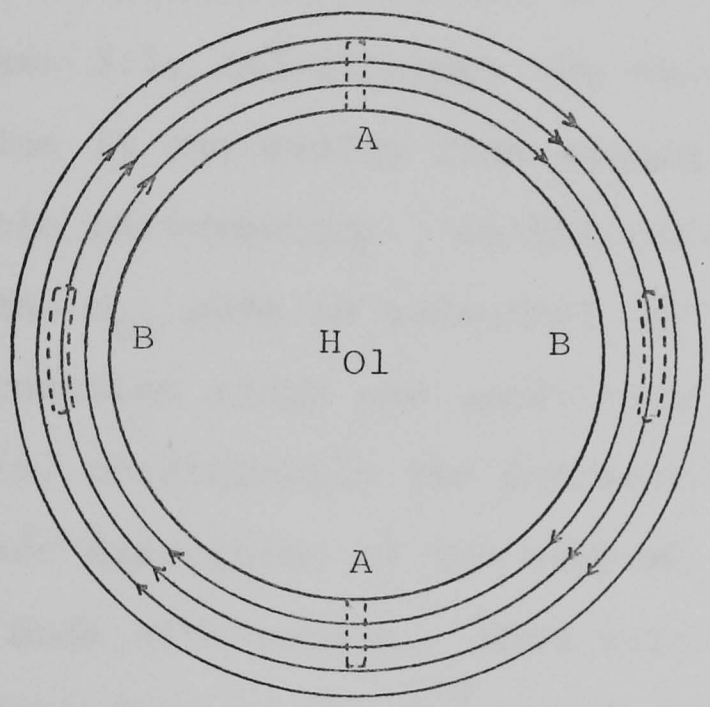

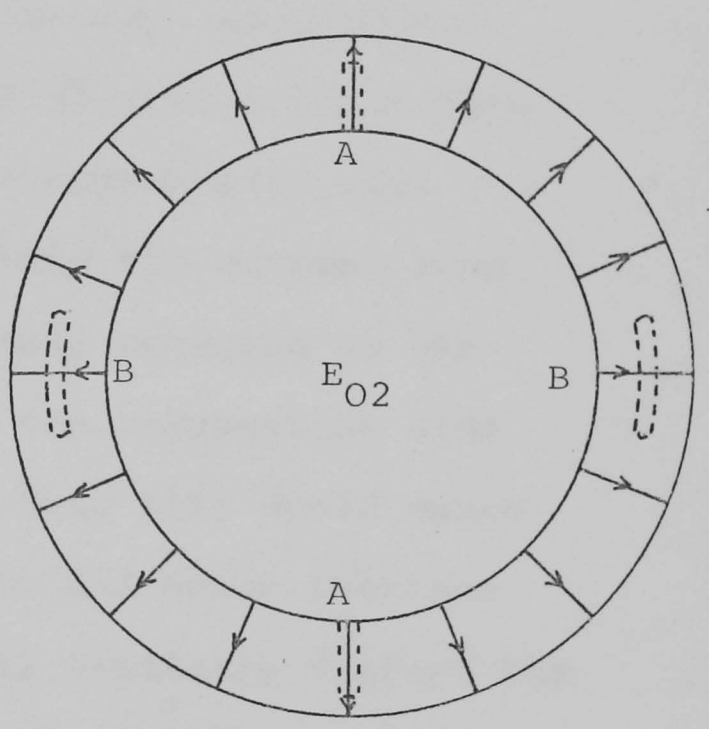

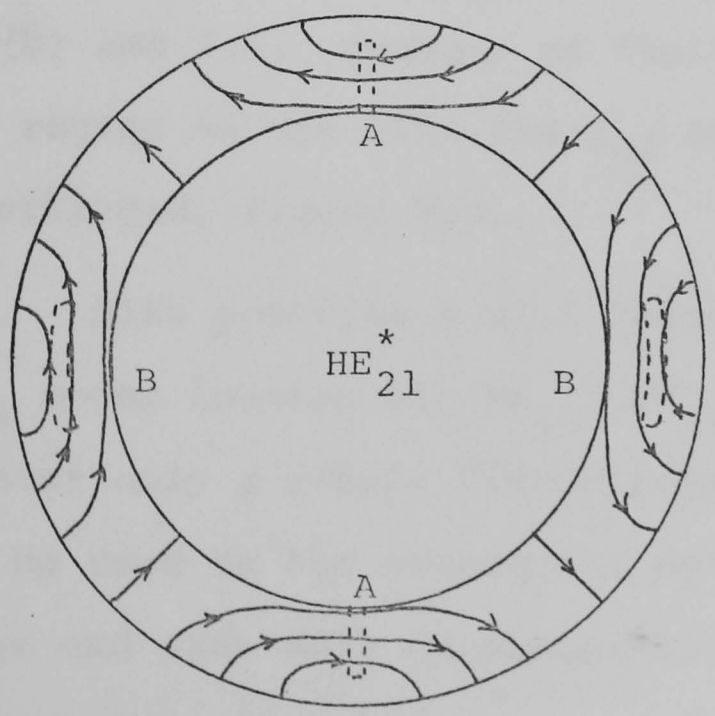

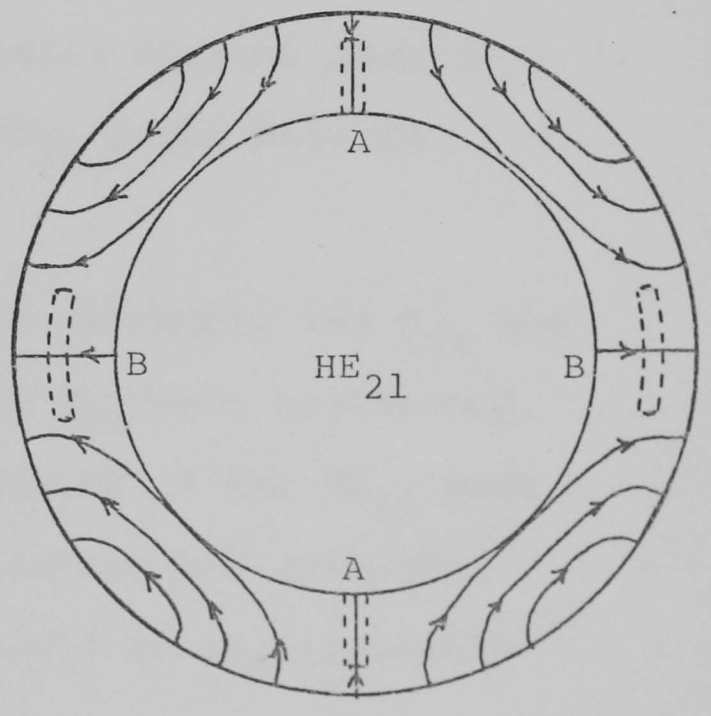

Fig. 7.3 Current flow patterns on the corrugation side wall for all four propagating modes; proposed slit positions are shown dotted

the corresponding current magnitudes, a number of slit positions that may achieve mode filtering action are proposed. These slit positions are shown on figures 7.1 to 7.3, and the reasoning behind the choice of each slit position will now be discussed.

Slit position A: proposed H_{01} and HE^{*}_{21} mode filter

For this slit position the HE_{11} mode currents on the side walls are radial and on the ridge top longitudinal, figure 7.1, and although the current flow is high in this region it can easily flow around the narrow slit with little perturbation. On the other hand the current flow of the H_{01} mode is azimuthal and mainly confined to the corrugation ridge and upper half of the corrugation side walls, consequently the presence of this slit would cause severe disruption of the current flow and hence increase the mode attenuation. This slit will similarly disrupt the current flow of the HE^{*}_{21} mode as can be seen from figures 7.1(b) and 7.3. Because of their radial current flow in the region of the slit the E_{02} and HE_{21} modes will be unperturbed, figure 7.3.

Slit position A will therefore attenuate the H_{01} and HE^{*}_{21} modes leaving the HE_{11}, HE_{21} and E_{02} mode unaffected. However only a *single linear* polarisation of the HE_{11} mode can be used as the orthogonal polarisation has azimuthal ridge and side wall currents which would be significantly perturbed by the slit.

Slit position B: proposed E_{02} and HE_{21} mode filter

In the region of this slit position the HE_{11} mode current is quite weak and mainly azimuthal, resulting in little perturbation of the current flow. Similarly the HE_{21}^{*} and H_{01} modes have azimuthal currents in this region, figure 7.3, and will also remain substantially unperturbed. However, the E_{02} and HE_{21} modes have quite high radial currents in the region of this slit position and will therefore be attenuated. As in the case of slit position A, only a single polarisation of the HE_{11} mode can be used, the high radial current of the orthogonally polarised mode being severely perturbed.

Slit position C: proposed E_{02}, HE_{21} and HE_{21}^{*} mode filter

For this slit, positioned at the base of the corrugations, the currents of the HE_{11} and H_{01} modes are relatively weaker than those of the HE_{21}, HE_{21}^{*} and E_{02} modes, resulting in some increase in the attenuation of the latter modes. As in the previous designs only a single polarisation of the HE_{11} mode can be used, the base current of the orthogonally polarised component being relatively strong in the region of the slit, resulting in significant leakage of dominant mode power. The currents on the corrugation base are weaker than those on the corrugation side walls for all four propagating modes and therefore the degree of suppression obtained with this design would not be expected to be as high as in the previous two designs. Because of the weak HE_{11} mode currents in the region of

this slit position the use of a larger azimuthal slit dimension may be possible with little extra HE_{11} mode perturbation.

All three mode filter designs presented in this section only permit operation with a single linear polarisation of the HE_{11} mode. The effect on the HE_{11} mode of using the above slit types at other azimuthal positions in the waveguide can be determined by resolving the HE_{11} mode polarisation parallel and perpendicular to the longitudinal plane containing the slit. It becomes evident that there is no mode filtering slit position that can permit dual polarisation operation with the HE_{11} mode.

7.4 INITIAL EXPERIMENTAL PERFORMANCE EVALUATION OF MODE FILTER DESIGNS

In order to determine the increase in higher order mode attenuation and the HE_{11} mode insertion loss for the mode filter designs proposed in the previous section the resonant cavity measurement method described in chapter 4 was used. Filter configurations A and B were manufactured using the thermal contraction method, figure 4.3, whilst the configuration C was manufactured using the multiple section form of waveguide construction, figure 4.2. This latter waveguide is slightly more overmoded than the normal 4 propagating mode design but helps to determine the effect of a slit in the corrugation base. The dimensions of the waveguides and mode filtering slits used

A

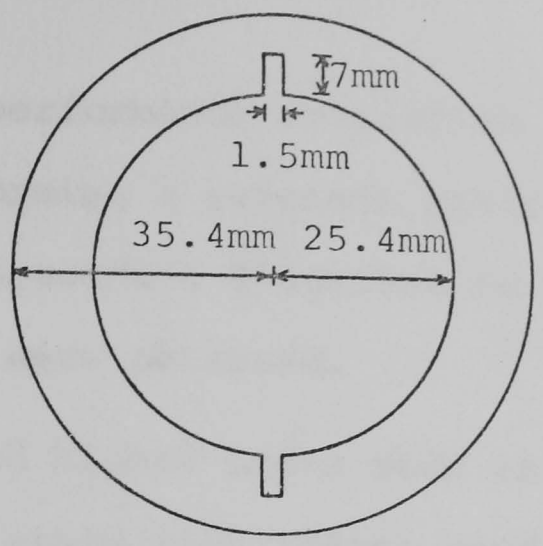

B

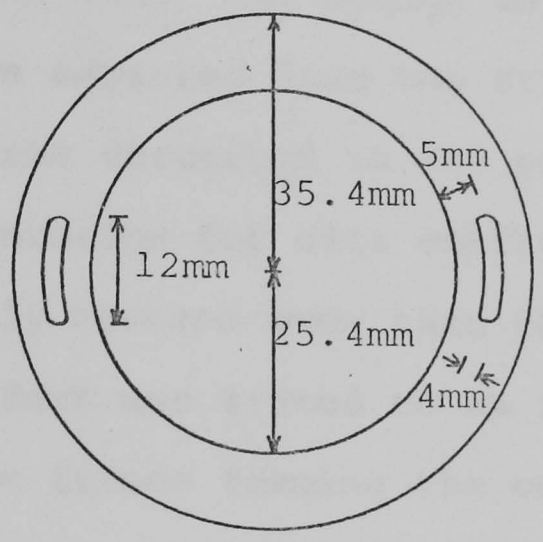

C

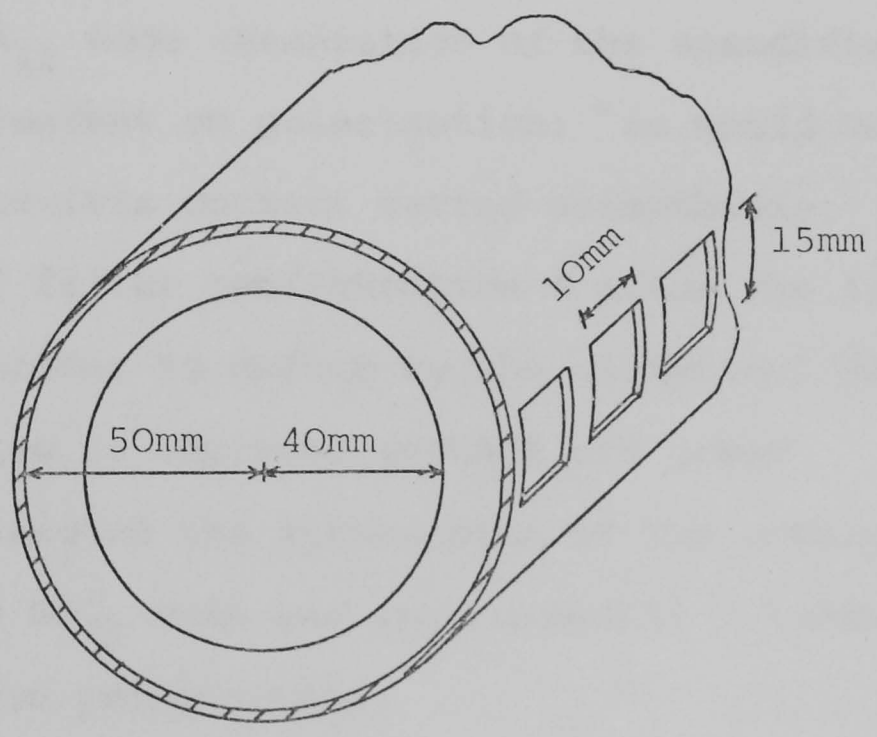

Fig. 7.4 Slit dimensions used in the initial experimental evaluation; electric field vertically polarised

for this initial performance evaluation are shown in figure 7.4. By forming a resonant cavity and following the experimental procedure described in chapter 4 the following results were obtained.

The measured higher order mode attenuation ratios (equation 4.2) obtained with filter configurations A and B are shown in table 7.1. The change in attenuation follows the pattern expected from the study of the mode current flow patterns described in the previous section. The HE_{11} mode attenuation for slit configuration A was found to be slightly *reduced* over that obtained without the slit. This effect was traced to an improvement in contact between the irises forming the corrugations and the pipe wall. The pipe used in the construction of these waveguides was found to be approximately 50μm elliptical, which caused the HE_{11} mode attenuation of the unmodified waveguide to be dependent on polarisation; as would be expected if the pipe-iris contact varied azimuthally. The two radial slits of filter configuration A allow the iris forming the corrugations to deform to the elliptical shape of the pipe resulting in improved contact and lower attenuation. As expected the attenuation of the orthogonal polarisation of the HE_{11} mode was approximately 7 times greater than the main polarisation.

For slit configuration B an HE_{11} mode attenuation increase of ≈1.5 times was measured, this rather high value was attributed to the large radial width used for this slit, figure 7.4. Measurements on a similar slit

Iris Type	Mode	Frequency (GHz)	Attenuation Ratio
A	H_{01}	10.1	9.0
		11.1	3.0
	HE^{*}_{21}	10.0	3.0
		11.0	4.0
	E_{02}	10.0	1.0
		10.9	1.0
	HE_{21}	10.0	1.4
		11.0	1.0
B	H_{01}	10.1	1.1
		11.1	1.8
	HE^{*}_{21}	10.0	1.2
		11.0	1.0
	E_{02}	10.0	8.5
		10.9	30
	HE_{21}	10.0	20
		11.0	30

Table 7.1 Measured higher order mode attenuation ratios for filter configurations A and B

slit A = 7mm x 1.5mm

slit B = 4mm x 12mm

configuration having a smaller radial dimension showed a negligible HE_{11} mode attenuation increase, although a reduced level of higher order mode suppression also occurred. It can be concluded that the high measured values for the E_{02} and HE_{21} mode attenuations shown in table 7.1 also result from the large slit dimension used. Attenuation increases to the orthogonal polarisation of the HE_{11} mode were found to be of order 3 times for this slit configuration.

Measurements performed with the mode filtering slits cut in the base of the corrugations, configuration C, indicated some degree of suppression to the HE_{21} and E_{02} modes. As expected the H_{01} mode was totally unaffected by this slit position, verifying the fact that this mode is bounded by the tops of the corrugations. The maximum azimuthal dimension for the slit before the HE_{11} mode attenuation becomes significantly increased was found to be about 0.8λ for the large waveguide diameter used. Measurements with a smaller, more practical corrugated waveguide (4 propagating modes), suggested that the maximum slit width was reduced to about 0.5λ; this being due to the higher corrugation current flow in this case. With the E-field polarisation of the HE_{11} mode in the plane of the slit considerable leakage of the HE_{11} mode resulted, an increase in attenuation of order 100 times being observed. It was found that by covering the slit with adhesive copper tape this HE_{11} mode attenuation increase was eliminated. Depressing the copper tape

inwards, forming a slight perturbation of the corrugation base, was found to have no effect on the mode resonance. This suggests that a lightweight form of corrugated waveguide could be constructed using aluminium foil to form the outer waveguide wall. The details of this construction, and the experimental results obtained with it, are described in appendix 7.1.

The two filter configurations A and B together form a mode filter suppressing all three higher order modes. They both interrupt the current flow of the higher order modes in the region where it is largest, enabling the maximum amount of mode suppression to be obtained. Alternatively, configuration C operates in a relatively low current flow region and introduces no suppression to the H_{01} mode, the most troublesome higher order mode. In view of these facts this latter configuration was rejected for use as a mode filter.

7.5 LOADING OF THE MODE FILTERING SLITS WITH RESISTIVE MATERIAL

From the results of the initial performance study for mode filter configurations A and B it is evident that they do not exhibit the degree of higher order mode suppression specified in section 7.2. In this section a study of the mechanism by which the mode attenuation is increased by a slit reveals that some form of *resistive* loss is required in the slits to make the current interruption fully effective.

The mechanism of mode suppression by a slit will be considered here with reference to configuration A, but it equally applies to any of the mode filtering slits.

The presence of a slit in the waveguide structure modifies the current flow patterns of the modes and establishes an electric field in the slit, the magnitude of which is dependent on the direction of the mode current flow at the slit. A current flow parallel to the longest dimension of the slit only undergoes a minor perturbation, the current being easily able to flow around it resulting in the generation of only a weak electric field density in the slit, figure 7.5(a). On the other hand for current flow perpendicular to the longest slit dimension severe truncation of the current flow occurs resulting in the generation of a high electric field density in the slit, figure 7.5(b). By allowing this high electric field to remain in the slit the full potential of the slit in truncating the current flow is lost. Placing resistive material in the slit will absorb this electric field.

Because the radial current flows around the slit the absorption of the weak slit electric field would have a negligible effect on the mode attenuation, permitting the low insertion loss of the HE_{11} mode to be retained. The increased higher order mode attenuation observed with the slits unloaded results purely from the perturbation of the mode current flow, the degree of attenuation increase indicating the severity of this perturbation.

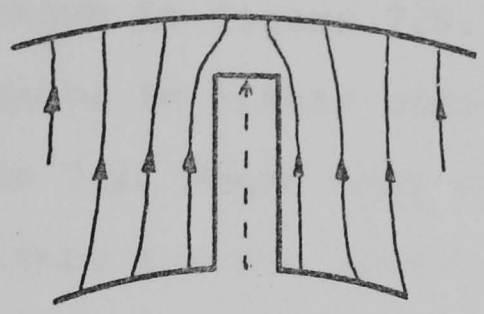

a) Weak electric field in slit

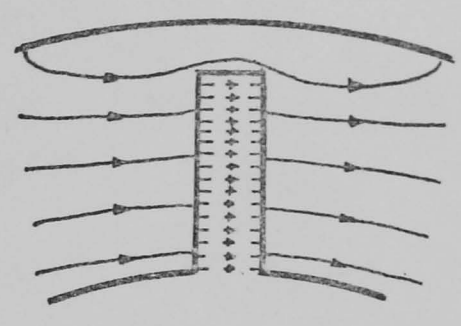

b) Strong electric field in slit

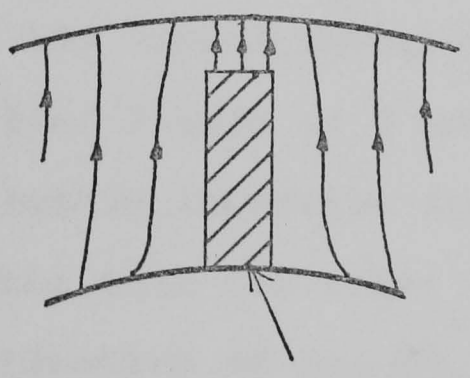

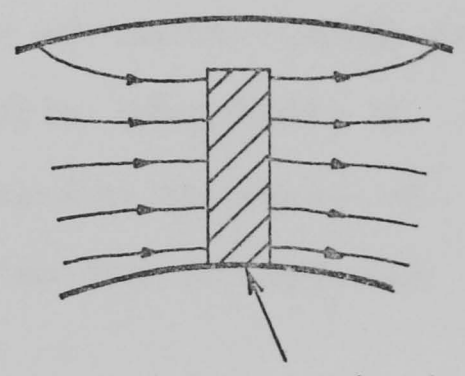

c) and d) Without slit electric field over resistive card is essentially that in unperturbed waveguide

Fig. 7.5 The mechanism of mode suppression by a slit in the corrugation side wall

——— current flow

------ electric field

Resonant cavity measurements were made with the slit configurations A and B loaded with resistive card† as shown in figure 7.6. The results obtained for the increase in higher order mode attenuation are tabulated in table 7.2, where they are compared with the results obtained for the same slit dimensions but without the resistive card loading. As expected significant attenuation increases were observed for both the H_{01} + HE^{*}_{21} and E_{02} + HE_{21} mode combinations for slit configurations A and B respectively. The measured attenuation increase of 100 times is the largest that can be measured using the resonant cavity measurement method (chapter 4). The HE_{11} mode attenuation was found to be increased by a factor of about 1.4 times for both mode filter configurations. In a typical X-band waveguide this represents an increased loss over the normal waveguide attenuation of about 0.05dB for a filter length of 2 metres, and clearly represents a negligible insertion loss. An attenuation increase of greater than 100 times was observed for the orthogonal polarisation of the HE_{11} mode.

The presence of the resistive card without the slit would not significantly alter the current flow patterns on the corrugation side walls, figures 7.5(c) and (d). The resistive card absorbs the electric field tangential to it, the magnitude of this field being essentially that in the unperturbed waveguide. In the

†A thin layer of resistive material mounted on cardboard.

A

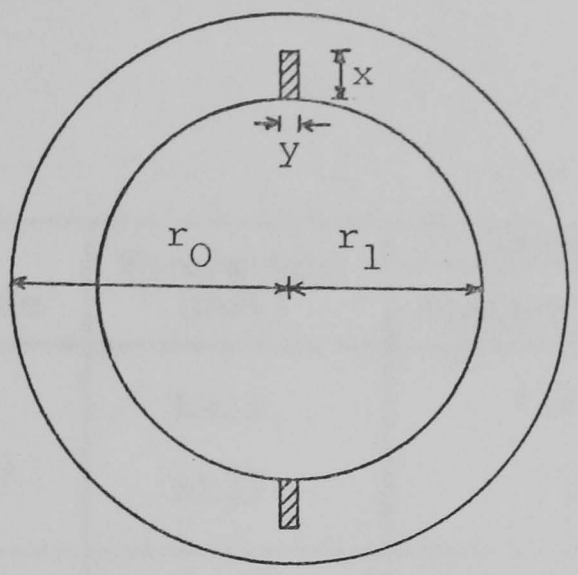

B

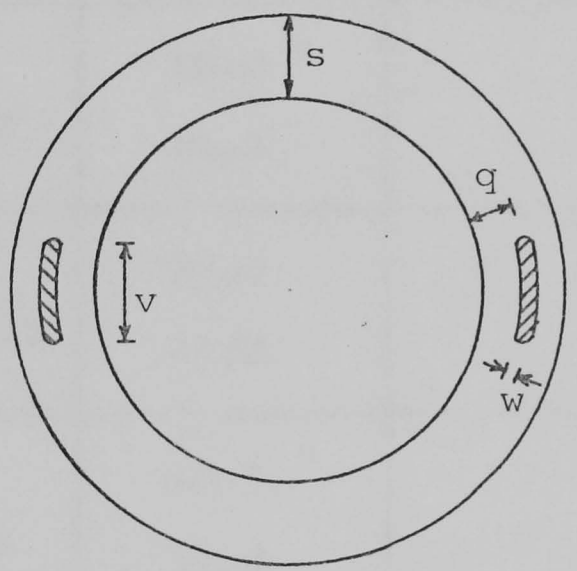

C

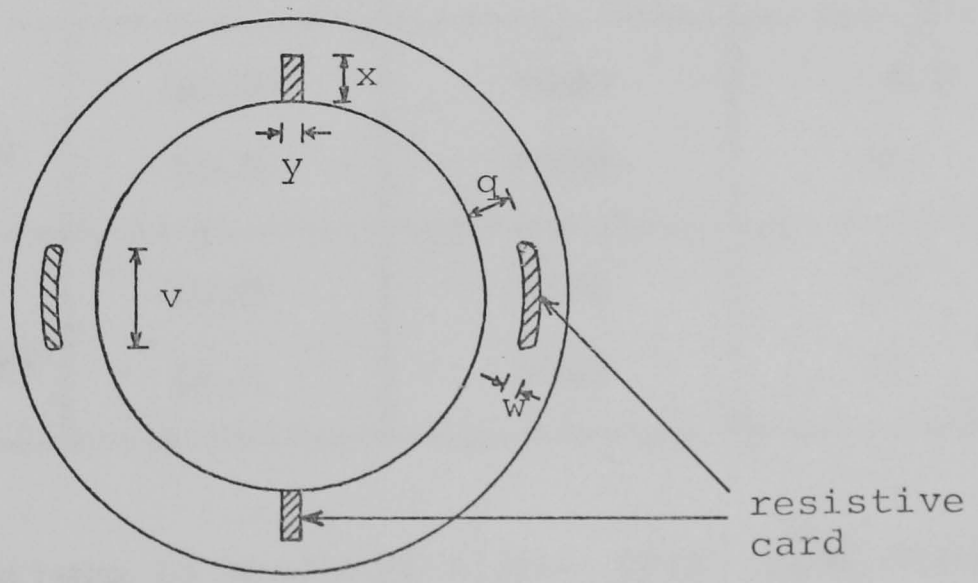

Fig. 7.6 Resistive card loaded slit configurations

Iris Type	Mode	Frequency (GHz)	Attenuation Ratio	
			Loaded Slit	Unloaded Slit
A	H_{01}	10.1	>100	9.0
		11.1	10	3.0
	HE^{*}_{21}	10.0	>100	3.0
		11.0	>100	4.0
	E_{02}	10.0	1.3	1.0
		10.9	1.1	1.0
	HE_{21}	10.0	1.4	1.4
		11.0	1.3	1.0
B	H_{01}	10.1	1.5	1.1
		11.1	2.2	1.8
	HE^{*}_{21}	10.0	3.9	1.2
		11.0	3.0	1.0
	E_{02}	10.0	>100	8.5
		10.9	>100	30
	HE_{21}	10.0	>100	20
		11.0	>100	30

Table 7.2 Comparison of measured higher order mode attenuation ratios for the loaded and unloaded mode filter configurations A and B

case of the radial current flow of slit A the presence of the slit means that the HE_{11} mode current flow is *steered away* from the slit and no undesirable increase in HE_{11} mode loss occurs. In the case of the azimuthal current flow the presence of the slit gives a high electric field *concentration* in the region of the resistive card and the attenuation is correspondingly high.

7.6 TRANSMISSION TEST MEASUREMENTS WITH THE RESISTIVELY LOADED SLIT MODE FILTERS

In this section transmission test measurements are described to determine the degree of trapped mode suppression obtainable with the mode filters. From the results a quantitative assessment of the increase in higher order mode attenuation can be made, enabling the optimum slit dimensions required to achieve maximum higher order mode suppression to be experimentally determined. Measured transmission characteristics obtained with the *composite* mode filter of figure 7.6C are also presented in this section, this filter combining the optimum designs of both filter types A and B into one structure.

Transmission test measurements on the mode filter configurations A and B of figure 7.6 were made with the 2m length of flexible corrugated waveguide, figure 4.6, using the technique described in chapter 4. Short lengths (37mm) of mode filter were manufactured using this flexible waveguide and a photograph of a typical section is shown in figure 7.7(a). The resistive card and carbon loaded

a)

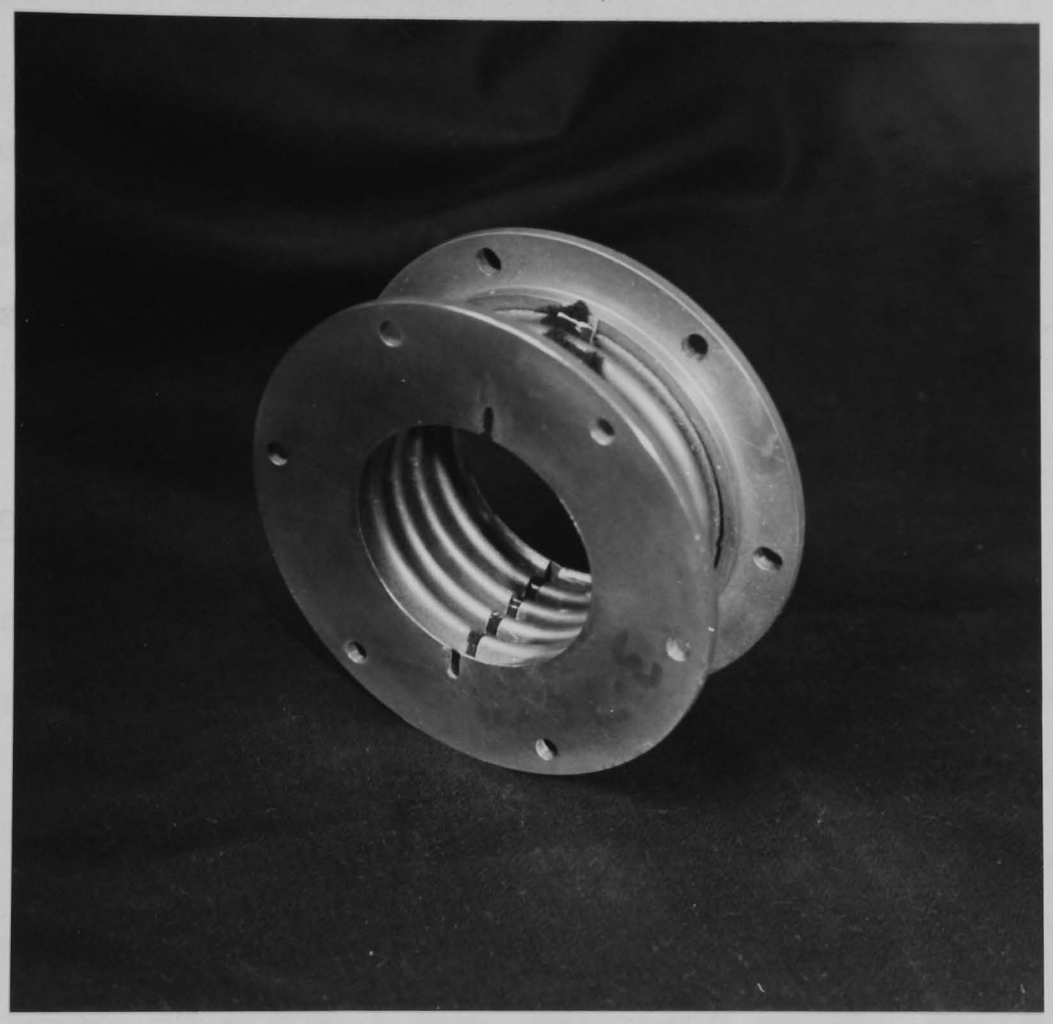

b)

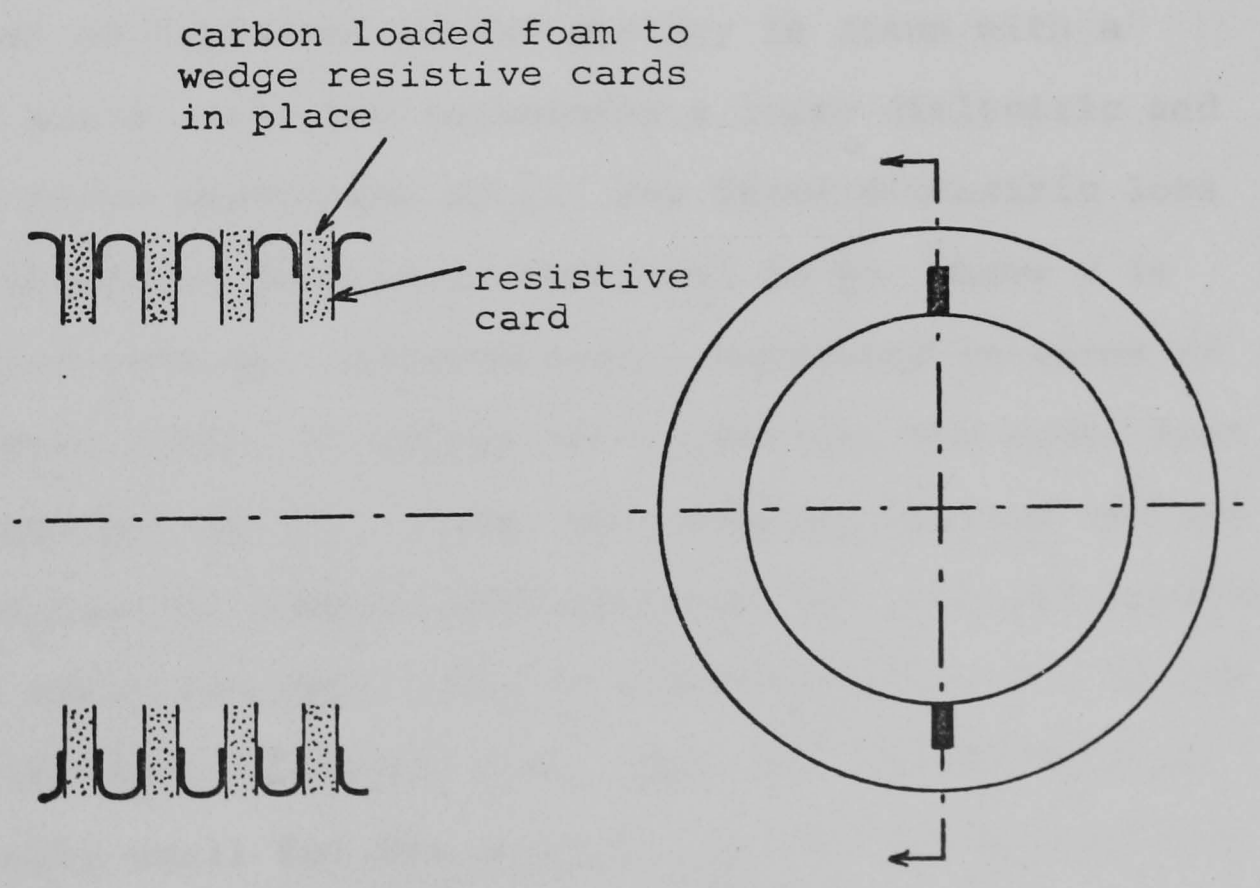

Fig. 7.7 Mode filter configuration A fabricated from the flexible waveguide of figure 4.6

foam is inserted from the outside of the waveguide structure as shown in figure 7.7(b). This simple method of construction enables changes in the slit dimensions required for the parametric study to be easily made. A similar method of construction is used for the mode filter with slit configuration B.

7.6.1 The H_{01} and HE^{*}_{21} mode filter

Because the H_{01} mode filter produces the most serious trapped mode resonance loss in the corrugated waveguide the parameters of the mode filtering slit were optimised to exhibit maximum attenuation to this mode. Measurements showed that the reduction in maximum relative insertion loss (M.R.I.L.) was dependent on the depth of the slit, x, (figure 7.6A) but not on its width, y. This effect can be explained if the analogy is drawn with a parallel plate capacitor containing a lossy dielectric and having a plate separation of y. For fixed dielectric loss tangent the power loss is proportional to $\frac{V^2}{y}$, where V is the applied voltage. Alternatively, expressed in terms of the electric field, E, across the capacitor, the power loss is proportional to E^2y. Thus, for constant applied voltage the power loss is proportional to $\frac{1}{y}$ but for constant applied electric field the power loss is proportional to y. In the case of the mode filtering slit, where the dimension y is sufficiently small for the above analogy to hold, widening the gap (y) further perturbs the waveguide structure, resulting in neither the electric field, E, across the gap nor the applied gap voltage, V, remaining constant. A

combined change in both E and V most probably occurs suggesting that this loss is mainly independent of y.

An experimental parametric study was undertaken to determine the dependence of slit depth x on the M.R.I.L. due to the H_{01} mode. The results of this study are shown in figure 7.8 and suggest that a slit depth of $\frac{s}{2}$ (figure 7.6) is optimum for maximum H_{01} mode suppression. The reason for this dependence on the slit depth and the existence of an optimum depth for H_{01} mode suppression will now be considered.

For small values of x the mode current is able to flow around the slit with little perturbation, resulting in a low electric field density in the slit and hence a low level of mode suppression, figure 7.9(a). Alternatively, for a very deep slit the mode is severely perturbed and it is probable that the mode is sustained by a very high *fringing field* across the top of the slit where no absorbent material is present, figure 7.9(b). The remainder of the slit would have a low electric field density and so again only a low level of mode suppression would be obtained. For the optimum slit depth the mode is sufficiently perturbed to produce the highest electric field density in the slit with only a small fringing field (figure 7.9(c)) and so maximum mode suppression occurs.

Figure 7.10 compares the measured transmission characteristic for: a) the 2m length of flexible corrugated waveguide together with two 37mm long corrugated waveguide sections with b) the same 2 metre length (having

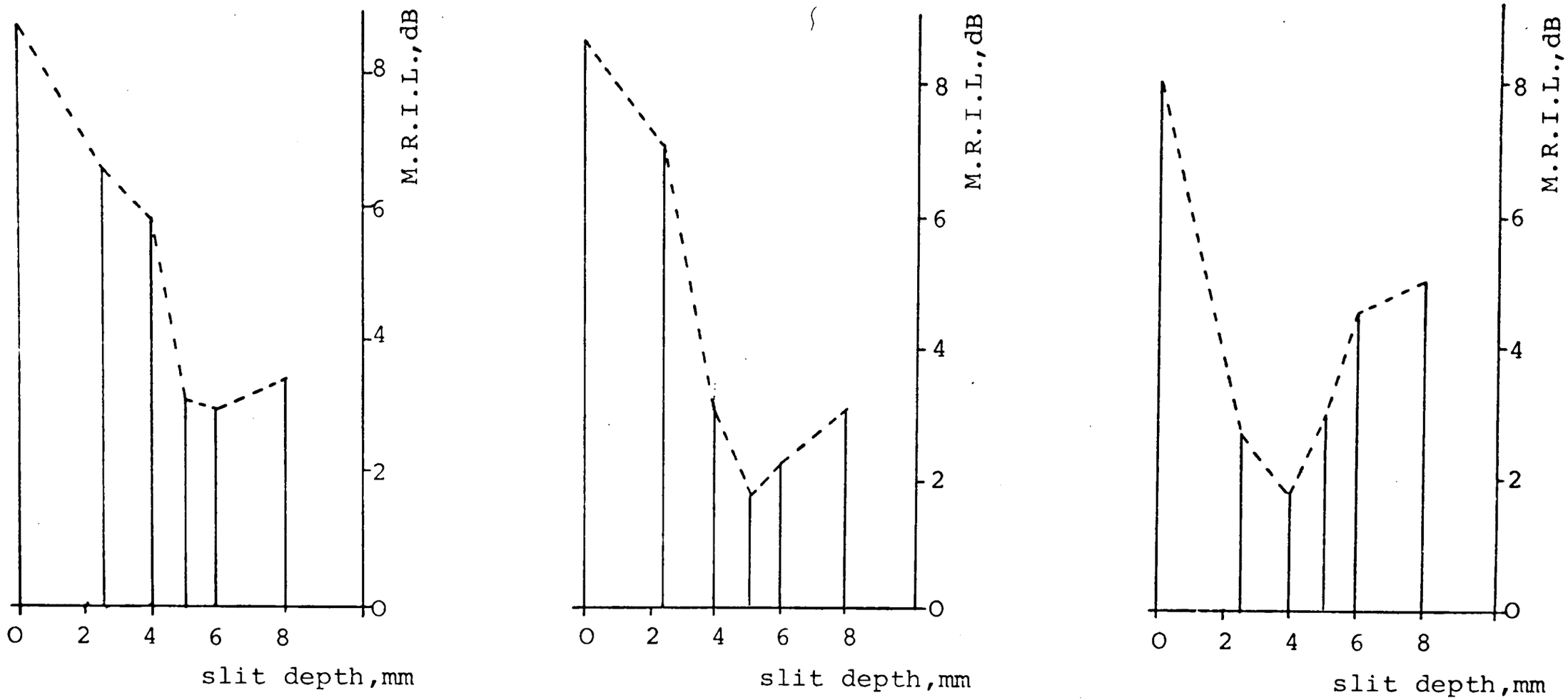

Fig. 7.8 Maximum relative insertion loss (M.R.I.L.) due to the H_{01} mode as a function of slit depth x

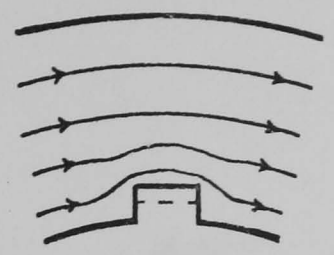

a) Shallow slit resulting in a low electric field density in the slit

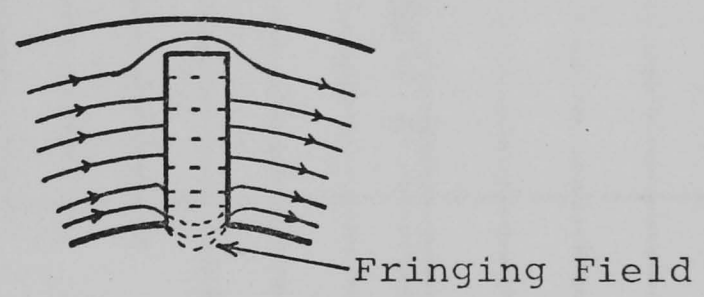

b) Deep slit requiring a high fringing field to sustain the mode resulting in a low electric field density in the slit

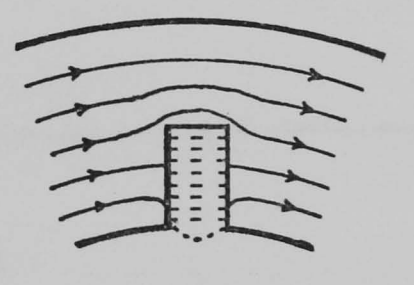

c) Optimum slit depth producing minimal fringing field and maximum electric field density in the slit

Fig. 7.9 Mechanism yielding optimum slit depth for the H_{01} and HE^{*}_{21} mode filter

——— current flow

----- electric field

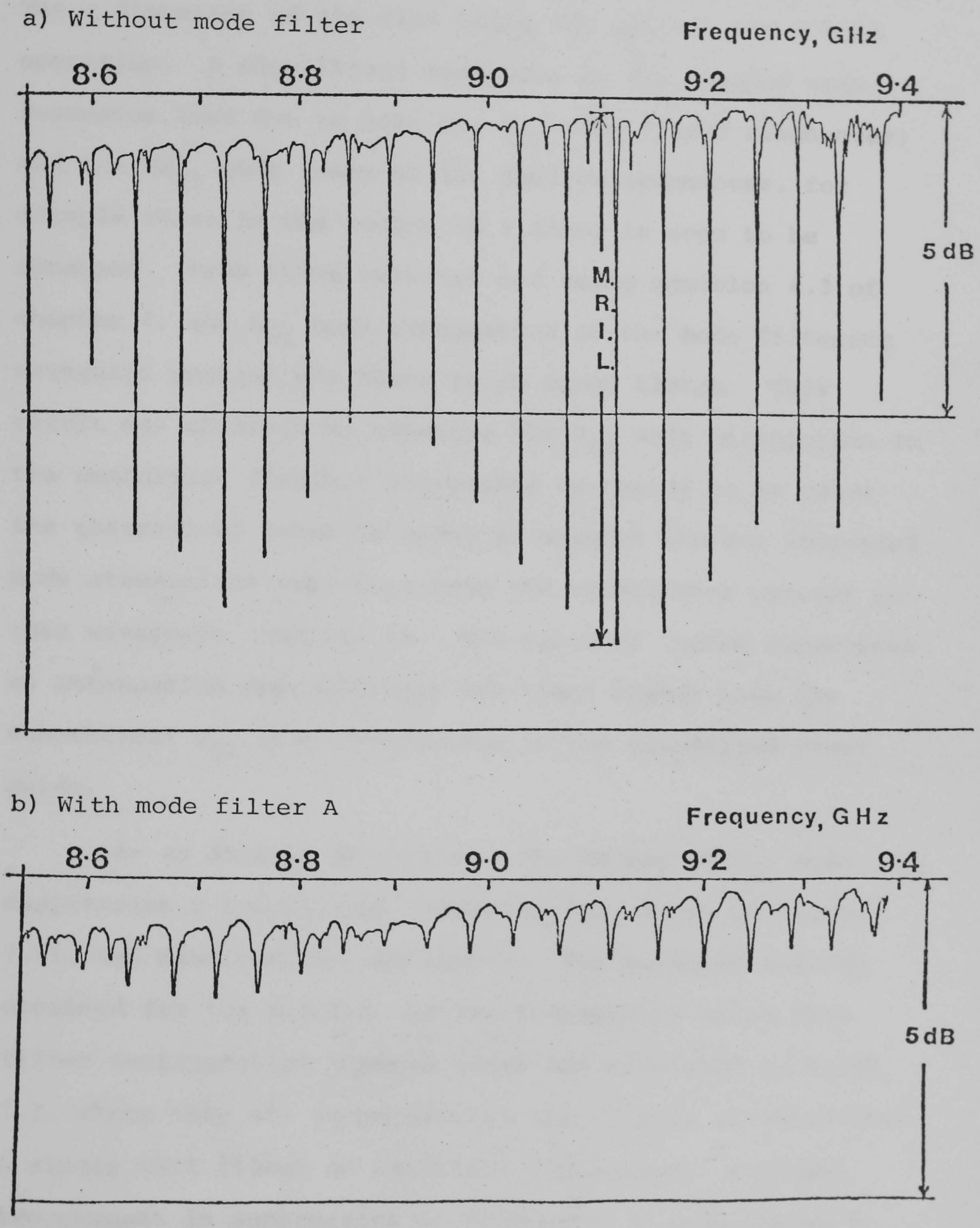

Fig. 7.10 Comparison of the measured transmission characteristics for the 2 metre length of flexible corrugated waveguide with and without the mode filter of figure 7.7.
Slit dimensions: x=5mm, y=1.5mm.
frequency scale not an amplitude reference line

the same orientation and hence coupling levels) together with two of the 37mm long mode filters shown in figure 7.7. The x dimension of the slit being the optimum for 9.1GHz operation. A significant reduction in the trapped mode resonance loss due to both the H_{01} mode (large resonances) and the HE^{*}_{21} mode (many of the smaller resonances, for example those in the region of 9.1GHz) is seen to be obtained. From these results, and using equation 4.3 of chapter 4, the H_{01} mode attenuation in the mode filtering waveguide section was found to be about 13dB/m. This result was obtained by assuming the H_{01} mode attenuation in the unmodified flexible corrugated waveguide to be twice the theoretical value in order to account for the increased mode attenuation resulting from the welded seam present in this waveguide (chapter 5). The value of 13dB/m represents an attenuation approximately 400 times higher than the theoretical H_{01} mode attenuation in the unmodified waveguide.

In an attempt to increase the degree of H_{01} mode suppression a triple slit configuration, shown in figure 7.11, was manufactured and tested. The measured results obtained for the M.R.I.L. at two frequencies using this filter configuration (length 37mm) are presented in table 7.3, where they are compared with the results obtained for a single slit filter of identical dimensions. A slight improvement in suppression is evident at 9.1GHz whilst a greater improvement is obtained at 8.8GHz. The results suggest that the H_{01} mode attenuation increase obtained

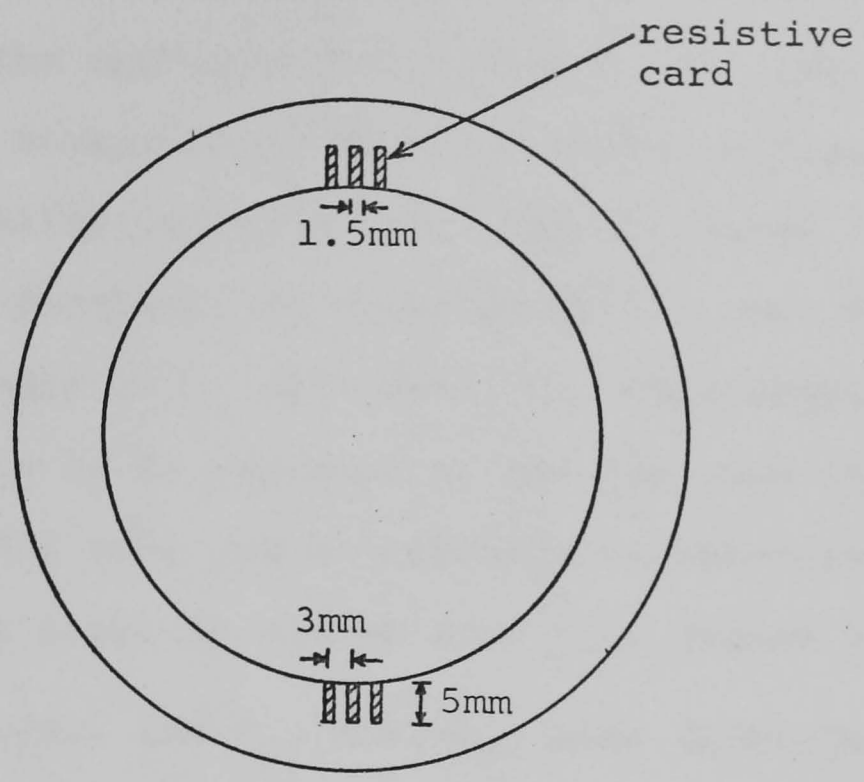

Fig. 7.11 Diagram of the triple slit mode filter configuration

Frequency	Maximum Relative Insertion Loss		
	Plain	Single Slit	Triple Slit
8.8GHz	8.8dB	3.0dB	1.7dB
9.1GHz	8.6dB	1.8dB	1.4dB

Table 7.3 Comparison of the measured M.R.I.L. for the 2 metre length of flexible corrugated waveguide obtained with the single and triple slit mode filters shown in figures 7.7 and 7.11.

parameters: filter length 37mm

slit dimensions as figure 7.11.

with the triple slit configuration is less frequency sensitive than the corresponding single slit configuration. Resonant cavity measurements on this filter configuration using unloaded slits indicated that the HE_{11} mode attenuation was increased by a factor of 1.4 over that of the unloaded single slit configuration. This higher insertion loss is to be expected as the two side slits of this configuration will cause increased perturbation to the HE_{11} current flow, as can be seen from figure 7.3.

To summarise, the H_{01} and HE^{*}_{21} mode filter with experimentally optimised slit dimensions has been shown to increase the theoretical H_{01} mode attenuation in the unmodified waveguide by approximately 400 times, whilst exhibiting an HE_{11} mode attenuation increase of only about 1.4 times. A triple slit configuration of mode filter was found to have an improved mode filtering performance at the expense of an inferior HE_{11} mode insertion loss.

7.6.2 The HE_{21} and E_{02} mode filter

The slit configuration for this mode filter is shown in figure 7.6B. Before the dependence of the slit dimensions on the mode suppression can be studied it is necessary to first identify the HE_{21}, HE^{*}_{21} and E_{02} mode resonances occurring in the transmission characteristic of figure 7.10. Figure 7.12(a) shows a section of this transmission characteristic with no mode filter present, the large resonances being due to the H_{01} mode and the pairs of smaller resonances being attributed to the HE_{21}

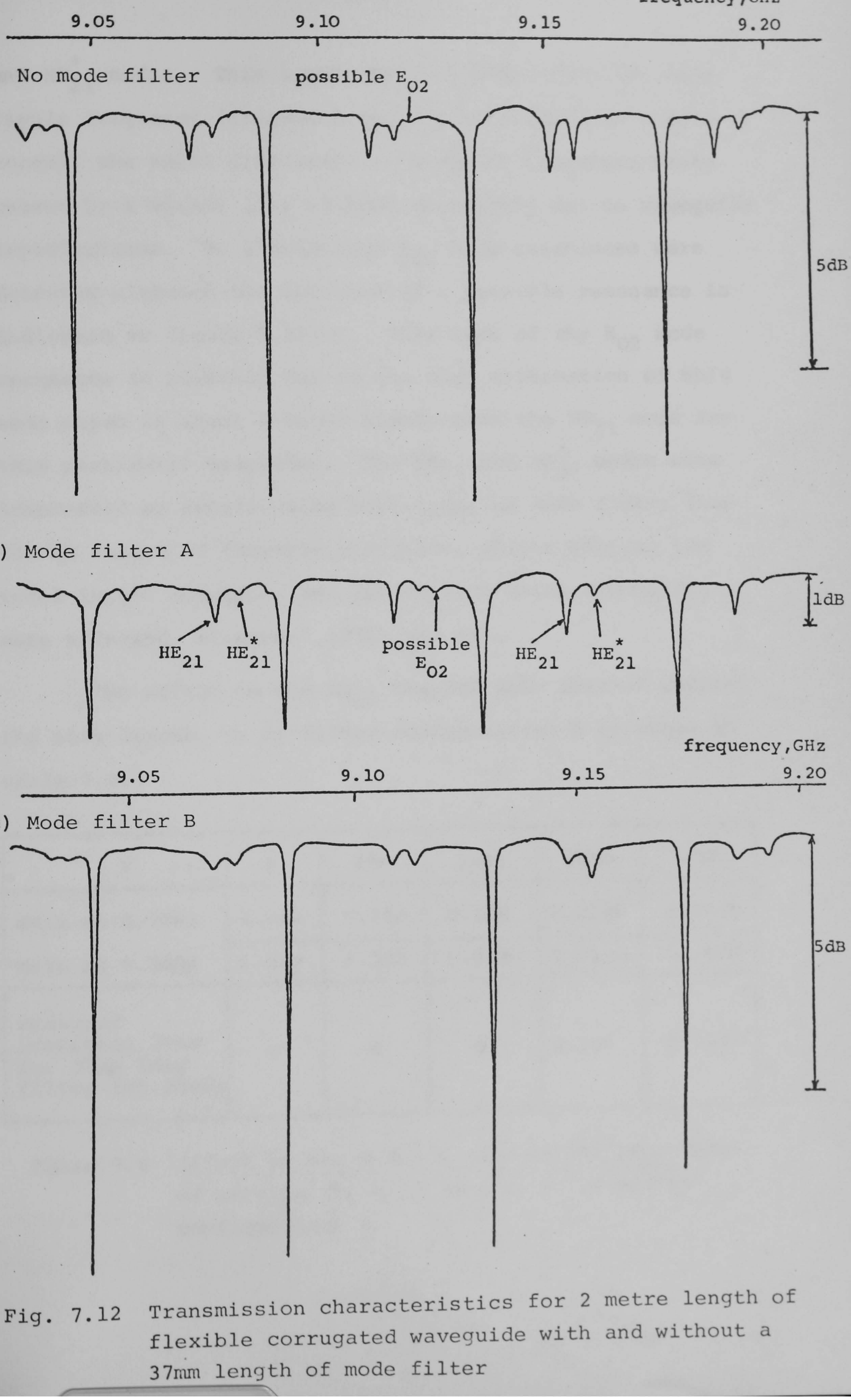

Fig. 7.12 Transmission characteristics for 2 metre length of flexible corrugated waveguide with and without a 37mm length of mode filter

and HE_{21}^{*} modes. This latter pair of modes have the same ripple frequency (frequency spacing of successive resonances), the small difference in resonant frequency being caused by a slight loss of mode degeneracy due to waveguide imperfections. No significant E_{02} mode resonances were detected although the location of a possible resonance is indicated in figure 7.12(a). This lack of any E_{02} mode resonance is probably due to the high attenuation of this mode which is about 4 times higher than the HE_{21} mode for this particular waveguide. The HE_{21} and HE_{21}^{*} modes were identified by substituting both types of mode filter into the 2m length of flexible waveguide, whilst keeping the total length constant, and determining which resonances were affected, figures 7.12(b) and (c).

The effect on the HE_{21} trapped mode loss of varying the slit length, v, of filter configuration B is shown in table 7.4.

V	O	6mm	10mm	12mm	15mm
MRIL at 8.7GHz	1.0dB	0.7dB	0.6dB	0.25dB	0.35dB
MRIL at 9.0GHz	1.5dB	1.3dB	0.6dB	0.35dB	0.25dB
Measured insertion loss for 37mm long filter (±0.05dB)	O	O	O	0.1dB	0.15dB

Table 7.4 Effect on the M.R.I.L. due to the HE_{21} mode of varying the slit length, v, of filter configuration B.

Unlike the H_{01} mode filter there is no *fringing field* effect and the HE_{21} mode attenuation continually increases for increasing slit length. Because of the small insertion loss and the error involved in its measurements using the transmission test method, the results obtained for this parameter can only be interpreted qualitatively. However, the results do suggest v = 10mm to be the optimum size. The insertion loss of this slit dimension was measured using the resonant cavity method and an HE_{11} mode attenuation increase of about 1.4 times was observed. Resonant cavity measurements also indicated that w < 3mm should be adhered to for low insertion loss.

From the current flow patterns of figure 7.3 a slit nearer to $r=r_1$ would be expected to increase the HE_{11} mode attenuation. Alternatively for a slit nearer to $r=r_o$ the HE_{21} mode suppression would be inferior because of the weaker current amplitude. It would therefore appear that $q=\frac{s}{2}$ is an optimum position for this slit configuration.

The degree of HE_{21} mode suppression obtained with the optimum filter dimensions is shown in figure 7.12(c) indicating an HE_{21} mode attenuation increase of about 250 times over that of the theoretical value in the unmodified waveguide.

7.6.3 The composite mode filter

In this sub-section results are presented for the composite mode filter shown in figure 7.6C which combines both slit configurations A and B in the same waveguide

structure. Firstly, measurements are described to determine any change in performance of the individual slit configurations resulting from the presence of the other slit configuration in the same corrugation side wall. Results are then presented for the composite mode filter having the optimum slit dimensions determined from the results of the previous two sub-sections.

A typical set of transmission characteristics is shown in figures 7.13 for both possible configurations of mode filters A and B, together with the results for the composite mode filter having equivalent slit dimensions. Figures 7.13(a) and 7.13(b) show a difference in H_{01} trapped mode loss of order 10% between filter combinations A+B and B+A. This is probably caused by the modification of the H_{01} mode current flow by filter B changing the performance of filter A. The transmission characteristics for the composite filter, figure 7.13(c) show the H_{01} trapped mode loss to be significantly reduced over that obtained for the individual mode filters. Physically it is probable that the side slits (B) of the composite filter constrain the H_{01} mode current flow near to $r=r_1$ whilst slits (A) will cause much of the remaining unsuppressed current to flow near to $r=r_o$. This *conflict* in current flow would result in slit A capturing more of the current flow and slit B contributing some extra H_{01} mode suppression. It should be pointed out that the dimensions of slit A used in the above investigation is not the optimum, but served to demonstrate the difference in

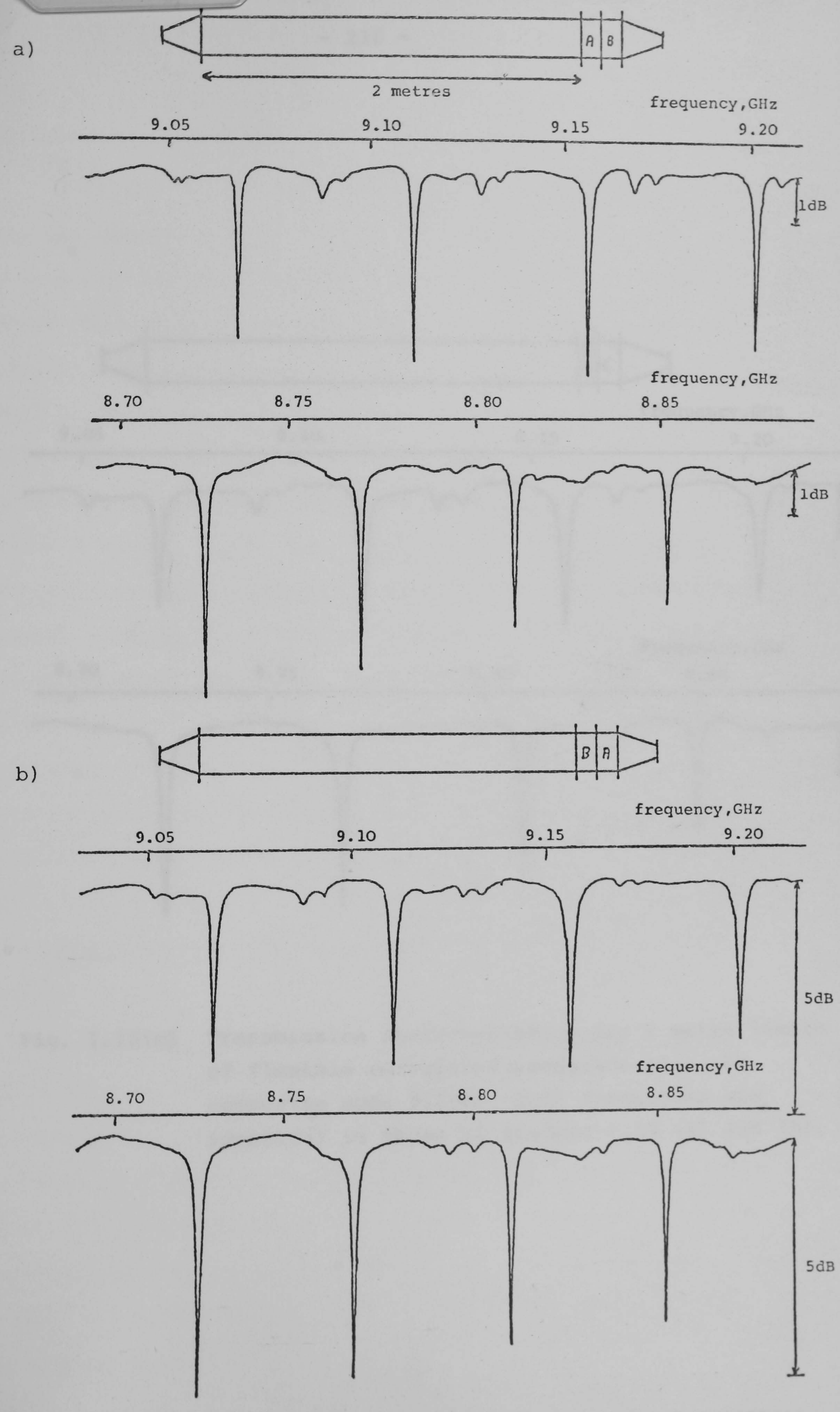

Fig. 7.13 Transmission characteristics for the 2 metre length of flexible corrugated waveguide with both combinations of mode filters A and B

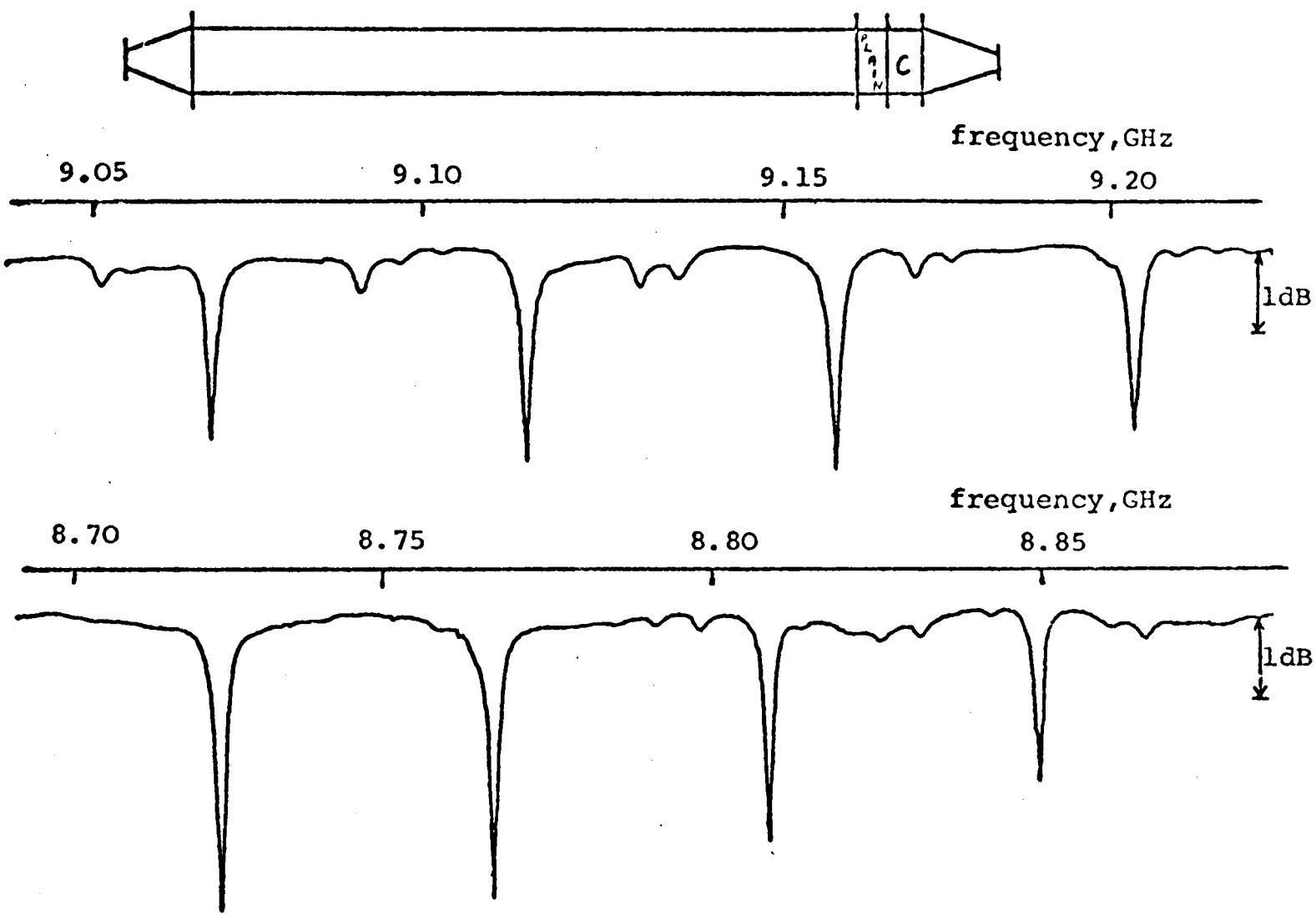

Fig. 7.13(c) Transmission characteristics for 2 metre length of flexible corrugated waveguide plus the composite mode filter. Slit dimensions are identical to those of figures 7.13 (a) and (b).

performance of the composite filter design.

Figure 7.14 shows the transmission characteristics for the composite mode filter having the optimum slit dimensions for mode suppression in the region of 9.2GHz, these dimensions being obtained from the results of the previous two sub-sections. Figure 7.14 indicates an H_{01} mode attenuation over the filter section of about 17.5dB/m, an increase over the theoretical attenuation in the unmodified corrugated waveguide of about 580 times. This shows a useful improvement in H_{01} mode attenuation over the 400 times increase obtained with slit configuration A alone. Comparison of the transmission characteristics obtained using these two mode filters is shown in figure 7.15, the total waveguide and mode filter lengths being the same in each case. The improvement in the H_{01} mode suppression over the 9.2GHz region obtained with the composite mode filter is evident, also evident is the HE_{21} mode suppression. For comparison, figure 7.15 also shows the unfiltered transmission characteristic of the waveguide.

To improve the H_{01} mode suppression in the region of 8.7GHz the dimension x of slits A should be increased to 6mm in accord with the results presented in figure 7.8. Consequently in a practical waveguide feeder employing two mode filter sections the x dimension of slits A should be slightly different between the two filter sections in order to achieve high H_{01} mode suppression over a wider frequency band.

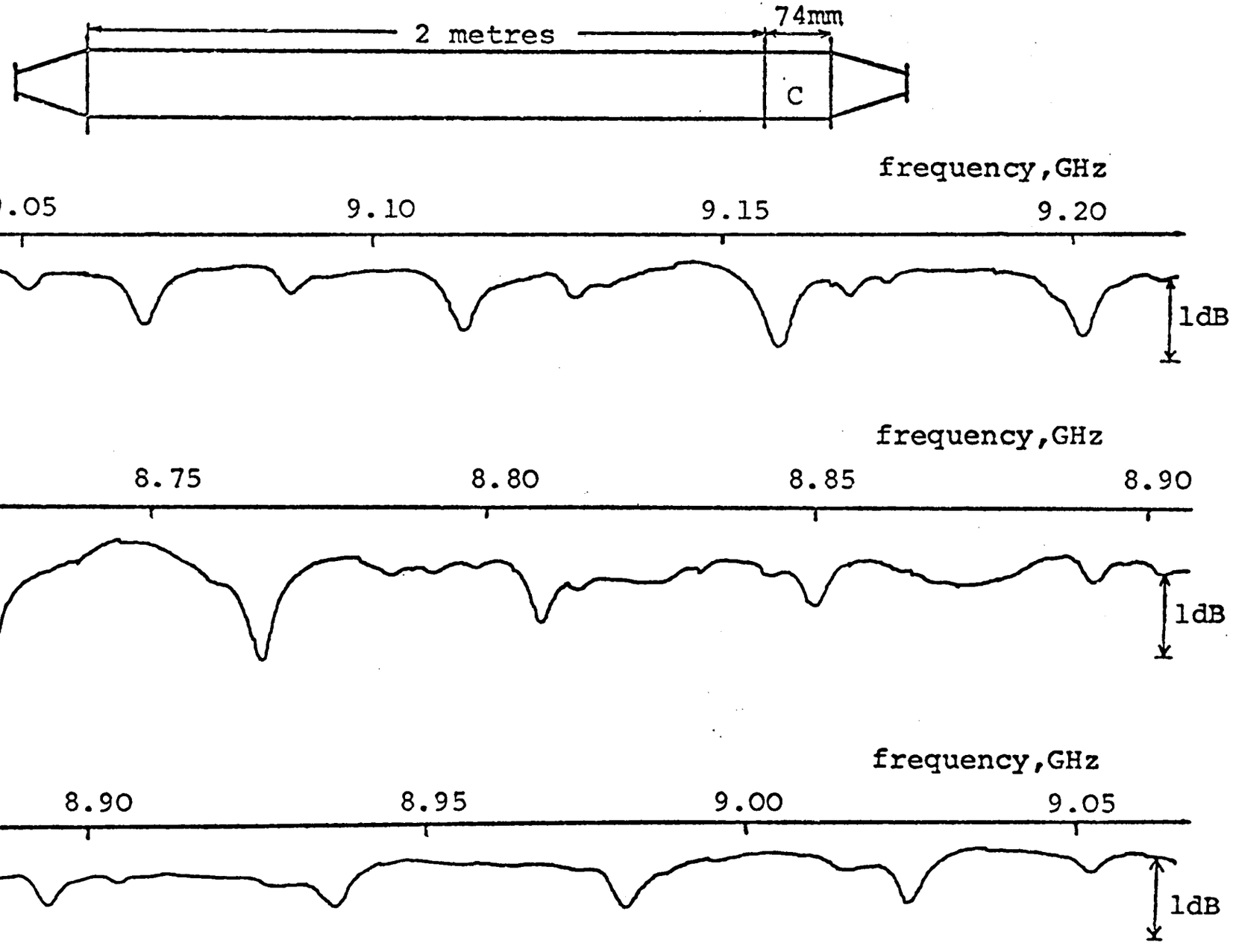

Fig. 7.14 Transmission characteristics for 2 metre length of flexible corrugated waveguide plus a 74mm length of composite mode filter
Slit dimensions: x=5mm, y=1.5mm, v=10mm, w=1.5mm.
frequency scale not an amplitude reference line

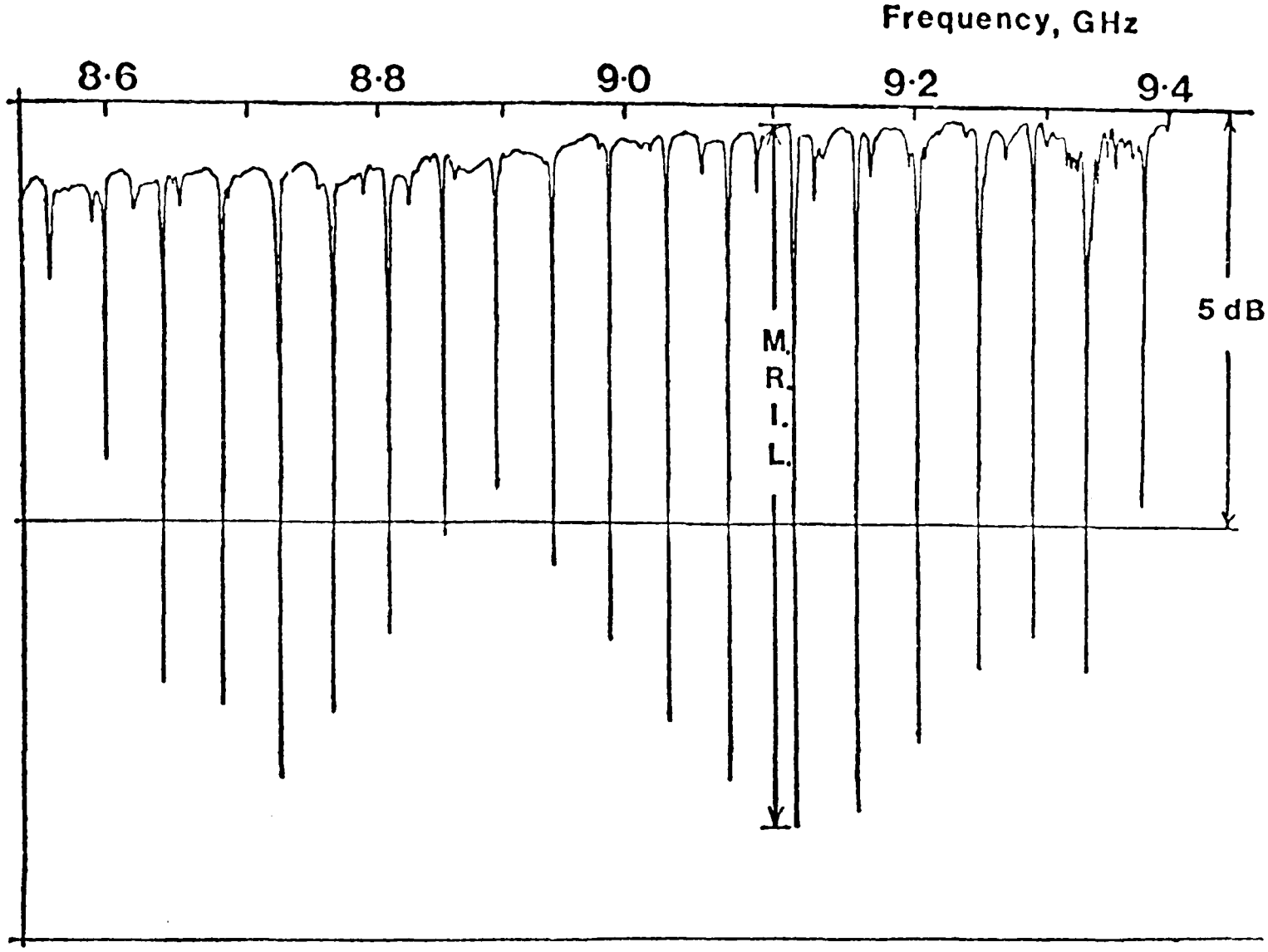

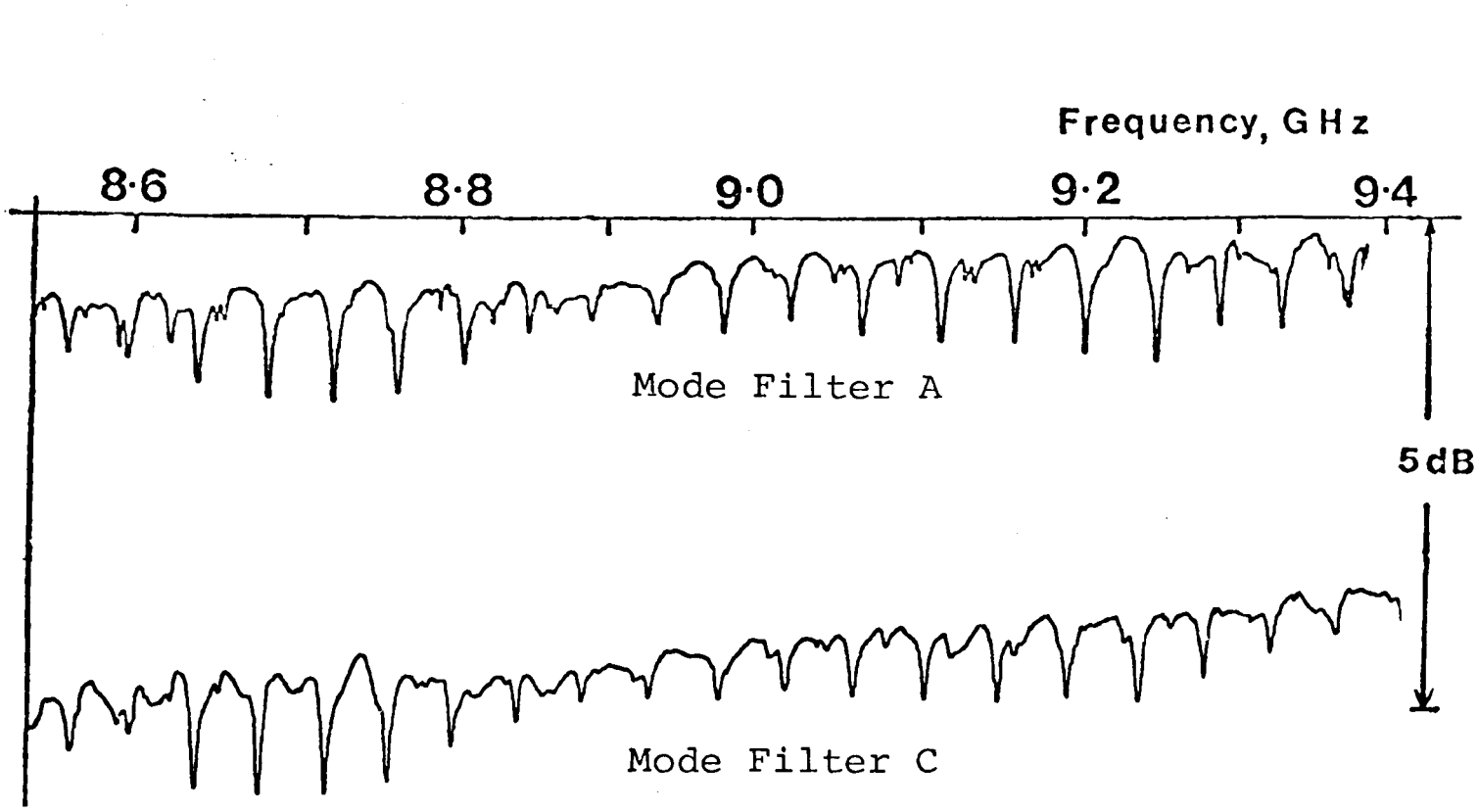

Fig. 7.15 Comparison of the measured transmission characteristics for the 2 metre length of flexible corrugated waveguide with and without the mode filters of optimum design

frequency scale not an amplitude reference line

The optimum dimensions for the mode filter slits described in this section are only strictly applicable to the flexible corrugated waveguide used in this investigation. For example, the optimum slit dimension x for filter configuration A produces the maximum electric field density in the slit, a condition which must depend on the corrugation dimensions. This was found to be the case when a mode filter of configuration A was constructed from the thermal contraction waveguide of figure 4.3, this waveguide having the same r_1 and similar $\frac{r_1}{r_o}$ to that of the flexible corrugated waveguide but with a different ridge width and corrugation periodicity. When this waveguide was added to the flexible waveguide run the optimum H_{01} mode suppression was found to occur at a considerably higher frequency than that obtained with the flexible waveguide mode filter of equivalent slit dimensions. The *degree* of mode suppression obtained may also depend on the corrugation dimensions and so in a practical system it may be necessary to change the corrugation dimensions in the mode filter section to achieve optimum mode suppression over the desired frequency band.

The study described in this section has shown the dependence of the various mode filter parameters in determining the mode filter performance. It has also demonstrated the development procedure required to achieve optimum filter performance and shown the order of mode suppression that can be expected from this type of mode filter.

7.7 THE USE OF THE LOW INSERTION LOSS MODE FILTER IN A CORRUGATED WAVEGUIDE ANTENNA FEEDER

In this section consideration is given to the main factors involved in the use of the low insertion loss mode filter to maintain operation of a corrugation waveguide antenna feeder below the specified maximum higher order mode level.

The primary consideration in using the mode filter is to determine the minimum length required to achieve the desired degree of higher order mode suppression. Consider first the case when the corrugated waveguide is operated with single mode input and output waveguides. Assuming that the level of higher order mode in the waveguide run is known or can be determined equation 4.3 can be rearranged to yield the required filter length, L_f, to achieve an M.R.I.L. of less than 0.1dB. This relationship is given by:-

$$L_f = \left[\frac{1500 \times 10^{-\left(\frac{C_m}{10}\right)}}{\alpha_m} - L \right] \frac{1}{A_{fm}} \qquad (7.1)$$

where: C_m is the power coupling level of the higher order mode (dB);

α_m is the attenuation of the higher order mode in the corrugated waveguide (dB/m);

L is the total length of the corrugated waveguide feeder (m);

A_{fm} is the higher order mode attenuation increase factor produced by the mode filter ($A_{fm} >> 1$).

In most cases application of this equation for the H_{01} mode will yield the minimum length required for the composite mode filter design. As an example table 7.5 shows the required filter length as a function of mode coupling level for several lengths of the overmoded corrugated waveguide design having a total of 4 propagating modes and an operating frequency of 9GHz. The higher order mode attenuation, α_m, being obtained from figure 7.16 and A_{fm} being estimated from the experimentally obtained values presented in the previous section. For a flexible waveguide having a number of waveguide bends or poor mechanical tolerances resulting in a higher order mode level of -20dB the mode filter length required is not unrealistically long.

In the alternative situation where the corrugated waveguide is operated with one end open or directly feeding a corrugated horn the trapped mode effect does not occur and the calculation of the required mode filter length takes a more simplified form. It will be shown in chapter 10 that a mode coupling level of less than about -35dB is required in order not to significantly degrade the antenna system performance. Therefore if the level of higher order mode in the waveguide is $-C_m$ dB the mode filter must introduce a higher order mode attenuation of $(35-C_m)$dB. With a knowledge of the higher order mode attenuation, figure 7.16, and the attenuation increase factor of the mode filter, the filter length is obtained from the following equation:-

C_m \ L	H_{01}		HE_{21}		E_{02}	
	100m	50m	100m	50m	100m	50m
-15dB	5.4m	5.5m	3.0m	3.3m	0.7m	0.9m
-20dB	1.6m	1.7m	0.7m	0.9m	-	0.2m
-25dB	0.4m	0.5m	-	0.2m	-	-
-30dB	-	0.08m	-	-	-	-
	A_{fm} = 500		A_{fm} = 250		A_{fm} = 250	

Table 7.5 Estimated mode filter lengths required to achieve a trapped mode resonance loss of less than 0.1dB.

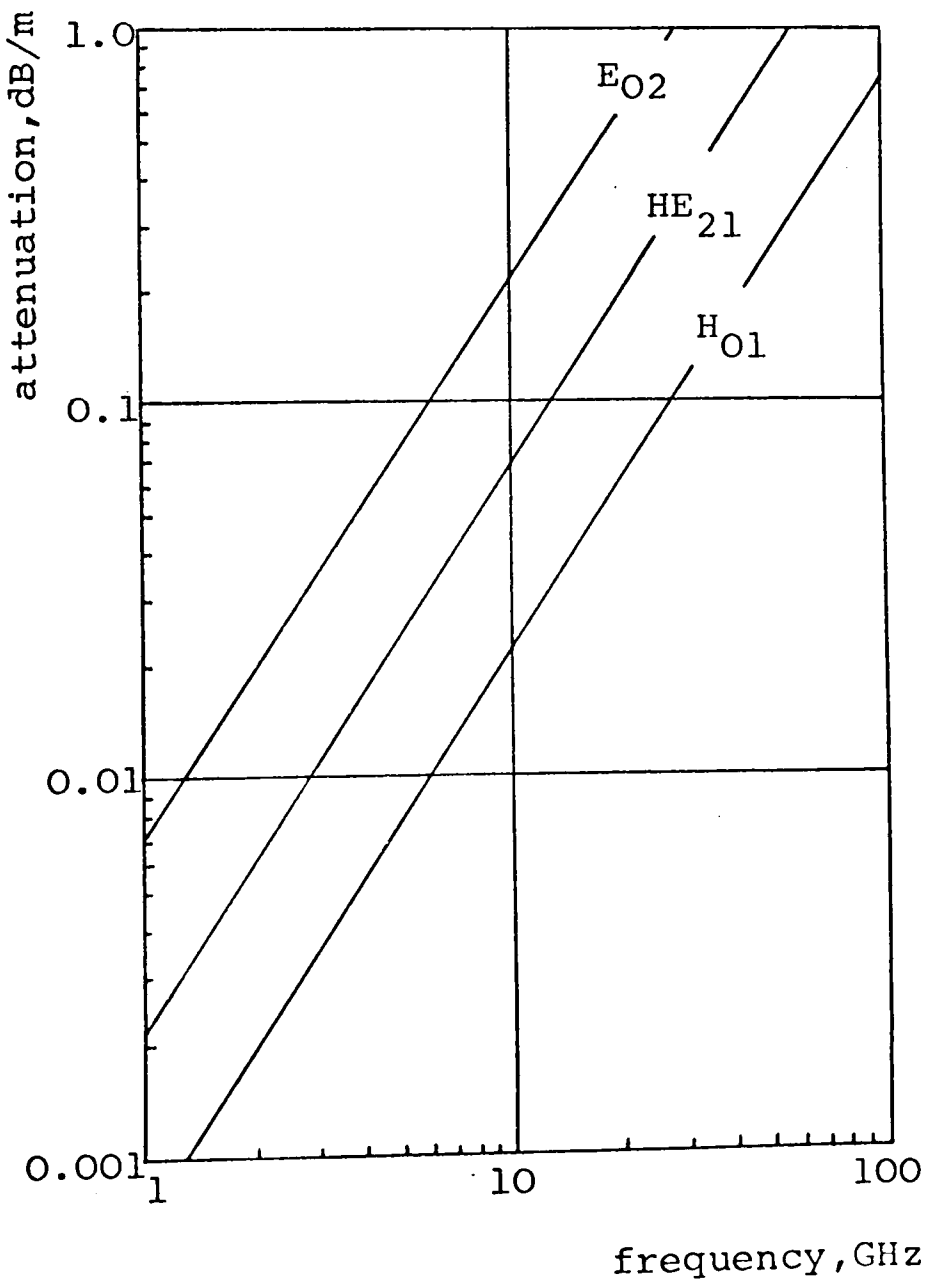

Fig. 7.16 Higher order mode attenuation corresponding to waveguide design of figure 2.8.

$$L_f = \frac{(35-C_m)}{\alpha_m A_{fm}} \qquad (7.2)$$

Both equations 7.1 and 7.2 require a knowledge of the level of higher order mode at the output of the waveguide run and ideally this would be measured for the particular waveguide under consideration, but for commercial use of the corrugated waveguide feeder this is not practical. However, Karbowiak < 4 > has shown that for statistically random higher order mode coupling the *average* power converted into the higher order mode at the output of the waveguide is a *constant* proportion of the received main mode power. Therefore for a given size of antenna feeder waveguide, with given mechanical tolerances, measurement of the levels of higher order modes generated over several different lengths would yield the *average* level of coupled mode power. So long as the waveguide lengths measured were sufficiently long to ensure the coupling process was *random* the average coupling level obtained represents the coupling level *expected* for *any* length of waveguide which was manufactured with the same degree of mechanical tolerances. This expected mode coupling level can then be used in equations 7.1 and 7.2 in order to estimate the length of mode filter required.

When the mode filter is to be used with a relatively cheaply manufactured corrugated waveguide of poor mechanical tolerances a rather long length of mode filter is required, as demonstrated by the results of table 7.5 for a -15dB coupling level. However, construction of the flexible

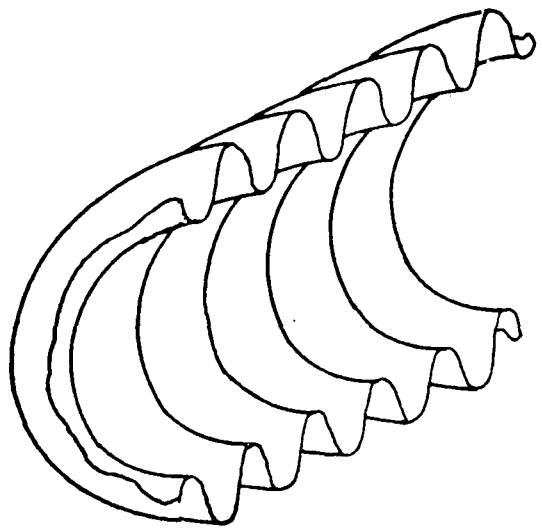

Semi-circular shell forming one half of the flexible corrugated waveguide

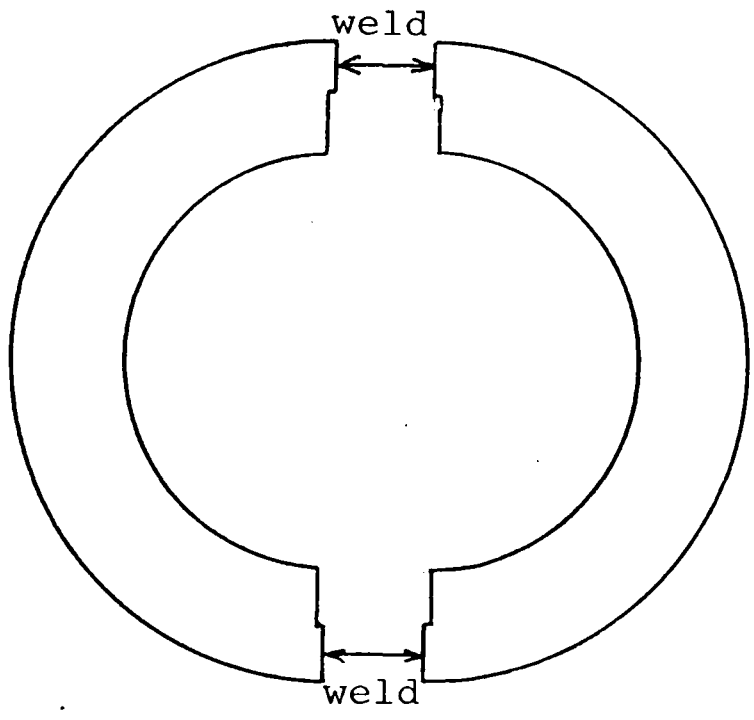

Two semi-circular shells welded together to form the waveguide

Fig. 7.17 Proposed method of construction for continual mode suppression flexible corrugated waveguide

corrugated waveguide from two semi-circular shells welded together would enable the H_{01} mode filtering slit to be incorporated into the manufacture, and this is shown in figure 7.17. The resistive loading for the slit could be incorporated into the plastic compound moulded around the outside of the waveguide which is necessary to ensure that the flexible waveguide structure is resistant to microbends and kinks (chapter 5). This form of construction would add little to the production cost, and may well reduce them, as the waveguide only needs to be welded at the bottom half of the corrugations. Consequently it becomes possible to have a flexible corrugated waveguide structure exhibiting continual H_{01} + HE_{21}^{*} mode suppression with an HE_{11} mode attenuation of ≈1.5 times higher than the unmodified structure. Using the results of figure 2.9 (chapter 2) this waveguide would have an attenuation approximately one-half that of the rigid overmoded smooth wall waveguide structure.

7.8 CONCLUSIONS

The presence of higher order modes in the corrugated waveguide and the inability to suppress them without incurring higher HE_{11} mode loss has been a major factor in deterring the use of the corrugated waveguide as a low attenuation feeder. In this chapter a new type of mode filter for use with the overmoded corrugated circular waveguide antenna feeder has been described. The filter has been shown experimentally to increase the higher order mode

attenuation by up to about 500 times whilst introducing a negligibly low insertion loss to the HE_{11} mode. This ability to suppress the higher order modes with negligible insertion loss allows the very low attenuation of the HE_{11} mode in the corrugated waveguide to be practically realised.

The principal application for this mode filter is seen with the flexible form of corrugated waveguide construction, enabling the mode coupling level resulting from waveguide bends to be maintained at an acceptable level. Alternatively a form of flexible waveguide construction has been proposed exhibiting continual H_{01} mode suppression, which would enable a relatively cheaply manufactured flexible corrugated pipe of poor mechanical tolerances to successfully perform as a low attenuation feeder. This flexibility, coupled with an attenuation which is half that of the rigid overmoded smooth wall waveguide and about 7 times lower than flexible elliptical waveguide, suggests that the continual mode suppression corrugated waveguide antenna feeder has a significant performance advantage over its competitors.

The fundamental disadvantage of this type of mode filter is that it constrains the waveguide to single linear polarisation operation. However, in many antenna feeder applications for a flexible waveguide, such as those discussed in chapter 2 under class 3 systems, this is not a disadvantage.

CHAPTER 8

THE MONO-MODE CORRUGATED CIRCULAR WAVEGUIDE

8.1 INTRODUCTION

An alternative approach to overcoming the problems of mode conversion in a flexible corrugated waveguide is to operate it such that only a single mode is propagating. The EH_{11} mode, which is the first mode to propagate in the corrugated circular waveguide, has been shown by Chong <2> to have an attenuation practically the same as the corresponding diameter of smooth wall circular waveguide, for the case when the corrugations are shallow. The EH_{11} mode can be considered to be a perturbed TE_{11} mode in this case and so operating the waveguide with this mode holds little practical performance advantage. In this chapter it will be shown that there exists an optimum corrugation slot depth that enables the HE_{11} mode in a corrugated circular waveguide to be the only propagating mode, a property not previously reported. This region of HE_{11} mono-mode operation is maintained over a frequency band of about 8% and the waveguide exhibits an attenuation similar to that of the overmoded smooth wall circular waveguide propagating the TE_{11} mode. The advantage of this design of corrugated waveguide is that it enables a flexible form of waveguide construction to exhibit low attenuation coupled with mono-mode, dual polarisation, operation.

In section 8.2 the theoretical design and predicted

performance for the mono-mode corrugated waveguide is presented. Firstly, the design theory and predicted performance for the mono-mode corrugated waveguide exhibiting an optimially large bandwidth is described, this design including the effect of using a rounded corrugation slot profile which might be necessary in a practical flexible waveguide construction. A method is then described of increasing the size of the operating band whilst still retaining the desirable properties of mono-mode operation.

Section 8.3 describes an experimental study to verify the existence of the mono-mode operating region and to compare the measured HE_{11} mode attenuation with that predicted in section 8.2.

Finally in section 8.4, the use of the mono-mode corrugated waveguide as an antenna feeder is considered and the conclusions resulting from this study are presented.

8.2 DESIGN STUDY FOR HE_{11} MONO-MODE OPERATION OF A CORRUGATED CIRCULAR WAVEGUIDE

The HE_{11} mono-mode region for the corrugated circular waveguide lies between the slow-wave condition of the EH_{21} mode and the low frequency cut-off of either the H_{01} or HE_{21} modes, depending on the value of $\frac{r_1}{r_o}$ used. When the EH_{21} mode is in the slow-wave region ($\bar{\beta}>1$) it can be considered non-propagating as it possesses a very high attenuation. Figure 8.1 shows, as a function of $\frac{r_1}{r_o}$, the

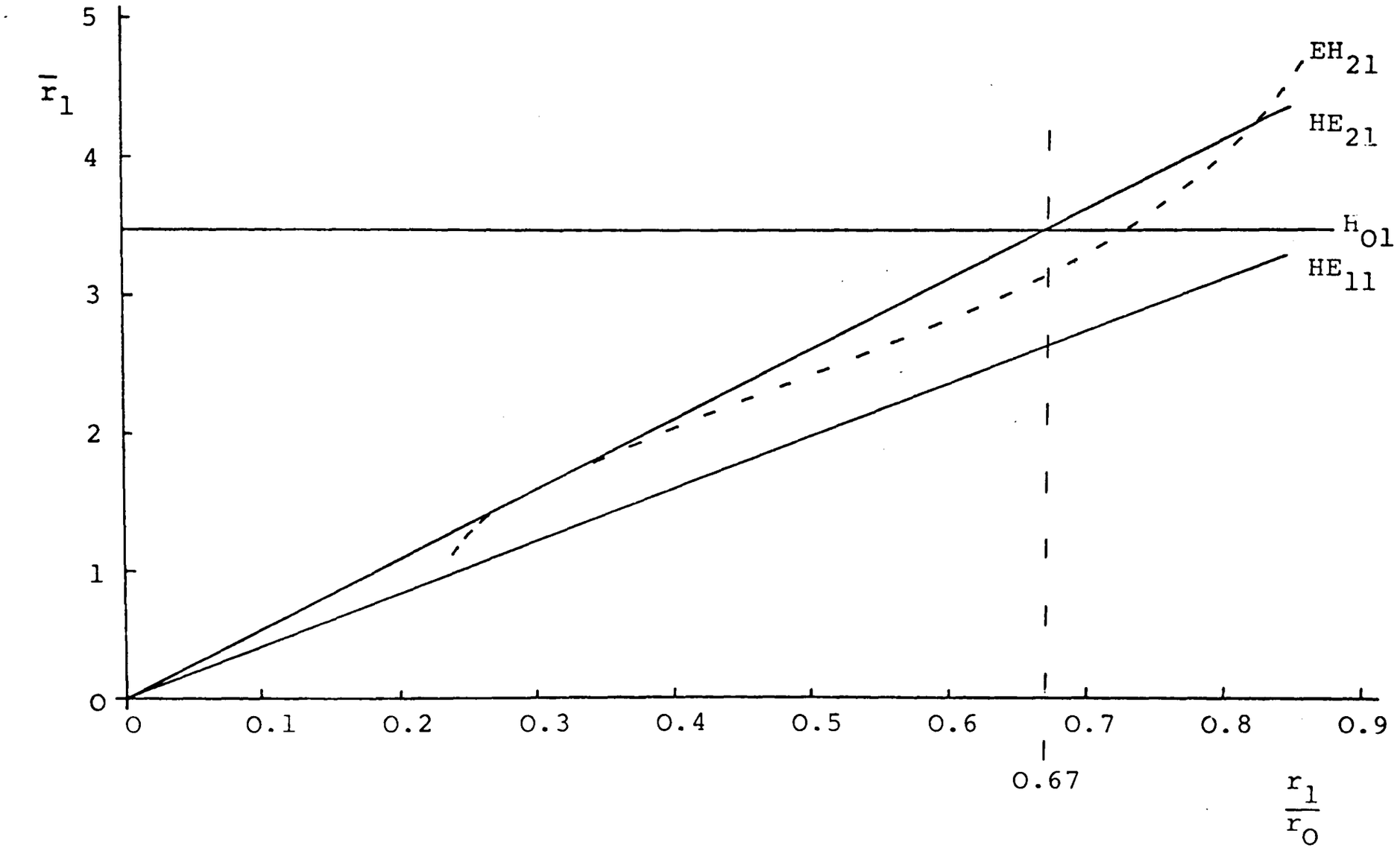

Fig. 8.1 Approximate low frequency cut-off for HE_{11}, H_{01}, and HE_{21} modes together with the slow-wave condition for the EH_{21} mode, shown as a function of r_1/r_0

approximate low frequency cut-off of the relevant waveguide modes together with the slow-wave condition for the EH_{21} mode. The existence of the mono-mode region is seen to occur for $0.4 < \frac{r_1}{r_o} < 0.725$, the widest bandwidth† occurring over the range $0.62 < \frac{r_1}{r_o} \leq 0.67$. The smaller the value of $\frac{r_1}{r_o}$ used the more dispersive the operating point of the HE_{11} mode becomes, resulting in a deterioration of the delay distortion of the waveguide. The largest value of $\frac{r_1}{r_o}$ should therefore be used and this implies a value of 0.67.

The curves shown in figure 8.1 are for a waveguide with a rectangular corrugation profile, but in a practical form of flexible waveguide construction it is probable that this profile will be rounded. The effect of this rounded corrugation profile will be to slightly modify the surface impedance presented by the corrugations, which in turn will modify the propagation and attenuation characteristics of the modes. Using the surface impedance model for the corrugated waveguide and a staircase approximation to the corrugation profile Al-Hariri <3> has studied this effect and shown that for non-rectangular corrugations a deeper slot depth is required to produce a given surface impedance. Using a computer program developed by Al-Hariri the effect of using a rounded corrugation profile on the optimum value of $\frac{r_1}{r_o}$ for mono-mode operation has been quantified. The profile used is shown in figure 8.2, having similar ridge dimensions to

†In this chapter the term bandwidth will refer to the frequency band over which the waveguide remains single mode.

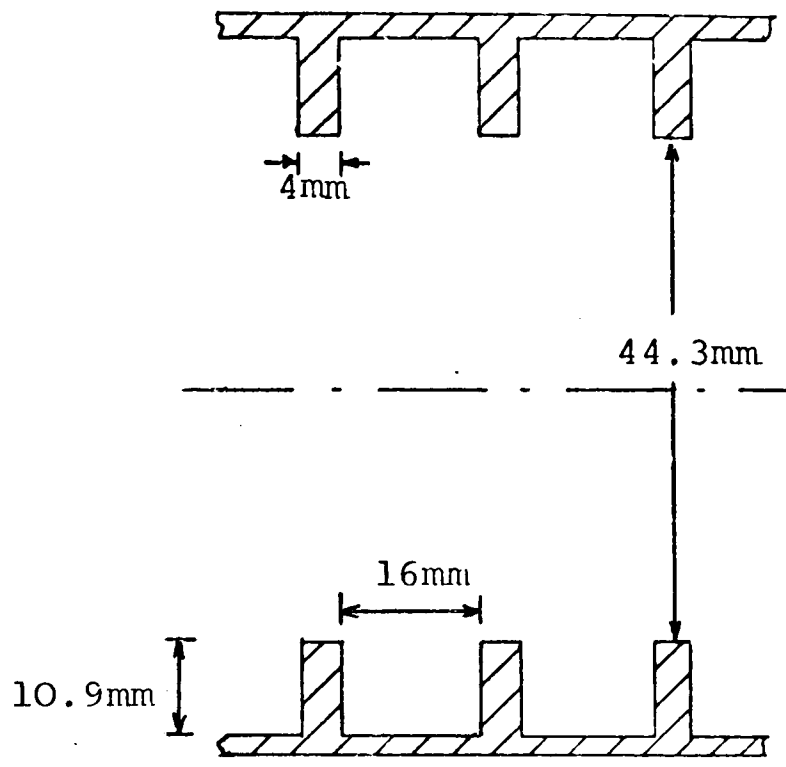

a) Rectangular slot profile

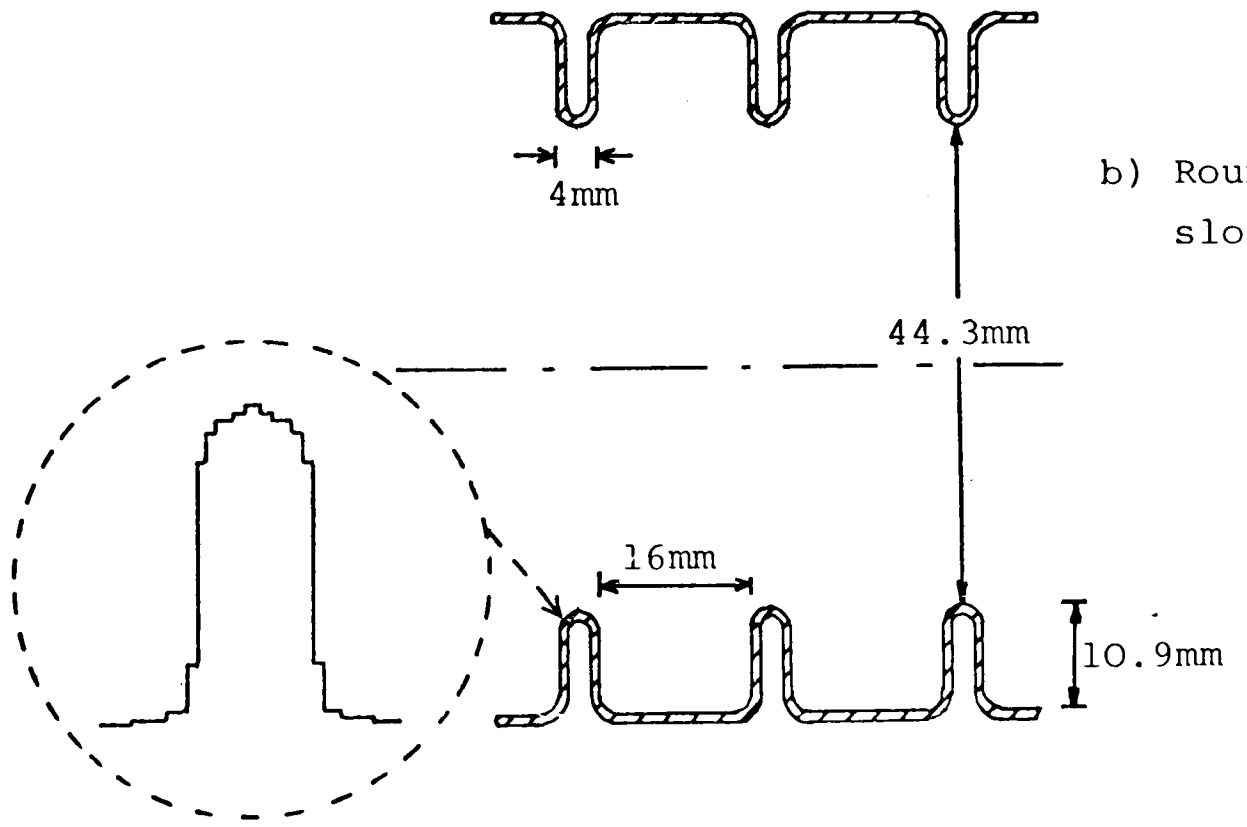

b) Rounded slot profile

Fig. 8.2 Corrugation profiles used in the 7GHz design of mono-mode corrugated waveguide

the overmoded flexible corrugated waveguide described in chapter 5 and so it is representative of a profile that can be practically manufactured. Figure 8.3 shows the low frequency cut-off of the HE_{21} and H_{01} modes and the slow-wave condition for the EH_{21} mode, for both the rectangular and rounded corrugation profiles. This result shows that for the rounded profile $\frac{r_1}{r_o} = 0.66$ is required for optimum bandwidth and that a significant loss in bandwidth would result if $\frac{r_1}{r_o} = 0.67$ were used.

The curves of figures 8.1 and 8.3 are only approximate, as they have been derived using the surface impedance model, but they serve to identify the $\frac{r_1}{r_o}$ value required. To determine the performance of the mono-mode corrugated waveguide a theoretical design study using space-harmonics was undertaken for $\frac{r_1}{r_o} = 0.66$, an operating frequency of 7.15GHz being chosen. The waveguide dimensions used are shown in figure 8.2(a), the ridge width of 4mm being a practical size for a flexible form of waveguide construction at this frequency. The slot width was obtained by optimising to give the lowest HE_{11} mode attenuation subject to the constraint that the H_{01} mode low frequency cut-off was not significantly lowered. Increasingly large slot widths allow the H_{01} mode, normally bounded at $r=r_1$, to begin to penetrate the corrugations resulting in a reduction of the mode cut-off frequency < 2 >. The largest slot width that could be used was found to be 16mm, this corresponding to a corrugation periodicity of $0.36\lambda_g$ (where λ_g is the guide wavelength).

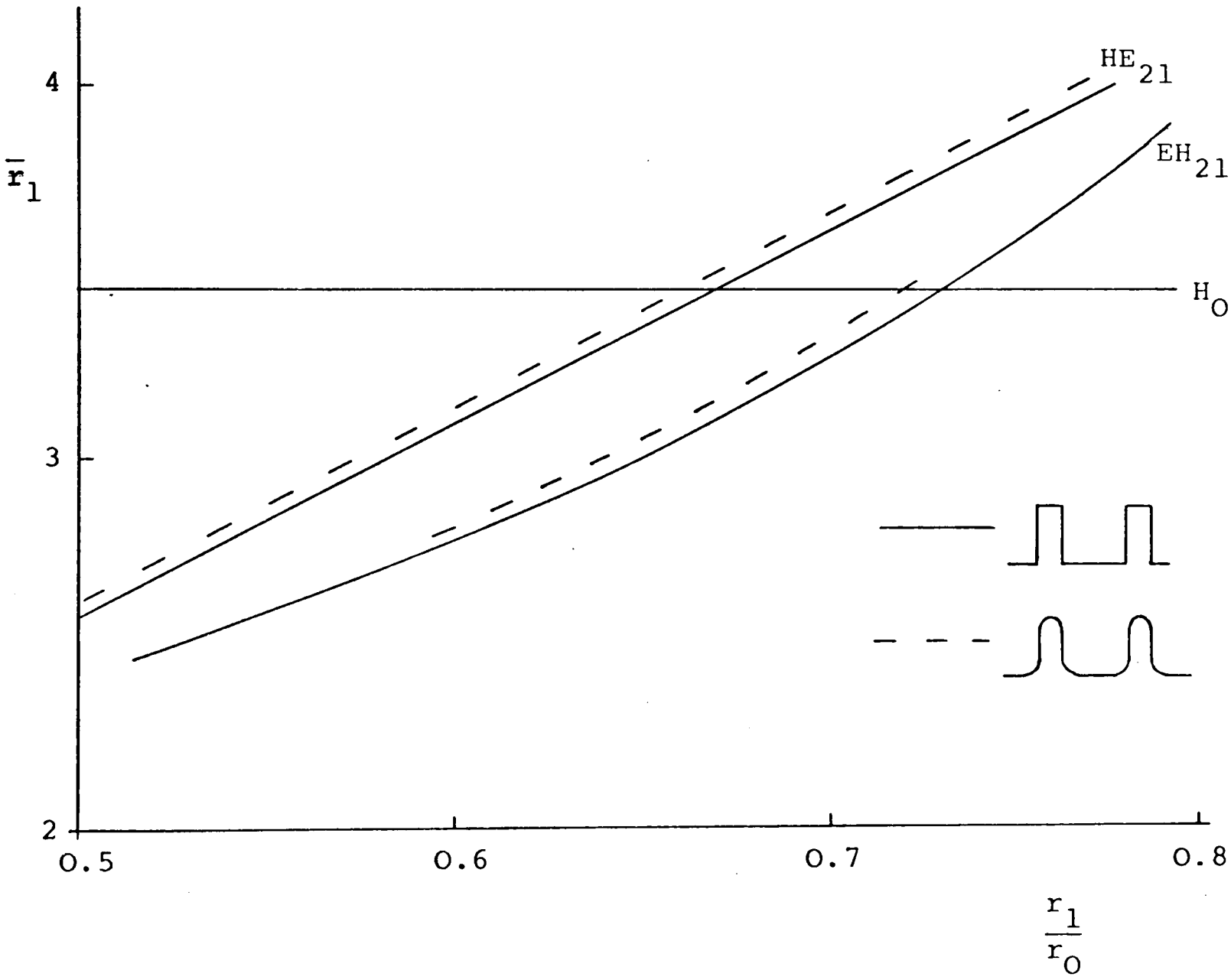

Fig. 8.3 Low frequency cut-off of the HE_{21} and H_{01} modes and the slow-wave condition for the EH_{21} mode as a function of r_1/r_0 for both the rounded and rectangular corrugation profiles

The propagation and attenuation characteristics for the waveguide of figure 8.2(a), obtained using the space-harmonic analysis, are shown in figures 8.4 and 8.5. Figure 8.4 clearly shows the single mode operating region which for this design has a bandwidth of 8.4%, when calculated from the EH_{21} mode slow-wave condition to the H_{01} mode low frequency cut-off. The attenuation characteristics, figure 8.5, show the high attenuation of the EH_{21} mode above the slow-wave condition, justifying the assumption that this mode can be considered non-propagating. This figure also shows that the HE_{11} mode attenuation varies considerably over the operating band, suggesting that some form of signal equalisation may be required for practical operation of the waveguide.

A similar design of mono-mode corrugated waveguide with a 1.5mm ridge width and re-optimised slot width yielded no practical reduction in attenuation of the HE_{11} mode. This suggests that unlike the overmoded corrugated waveguide there is no attenuation advantage in using the thin ridge width obtainable with a rigid form of waveguide construction.

The percentage change in the propagation and attenuation characteristics of the rectangular corrugation profile waveguide resulting from the use of a rounded corrugation profile can be determined by comparing the surface impedance derived characteristics for both waveguide types. Using this data the performance of the rounded corrugation profile waveguide, shown in figure 8.2(b), can

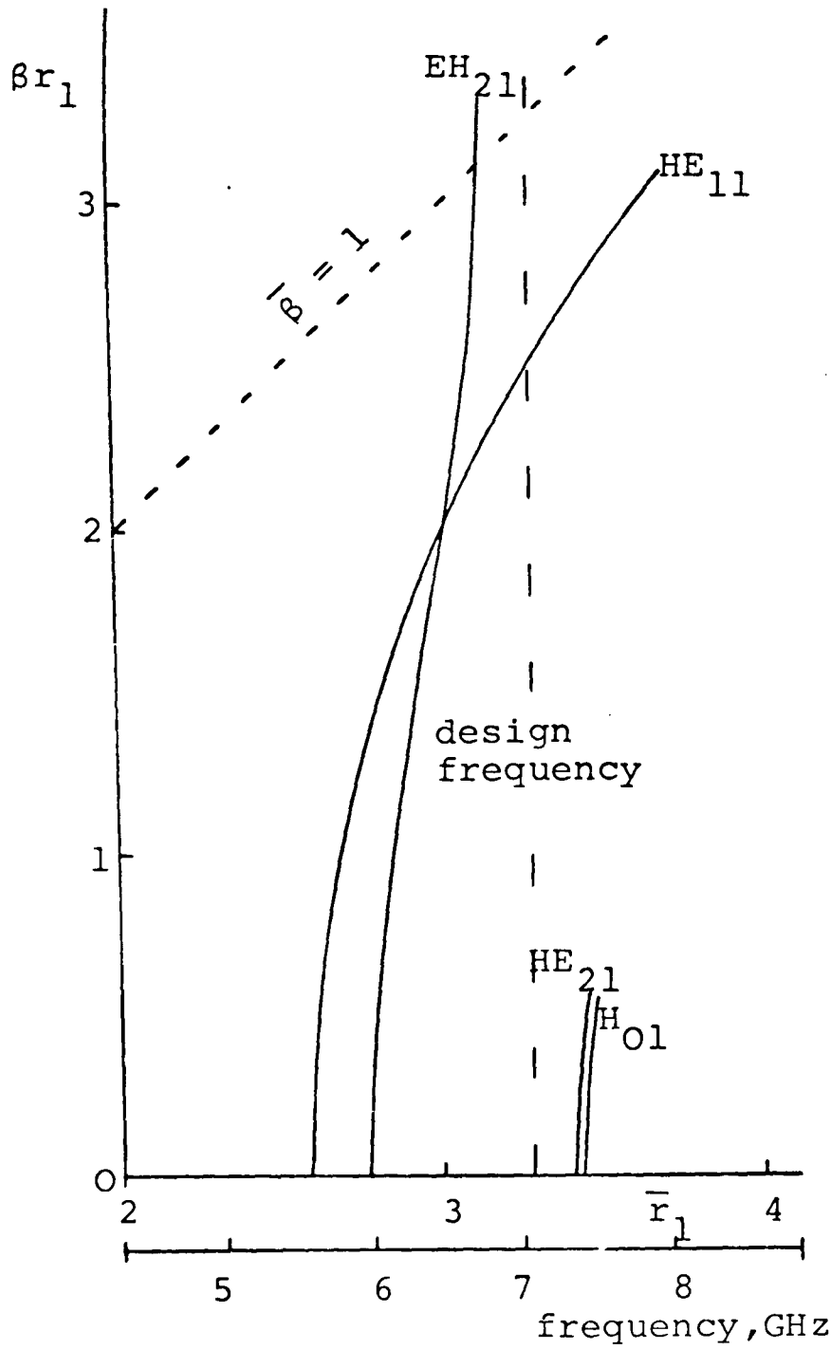

Fig. 8.4 Propagation characteristics for the mono-mode corrugated waveguide shown in figure 8.2(a)

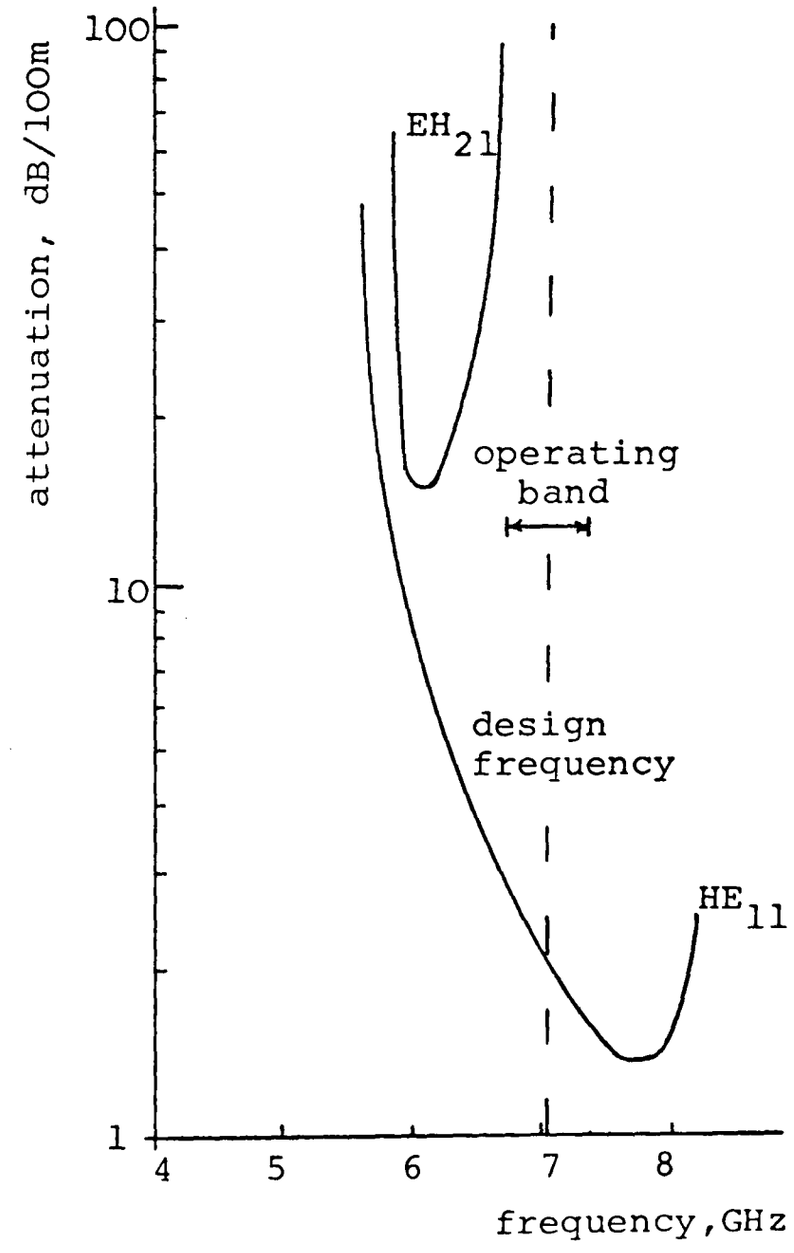

Fig. 8.5 Attenuation characteristics for the mono-mode corrugated waveguide shown in figure 8.2(a)

be estimated from the space-harmonic derived results for the rectangular corrugation profile waveguide of figure 8.2(a). The results obtained for the waveguides shown in figure 8.2 suggest that a negligible change in attenuation and bandwidth performance results from the use of the rounded corrugation profile, the main effect being to very slightly increase (~1.5%) the bandwidth centre frequency.

Figure 8.6 shows the HE_{11} mode attenuation at the mid-band frequency for a copper mono-mode corrugated waveguide, plotted as a function of the design frequency. Shown for comparison are the attenuations of the rigid rectangular, smooth wall circular, flexible elliptical and overmoded corrugated circular copper waveguides. The results suggest that the mono-mode corrugated waveguide has a similar attenuation to the overmoded smooth wall circular waveguide but it has the advantage of single mode operation and a flexible form of construction. In addition the mono-mode corrugated waveguide has an attenuation lower than any of the single mode waveguide structures at present used as antenna feeders.

A summary of the design parameters for HE_{11} mono-mode operation in a flexible corrugated circular waveguide, exhibiting optimial attenuation and bandwidth performance, are given below.

$$r_1 = \frac{0.158}{f_o} \text{ (m)}, \quad \text{where } f_o \text{ is the design frequency in GHz}$$

$$\frac{r_1}{r_o} = 0.66$$

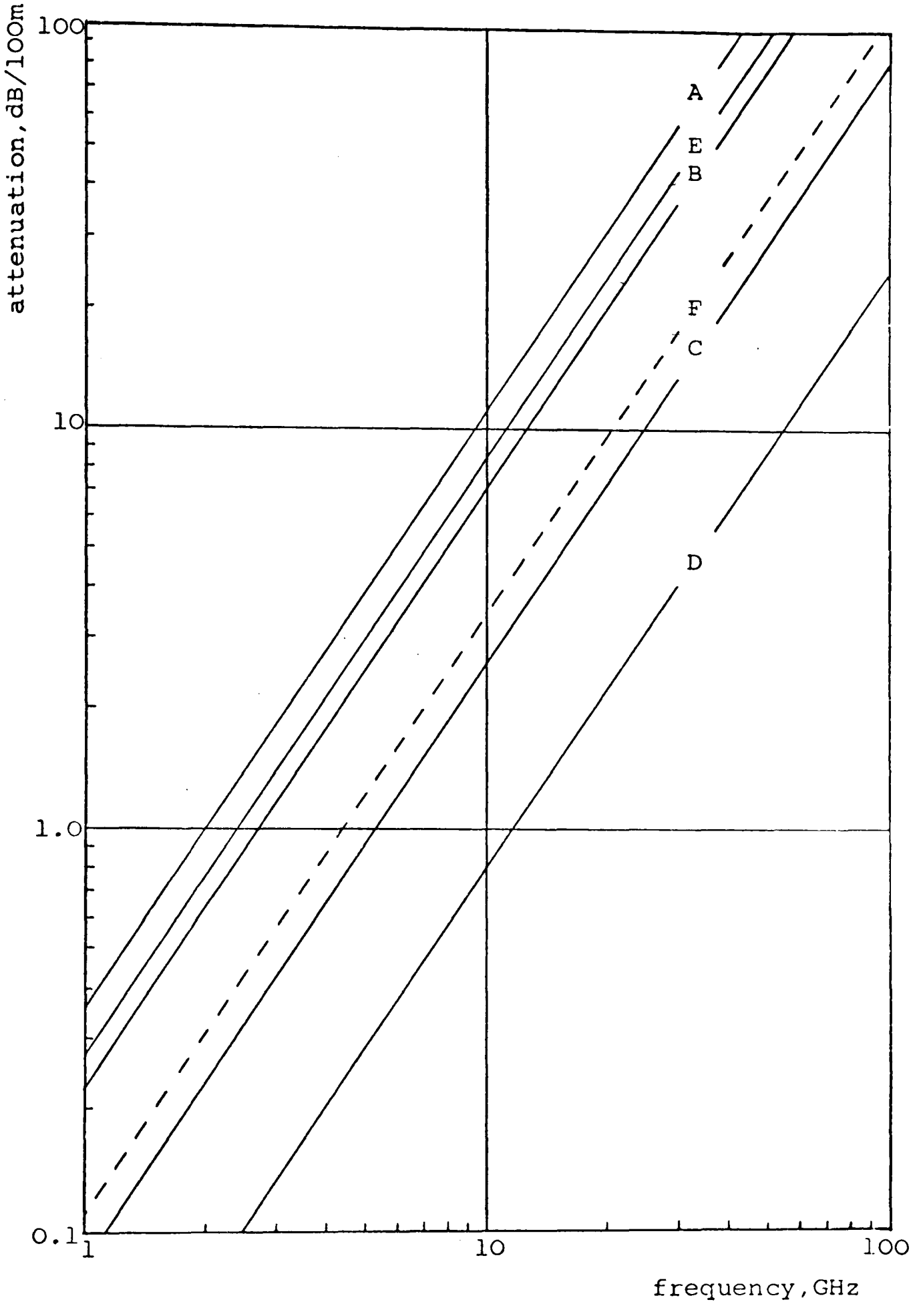

Fig. 8.6 Comparison of the mono-mode corrugated waveguide attenuation with various other copper waveguides for fixed electrical operating conditions.

A Rectangular waveguide, TE_{10} mode, single mode

B Smooth wall circular, TE_{11} mode, single mode

C Smooth wall circular, TE_{11} mode, 3 propagating modes

D Corrugated circular, HE_{11} mode, 4 propagating modes

E Flexible elliptical, TE^{e}_{11} mode, single mode

F Mono-mode corrugated circular, HE_{11} mode, single mode

$\lambda_g = 2.468 r_1$ (m)

corrugation periodicity = $0.36\lambda_g$

slot width = $0.29\lambda_g$

In view of the dispersive nature of the HE_{11} mode at the mono-mode operating frequency (figure 8.4) a study of the delay distortion of this waveguide has been made. The delay distortion is the rate of change of group delay and is a measure of the time between receiving two signals of different frequencies sent simultaneously. When the signal is modulated (A.M., F.M., P.C.M.) these two signals represent the upper and lower sidebands and so a large delay distortion in a transmission system will result in distortion of the demodulated signal < 4 >. The delay distortion of the mono-mode corrugated waveguide for fixed electrical operating conditions (corresponding to figure 8.6) is shown as a function of the design frequency in figure 8.7, where comparison is made with the performance of other types of antenna feeder. Clearly, the mono-mode corrugated waveguide exhibits an inferior delay distortion performance which for long lengths of waveguide could further limit the operating bandwidth.

For the portable antenna communications systems, where the use of the flexible mono-mode corrugated waveguide would exhibit the greatest advantage, the bandwidth for mono-mode operation of about 8% is generally adequate (table 2.2 of chapter 2). However, if the waveguide is to

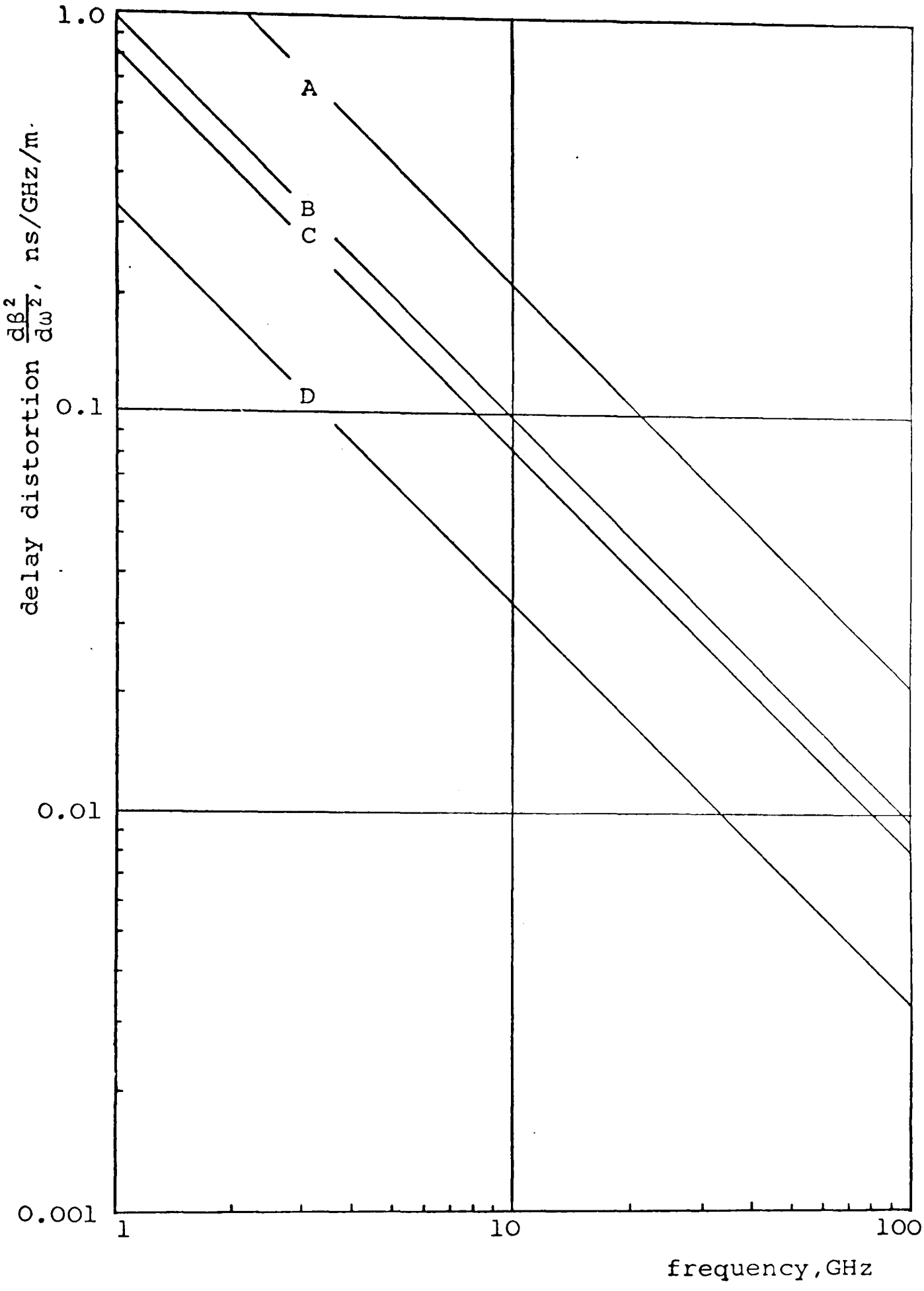

Fig. 8.7 Delay distortion for fixed electrical operating conditions

Waveguide types:

A Mono-mode corrugated circular, HE_{11} mode, $\frac{f}{f_c}$ =1.25

B Single mode smooth wall circular, TE_{11} mode, $\frac{f}{f_c}$ =1.35

C Overmoded corrugated circular, HE_{11} mode, $\frac{f}{f_c}$ =1.75

D Overmoded smooth wall circular, TE_{11} mode, $\frac{f}{f_c}$ =2.0

be used as a feeder for microwave relay systems (class 2 of table 2.2) a bandwidth of order 10% is generally required. In view of the high EH_{21} mode attenuation, it would appear possible to extend the bandwidth of *mono-mode* operation into the fast-wave region of the EH_{21} mode. To assess the typical coupling level figure 8.8 shows, as a function of frequency, the EH_{21} mode coupling coefficient for the waveguide of figure 8.2(a) resulting from a 1 metre radius waveguide bend. When the HE_{11} and EH_{21} modes become degenerate there is complete *energy shuttling* between these modes < 4 >. This effect must be avoided and so the degenerate frequency sets an absolute lower limit for the *mono-mode* operating band. By taking the lower frequency limit of operation to be 1.5% above the degenerate frequency figure 8.8 indicates that the peak EH_{21} mode coupling level, resulting from the several waveguide bends typical in an antenna feeder, would be of order -30dB. In the case where trapped mode resonances can occur in the waveguide, application of equation 4.3 suggests that a total EH_{21} mode attenuation ($\alpha_m L$) of 1.5dB would be required to maintain the ripple on the transmission characteristic to below 0.1dB. In view of the high EH_{21} mode attenuation (figure 8.5) this value of total attenuation is easily obtainable for all practical waveguide lengths. Using this extended bandwidth design an operating bandwidth of about 10% can be achieved without significantly sacrificing the desirable properties of single mode operation. For this design the HE_{11} mode

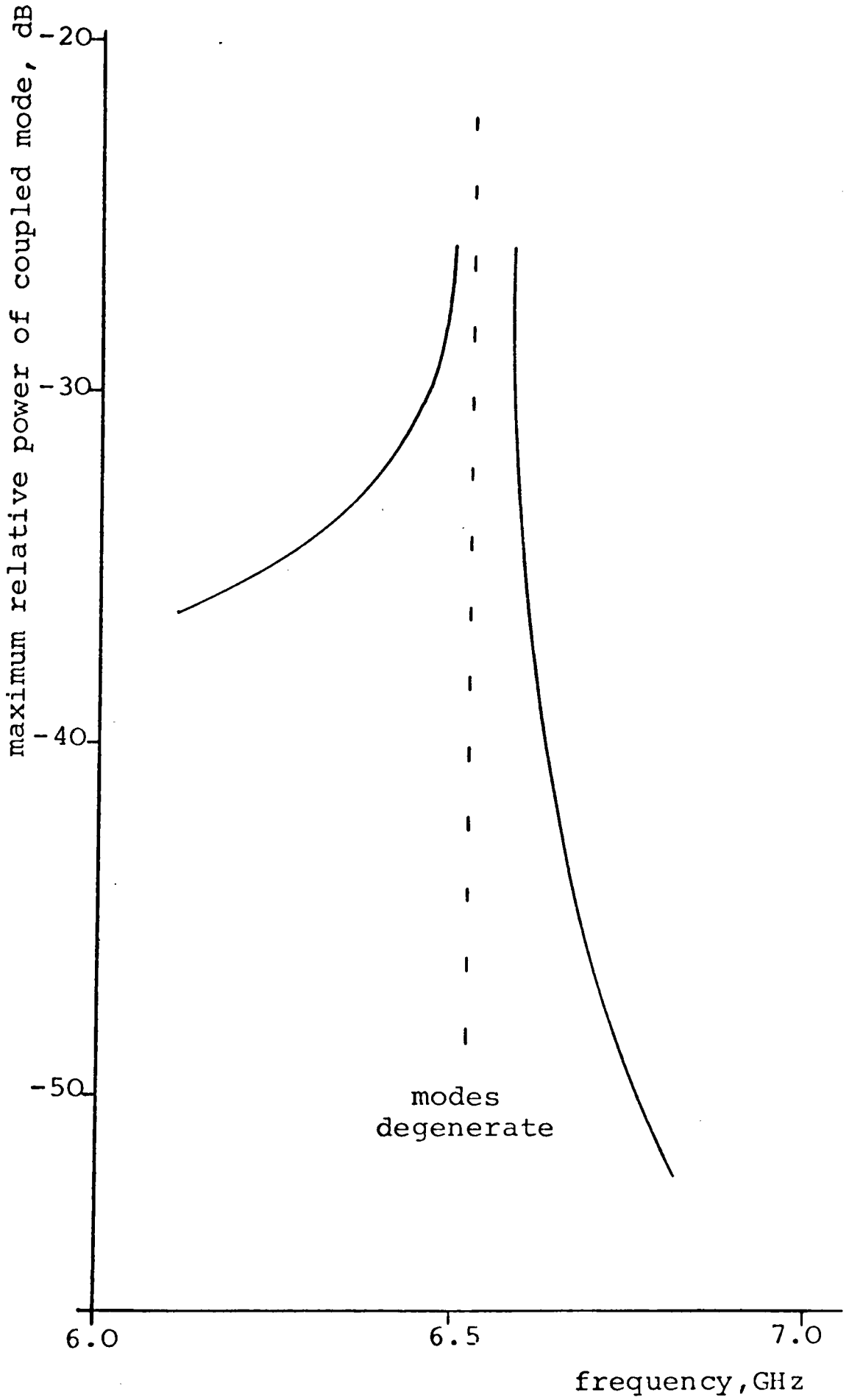

Fig. 8.8 EH_{21} mode coupling level due to a 1.0 metre radius waveguide bend; waveguide parameters as figure 8.2

attenuation changes over the operating band by a factor of approximately 2:1 and in some cases this could represent a significant disadvantage.

The results presented in this section are for a particular set of waveguide dimensions and, where possible, results obtainable at other design frequencies have been given. For every ridge width chosen there exists an optimum slot width for minimum attenuation and maximum bandwidth. Use of a smaller slot width for the design considered in this section has been found to slightly increase the HE_{11} mode attenuation and the bandwidth centre frequency, the bandwidth remaining substantially the same. For the waveguide considered in this section the corrugation dimensions used represent a practical size for flexible waveguide construction and so the results presented are representative of a practical mono-mode design.

8.3 EXPERIMENTAL VERIFICATION OF MONO-MODE OPERATION AND MEASUREMENT OF HE_{11} MODE ATTENUATION

In this section resonant cavity measurements to verify the H_{01} and HE_{21} mode cut-off frequencies and to assess the HE_{11} mode attenuation at the centre of the mono-mode operating band are presented. Transmission test measurements on a 2 metre length of rigid corrugated circular waveguide, known to exhibit a serious trapped mode loss when operated overmoded, were performed to verify the existence of the mono-mode operating region.

Although one of the virtues of the mono-mode

corrugated waveguide is seen to be in its flexible form of construction, manufacturing facilities dictated that a rigid form of waveguide construction would have to be used for this experimental investigation.

8.3.1 Resonant cavity measurements

Short lengths of mono-mode corrugated circular waveguide designed for an operating frequency of 9.26GHz were manufactured using the thermal contraction process (chapter 4) and a typical length is shown in figure 8.9. This method of construction requires that thin irises are

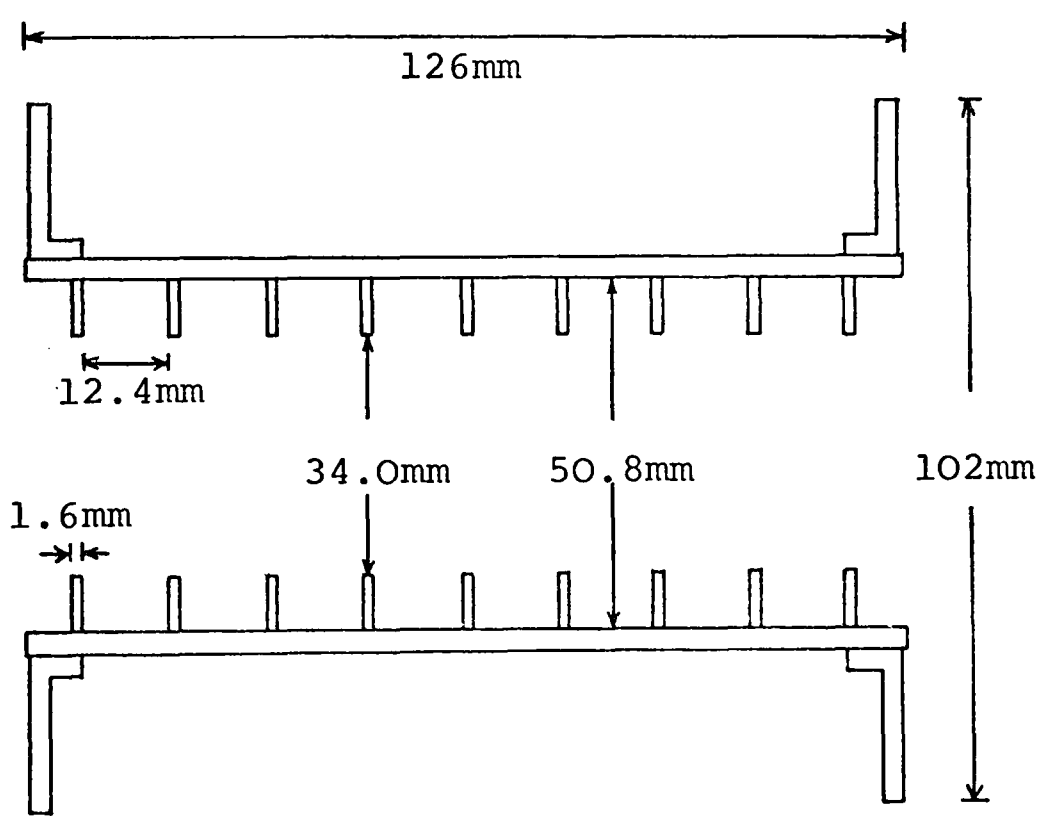

Fig. 8.9 Mono-mode corrugated waveguide resonant cavity, operating frequency 9.3GHz.

used in order to achieve good electrical contact, and so the mono-mode waveguide design was modified to accommodate this requirement.

With the waveguide of figure 8.9 made to form a resonant cavity, and using the measurement technique described in chapter 4, the H_{01} mode low frequency cut-off was found to be 9.68GHz compared with the theoretical value of 9.70GHz. This small error is due partly to manufacturing tolerances (i.e. corrugations not being evenly spaced) and partly to the calculation error involved at the mode low frequency cut-off < 2 >. The HE_{21} mode was only very weakly coupled near to the low frequency cut-off, due to the confinement of the mode power near to the corrugations (cavity coupling holes at $r=\frac{r_1}{2}$ being used). Exact measurement of the cut-off frequency was therefore not possible but as predicted it was slightly higher than that of the H_{01} mode.

Measurements on the HE_{11} mode showed that double-resonance effects were occurring at some polarisations in the single lengths of resonant cavity, indicating that poor iris contact was occurring in places. This is caused by the fact that the small waveguide diameter used allows less thermal expansion when manufacturing the waveguide and consequently the irises do not grip the pipe so well as in the larger corrugated waveguides previously manufactured using this process. In addition the inner surface of the pipe was machined and so surface roughness effects could also contribute to a poor iris-pipe contact. Measurement

of the 3dB linewidths for the HE_{11} mode resonances was made possible by selecting the most favourable polarisation. Two different lengths of waveguide were manufactured (84mm and 126mm) and linewidth measurements were obtained at 9.3GHz for 4 lengths of resonant cavity, 84mm, 126mm, 210mm, 252mm. These lengths gave a fairly consistent set of resonant linewidths and using the regression line method (chapter 4) yielded an unloaded 3dB linewidth of 0.86MHz. This gave an HE_{11} mode attenuation for the brass waveguide of 13dB/100m, approximately 2.1 times higher than the theoretical value. This difference between experiment and theory is consistent with the attenuation results obtained for the HE_{11} and HE_{12} modes in the overmoded corrugated waveguide described in chapter 4. The high value being principally attributed to surface roughness effects.

8.3.2 Transmission test measurements

A prototype length (2.08m) of thermal contraction corrugated waveguide manufactured by Andrew Antenna Systems for overmoded operation at 17GHz was found to have an $\frac{r_1}{r_o}$ value of 0.68. This value of $\frac{r_1}{r_o}$ is close to the optimum value of 0.66 for mono-mode operation and below the value of 0.715 where mono-mode operation ceases to occur. Using the design formulae presented in section 8.2 this waveguide was found to have the centre of the mono-mode operating band at 12.1GHz. The high frequency limit to this mono-mode band occurring at the low-frequency cut-off of the H_{01} mode, 12.67GHz. This waveguide is known to

exhibit a severe trapped mode resonance loss when operated overmoded, mainly due to poor iris-pipe contact. Consequently the absence of any trapped mode resonances over the mono-mode band of the measured transmission characteristics would verify the existence of the mono-mode operating region. This measurement is now described.

The experimental equipment available covered the frequency band 12.4GHz to 18GHz and so only part of the mono-mode operating band could be studied. A schematic of the experimental measurement system is shown in figure 8.10. This differs slightly from that described in chapter 4 as no Network Analyser was available, however the source was found to be very stable over the short time required to record the transmission characteristic. To enable the rectangular to smooth wall circular transitions to operate above cut-off in the region of 12.4GHz, it was necessary to use tuning screws in the transitions to permit propagation. This resulted in an oscillatory narrow band transmission characteristic but was sufficient to show if any trapped mode resonances occurred over the mono-mode band. Figure 8.11(a) shows the transmission characteristic over part of the mono-mode band from 12.37GHz to 12.56GHz, this being the widest band obtainable with the two tuning screws on each transition. The slight resonant "pips" are due to the HE_{11} mode, caused by slight mis-alignment of the output polarisation and/or transitions. The overall ripple on the transmission pattern being caused by the frequency sensitivity of the tuning screws.

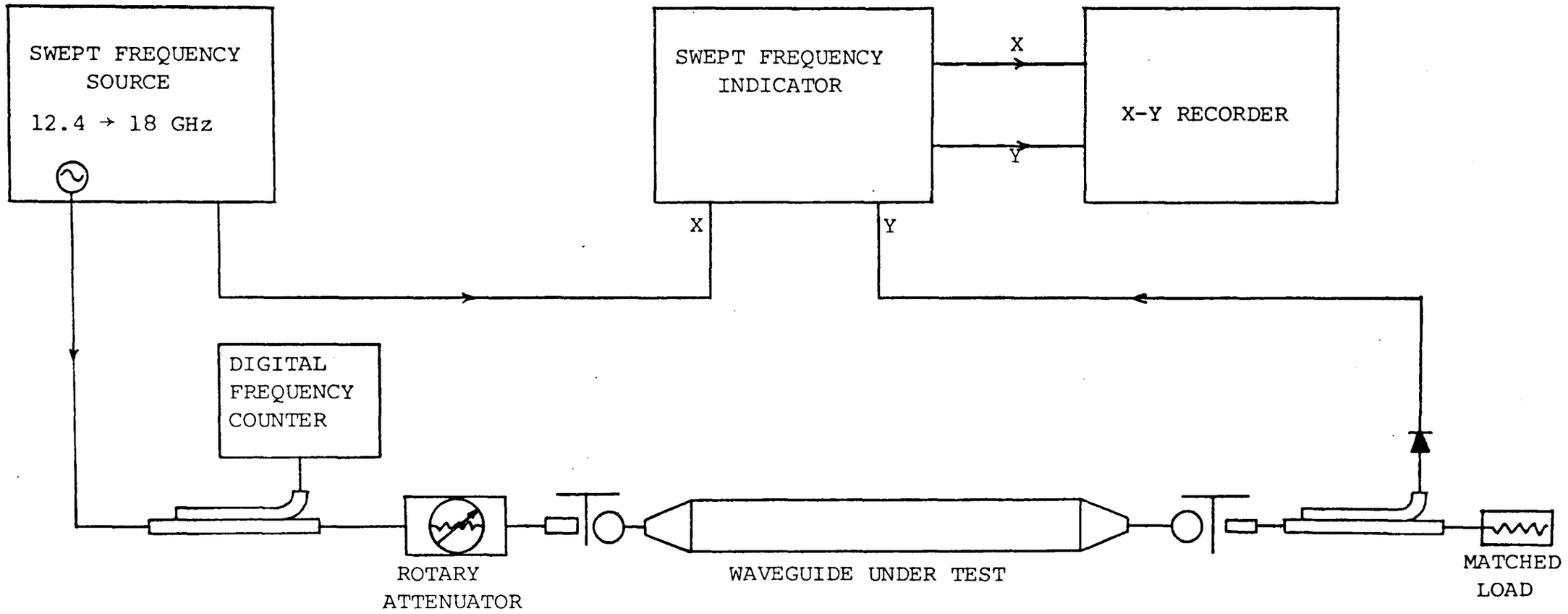

Fig. 8.10 Schematic of transmission test measurement apparatus for mono-mode corrugated waveguide

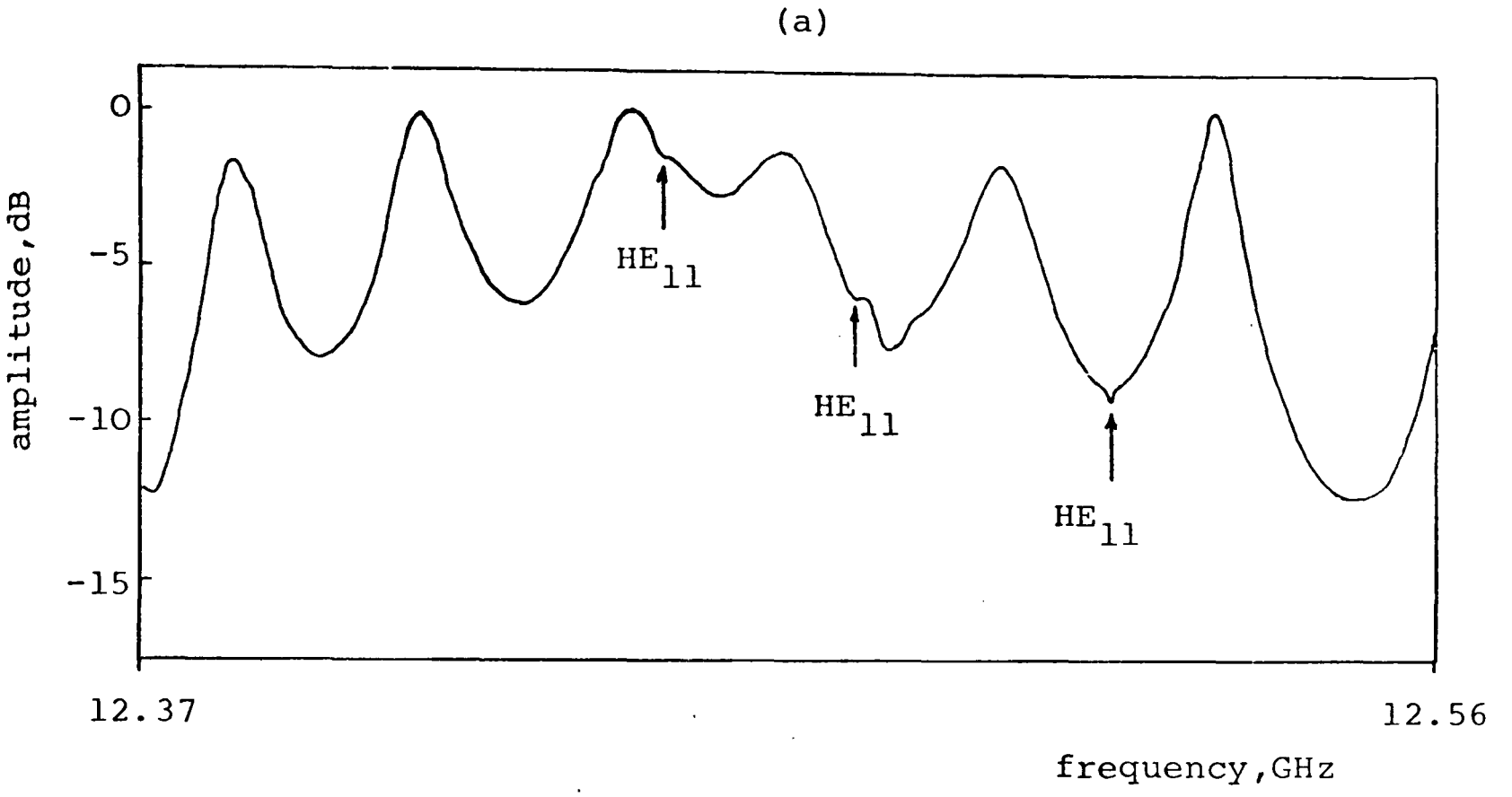

Fig. 8.11 Measured transmission characteristics for HE_{11} mono-mode corrugated waveguide

Apart from the slight alignment problem the transmission pattern over this band is free from trapped mode resonances, demonstrating the existence of the mono-mode band. Figure 8.11(b) shows the next section of the transmission characteristic, 12.56GHz to 12.86GHz, obtained by re-tuning the rectangular to circular transitions. The cut-off frequency of the H_{01} mode is clearly indicated by the trapped mode resonances starting at 12.71GHz. This marks the top end of the mono-mode operating band and corresponds well with the theoretical value of 12.67GHz.

Although the corrugated waveguide and especially the transitions were not designed for this frequency of operation this investigation has verified the existence of HE_{11} single mode operation. The theoretical upper limit to mono-mode operation has been shown to agree fairly well with the measured value using both the transmission test and resonant cavity methods. It has not been possible to experimentally study the lower limit to mono-mode operation and so the predicted bandwidth has not been verified.

8.4 THE MONO-MODE CORRUGATED CIRCULAR WAVEGUIDE AS AN ANTENNA FEEDER

In this section the advantages and disadvantages of using the mono-mode corrugated waveguide as an antenna feeder are considered for each of the main performance categories.

1) Attenuation: The mono-mode corrugated waveguide has the lowest attenuation of any single mode flexible waveguide, the attenuation being only slightly higher than the overmoded smooth wall circular waveguide at present used as a low attenuation antenna feeder. A considerable variation in attenuation over the operating band of the mono-mode corrugated waveguide occurs and consequently some form of signal equalisation may be necessary.

2) Bandwidth: The theoretical optimum mono-mode bandwidth has been shown to be of order 8% and a method has been proposed of extending this to about 10% with little degradation in performance. These bandwidths are generally sufficient for the waveguide to be used in the class 2 and 3 antenna systems discussed in chapter 2. However, an experimental study of the lower frequency limit to mono-mode operation has not been possible and so these predicted bandwidths have not been experimentally verified.

3) Dual polarisation operation: For dual polarisation operation where a flexible antenna feeder is required the mono-mode corrugated waveguide exhibits a significant reduction in attenuation and a more convenient form of installation over the alternative of using two flexible elliptical waveguides. Use of the mono-mode corrugated waveguide has the added advantage that it can be initially installed as a single polarisation waveguide and later upgraded to dual polarisation operation with little extra feeder expenditure.

4) Mechanical construction: The mono-mode corrugated waveguide is larger in diameter than other forms of antenna feeder at present employed and represents a disadvantage to its use. Where dual polarisation operation with a flexible waveguide is required the cross-sectional area of the mono-mode corrugated waveguide is practically the same as that of two flexible elliptical waveguides of equivalent operating frequency.

Deeper corrugations are required for mono-mode operation of a corrugated waveguide than for the equivalent design of overmoded waveguide and this may result in the waveguide being more difficult to manufacture.

5) Cross-polarisation: It has been shown in figure 6.8 of chapter 6, that the mono-mode corrugated waveguide exhibits a considerably lower level of cross-polarisation due to random waveguide ellipticity than its smooth wall circular waveguide counterparts. An additional contribution to the cross-polarisation generated in a flexible circular waveguide comes from the cross-sectional ellipticity occurring along a waveguide bend, caused by the bending stress present in the waveguide structure. This effect can be kept to a negligibly low level if waveguide bends with small radii of curvature are avoided.

To conclude, this chapter has shown that there exists a mono-mode operating region for the HE_{11} mode in a corrugated circular waveguide. Agreement between the measured and predicted HE_{11} mode attenuation has been

obtained to within experimental error. A mono-mode bandwidth of up to about 10% has been predicted, but manufacture and measurement of a long length of this waveguide is required to completely verify these predictions. The mono-mode corrugated waveguide therefore holds a potentially significant performance advantage over currently available antenna feeders where flexibility and single mode, dual polarisation, operation are the prime requirements.

CHAPTER 9

THE CALCULATION OF THE CO-POLAR AND CROSS-POLAR RADIATION PATTERNS OF OPEN-ENDED CORRUGATED CIRCULAR WAVEGUIDES AND NARROW FLARE-ANGLE CORRUGATED CONICAL HORNS

9.1 INTRODUCTION

The co-polar radiation characteristics of corrugated circular waveguides has been extensively studied <26> and good agreement between predicted and measured patterns has been obtained. However subject to the same assumptions made in determining the co-polar pattern, rather poor agreement between predicted and measured cross-polar patterns is obtained, as figure 2.13 of chapter 2 demonstrated. In this chapter the assumptions made by earlier authors when calculating the co-polar radiation patterns of corrugated circular waveguides are examined to determine their validity when used in calculating cross-polar patterns. It is found that many of these assumptions are not justifiable, and so a more accurate analysis then attempted by previous workers is presented in section 9.3. Comparison of the predicted results obtained using this analysis with measured co-polar and cross-polar patterns is presented in chapter 10, excellent agreement being obtained. With this confidence the analysis was extended to enable calculation of the co-polar and cross-polar radiation patterns of narrow

flare-angle corrugated conical horns and this is described in section 9.4. Before considering this formulation for the radiation patterns, section 9.2 considers the important problem of the definition of cross-polarisation, a term which in the author's opinion is used far too generally. In section 9.2 the definition of cross-polarisation relating to antenna feeds is clarified and the various mechanisms contributing to the total radiated cross-polar power are described.

9.2 THE DEFINITION OF CROSS-POLARISATION

Consider the case of an antenna radiating a linearly polarised field in the x direction. The radiated power measured in the orthogonal, y, direction then defines the cross-polar power. However, this does not give a unique definition as there are three possible coordinate systems that can be used, each leading to a different definition. This fact has been studied in detail by Ludwig <33> and has led to his three definitions of cross-polarisation. The coordinate system applicable to antenna and antenna feed polar pattern measurement has been termed Ludwig's third definition of cross-polarisation and is defined in his paper as *what one measures when antenna patterns are taken in the normal manner.* This coordinate system (R,θ,ϕ) is shown in figure 9.1(a), the experimental technique already having been considered in chapter 3. The co-polar, E_c, and cross-polar, E_x, E-field directions on the spherical surface of measurement are

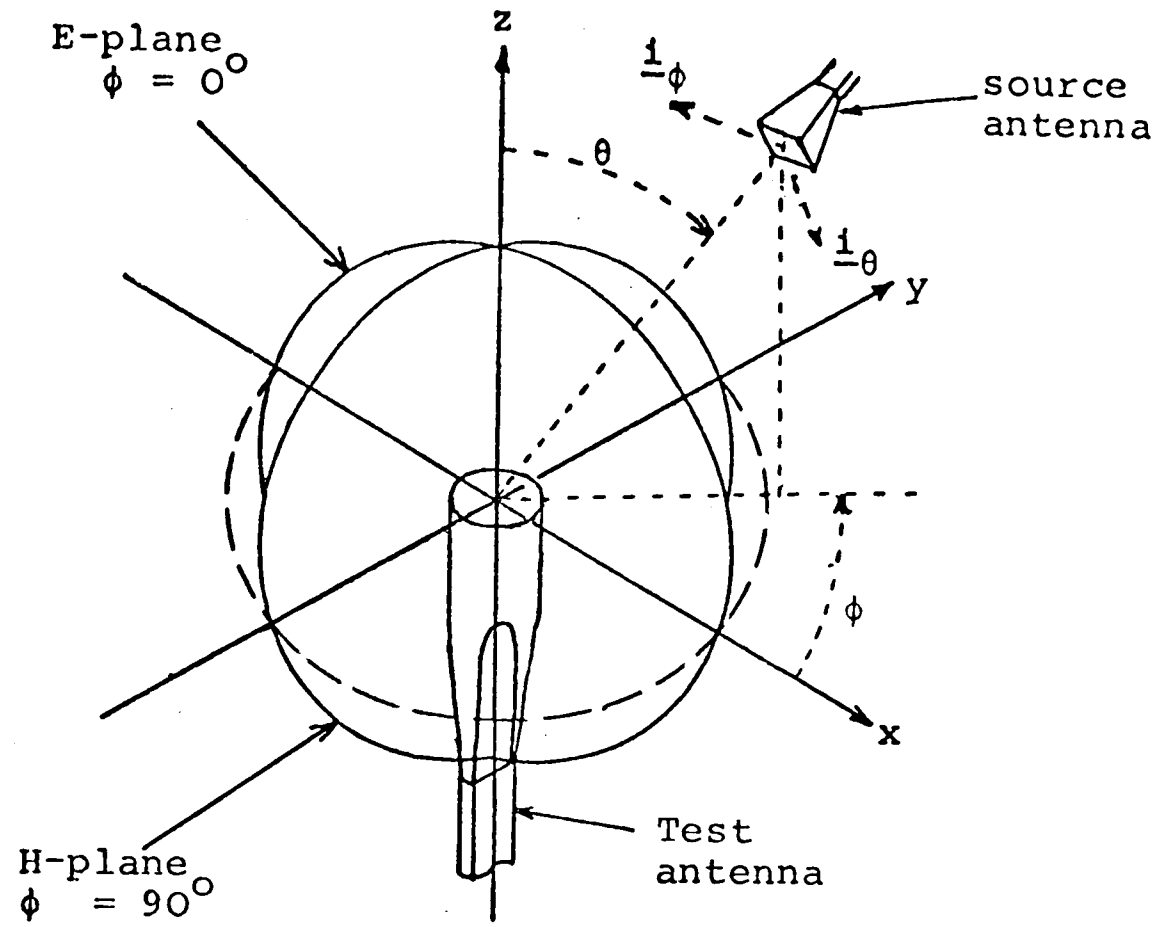

Fig. 9.1(a) Coordinate system for radiation pattern measurement

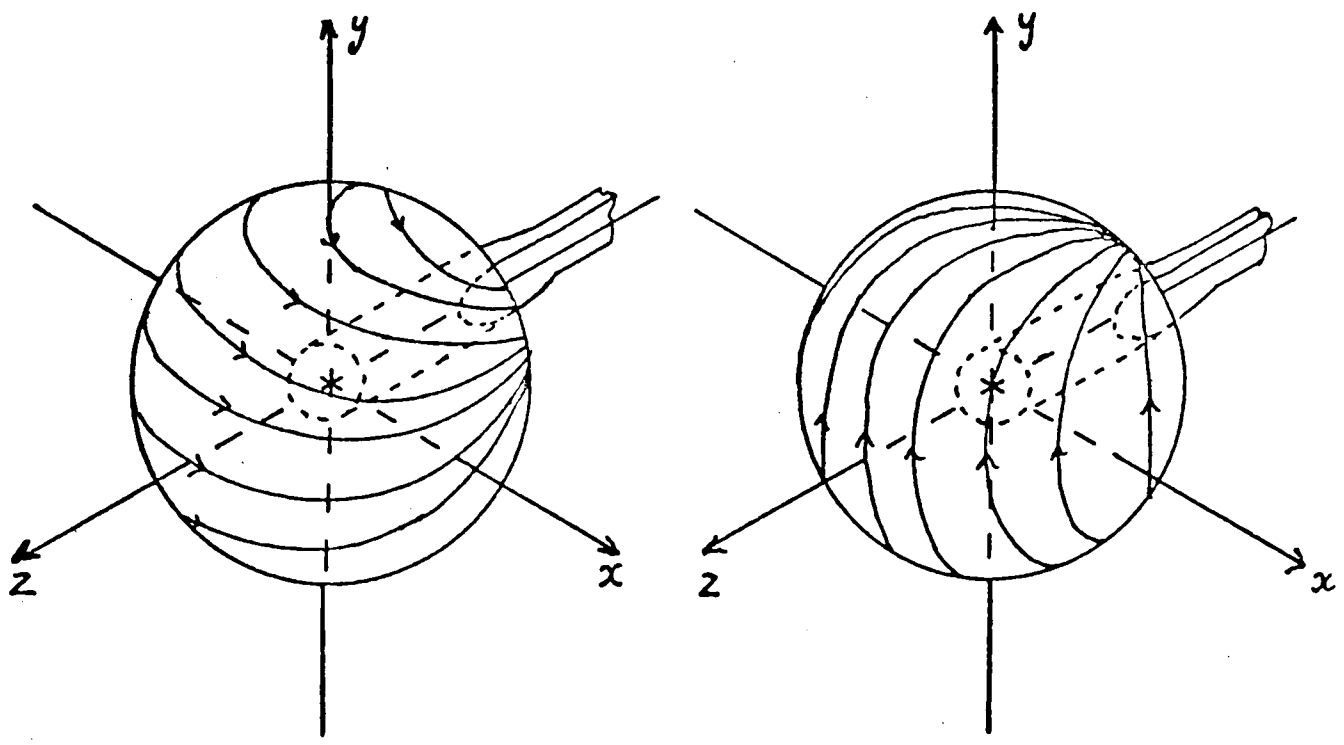

Fig. 9.1(b) Co-polar and cross-polar E-field directions on the spherical surface of measurement, Ludwig's third definition of cross-polarisation.

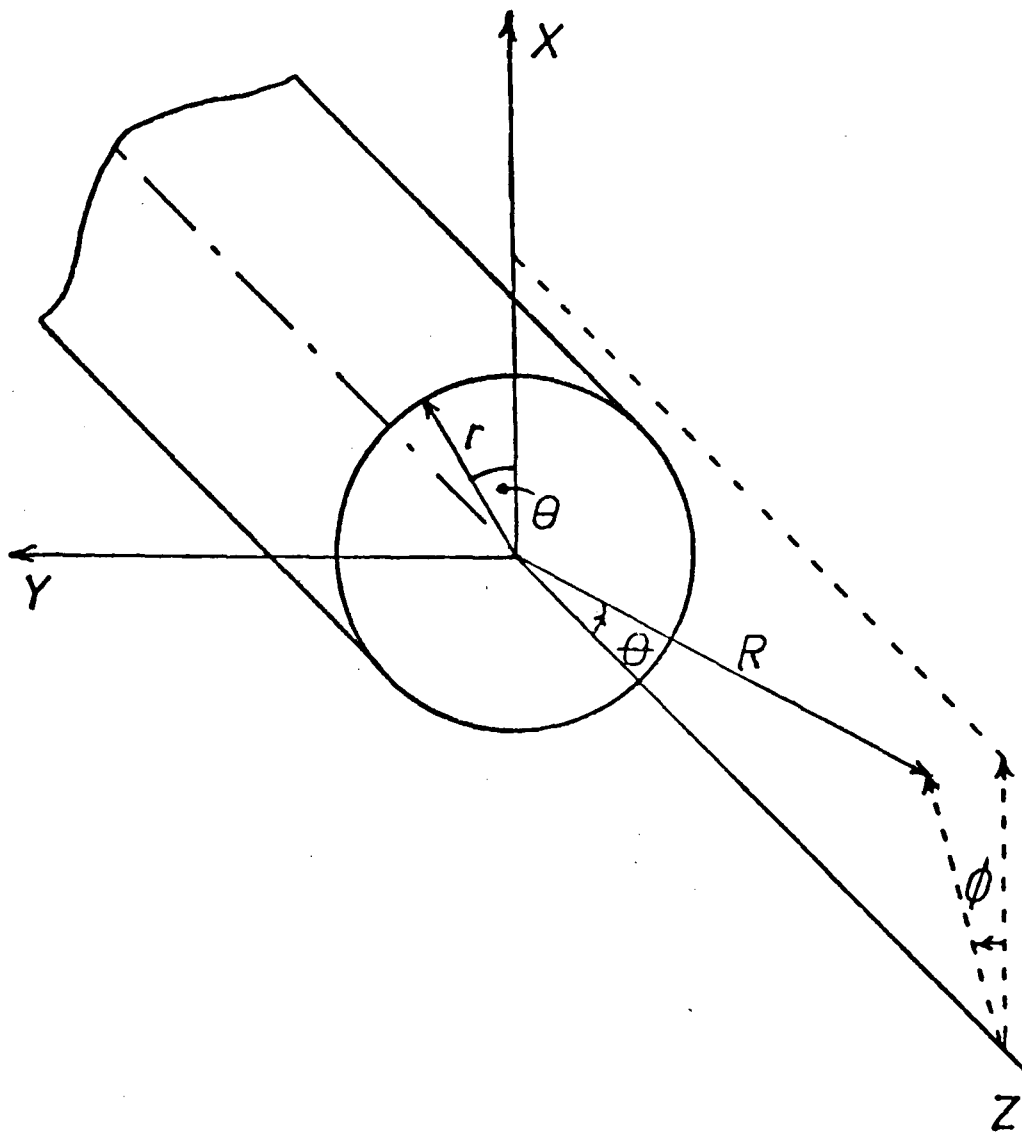

Fig. 9.1(c) The coordinate system for a radiating waveguide

shown in figure 9.1(b) and are given mathematically by

$$E_c = \underline{E}(\theta,\phi).\{\underline{i}_\theta \cos\phi - \underline{i}_\phi \sin\phi\}$$
$$E_x = \underline{E}(\theta,\phi).\{\underline{i}_\theta \sin\phi + \underline{i}_\phi \cos\phi\} \qquad (9.1)$$

where $\underline{E}(\theta,\phi)$ is the spherically radiated electric field from the test antenna shown in figure 9.1(a). For the case of interest here, where the radiating aperture of the test antenna is circular, $E(\theta,\phi)$ can be expressed in terms of the cylindrical coordinate system (r,θ,z) shown in figure 9.1(c) by:

$$\underline{E}(\theta,\phi).\underline{i}_\theta = C_\theta(\theta)\cos n\phi$$
$$\underline{E}(\theta,\phi).\underline{i}_\phi = C_\phi(\theta)\sin n\phi \qquad (9.2)$$

where $C_\theta(\theta)$ and $C_\phi(\theta)$ are the co-polar E-plane and H-plane *pattern functions* respectively, and n is the azimuthal number of the radiating mode. The pattern functions $C_\theta(\theta)$ and $C_\phi(\theta)$ depend on the *desired* aperture field distribution of the antenna and the geometry of both the aperture and the region surrounding the aperture. For a corrugated circular waveguide aperture radiating the dominant HE_{11} mode, n is unity and the co-polar radiation pattern is given from equations 9.1 and 9.2 by

$$E_c = C_\theta(\theta)\cos^2\phi + C_\phi(\theta)\sin^2\phi \qquad (9.3)$$

where $\phi = 0^o$ and 90^o yield the E and H-plane radiation pattern cuts respectively. The corresponding cross-polar radiation pattern for this case is then

$$E_x = C_\theta(\theta)\cos\phi\sin\phi - C_\phi(\theta)\sin\phi\cos\phi$$
$$= \tfrac{1}{2}\{C_\theta(\theta) - C_\phi(\theta)\}\sin 2\phi \qquad (9.4)$$

Equation 9.4 defines the *pattern function cross-polarisation* radiated from a circular aperture containing only the desired unity azimuthal number mode. From this equation several properties concerning the pattern function cross-polarisation can be determined.

1) The pattern is a maximum in the 45^{o} planes ($\phi=45^{o}$ in equation 9.4) and zero in both principal planes.
2) The 45^{o}-plane pattern is given by half the difference between the co-polar E and H-plane patterns.
3) If the co-polar radiation is circularly symmetric (i.e. independent of ϕ), $C_{\theta}(\theta) = C_{\phi}(\theta)$ and the radiated cross-polar power is everywhere zero.

The latter property indicates why the corrugated circular waveguide and horn exhibiting a near circular symmetric co-polar radiation pattern over a wide band, have a potentially good cross-polarisation performance.

Whilst the pattern function cross-polar component is often referred to as producing the required *feed cross-polarisation* another contributing component exists which arises from the presence of undesirable modes in the feed aperture. These undesirable modes are of two principal kinds.

1) Higher order propagating modes generated in the feed due to mechanical imperfections, or more commonly, in the waveguide feeder due to bends and other mechanical imperfections along the waveguide run.

2) The orthogonally polarised component of the desired aperture field mode, caused by such effects as random ellipticity in the waveguide feeder (chapter 6).

These undesirable higher order modes can distort the co-polar radiation pattern, destroying the near circular symmetry of the dominant mode pattern and consequently producing a high level of radiated cross-polar power. The principal distorting effect of the orthogonal component of the dominant mode is to fill-in the boresight cross-polar null with a small *co-polar* pattern component. The effects will be considered again in the next section.

9.3 FORMULATION OF THE CO-POLAR AND CROSS-POLAR RADIATION PATTERNS FOR OPEN-ENDED CORRUGATED CIRCULAR WAVEGUIDES

In this section the formulation of the co-polar radiation pattern of an open-ended corrugated circular waveguide is derived and from this the pattern function cross-polarisation is obtained via equation 9.4.

The Kirchhoff-Huygens method used by many workers <26> to obtain the co-polar radiation pattern of a corrugated circular waveguide is a method commonly used for calculating the far-field radiation pattern of an aperture antenna <50> <51>. For convenience this method will henceforth be termed the K.H. method. In its exact form, specification of the fields over a closed surface that surrounds the antenna and source yields the radiated

field at any point outside this surface but within a sphere of infinite radius. Practically however, the fields over the closed surface are rarely, if ever, known and therefore it is usually approximated to be a hemispherically open surface of infinite radius. In this form the method leads to a calculation of the radiated field arising from a distribution of sources over the surface and yields a non-zero field intensity in the region of space not covered by direct rays from the antenna. This deviation from the Geometric Optics propagation is the diffraction phenomena. Experiments have shown <50> this diffraction effect to be small for apertures large compared to the wavelength and so the high frequency approximation has evolved which takes the open surface to be an infinite plane, S, containing the antenna aperture A, figure 9.2. This aperture is bounded by a contour τ, and over the remainder of the infinite plane the fields are assumed to be zero. This field distribution over S is discontinuous with non-zero field over A and zero field over the remainder of S, and in order to make this distribution compatible with the equation of continuity a line distribution of electric and magnetic changes is introduced along τ. This method when applied to the corrugated circular waveguide leads to the assumption that the waveguide is terminated in an infinite plane with zero field everywhere except over the waveguide aperture. In practical terms this implies that the waveguide is terminated in an infinitely small conducting flange. Although the requirement for the waveguide aperture to be

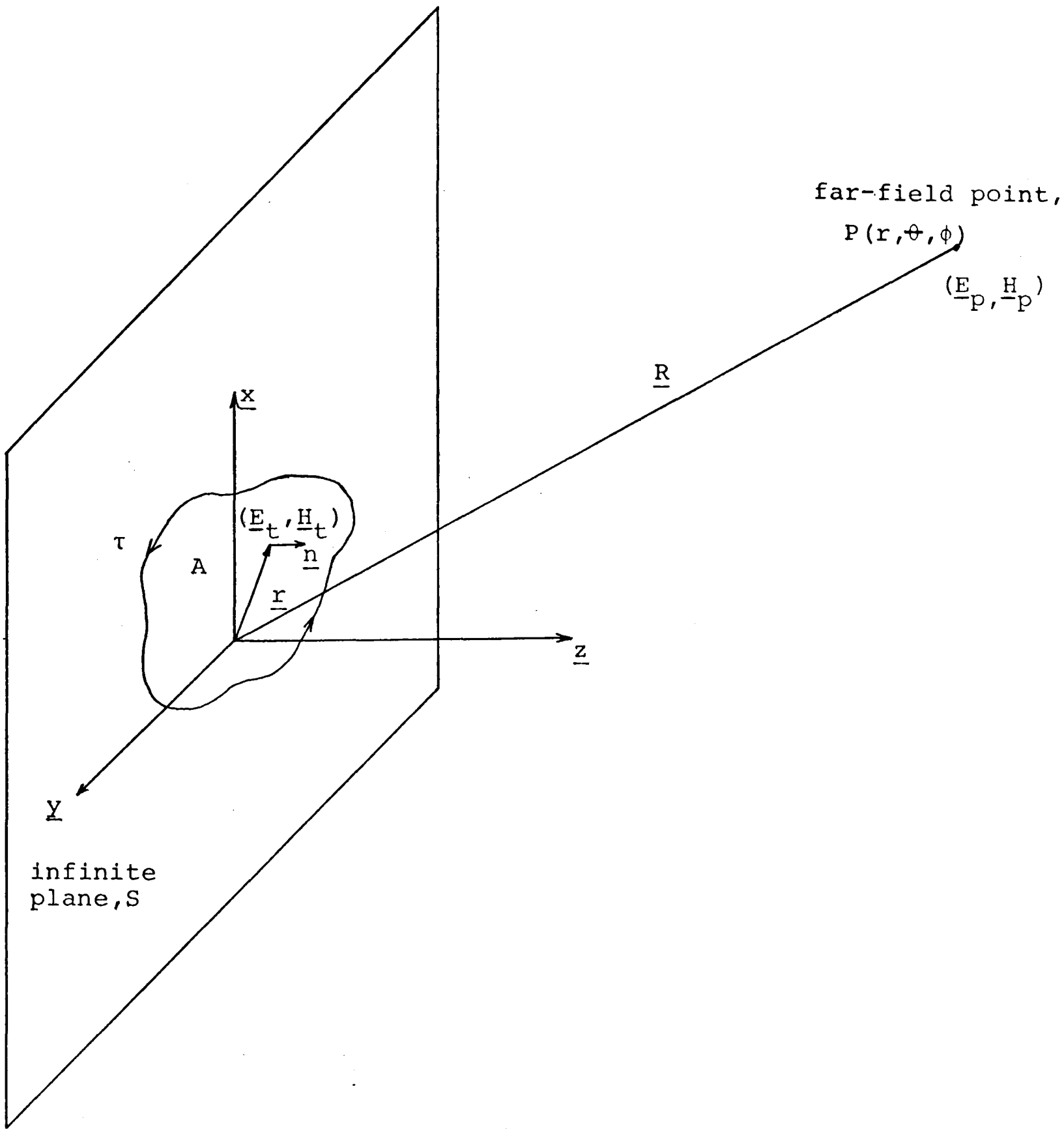

Fig. 9.2 Geometry used for the calculation of far-field radiation patterns

large compared to the wavelength is not normally met, good agreement with measured co-polar patterns is obtained <26>. The following assumptions concerning the aperture field of the corrugated waveguide are normally made when co-polar patterns are determined by this K.H. method.

1) The field of the HE_{11} mode is that of the fundamental space-harmonic of the periodic waveguide structure and in deriving the field only the lowest order standing-wave is present in the slots. This assumes the corrugations produce a surface impedance , the analysis being called the surface impedance method <26>.
2) The effect of the finite flange at the aperture of the waveguide is neglected.
3) Only the forward propagating wave is significant.
4) If the corrugated waveguide is joined at one end to a smooth wall circular waveguide supporting a TE_{11} mode, only the HE_{11} mode is excited in the corrugated waveguide.

It was shown in section 9.2 that the peak cross-polar radiation pattern is given by the difference between the E and H-plane co-polar patterns, and therefore any small error in calculating the co-polar patterns caused by the above assumptions results in the quite erroneous cross-polar pattern prediction shown in figure 2.13 of chapter 2. The remainder of this section will show that by removal of many of the above listed assumptions a more accurate formulation for the co-polar and cross-polar radiation

patterns can be obtained.

Considering the first of these assumptions, Clarricoats, Olver and Chong < 5 > have described an analysis for the corrugated circular waveguide using a field expansion in terms of space-harmonics, together with the inclusion of higher order modes in the slots. This study showed that the transverse field of the HE_{11} mode in the inner region of the waveguide is noticeably modified with the inclusion of the first pair of higher order space-harmonics, in addition to the fundamental wave. Inclusion of further higher order space-harmonics had a far less significant effect. Matching of the field at the boundary of the corrugations was accomplished by inclusion of one pair of higher order standing-waves in the slot, in addition to the lowest order wave. A detailed description of this analysis has been given by Chong < 2 >. The formulation of the co-polar radiation using the K.H. method and the space-harmonic representation for the aperture field is presented in appendix 9.1. Figure 9.3 shows the co-polar E and H-plane patterns calculated with the first pair of higher space-harmonics included, compared with the circularly symmetric pattern obtained using only the fundamental space-harmonic to describe the aperture field. Both these patterns were calculated at the *balanced hybrid* frequency. At this frequency the surface impedance analysis predicts that the electric and magnetic fields of the HE_{11} mode are directly related (balanced) through the free-space wave impedance. This causes the radiated

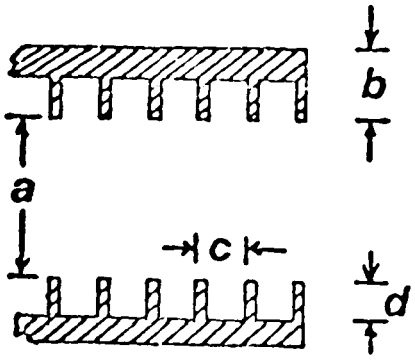

a = 50mm

b = 25mm

c = 11·6mm

d = 10 mm

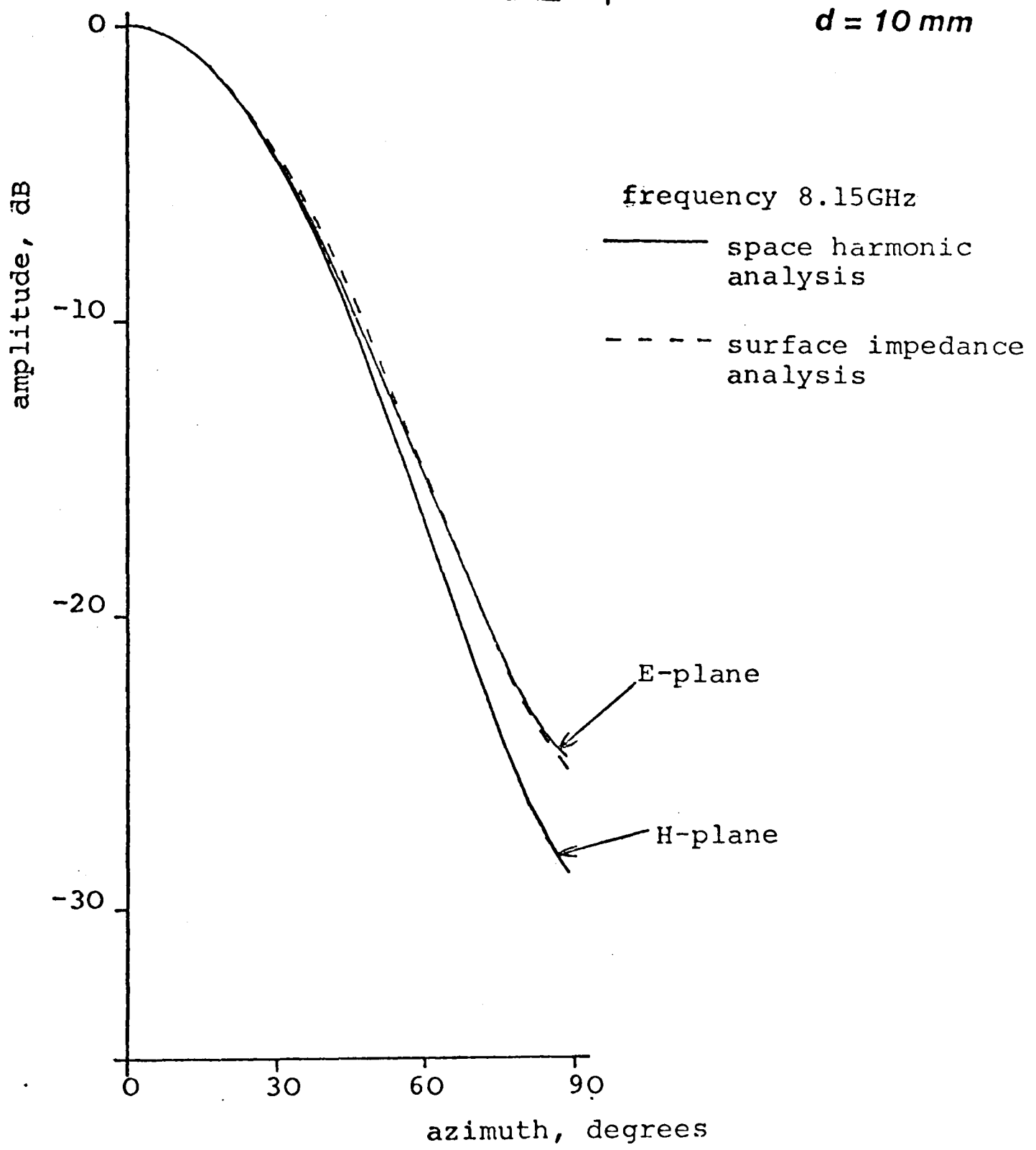

Fig. 9.3 Comparison of the circularly symmetric co-polar radiation pattern obtained at the "balanced hybrid frequency" with that obtained when one pair of higher order space harmonics are included in the aperture field

co-polar pattern, as calculated using the K.H. method, to be circularly symmetric resulting in zero radiated cross-polar power in all space <26>. With the inclusion of space-harmonics this balance between E and H fields no longer *exactly* occurs, figure 9.3, and the frequency at which it becomes closest to being true is generally slightly higher than the predicted balanced hybrid frequency. Consequently the concept of *balanced hybrid* becomes of little practical use when the effects of space harmonics are included. As expected, inclusion of even higher order space-harmonic terms was found to have a negligible effect on the radiation pattern.

Adding equations (xi) and (xii) of appendix 9.1 to equation 9.4, the radiated cross-polar power in the 45^{o}-plane, normalised to the boresight co-polar power, is obtained as:

$$E_x = \sum_{N=-1}^{N=+1} \frac{\bar{r}_1 (K_N r_1)(\bar{A}_N - \bar{B}_N)}{2(K_N r_1)^2 E_{p\theta}(O)} \left[T_N(\theta)(\beta_N r_1 + \bar{r}_1 \cos\theta) - \frac{(\bar{r}_1 + \beta_N r_1 \cos\theta) J_1(\bar{r}_1 \sin\theta)}{(K_N r_1)\bar{r}_1 \sin\theta} \right] \quad (9.5)$$

where $T_N(\theta)$ is defined in equation (x) of appendix 9.1 and $E_{p\theta}(O)$ is the boresight co-polar power. The effect of the inclusion of the first pair of space-harmonics on the maximum radiated cross-polar power, plotted as a function of frequency is shown in figure 9.4, curve B, compared with curve A calculated with the surface impedance derived

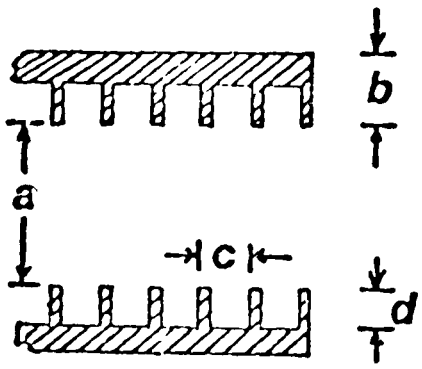

$a = 50mm$

$b = 25mm$

$c = 11{\cdot}6mm$

$d = 10\,mm$

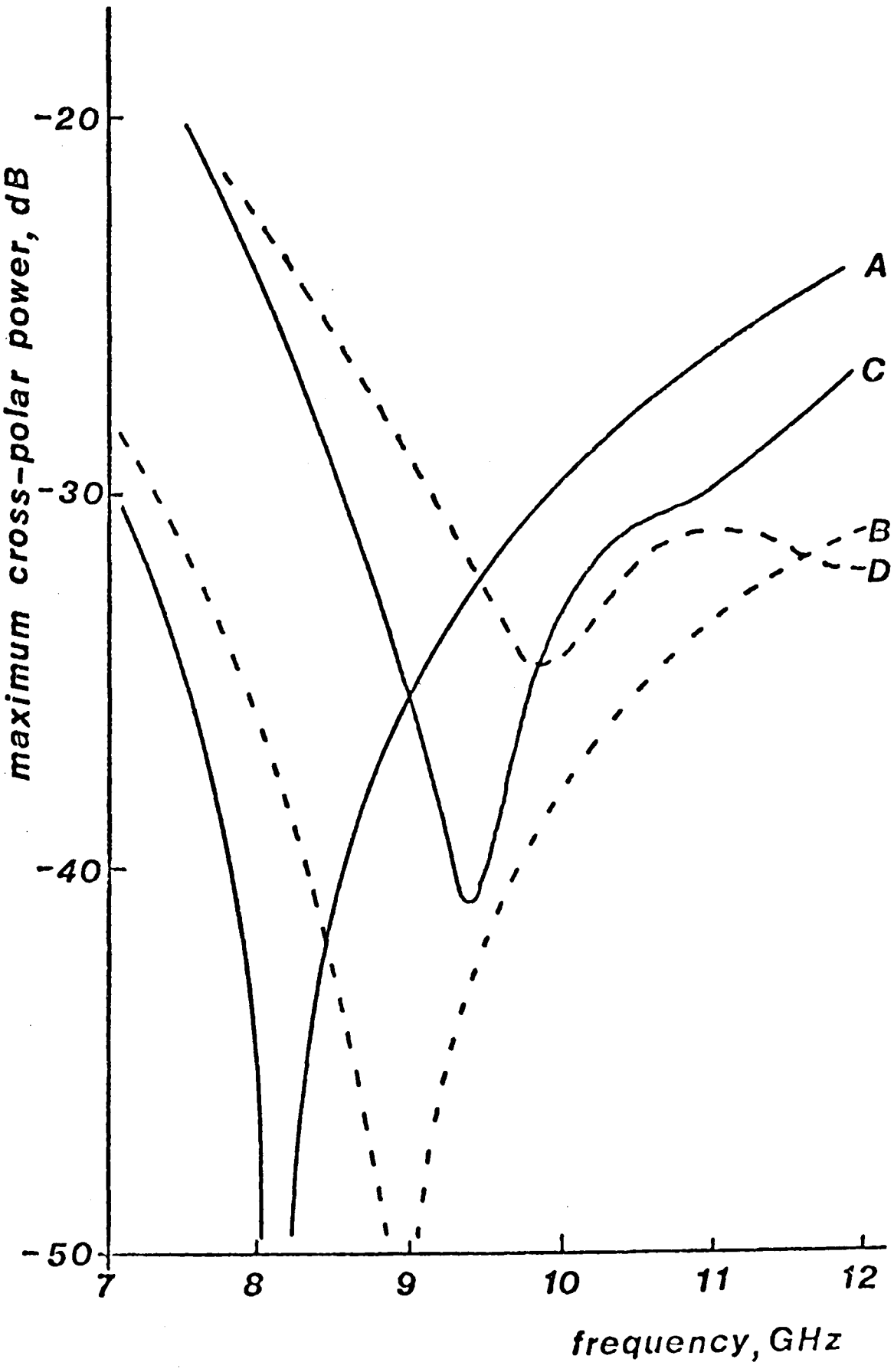

Fig. 9.4 Theoretical maximum radiated cross-polar power as a function of frequency calculated using the various assumptions explained in the text

aperture field. The frequency at which the co-polar pattern is closest to being circularly symmetric is given by the minima of curve B.

Turning now to the second assumption, the presence of the corrugations dictates that the radiating aperture of the corrugated waveguide be terminated in a small but finite flange. It has been found <52> that the current flow induced on a small flange at the radiating aperture of a smooth wall circular waveguide decays away very rapidly in the radial direction. Therefore the contribution to the forward radiated field from the currents on the outer edge of the flange become negligible, even for flanges with radial dimension less than a wavelength. This rapid decay of the currents allows the radial dimension of the flange to be approximated as being infinite in extent. For most practical sizes of corrugated waveguide the corrugations force the field edge taper at the aperture boundary to be significantly increased over that for the corresponding smooth wall waveguide. Therefore the magnitude of the flange currents are lower in the case of the corrugated waveguide, and hence the infinite flange approximation becomes valid for most practical radial dimensions of the terminating flange.

By assuming the radiating aperture is in a perfectly conducting plane an exact result for the field radiated into space on one side of the plane can be obtained. For this case it can be shown <51> that the far-field radiation is related in a direct way to the

Fourier Transform of the aperture field. This method will henceforth be called the F.T. method and the space harmonic formulation for the corrugated circular waveguide radiation pattern obtained by this method is presented in appendix 9.2.

Knop and Wiesenforth <53> have used this method of analysis to formulate the co-polar radiation pattern for an open-ended corrugated circular waveguide using the surface impedance analysis. Figure 9.5 shows the co-polar E and H-plane pattern for the waveguide shown inset to figure 9.3, calculated at the balanced hybrid frequency using the F.T. method and including one pair of higher order space-harmonics in the aperture field description. Comparing figures 9.3 and 9.5 shows the lack of circular symmetry at this frequency resulting from the presence of the infinite flange.

When the F.T. method is applied to determine the cross-polar radiation pattern via equation 9.4 and equations (ix) and (x) of appendix 9.2, the cross-polar power radiated in the 45^{o}-plane, normalised to the bore-sight co-polar power is obtained as:

$$E_x = \sum_{N=-1}^{N=1} \frac{\bar{r}_1}{(K_N r_1) E_{p\theta}\ (O)} \left[T_N(\theta)\,(\bar{A}_N \beta_N r_1 - \bar{B}_N \bar{r}_1 \cos\theta) - \frac{J_1(\bar{r}_1 \sin\theta)}{(K_N r_1)\bar{r}_1 \sin\theta}\,(\bar{A}_N \beta_N r_1 \cos\theta - \bar{B}_N \bar{r}_1) \right] \qquad (9.6)$$

where $T_N(\theta)$ and $E_{p\theta}\ (O)$ are defined as in equation 9.5.

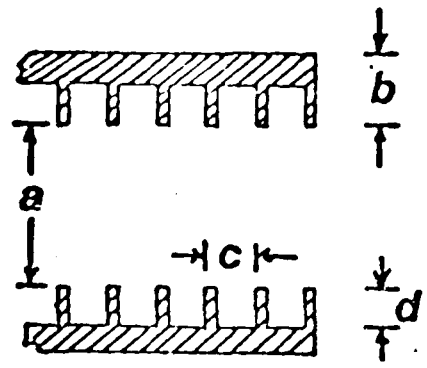

a = 50mm

b = 25mm

c = 11·6mm

d = 10 mm

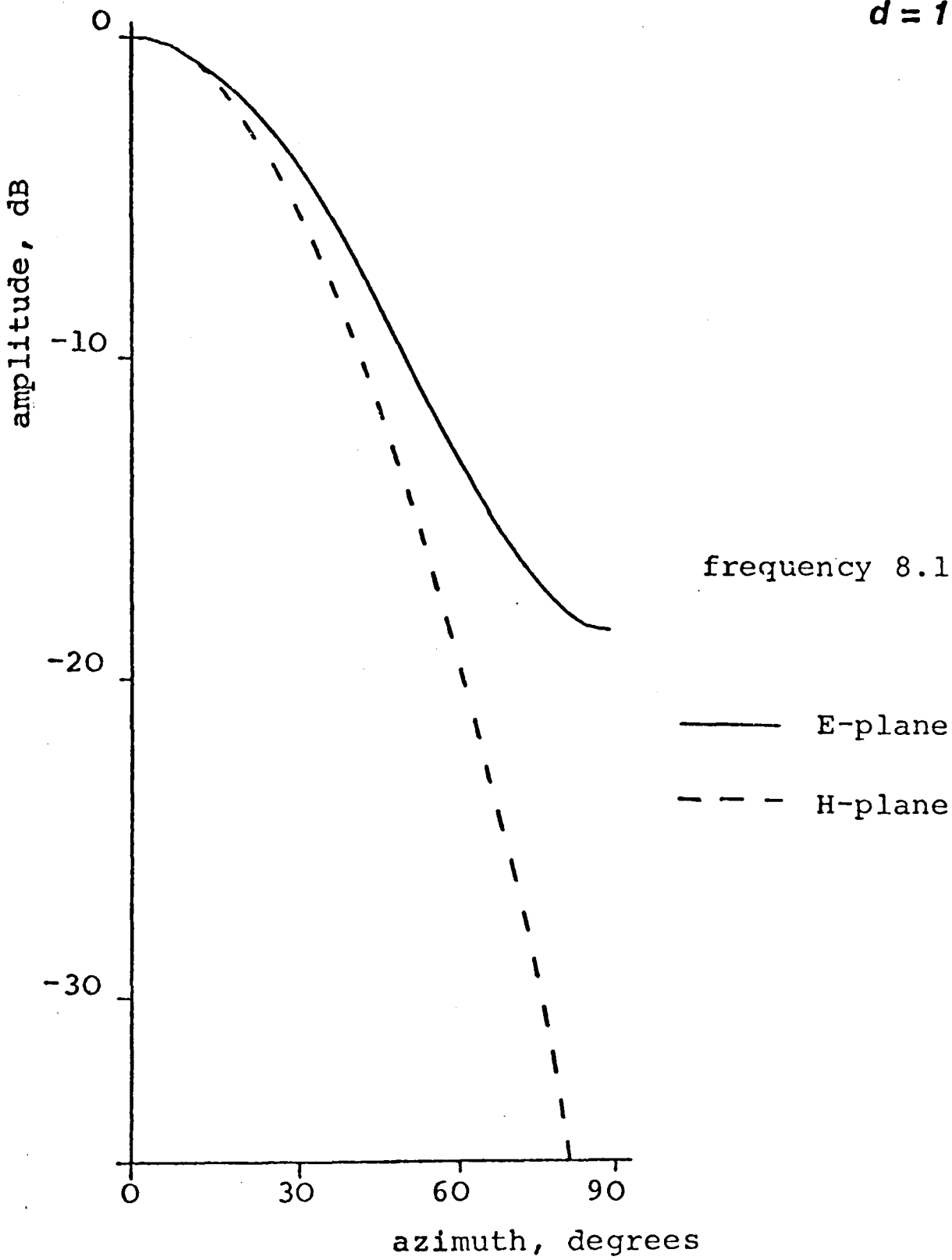

Fig. 9.5 Comparison of the E and H-plane co-polar radiation patterns at the "balanced hybrid frequency" calculated using the F.T. method with one pair of higher order space harmonics included in the aperture

The maximum cross-polar power as a function of frequency calculated using the F.T. method, with the fundamental space-harmonic only, is shown in figure 9.4 curve C, and when the first pair of higher order space-harmonics are included curve D is obtained. From equation 9.6, and the absence of any null in figure 9.4 curve D, it is clear that there is no frequency at which the maximum cross-polar power is zero, even for the case when only the fundamental space-harmonic aperture field is used. Consequently there is no frequency at which the co-polar pattern is exactly circularly symmetric, although the minimum of figure 9.4 curve D gives the frequency at which symmetry is nearly achieved. However, for all practical purposes the co-polar radiation at this frequency is circularly symmetric, as figure 9.6 shows. Figure 9.7 shows the maximum cross-polar power as a function of frequency for a waveguide of much larger normalised aperture diameter than used in figure 9.4. From the similarity of the K.H. and F.T. solutions, it is clear that the flange has a much smaller effect on the cross-polar radiation because of the larger aperture field edge taper. However, the presence of the first pair of higher order space-harmonics is still significant in determining the frequency at which the minimum occurs. This is not, however, due to the direct contribution to the radiated field from the first pair of space-harmonics, which becomes increasingly negligible as the normalised aperture diameter increases. It occurs from the change in the amplitude coefficients of the

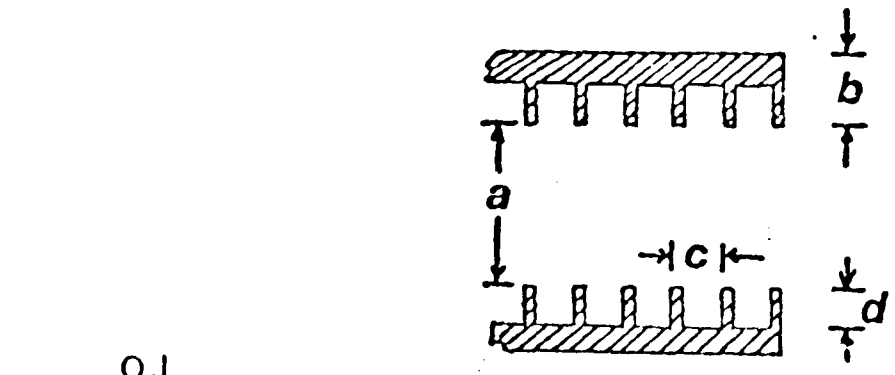

a = 50mm

b = 25mm

c = 11·6mm

d = 10 mm

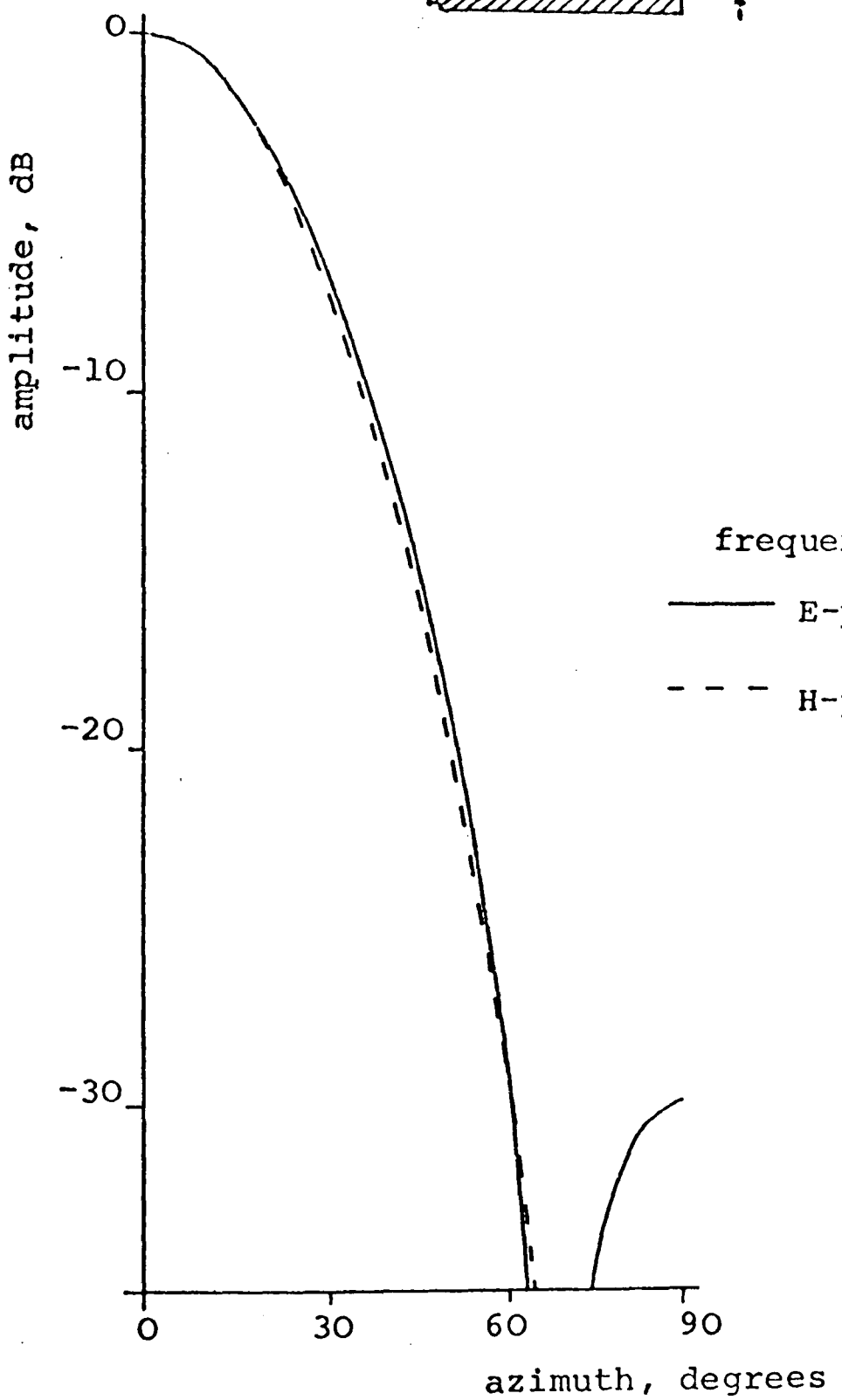

Fig. 9.6 Co-polar E and H-plane radiation patterns calculated at the frequency for which the peak radiated cross-polar power is a minimum, using the F.T. method with one pair of space harmonics

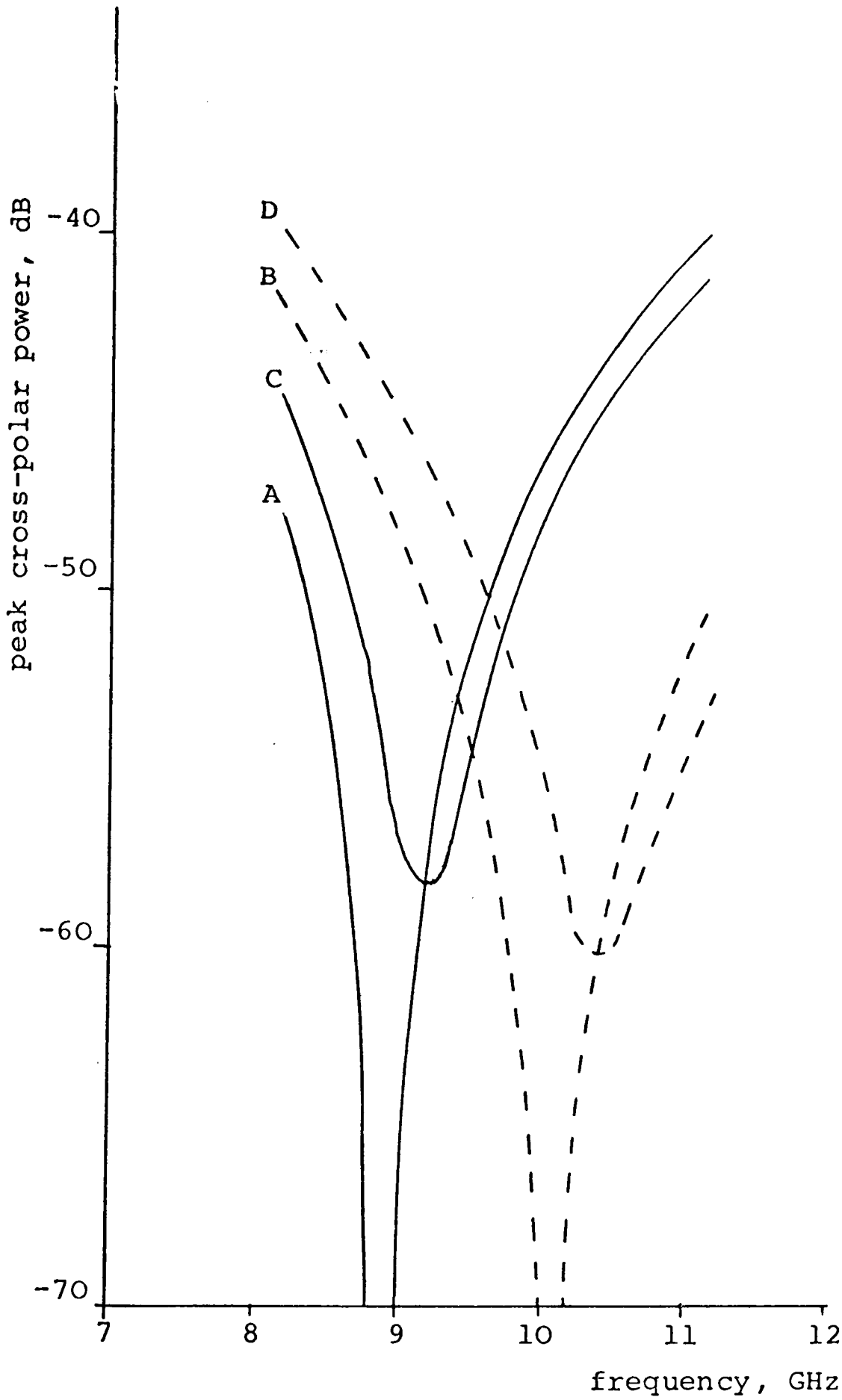

Fig. 9.7 Peak radiated cross-polar power as a function of frequency for corrugated waveguide with 7λ aperture diameter at 10GHz

A) K.H. method, surface impedance analysis
B) K.H. method, space-harmonic analysis
C) F.T. method, surface impedance analysis
D) F.T. method, space-harmonic analysis

fundamental space-harmonic brought about by the improved matching of the fields at the corrugation boundary. In fact for normalised aperture diameters greater than about 6λ the frequency for minimum radiated cross-polar power, calculated using space-harmonics, occurs where the fundamental components of the E_z and H_z fields in the waveguide are related through the free space wave impedance. It has been found by the author that for normalised aperture diameters greater than 2λ the direct contribution to the radiated cross-polar field from the first pair of space-harmonics can be neglected with minimal error.

The assumption of neglecting the reflected HE_{11} mode at the radiating aperture has been considered experimentally. The reflection coefficient of a narrow flare-angle corrugated conical horn with various aperture diameters has been measured by the author and a reflected power of less than -40dB was obtained. This level was found to be dominated by the throat region of the horn, the contribution from the aperture mismatch being negligible. This very good aperture match is to be expected when the HE_{11} mode is operated near the condition when the aperture electric and magnetic fields are directly related by the free space wave impedance. Therefore neglecting the reflected wave when calculating the radiation pattern of a corrugated waveguide is well justified.

The effect on the dominant mode radiation pattern of the presence of higher order modes has already been briefly considered in chapters 2 and 3. For a practical feed aperture diameter the corrugated circular waveguide will

propagate the H_{01}, E_{02}, HE_{21}, HE_{12} and EH_{12} higher order modes. The effect of higher order modes with non-unity azimuthal numbers in the aperture is to produce an asymmetrical distortion of the co-polar pattern and to increase the level of radiated cross-polar power. From the radiation pattern formulation presented in appendix 9.2, the vector direction of the radiated electric field for the H_{01}, E_{02} and HE_{21} modes can be easily determined and is shown in table 9.1. This table can be used to determine how these undesirable modes distort the co-polar and cross-polar HE_{11} mode radiation patterns. For example, the presence of the H_{01} mode in the radiating aperture will, produce a cross-polar pattern in the E-plane, distort the co-polar pattern in the H-plane, and affect both co-polar and cross-polar patterns in the 45^{o}-planes. This is shown diagramatically in figure 9.8, and using table 9.1, the effects of the other two modes can similarly be derived. The radiation patterns of the H_{01}, E_{02} and HE_{21} modes are all very similar as figure 9.9 shows.

The higher order modes of unity azimuthal number, HE_{12} and EH_{12}, have highly non-circularly symmetric co-polar radiation patterns, as shown by figure 9.10. Therefore the effect of these modes in the radiating aperture is to destroy the circular symmetry of the HE_{11} mode co-polar pattern and consequently produce a high level of radiated cross-polar power in the 45^{o}-planes.

MODE	TRANSVERSE FIELD PATTERN	E-plane	45°-plane	H-plane
HE_{11} co-polar	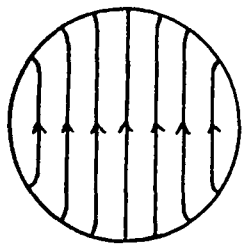	$\underline{i}_\theta$	$\underline{i}_\theta + \underline{i}_\phi$	$\underline{i}_\phi$
HE_{11} cross-polar		$\underline{i}_\phi$	$\underline{i}_\theta - \underline{i}_\phi$	$\underline{i}_\theta$
H_{01}	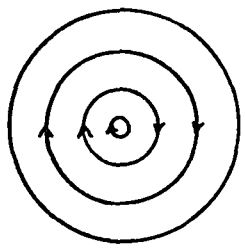	$\underline{i}_\phi$	$\underline{i}_\phi$	$\underline{i}_\phi$
E_{02}	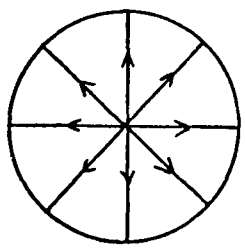	$\underline{i}_\theta$	$\underline{i}_\theta$	$\underline{i}_\theta$
HE_{21}	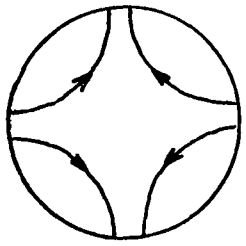	$\underline{i}_\theta$	$\underline{i}_\phi$	$\underline{i}_\theta$
HE_{21}^*	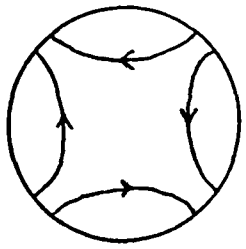	$\underline{i}_\phi$	$\underline{i}_\theta$	$\underline{i}_\phi$

Table 9.1 Electric field direction of radiation patterns using coordinate system shown in figure 9.1(c)

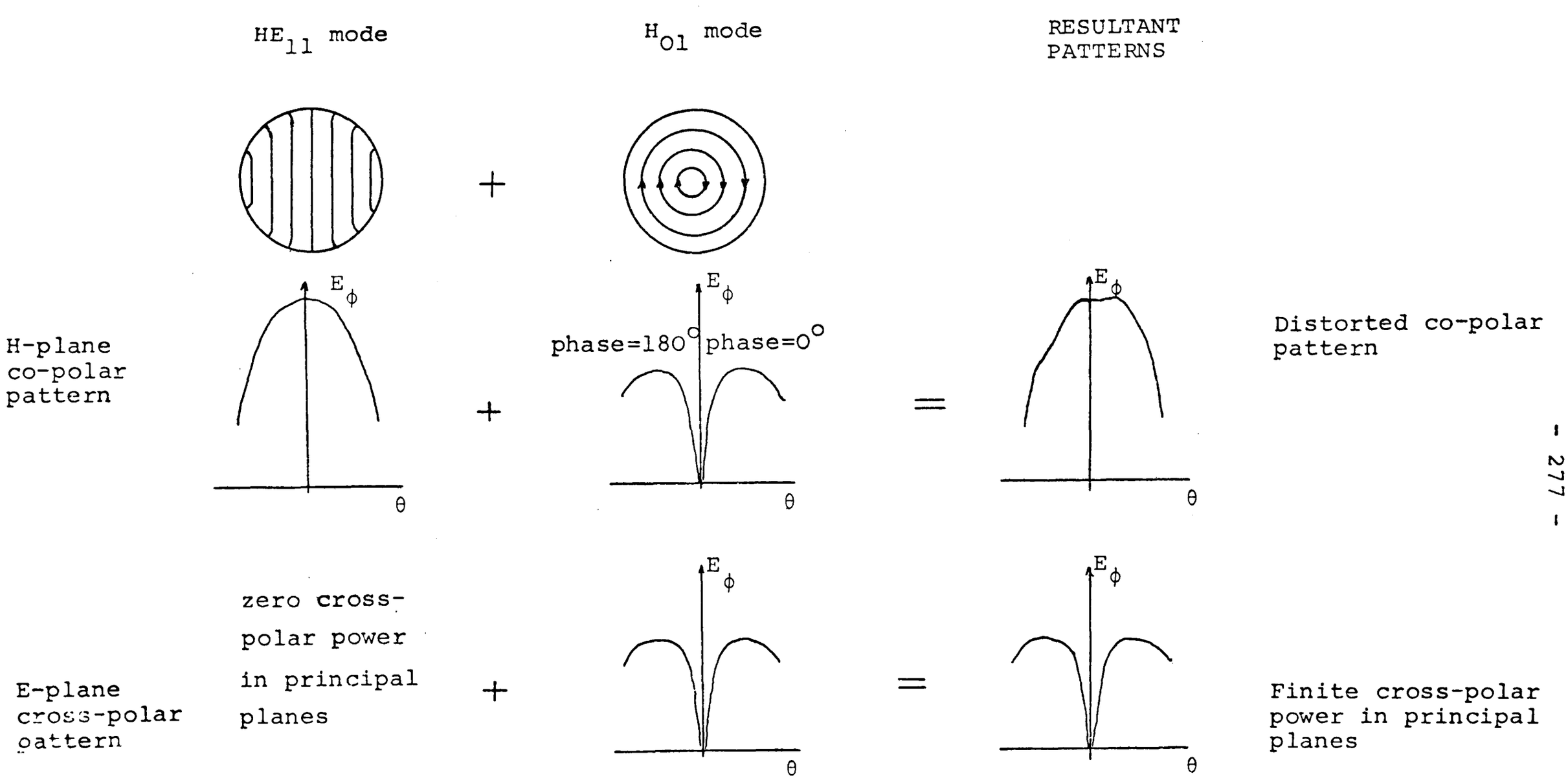

Fig. 9.8 The effect of the presence of one higher order mode on the principal plane co-polar and cross-polar HE_{11} mode radiation patterns

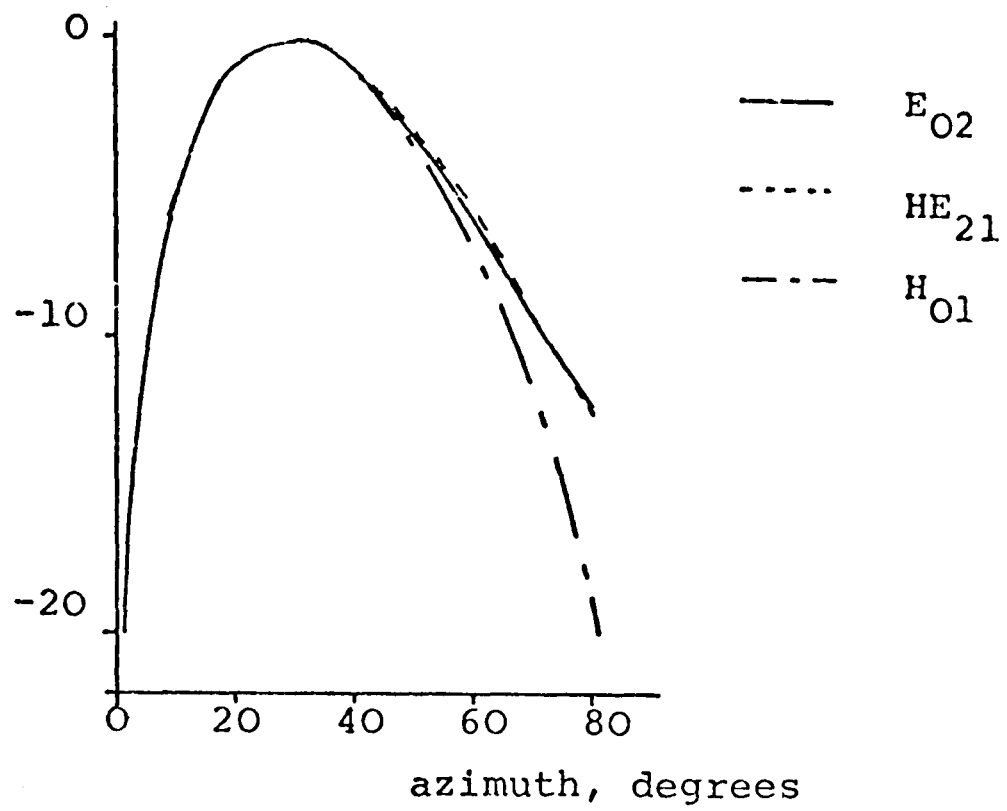

Fig. 9.9 Comparison of radiation patterns of the H_{01}, E_{02} and HE_{21} modes

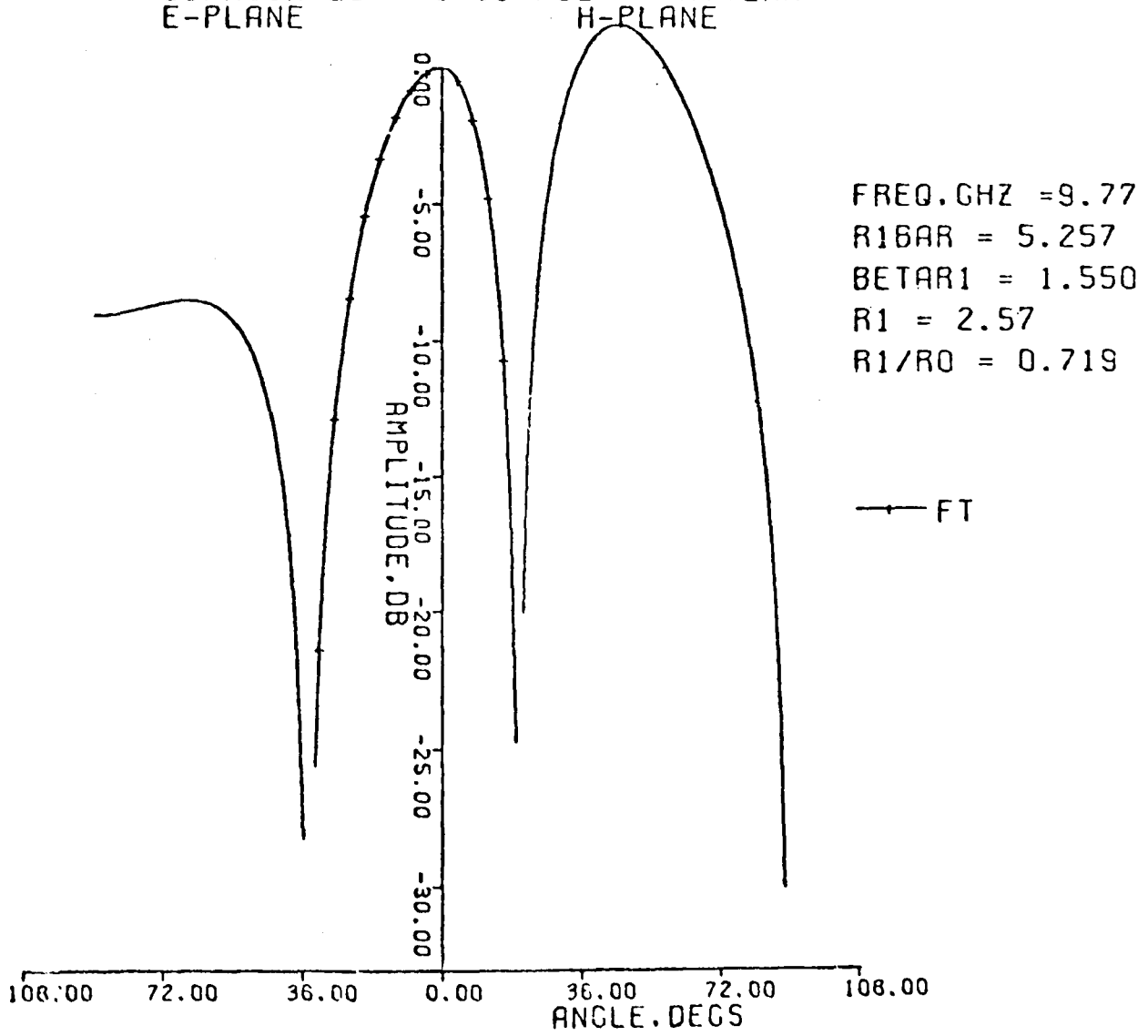

Fig. 9.10 Typical HE_{12} mode co-polar radiation pattern near to the mode low frequency cut-off

If the relative power coupling level of the higher order modes are known, or can be determined, the resulting co-polar and cross-polar electric field radiation patterns can be simply obtained by adding to the dominant mode pattern the individual patterns of each of the modes in proportion to their relative coupled powers. However, the relative phases at the aperture of these modes will generally be unknown and the value of 0^{o} or 180^{o} will, in practice, have to be assumed. But this does allow the maximum pattern distortion to be predicted. In chapter 10 it is shown that the presence of the HE_{12} mode in a corrugated waveguide aperture has to be accounted for if agreement between experiment and theory is to be achieved.

To conclude, this section has shown that a more accurate formulation for the radiation from an open-ended corrugated circular waveguide is obtained by approximating the terminating flange to be infinite, and to include one pair of higher order space-harmonics in the aperture field description. In addition, if higher order modes are known to be present in the aperture they should be accounted for in the pattern calculation. In chapter 10 radiation patterns predicted using this more accurate formulation are compared with measured co-polar and cross-polar patterns and good agreement is obtained.

9.4 EXTENSION OF THE CORRUGATED WAVEGUIDE RADIATION PATTERN ANALYSIS TO ENABLE RESULTS FOR NARROW FLARE-ANGLE CORRUGATED CONICAL HORNS TO BE OBTAINED

The co-polar radiation characteristics of corrugated conical horns have been successfully predicted by many workers. Clarricoats and Saha <26> have considered the two basic methods of analysis available, these both involve the description of the aperture field in terms of a single spherical hybrid mode. However the formulation, which is in terms of Associated Legendre Polynomials, becomes extremely complex unless a number of assumptions are made. One of these is to assume the corrugation depth is such that the longitudinal surface reactance is infinite, as in the optimum *balanced hybrid* operating condition for a corrugated feed horn. Having obtained the aperture field the far field pattern may be obtained by either a Kirchhoff-Huygens integration over a spherical constant phase surface at the aperture, or by expanding the aperture field in terms of free space spherical mode functions. This balanced hybrid approximation results in the prediction of a circularly symmetric co-polar radiation pattern and consequently zero radiated cross-polar power in all space. This analysis technique, whilst giving good co-polar pattern predictions <26>, is clearly inadequate for determining the cross-polar performance. However, it is possible to extend the theory developed in the previous section to enable the calculation of the co-polar and cross-polar radiation patterns for narrow flare-angle

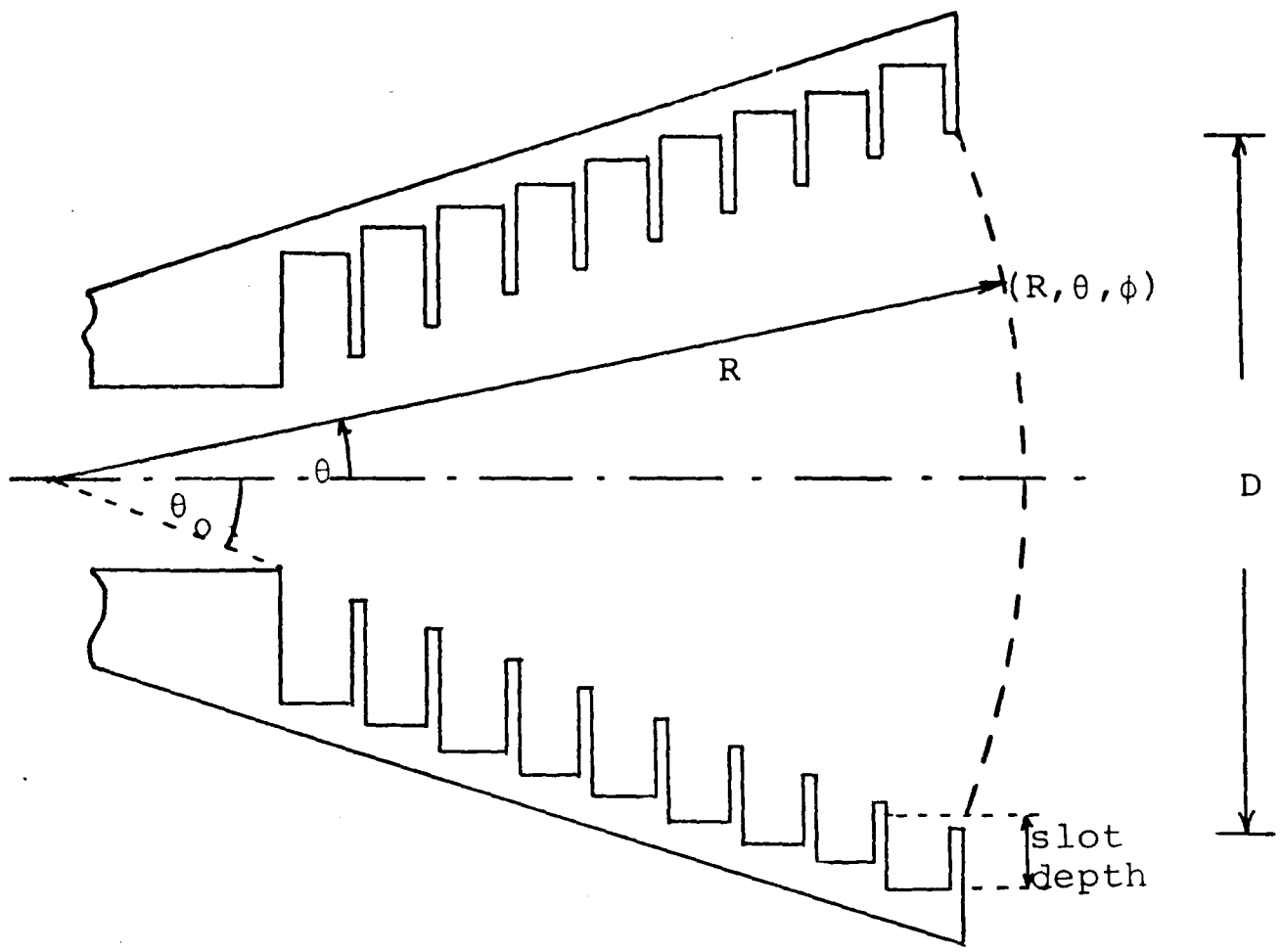

Fig. 9.11 Geometry for corrugated conical horn

corrugated conical horns. In appendix 9.3 it is shown that as the horn half angle, θ_o (figure 9.11), tends to zero, the formulation for the aperture fields of a conical corrugated horn, at the balanced hybrid condition and in terms of a single spherical mode, tends to the result obtained for the corrugated waveguide of equivalent aperture dimensions with the addition of a spherical phase distribution. The addition of this spherical phase distribution to the F.T. far-field radiation pattern formulation, appendix 9.3, means that the radial integral cannot be evaluated analytically. This integral was therefore evaluated numerically. Accuracy was checked by removing the spherical phase distribution and comparing the numerical result with the analytical result for the waveguide, excellent agreement being obtained.

Figure 9.12 compares the measured co-polar radiation pattern for a 12^o semi-flare-angle corrugated horn with theoretical points predicted using both the above waveguide approximation and the spherical wave expansion method <54>. Excellent agreement is obtained using the waveguide approximation, with even the first sidelobe being accurately predicted. In the waveguide approximation the slot depth at the aperture was taken to be that obtained at the midpoint of the slot, as shown in figure 9.11.

It is difficult to determine theoretically how large a horn flare angle can be used in this waveguide approximation because of the analytical complexity of the corrugated horn formulation. However Au <55> has shown

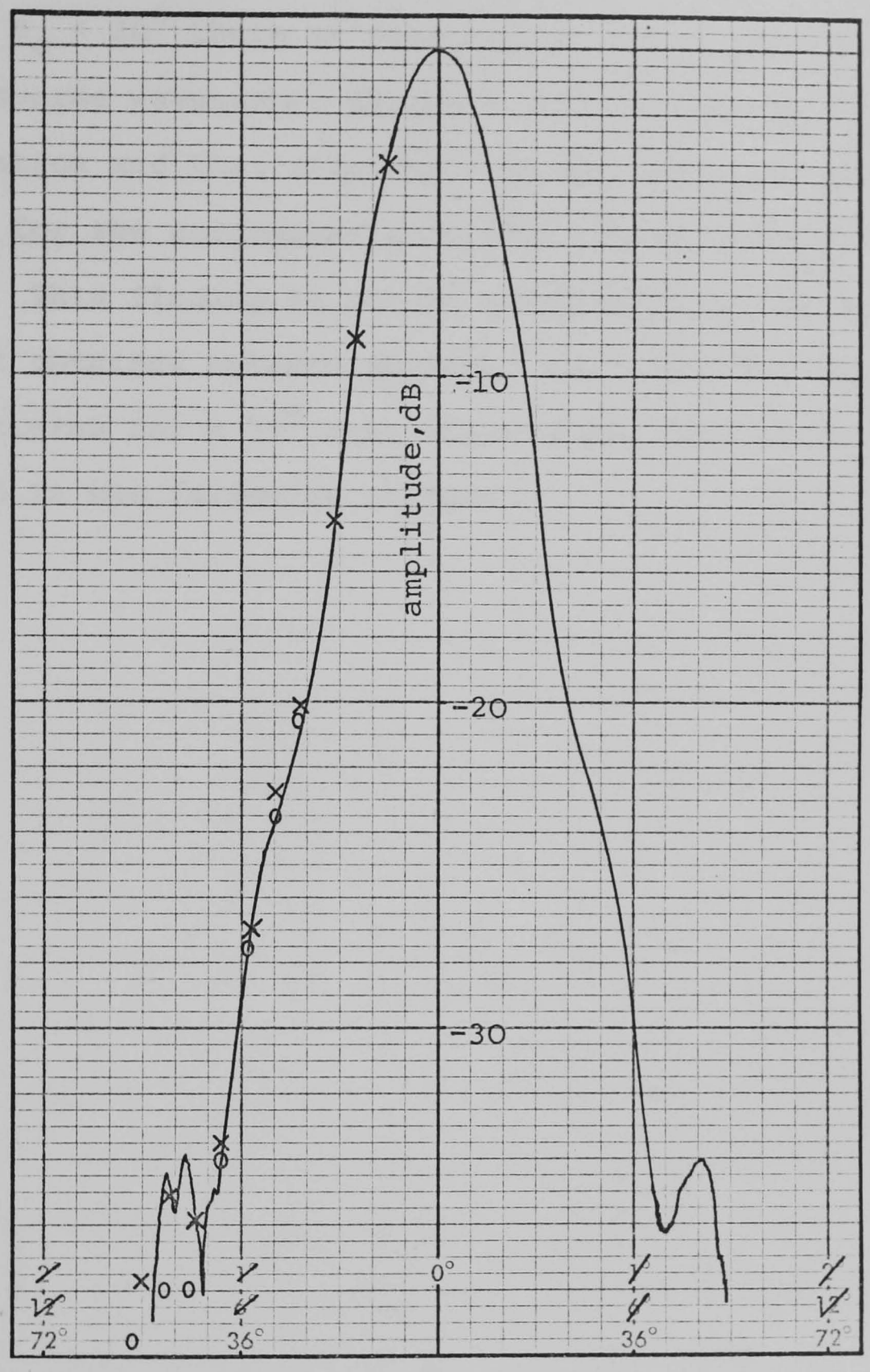

azimuth,degrees

Fig. 9.12 Measured and predicted co-polar radiation pattern for 12° semi flare-angle conical corrugated horn shown inset to figure 10.5

Theoretical points: X waveguide approximation

o spherical wave expansion

that for $\theta_o < 20^o$ there is very little difference between the transverse wavenumber obtained from the waveguide approximation and that obtained from the characteristic equation for the corrugated horn when the slant length is long. This finding is partly reinforced by the good agreement obtained between measured and predicted cross-polar patterns for a 12^o semi-flare-angle horn which are presented in the following chapter.

CHAPTER 10

THE DESIGN OF LOW CROSS-POLARISATION CORRUGATED CIRCULAR WAVEGUIDES AND NARROW FLARE-ANGLE CORRUGATED CONICAL HORNS

10.1 INTRODUCTION

The first part of this chapter compares the experimentally measured co-polar and cross-polar radiation patterns of corrugated waveguides and horns with results predicted using the improved theory developed in the previous chapter. Having verified that the F.T. method of analysis is a sufficiently accurate model for predicting the cross-polar radiation from corrugated waveguides, section 10.3 considers how the various waveguide parameters affect the cross-polar pattern. This study culminates in a set of design curves for optimum cross-polar performance. In section 10.4 a similar design study is performed for the narrow flare-angle conical corrugated horn. A quantitative study to determine the relative power level of higher order modes that can be tolerated before the cross-polar performance becomes significantly degraded is presented in section 10.5. In addition this section considers qualitatively the techniques required for efficient coupling into corrugated feeds and methods to reduce HE_{12} mode coupling, this latter effect being important if the full available cross-polar bandwidth is to be practically realised. Finally in section 10.6 the

general conclusions resulting from this study of cross-polarisation in corrugated waveguides and narrow flare-angle corrugated horns are presented.

10.2 COMPARISON OF MEASURED AND PREDICTED CO-POLAR AND CROSS-POLAR RADIATION PATTERNS FROM CORRUGATED WAVEGUIDES AND NARROW FLARE-ANGLE CORRUGATED HORNS

10.2.1 Co-polar radiation patterns of corrugated waveguides

In view of the difference between the predicted co-polar E and H-plane patterns for the corrugated waveguide, obtained using the K.H. and F.T. methods of analysis and illustrated by figures 9.3 and 9.5, it was considered necessary to verify experimentally that the proposed F.T. analysis of chapter 9 would yield accurate results. The waveguide used for these measurements is shown in figure 10.1, where the radiating aperture can be terminated in either a corrugation ridge or slot. The dimensions of this waveguide are equivalent to those used in calculating many of the example results of chapter 9. The E and H-plane patterns for this waveguide were measured at four different frequencies over X-band using the Q.M.C. Anechoic Chamber described in chapter 3. These measured patterns were compared directly with the theoretically predicted patterns which were drawn with identical scaling using a computer controlled plotter. Table 10.1 shows the pattern level, in dB, at which the theoretical pattern first deviates from that measured by $> \pm 1$dB. The results for the

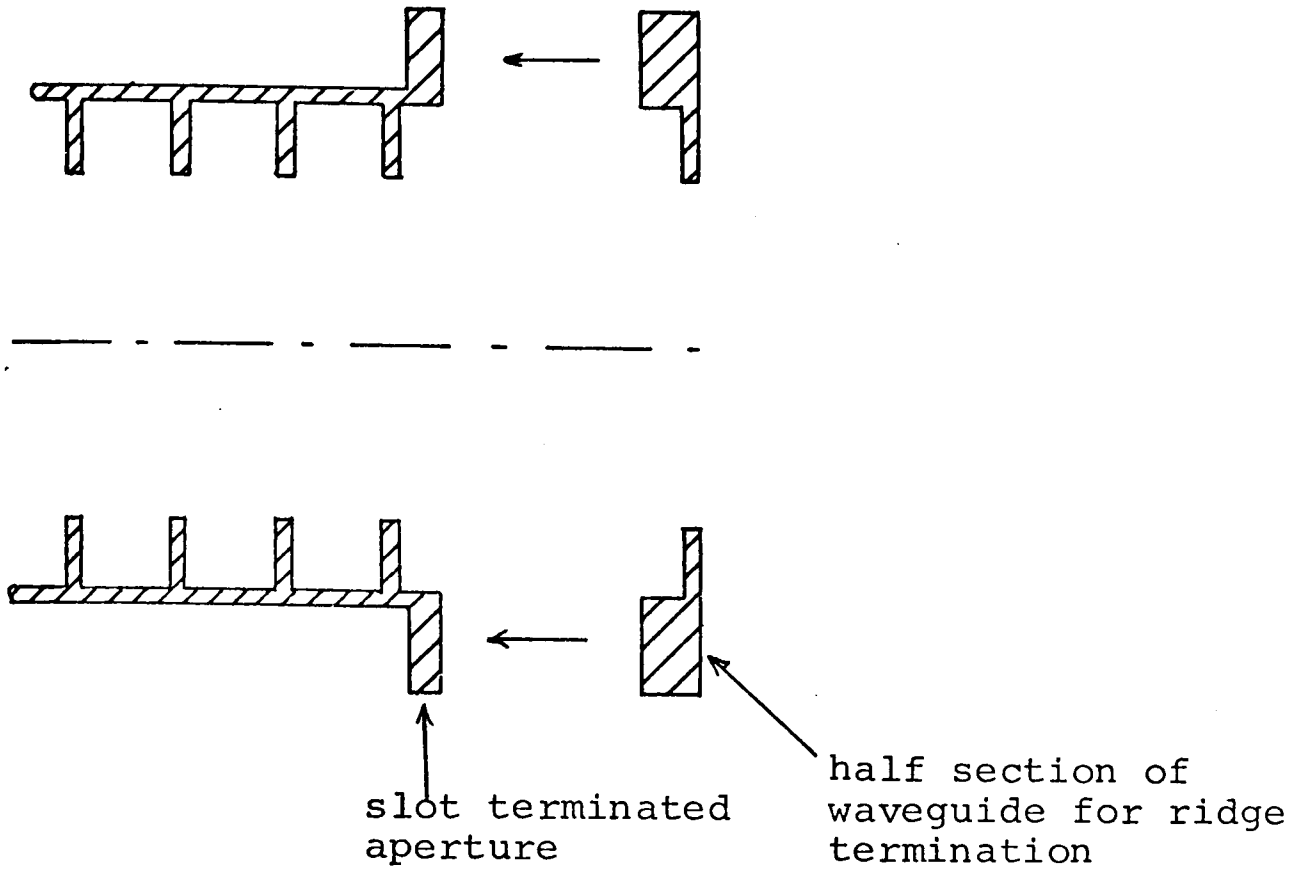

Fig. 10.1 Corrugated waveguide used in the radiation pattern measurement

Frequency, GHz	Normalised aperture diameter	F.T. Method		K.H. Method	
		E-Plane	H-Plane	E-Plane	H-Plane
8.2	1.4λ	-11dB	-25dB	-3dB	-10dB
9.0	1.5λ	-23dB	-20dB	-9dB	-30dB
10.0	1.7λ	-10dB	-8dB	-30dB	-8dB
11.0	1.9λ	-30dB	-30dB	-30dB	-30dB

Table 10.1 Level at which the theoretical patterns first deviate by 1dB from the measured patterns.

parameters: Measured waveguide terminated in ridge.
One pair of higher order space harmonics used in theory.

two lower frequencies, where the presence of the finite flange is more significant, indicate that the F.T. predicted results are more accurate. In the case of the two higher frequency results the measured patterns are slightly distorted by the presence of some HE_{12} mode present in the aperture (see section 10.3). The major pattern distortion occurs at 10GHz where the radiation pattern of the HE_{12} mode has an off-axis peak. At 11GHz the HE_{12} and HE_{11} mode radiation patterns are similar in shape and consequently the pattern distortion is considerably less, as indicated by the good agreement between the measured and predicted results. For the purposes of comparison, radiation patterns were first taken with a slot termination and then, without disturbing the waveguide position the ridge terminating section was added, figure 10.1, and the pattern retaken. The results obtained showed no practical difference in the measured co-polar patterns between the ridge and slot terminated aperture.

10.2.2 Cross-polar radiation patterns of corrugated waveguides

Cross-polar radiation patterns for the corrugated waveguide considered in the previous sub-section were measured in the 45^{o}-plane, using the method described in chapter 3. Figure 10.2 shows the measured cross-polar pattern, curve B, at a frequency of 9GHz compared with the predicted result, curve D, obtained using the infinite

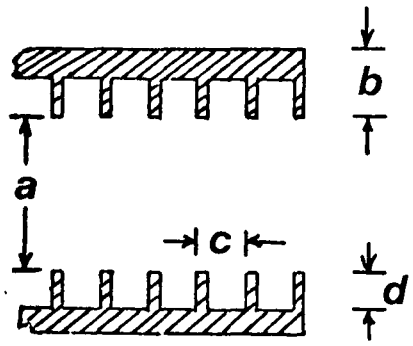

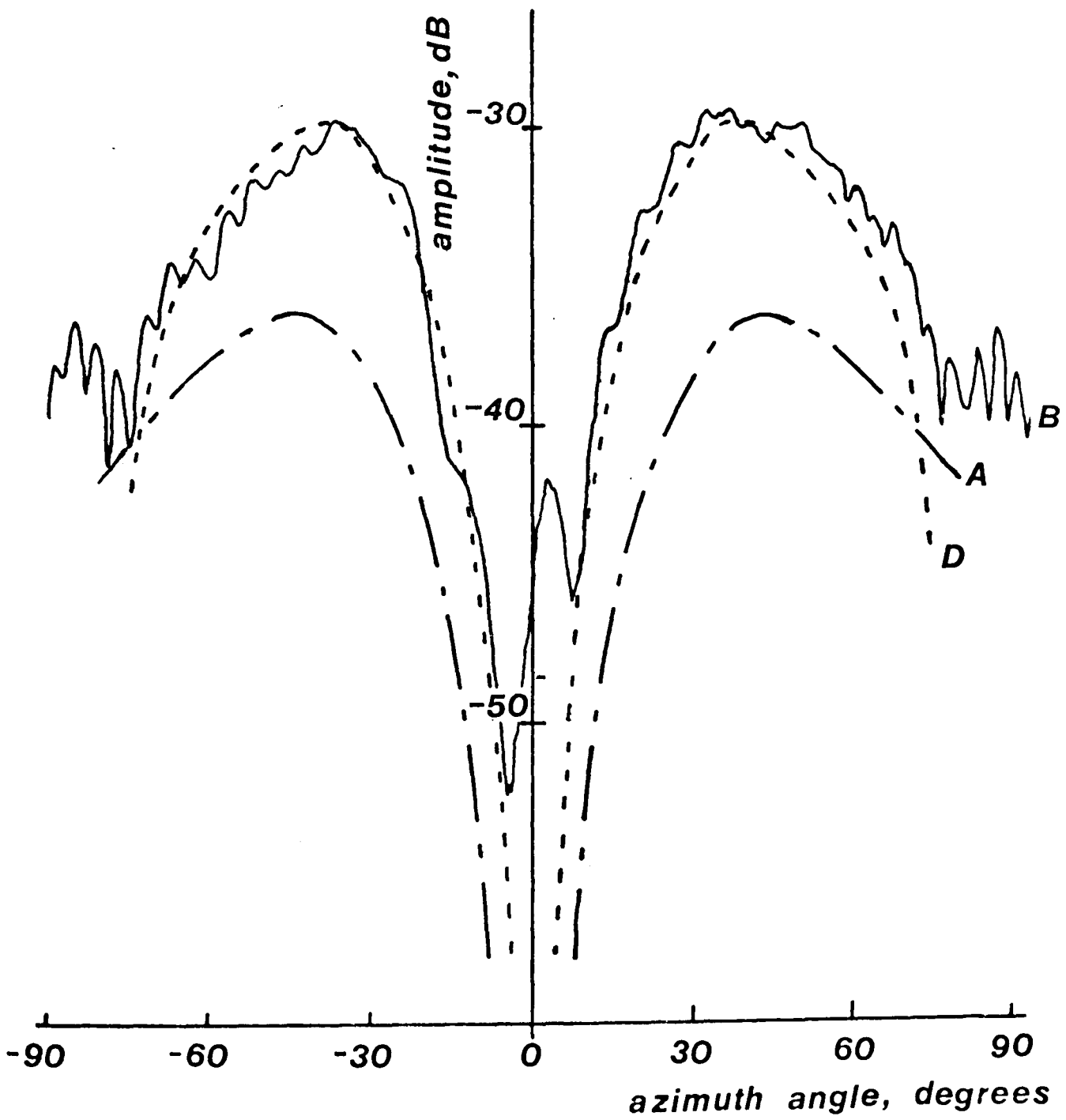

Fig. 10.2 Measured (curve B) and theoretical (curves A and D) cross-polar radiation patterns of open-ended corrugated circular waveguide shown in inset.

Parameters: a = 50mm, b = 25mm, c = 11.6 mm, d = 10mm
Frequency = 9GHz

flange approximation and including one pair of higher order space-harmonics to describe the aperture field. Very good agreement is obtained by using this analysis compared with curve A which shows the predicted pattern obtained using the K.H. method with surface impedance derived aperture field. The inadequacy of this latter method in predicting the cross-polar pattern is evident.

The maximum value of the measured cross-polar patterns is shown plotted as a function of frequency in figure 10.3, along with the predicted curve (D) obtained using the improved theory. Below 9.5GHz the agreement is within the experimental accuracy of ±1dB. This accuracy being made up from ±0.5dB due to range reflectivity (see chapter 3) and ±0.5dB for the microwave receiving equipment. Above 9.5GHz there exists an obvious discrepancy between the measured and predicted results. However, above 9.4GHz the HE_{12} mode can propagate in the waveguide and, as described in chapter 9, its presence will increase the level of radiated cross-polar power. After the transition from smooth wall to corrugated waveguide an increase in diameter is required to achieve the desired waveguide size, and this change in diameter can cause coupling to the HE_{12} mode. In chapter 3 a measurement technique was described to determine the level of HE_{12} mode at the radiating aperture. Using this method a power coupling level of about -20dB relative to the HE_{11} mode was measured for this particular waveguide and transition. When the presence of this level of HE_{12} mode

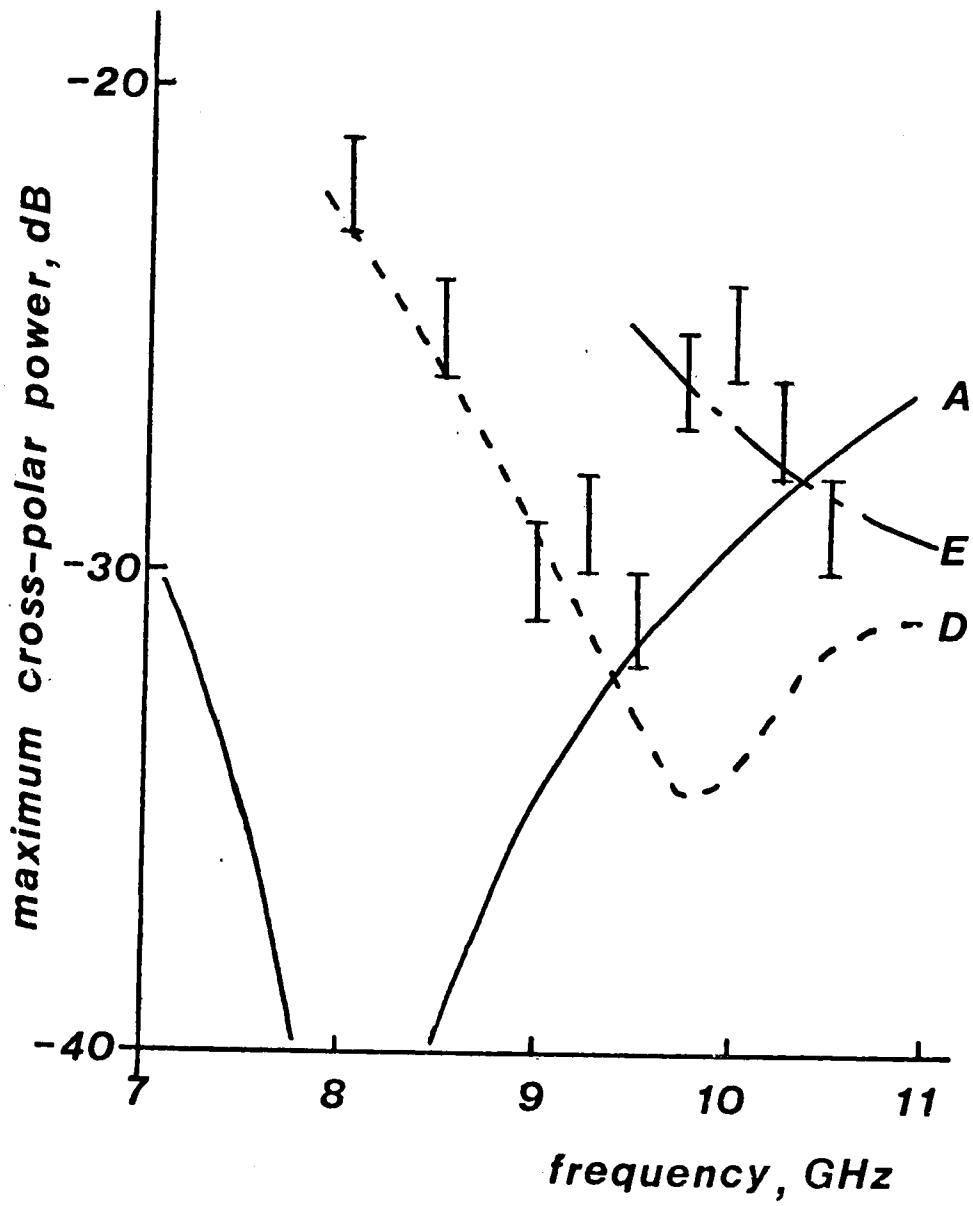

Fig. 10.3 Measured and predicted results for the peak radiated cross-polar power as a function of frequency for the waveguide of figure 10.2. See text for explanation of theoretical curves.

is included in the pattern calculations curve E is obtained for the maximum radiated cross-polar power above 9.4GHz and agreement to within experimental accuracy is again obtained. Because the relative phase between the HE_{12} and HE_{11} modes is unknown, and the fact that it will change with frequency, the phase difference of 0^{o} or 180^{o} giving the highest cross-polar power was used when calculating curve E of figure 10.3. Also shown in this figure is the theoretical curve, A, calculated using the K.H. method with surface impedance derived aperture field. The inaccuracies resulting from the approximations made when using this analysis are clearly demonstrated.

The measured cross-polar patterns, of which figure 10.2 is an example, exhibit quite definite on-axis nulls indicating a very low level of orthogonally polarised HE_{11} mode generated in the waveguide. This is to be expected over the short length (12cm) of corrugated waveguide forming the test antenna.

Cross-polar patterns were also measured to determine the effect of terminating the waveguide aperture in a ridge or a slot. The technique described in the previous sub-section was used and it was found that the cross-polar pattern was generally slightly lower for the slot termination. It is concluded that for this size of waveguide there is little practical difference in the radiation performance between terminating in a corrugation ridge or a slot. However, for smaller diameter waveguides ($<1.5\lambda$) where edge currents are higher this may not be the case.

10.2.3 Cross-polar radiation patterns of narrow flare-angle conical corrugated horns

Comparison of the measured co-polar pattern for the 12^{o} semi-flare-angle corrugated conical horn shown in figure 10.4 with the theoretically predicted pattern obtained using the waveguide approximation, developed in chapter 9, gave excellent agreement as figure 9.12 of that chapter showed. Figure 10.5 compares the measured and predicted cross-polar pattern for this same horn, shown inset to the figure, at a frequency of 10GHz. Good agreement between experiment and theory being obtained, the slight offset of the measured boresight null being due to the sensitivity of the measured pattern to minute misalignments between the horn and anechoic chamber source antenna. The peaks of the measured cross-polar patterns plotted as a function of frequency are shown in figure 10.6 and good agreement between experiment and theory is obtained up to a frequency of 10.4GHz. Above this frequency the measured pattern becomes higher than that theoretically predicted and this is attributed to coupling into the HE_{12} mode in the throat region of the horn, a problem which is considered in section 10.5.

10.2.4 Conclusions

In this section it has been shown that the F.T. theory developed in chapter 9 gives an accurate prediction of the cross-polarisation radiated from both corrugated circular waveguides and narrow flare-angle

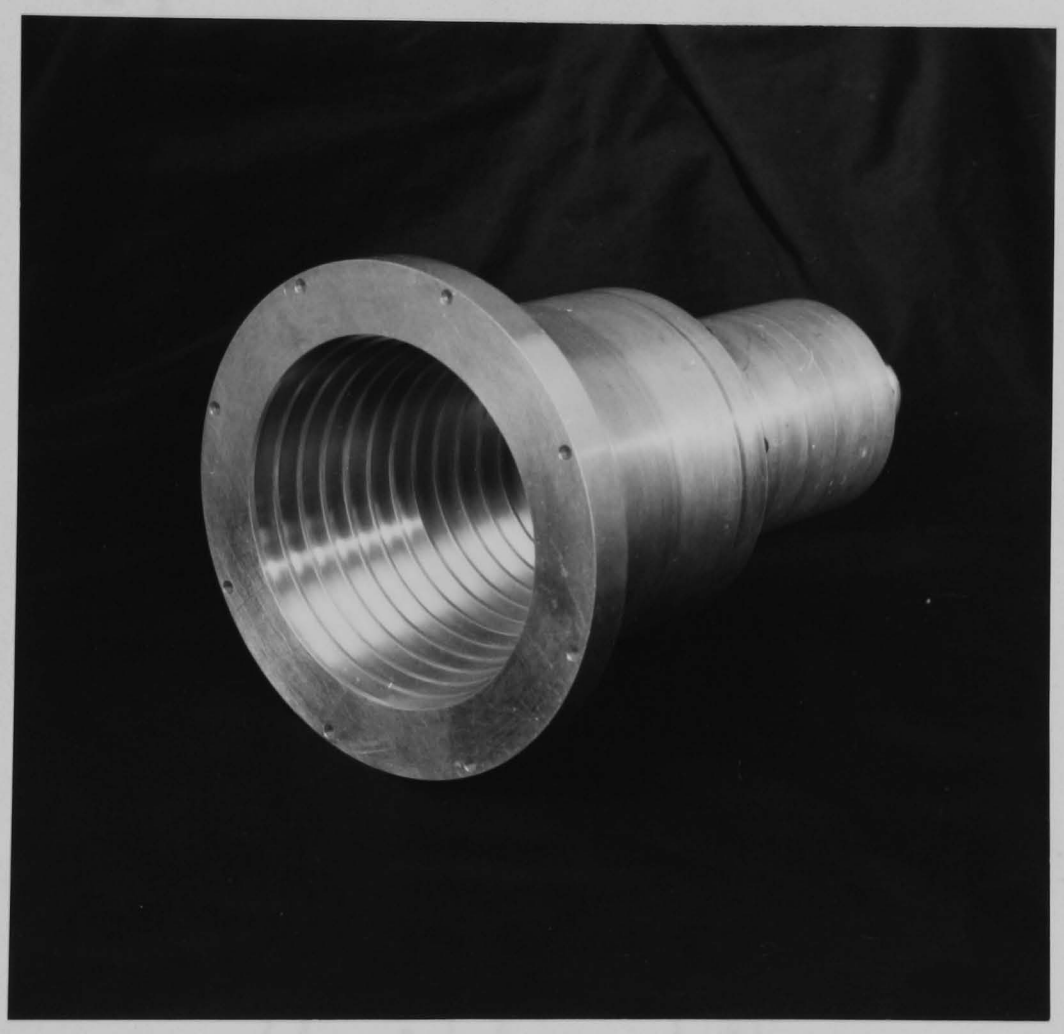

Fig. 10.4 The 12^{o} semi flare-angle corrugated conical horn; dimensions are shown in figure 10.5

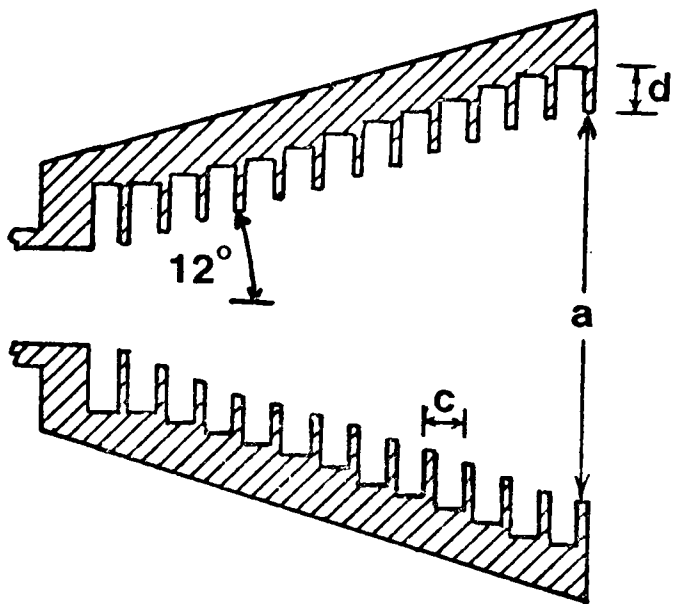

a = 127mm

c = 9·5mm

d = 9·5mm

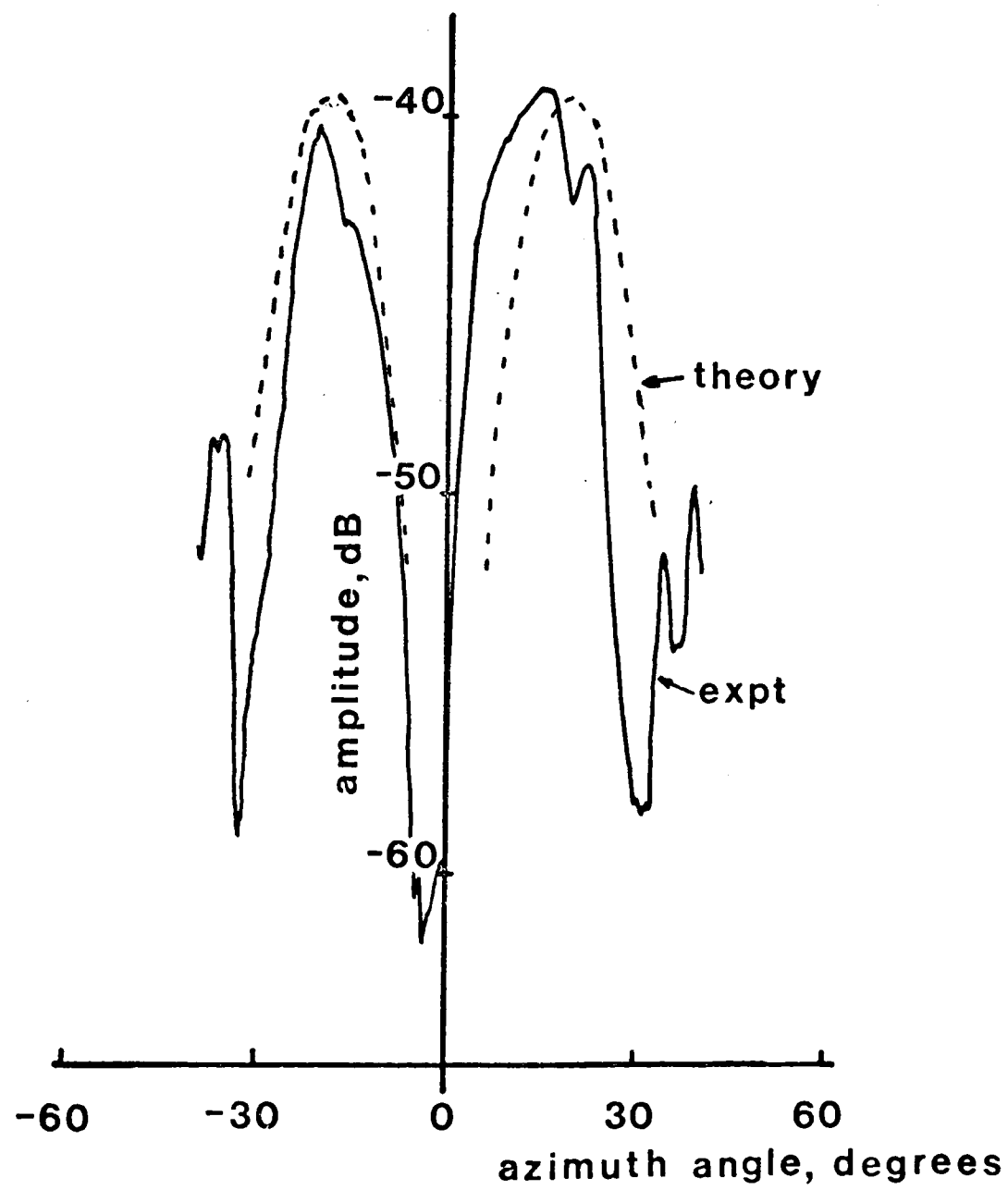

Fig. 10.5 Comparison of the theoretical and measured cross-polar radiation pattern for the corrugated horn shown inset, frequency 10GHz

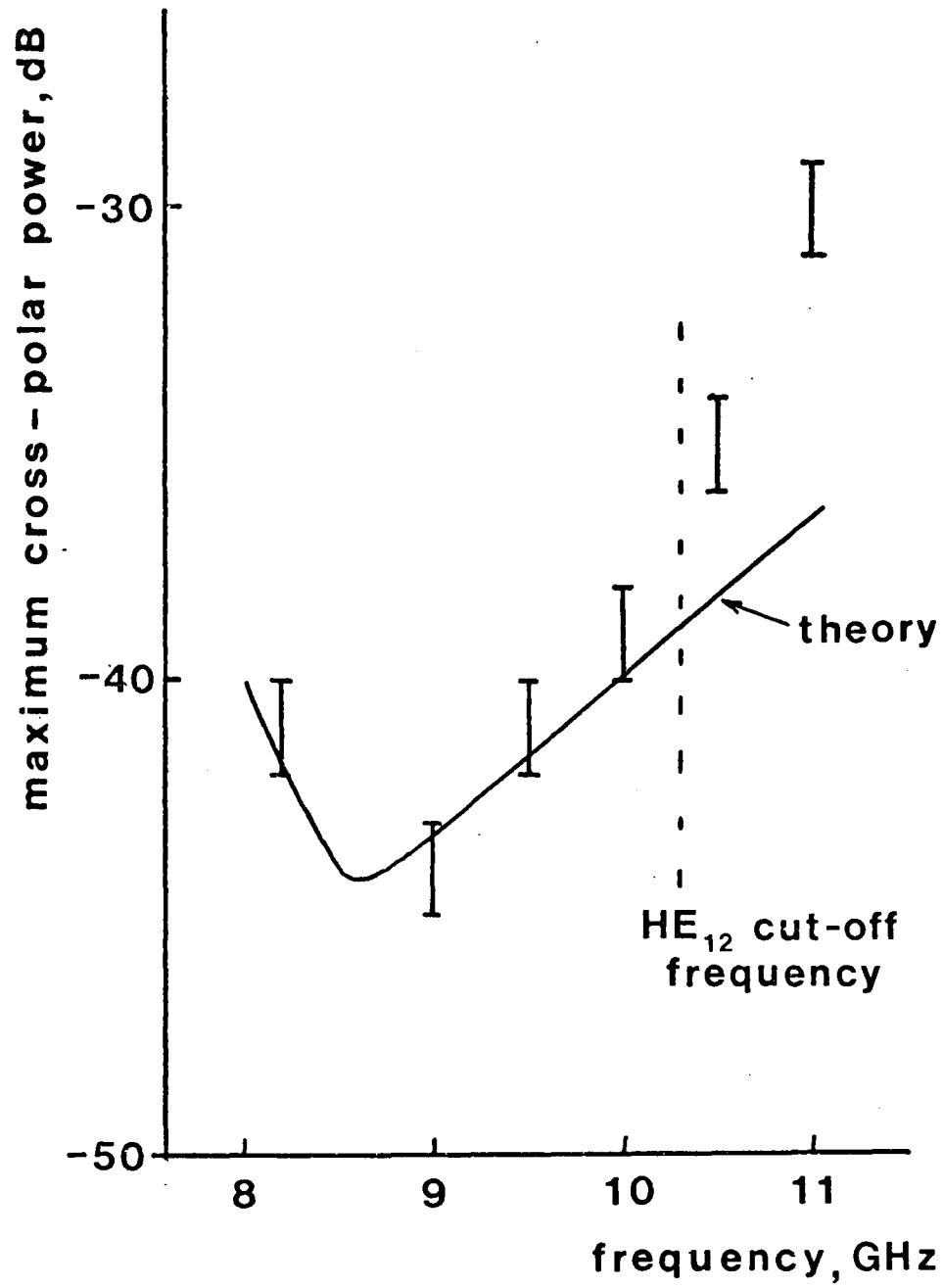

Fig. 10.6 Measured and predicted peak cross-polar power as a function of frequency for the corrugated horn shown in figure 10.5.

corrugated conical horns. It therefore becomes realistic to perform a parametric study to determine how the waveguide parameters control the radiated cross-polar power and hence derive design curves for optimum cross-polar performance. This study is described in the following section.

10.3 CORRUGATED WAVEGUIDE DESIGN FOR OPTIMUM CROSS-POLAR PERFORMANCE

It has been shown in the previous section that the frequency at which the peak cross-polar power is a minimum is considerably different from the balanced hybrid frequency previously thought to yield this property <26>. At the balanced hybrid frequency the normalised slot depth of the corrugations is $\lambda/4$ and this has, to date, been generally used as the design criteria for corrugated feeds. This is an adequate criteria for co-polar pattern design due to the wide bandwidth over which the corrugated feed exhibits a near circularly symmetric radiation pattern. However, it is a totally inadequate criteria for cross-polar pattern requirements. Using the improved F.T. theory developed in chapter 9 figure 10.7, curve A, shows the optimum slot depth, in wavelengths, as a function of waveguide aperture diameter, also in wavelengths, required for a minimum in the peak cross-polar frequency characteristics. This curve was obtained for a waveguide having 3 corrugations per wavelength, this being the optimum size for low

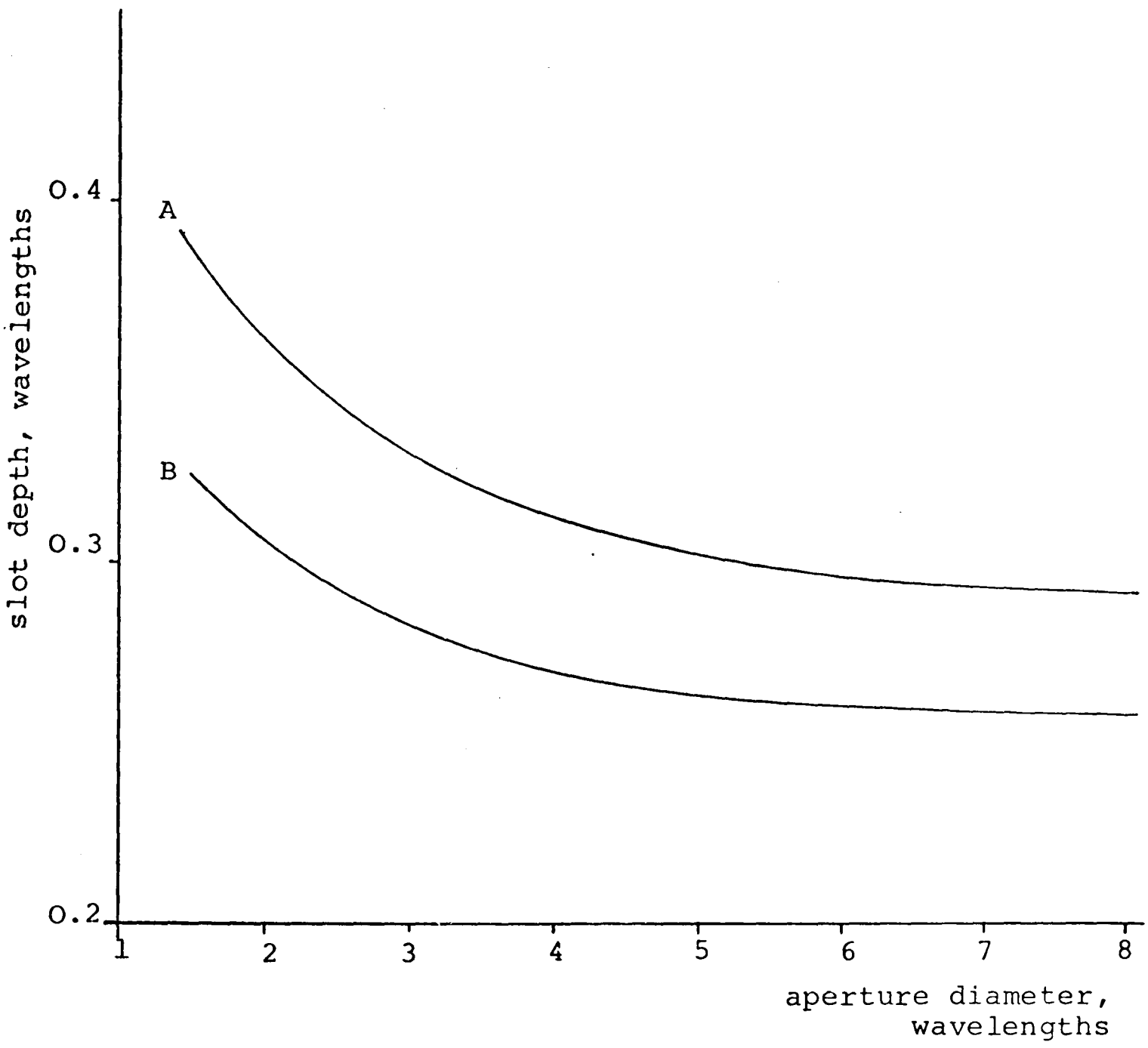

Fig. 10.7 Optimum normalised slot depth for minimum radiated cross-polar power as a function of normalised aperture diameter.

Parameters: curve A ridge width = 0.033λ
slot width = 0.3λ

curve B surface impedance result

attenuation < 5 >. For large normalised aperture diameters the normalised slot depth remains fairly constant for increasing aperture size at a value of 0.29λ. It is interesting to note that Clarricoats, Olver and Chong < 5 > have shown that the optimum slot depth for minimum attenuation is approximately 0.3λ. Figure 10.8 demonstrates the advantage of using the slot depth design curve of figure 10.7 as opposed to the λ/4 criteria when designing a waveguide feed for minimum cross-polarisation.

For a corrugated waveguide with smaller corrugation periodicity curve A of figure 10.7 slowly drops until there are a large number of corrugations per wavelength, at which point the surface impedance analysis becomes a very good approximation and curve B is obtained for the optimum slot depth. However, even in this case the λ/4 slot depth design criteria only applies to large normalised aperture diameters where the effect of the flange becomes negligible.

A normalised aperture diameter of 1.5λ represents about the smallest size of corrugated waveguide that can, in practice, be used and still exhibit the desirable properties of the hybrid mode. Below this size of waveguide the slot depth required to obtain minimum cross-polarisation rapidly becomes deeper and the HE_{11} mode begins to have properties more akin to the EH type modes <26>.

Figure 10.9 shows that by increasing the periodicity

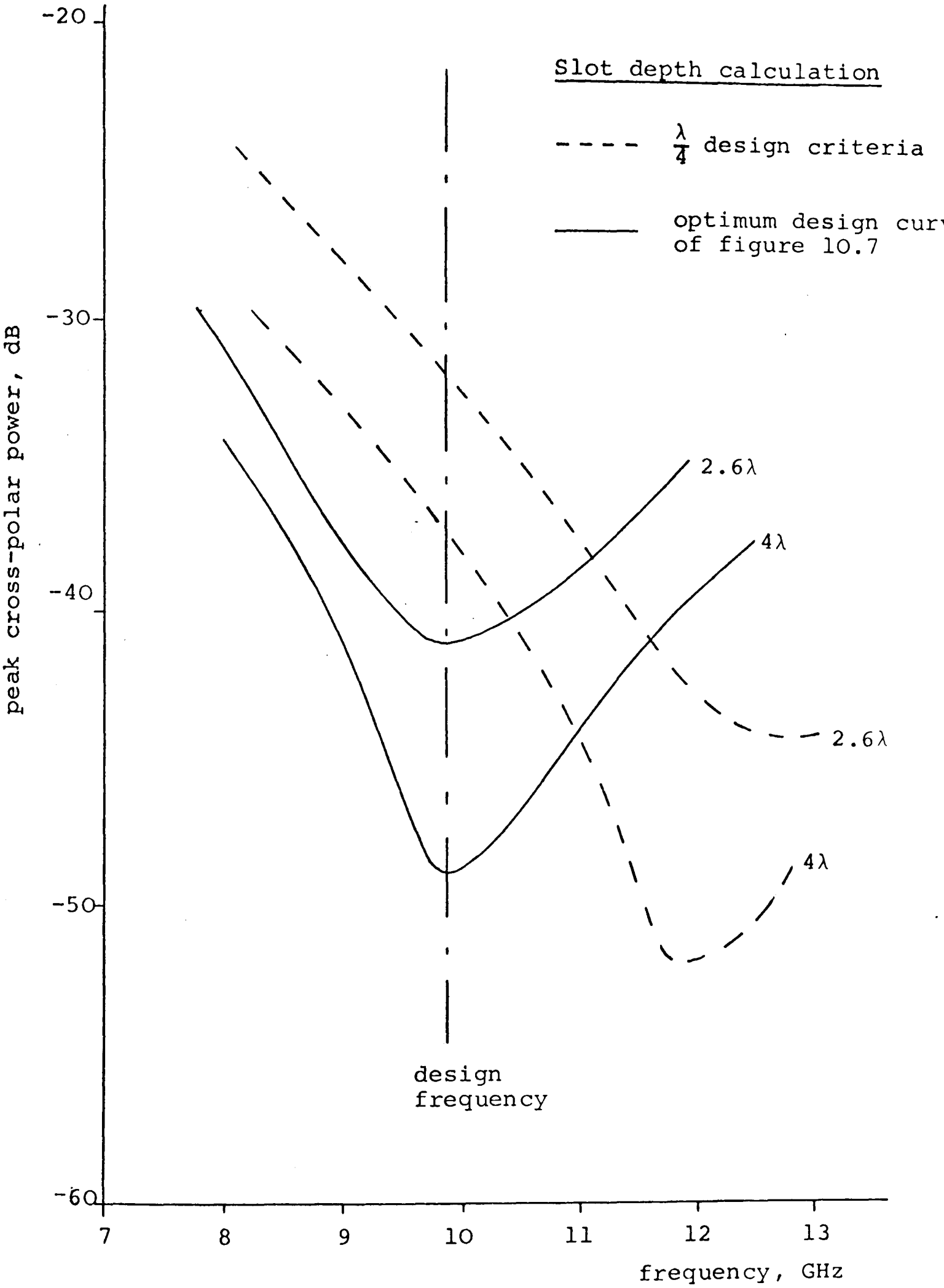

Fig. 10.8 Theoretical peak cross-polar power as a function of frequency for several corrugated waveguides designed using a slot depth of $\lambda/4$ compared with the results obtained using the optimum slot depth design of figure 10.7 curve A

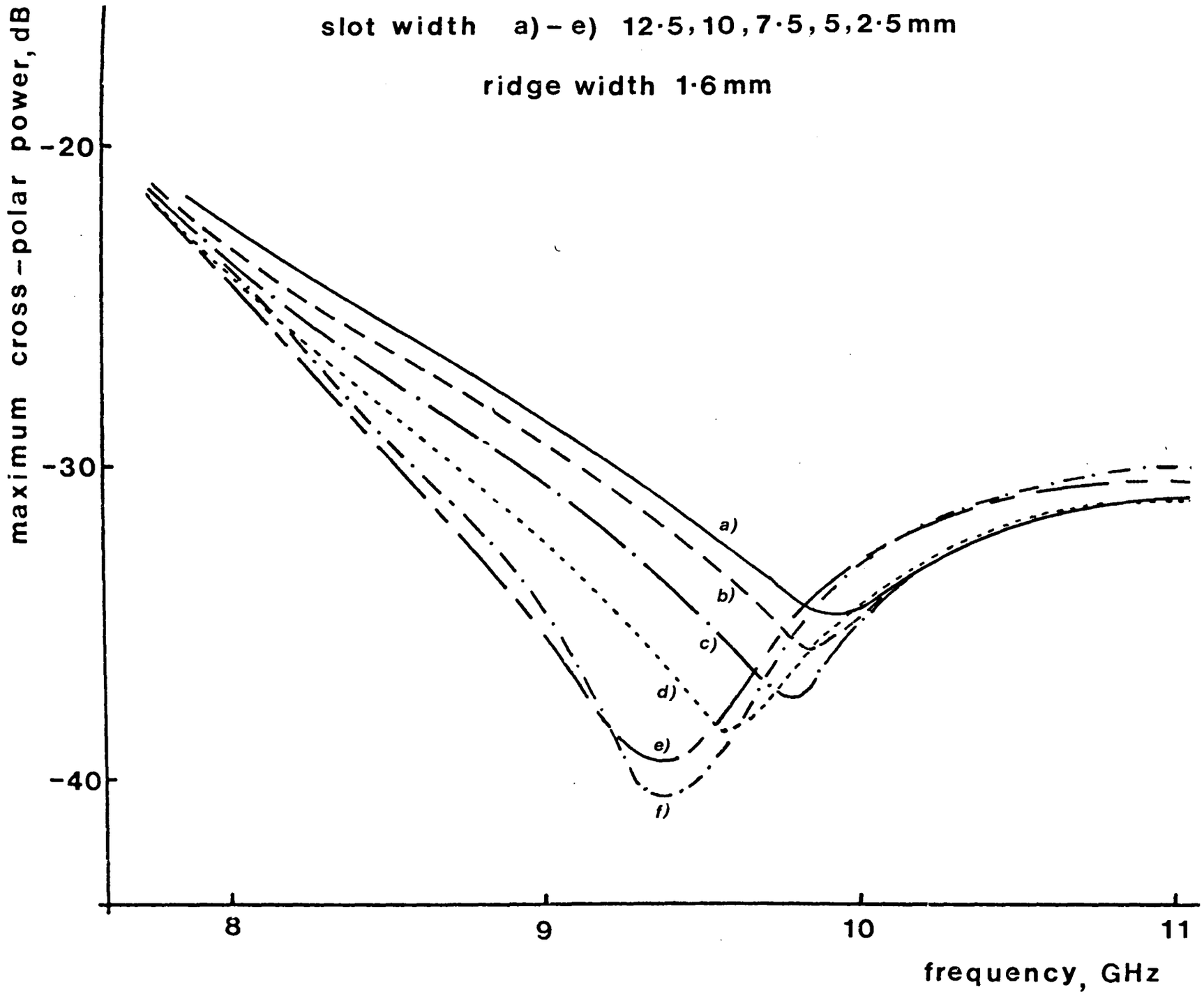

Fig. 10.9 Peak cross-polar as a function of frequency for the corrugated waveguide of figure 10.2, parameter slot width

of the corrugations and so decreasing the amplitude of the higher order space-harmonics, the cross-polar power radiated from the waveguide of figure 10.1 can be reduced. When the corrugation periodicity is 4.1mm, curve (e), the validity of using the surface impedance approximation, curve (f), becomes evident. To verify the low predicted cross-polarisation in this case a corrugated waveguide of the same dimensions as used in the previous measurements, but with a corrugation periodicity gradually increased to the value of 4.1mm at the aperture, figure 10.10, was manufactured and tested. The measured peak cross-polar, frequency characteristic obtained is shown in figure 10.11, good agreement with the predicted curve being obtained up to the frequency of HE_{12} mode propagation. The improvement over the measured results for the original 11.6mm corrugation periodicity design is evident. It has been found that this reduction in cross-polarisation obtained by the increased corrugation periodicity can be achieved for waveguides with normalised aperture diameters $<2\lambda$. This technique could therefore be advantageously employed in improving the cross-polar performance of small corrugated waveguide feeds. For larger diameter apertures the effect of the increased periodicity is to reduce the frequency at which the cross-polarisation minimum occurs. Therefore by making the last few corrugations at the aperture removable, sections which terminate in different corrugation periodicities could be substituted until the cross-polar minimum occurs at the desired frequency. This

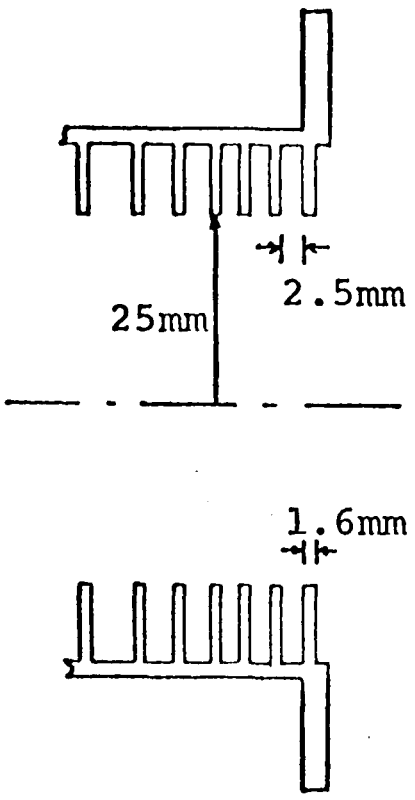

Fig. 10.10 Corrugated waveguide with increased periodicity at the radiating aperture

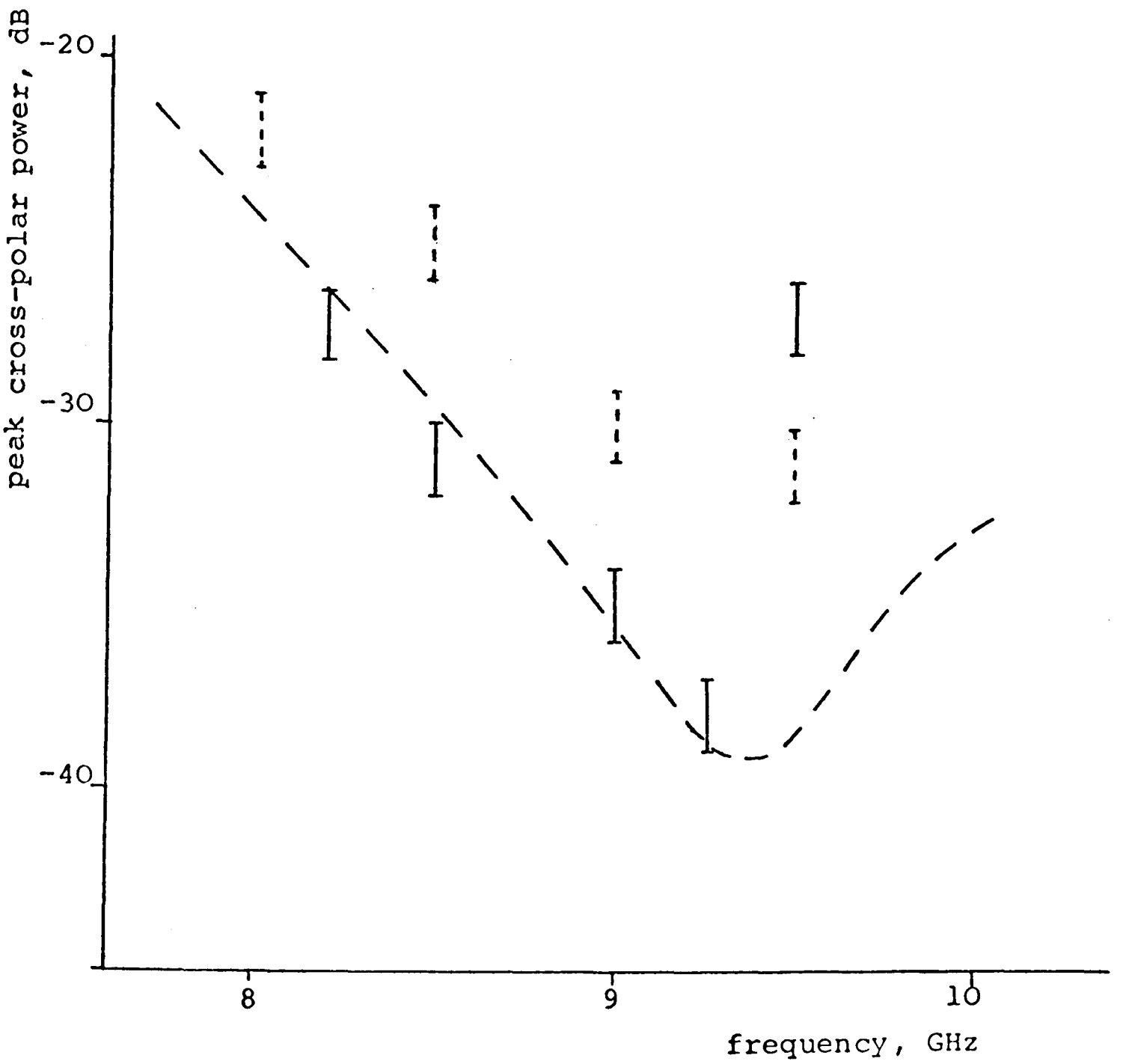

Fig. 10.11 Comparison of measured and predicted peak radiated cross-polar as a function of frequency for the corrugated waveguide of figure 10.10.

| measured points

– – – theoretical curve

¦ measured points for slot width = 10mm

technique could be usefully exploited in experimentally optimising the cross-polar performance of large expensive corrugated horns, used for example in satellite ground stations.

As an aid to design figure 10.12 curve A shows, as a function of normalised waveguide aperture diameter, the level of cross-polar power obtained over a certain bandwidth when the slot depth is chosen in the optimum way from figure 10.7 (curve A). The presence of the HE_{12} mode, as well as other higher order modes, are neglected and consequently figure 10.12 indicates the best cross-polar performance that can be achieved. Curve B of this figure shows a similar result for a waveguide with high corrugation periodicity corresponding to the optimum slot depth design of figure 10.7 (curve B).

Shown in figure 10.13 are the -10dB, -15dB and -20dB co-polar radiation pattern beamwidths obtained at the design frequency when the slot depth is chosen in an optimum way from figure 10.7. The beamwidth is practically independent of the higher order space-harmonics and consequently practically independent of the corrugation periodicity. Figures 10.7, 10.12 and 10.13 form a set of design graphs for corrugated waveguide feeds and these can be used in the following way.

1) Using figure 10.13 the normalised aperture diameter is found to achieve the desired beamwidth.

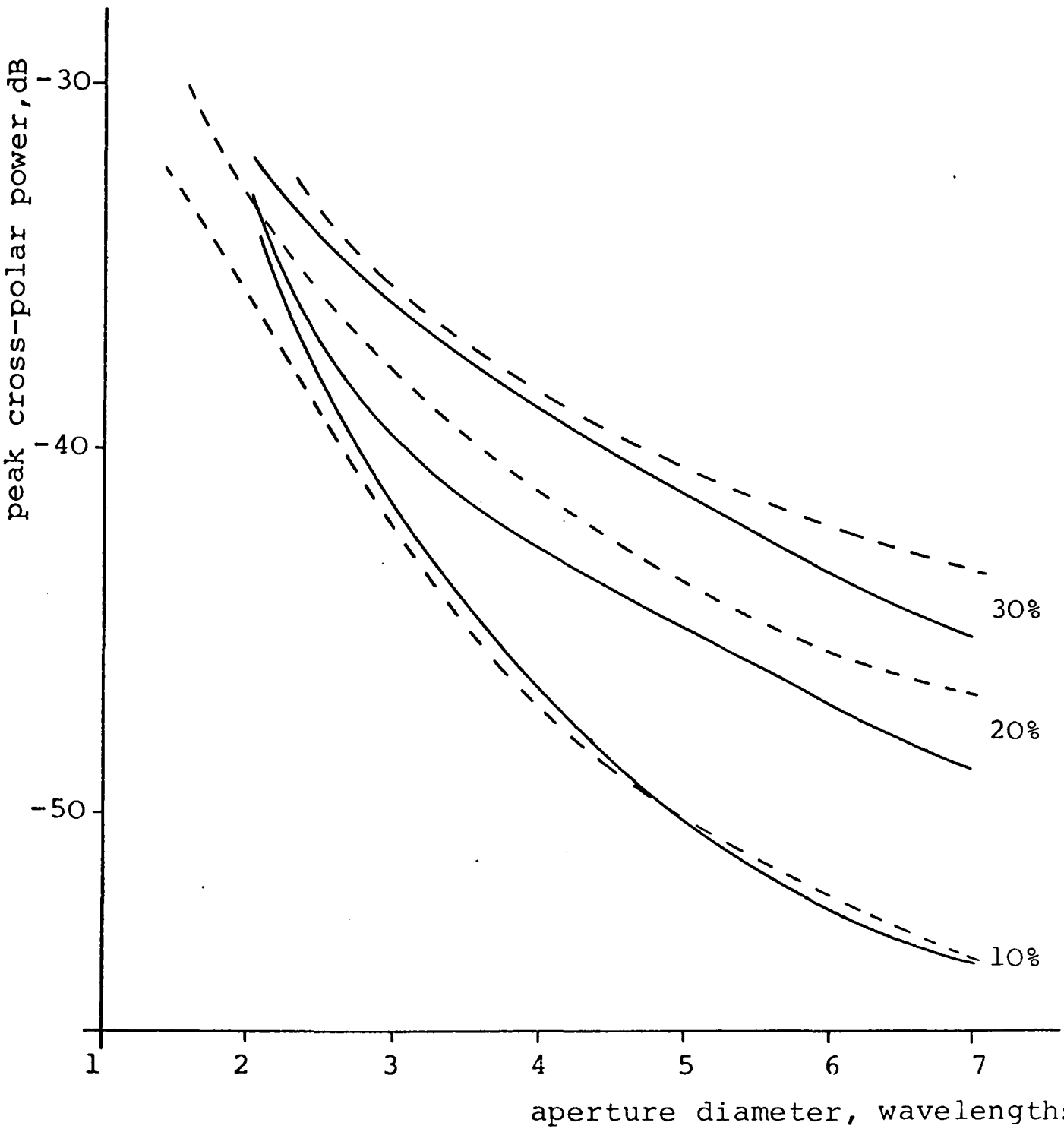

Fig. 10.12 Peak radiated cross-polar power over several percentage bandwidths as a function of normalised aperture diameter for corrugated circular waveguides designed optimially using figure 10.7

A —— space harmonic result; slot width = 0.3λ, ridge width = 0.03λ

B ---- surface impedance result

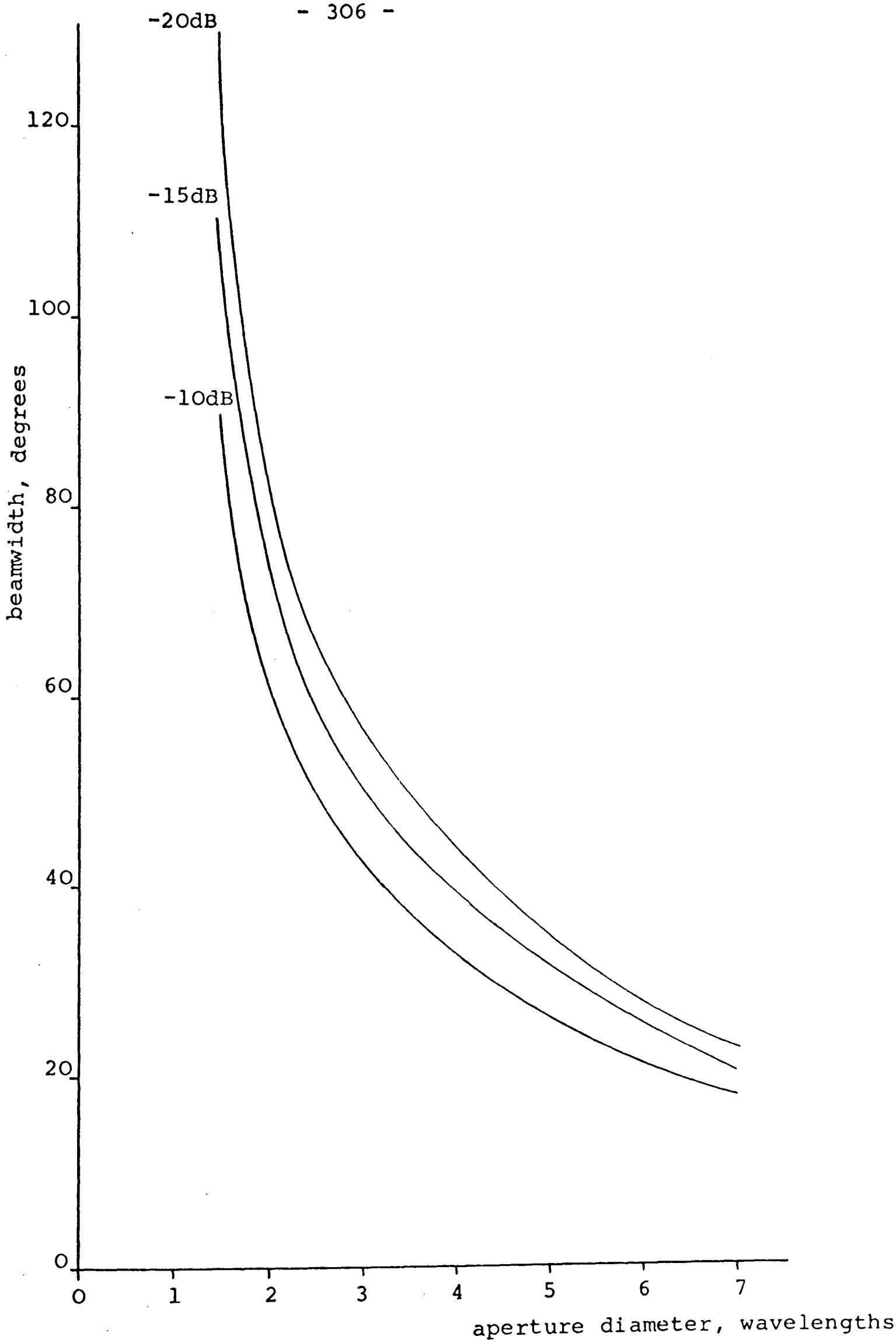

Fig. 10.13 Co-polar pattern beamwidth as a function of normalised aperture diameter for a corrugated waveguide designed for minimum cross-polarisation using figure 10.7. Parameter: co-polar pattern level

2) Figure 10.12 then gives the obtainable cross-polar power over the desired bandwidth when negligible HE_{12} mode coupling occurs. A choice of corrugation periodicity at the aperture is then made depending on the level of cross-polar power required.

3) Figure 10.7 is then used to obtain the normalised slot depth required.

Further improvements in the cross-polarisation performance of corrugated feeds will only follow if the undesirable effects of the plain metal flange can be reduced. The effect of the flange is to force the tangential E-field, but not the tangential H-field, to zero. This difference in the treatment of the E and H fields upsets the essential form of the exterior fields required for zero cross-polarisation. Rumsey <56> has shown that for a feed with a circular aperture zero cross-polarisation can be achieved so long as the boundary conditions at the aperture plane are the same for *both* the E and H fields. The presence of the finite flange at the corrugated waveguide aperture does not fulfil this requirement resulting in the *filling-in* of the cross-polar null predicted using the K.H. analysis (figure 10.3). One possible way of achieving the desired boundary conditions is to extend the corrugations around the flange as shown in figure 10.14(a), this method being originally proposed by Minnett and Thomas <57> for improving the co-polar radiation pattern symmetry. Good experimental pattern symmetry was obtained but with a slight decrease in beam-

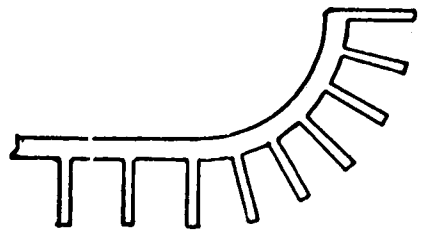

(a)

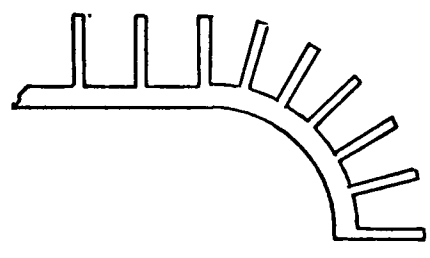

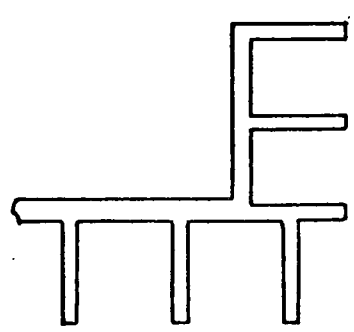

(b)

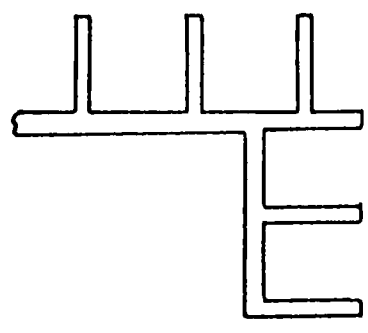

Fig. 10.14 Several proposed methods of achieving the desired boundary conditions at the radiating aperture of a corrugated waveguide.

width, due to the larger effective aperture caused by the flaring. This latter effect is a disadvantage when wide beamwidths are required to illuminate front-fed paraboloid reflectors.

In an attempt to overcome this beam narrowing effect the flange was corrugated as shown in figure 10.14(b). However, measurements showed that the peak cross-polar frequency characteristic was inferior when compared to that for the plain metal flange termination. The reason for this is most probably due to the fact that the *effective* radiating aperture is at the last corrugation ridge, thereby explaining the close similarity between the cross-polar patterns measured with slot and ridge terminated apertures.

10.4 NARROW FLARE-ANGLE CORRUGATED CONICAL HORN DESIGN FOR OPTIMUM CROSS-POLAR PERFORMANCE

In this section the presence of the horn spherical phase distribution on the cross-polar performance and its effect on the optimum design curves of the previous section are considered.

For horn apertures $> 2\lambda$ the main effect of increased periodicity is to reduce the frequency at which the cross-polar minimum occurs, as was the case for the corrugated waveguide. The effect of the spherical phase distribution in the horn aperture is to *flatten out* the peak cross-polar frequency characteristics, and generally increase the level of radiated cross-polar power when compared to

the results for a waveguide of equivalent dimensions. This is demonstrated in figure 10.15 where the peak cross-polar frequency characteristic of a horn of fixed aperture diameter (3.8λ) is shown for various values of semi-flare-angle. For horns with semi-flare-angles of up to about 10^{o} the frequency for minimum radiated cross-polar power is practically identical to that predicted for a waveguide of equal aperture and corrugation dimensions. These results also suggest that for horns with semi-flare-angle $<5^{o}$ the presence of the spherical phase distribution on the radiated cross-polar power is negligible for aperture diameters of this order. These facts allow the optimum slot depth design curve developed for the corrugated waveguide, figure 10.7, to be used in many cases for the design of narrow flare-angle corrugated conical horns. The -10dB and -15dB co-polar beamwidths for horns with semi-flare-angle up to about 15^{o} are practically identical to those obtained for an equivalent waveguide, enabling the beamwidth design curve of figure 10.13 to be used for corrugated horn design. The importance of obtaining an accurate slot depth at manufacture is demonstrated in figure 10.16 where the theoretical peak cross-polar frequency characteristic for the horn of figure 10.5 is compared with the characteristic obtained with the slot depth decreased by 6% (0.6mm). It should be noted that the aperture slot depth for the horn is taken to be the mean value at the last corrugation, if the slot is constructed in the way shown in figure 9.11 of chapter 9.

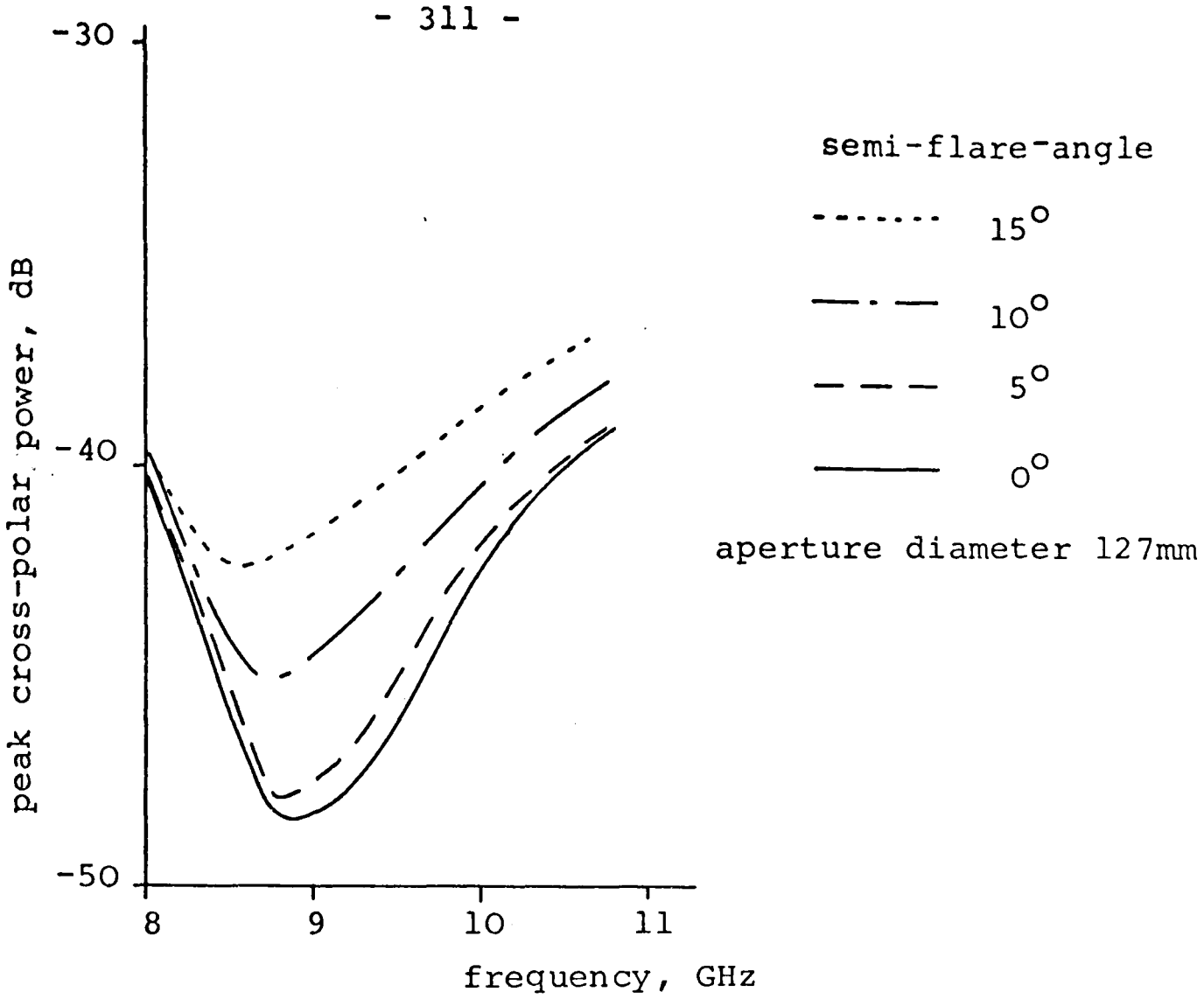

Fig. 10.15 Peak cross-polar power of corrugated conical horn as a function of frequency, parameter horn semi-flare-angle.

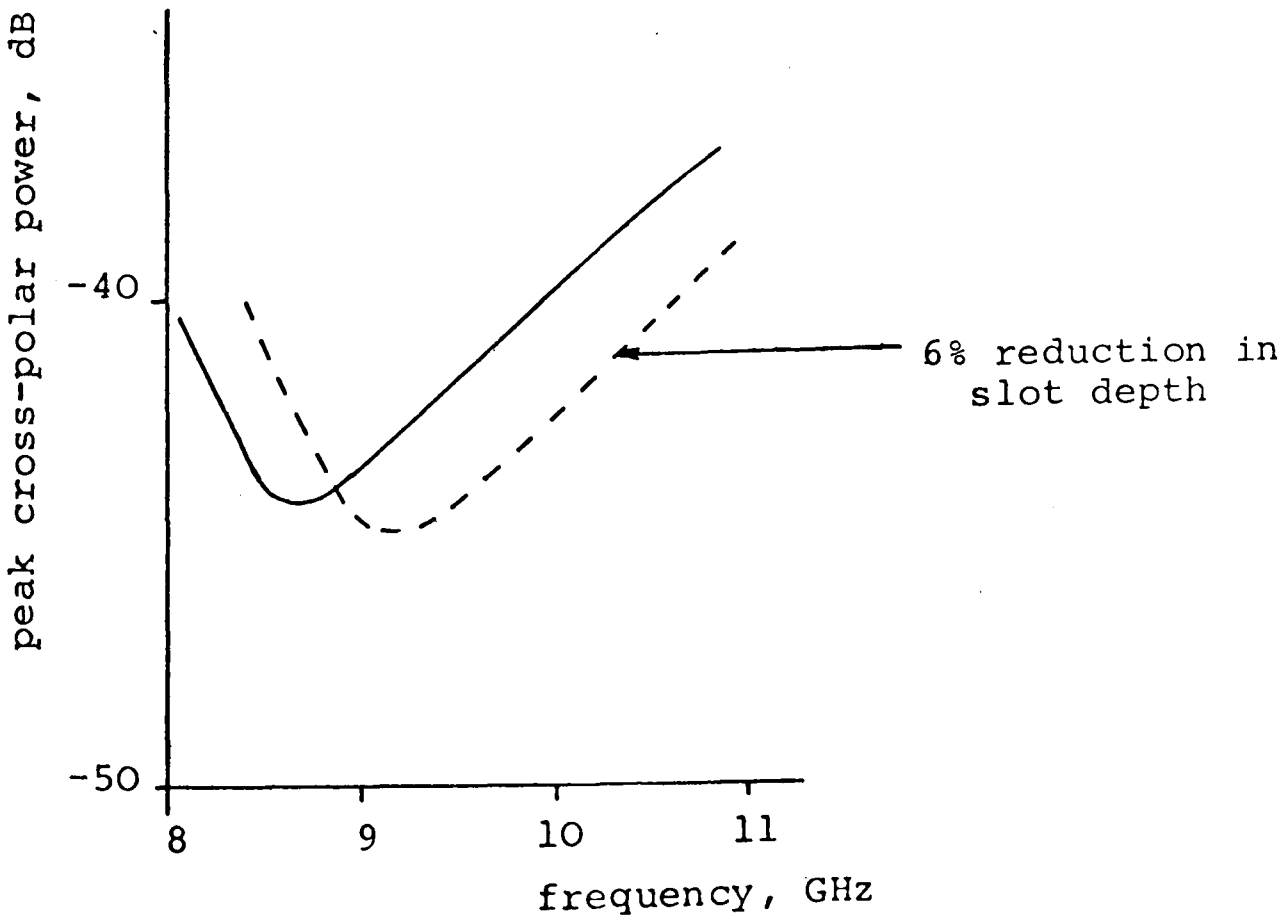

Fig. 10.16 Effect of 6% reduction in slot depth at the radiating aperture of a corrugated conical horn with 12° semi-flare-angle.

Because of the relatively narrow beamwidths, and therefore large apertures, of corrugated horn feeds required to illuminate dual reflector antennas the presence of the flange on the cross-polar radiation characteristics is less dominant than for smaller waveguide feeds; the K.H. and F.T. methods giving near identical predictions (see figure 9.7). Thus the flange modifications described in the previous section are unnecessary in this case, it being possible to achieve the required peak radiated cross-polar power of -40dB even for quite large flare angles (figure 10.15). Because of this the choice of flare-angle is more likely to be determined by the allowable loss of antenna efficiency due to the spherical phase distribution in the co-polar pattern than by any consideration of cross-polar performance. However care must be taken not to couple into the HE_{12} mode at the throat of the horn if the full cross-polar bandwidth available is to be practically achieved. This latter problem is considered in the next section.

10.5 THE EFFECT OF HIGHER ORDER MODES AT THE RADIATING APERTURE OF CORRUGATED FEEDS AND METHODS OF MINIMISING THEIR COUPLING

In this section the effect of the unity and non-unity azimuthal number higher order modes on the cross-polar patterns of corrugated waveguides will be quantified in order to set a recommended maximum level for these modes before the cross-polarisation performance becomes

significantly degraded. Techniques for efficiently coupling into corrugated horns, and methods of reducing HE_{12} mode coupling are also discussed.

10.5.1 Non-unity azimuthal number higher order modes

It has been previously shown (chapter 9) that the effect of these modes on the HE_{11} cross-polar pattern is to introduce a cross-polar component into the principal planes and increase the level already present in the 45^{o}-planes. It has been found that for most practical sizes of aperture ($>1.5\lambda$) the effect of a power coupling level of xdB for the $H_{01}+HE_{21}^{*}$ or the $E_{02}+HE_{21}$ mode combinations is to introduce a cross-polar pattern of peak level $\simeq -(x+5)$dB in the E-plane or H-plane respectively. To achieve the peak cross-polar level figure of -40dB the power coupling level for these mode combinations therefore needs to be kept below about -35dB. These modes are coupled by bends and imperfections along the waveguide feeder (chapters 2 and 5), consequently feeds being fed by a single mode waveguide would possess coupling coefficients for these modes well below this -35dB figure.

10.5.2 Unity azimuthal number higher order modes

The principal higher order mode in this case is the HE_{12} mode which is coupled by the diameter change in the corrugated waveguide occurring after the transition from the smooth wall waveguide input. The detremental effect of this mode on the cross-polar performance has been clearly demonstrated by the measured peak cross-polar frequency

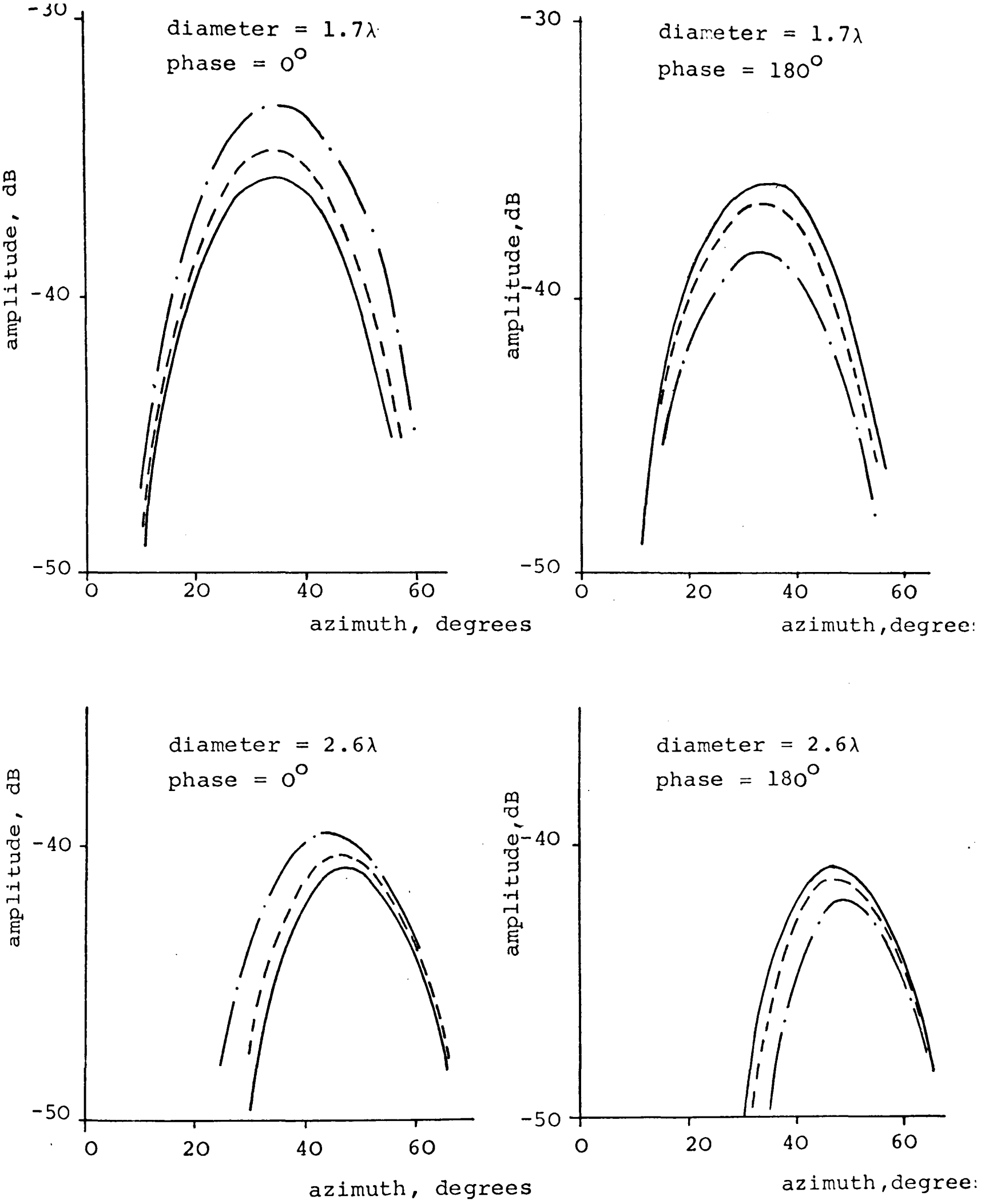

lg. 10.17 Effect of various relative powers of HE_{12} mode on the cross-polar pattern of the HE_{11} mode at the frequency for minimum cross-polar power, parameters: aperture diameter; relative phase of HE_{12} mode;

——— pure HE_{11} mode
- - - - -40dB of HE_{12} mode
—·— -30dB of HE_{12} mode

characteristics shown in figures 10.3 and 10.6. It has been found that for all practical sizes of aperture the HE_{12} mode is always propagating at the optimum frequency for minimum cross-polarisation. Figure 10.17 shows theoretically the effect on the 45^{o}-plane HE_{11} mode cross-polar pattern of various relative powers of the HE_{12} mode, for two sizes of normalised waveguide aperture, taken at the frequency for minimum cross-polarisation. These results suggest that to maintain an acceptable cross-polar performance the HE_{12} mode coupling level needs to be kept below about -30dB for larger aperture sizes and nearer -40dB for small apertures. This higher sensitivity for the smaller apertures occurs because the HE_{12} mode is nearer to its low frequency cut-off where the E and H-plane co-polar radiation patterns are considerably different, resulting in a high level of radiated cross-polarisation.

10.5.3 Matching into corrugated horn feeds and methods of minimising HE_{12} mode coupling

This sub-section describes methods to achieve optimum conversion between TE_{11} and HE_{11} modes at the throat of a horn, and to minimise HE_{12} mode coupling along the length of the horn. Although a corrugated horn is considered here, the conclusions drawn are equally applicable to a corrugated waveguide transition required for use with corrugated waveguide feeds. The problem can be split into two parts:

1) Efficiently transferring power from the TE_{11} mode in a smooth wall circular waveguide to the HE_{11} mode of a corrugated circular waveguide. This is synonymous with the requirement for low V.S.W.R., an important parameter in feed design.

2) Once into the HE_{11} mode, control of the slot depth is required in order to minimise coupling to the HE_{12} mode.

Considering point 1) first, the measured results of figure 10.18(a), curve (a), show that if in the corrugated horn used in the previous measurements of section 10.2 all the slot depths were $\lambda/4$ a very high level of cross-polarisation occurs. Considerable improvement occurs when the depth of the first slot is made equal to $\lambda/2$, curve (b). While best performance is achieved when the slot depth is tapered linearly over the first 7 corrugations of the horn throat, curve (c). The reason for the high level of curve (a), is that the HE_{11} mode is cut-off at the horn throat if the slot depth is $\lambda/4$. The EH_{11} mode is then excited in the throat region, and strong conversion occurs to the EH_{12} mode which propagates to the horn aperture where it radiates, producing a high level of cross-polar power.

The corresponding V.S.W.R. curves measured for the throat region of this horn are shown in figure 10.18(b), where the V.S.W.R. due to the rectangular to smooth wall circular waveguide transition has been subtracted out.

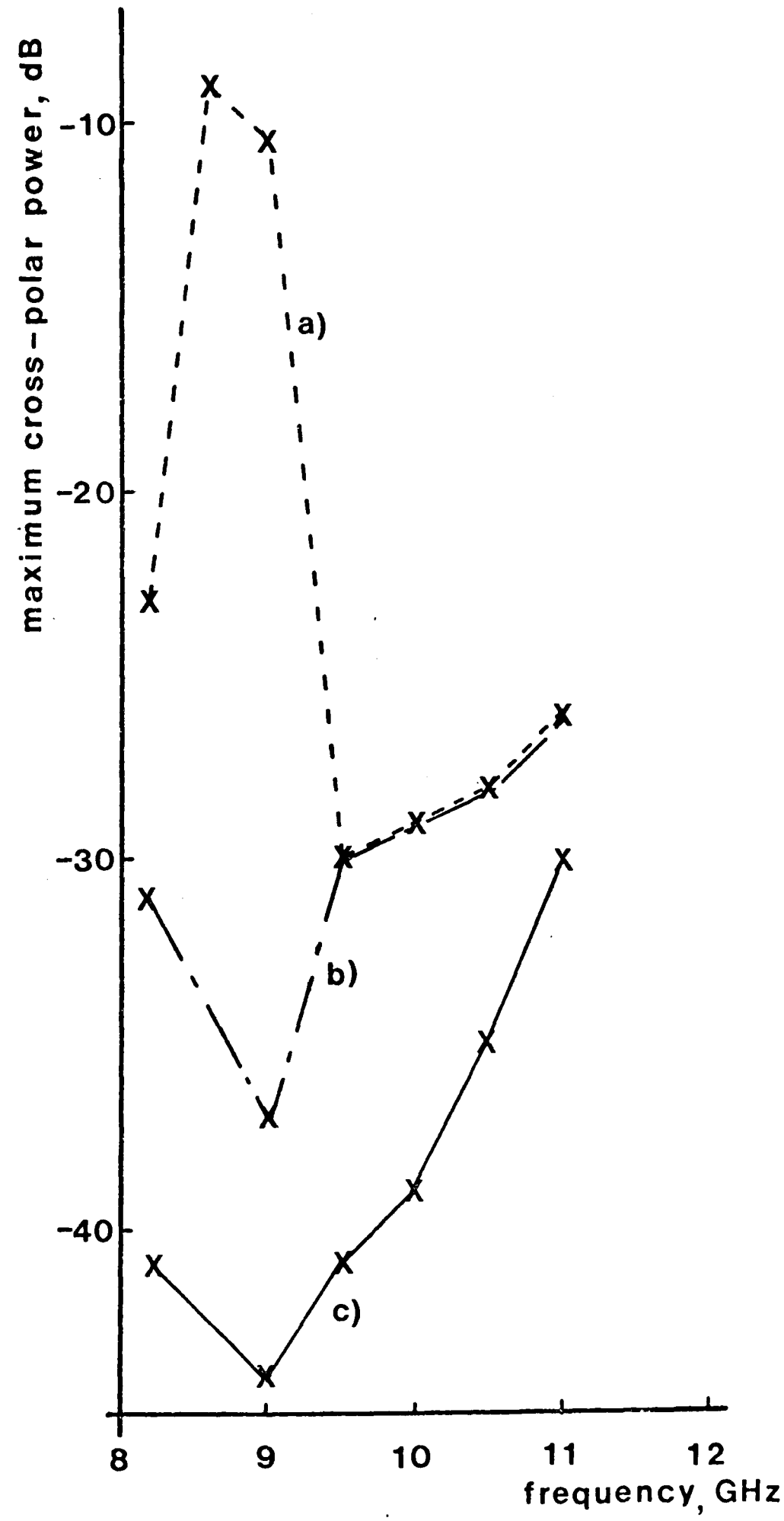

Fig. 10.18(a) Peak cross-polar power as a function of frequency for various slot depth profiles in the horn throat.
Corrugated horn parameters as figure 10.5.
See text for slot depth profiles.

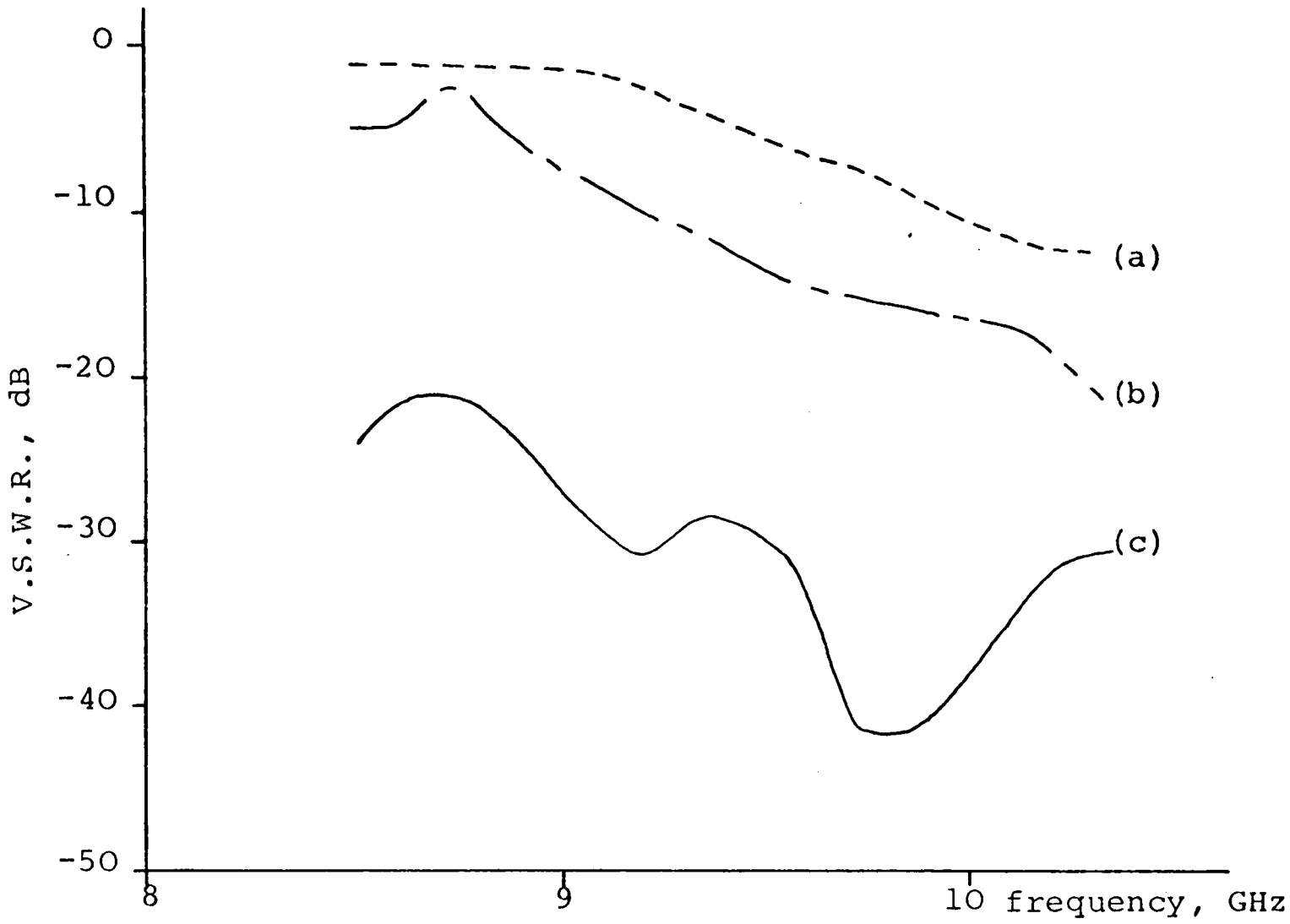

Fig. 10.18(b) Measured VSWR as a function of frequency corresponding to the result of figure 10.18(a)

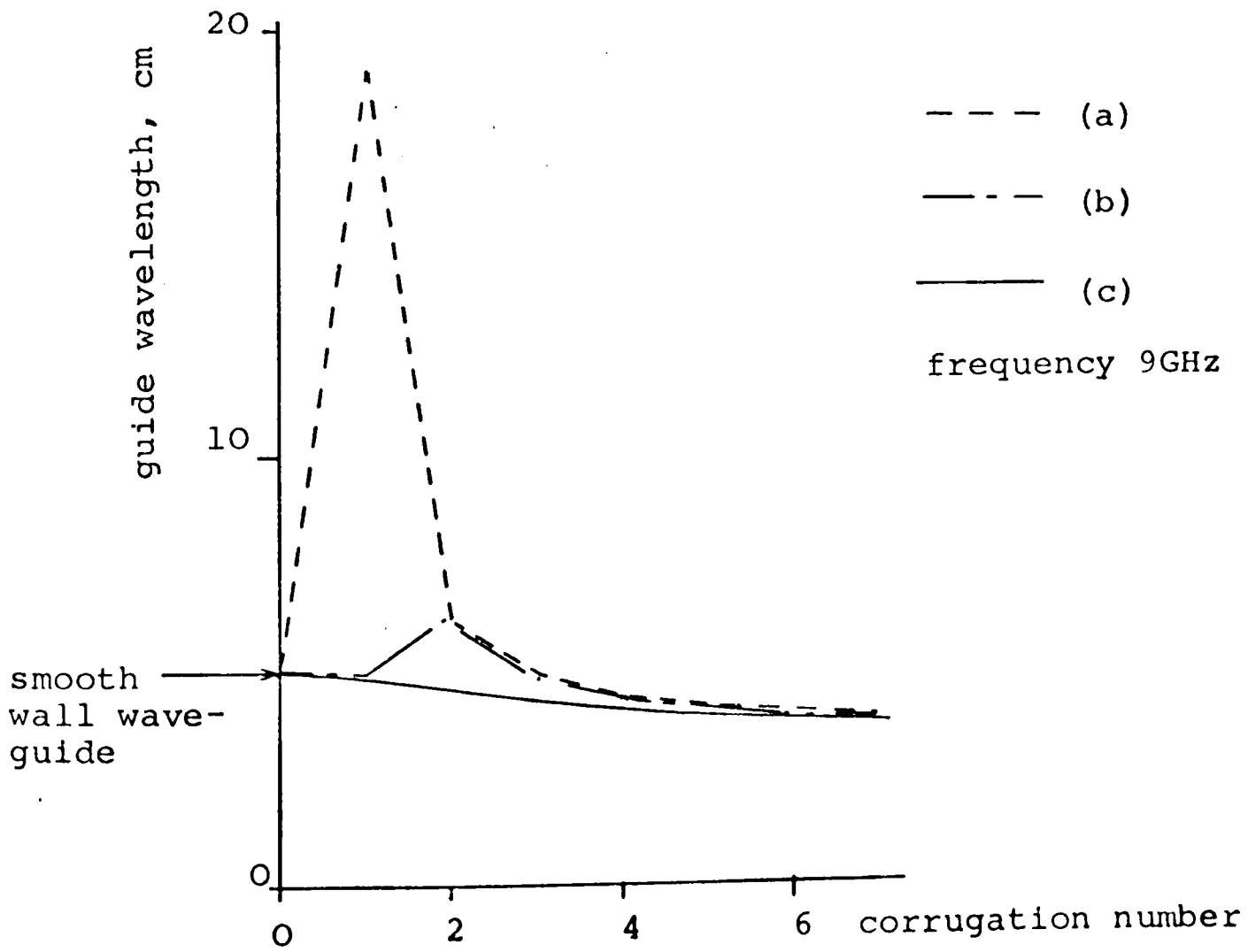

Fig. 10.18(c) Variation of guide wavelength over the first 7 corrugations of the horn throat region corresponding to the result of figure 10.18(a)

By assuming each corrugation of the horn to form a waveguide and calculating its guide wavelength, λ_g, the change in λ_g down the horn throat can be studied, and the results corresponding to the above example are shown in figure 10.18(c). These results suggest that for optimum conversion efficiency and minimum V.S.W.R. the guide wavelengths at the junction between the smooth wall and corrugated waveguides should be matched.

Once efficiently coupled into the HE_{11} mode coupling to the HE_{12} mode along the horn length must be minimised. A pure spherical HE_{11} mode at the throat of a corrugated horn will only remain pure as it propagates down the structure if the surface impedance of the corrugations remains constant. However, in practice, the surface impedance in the throat region of the horn is a function of R (figure 9.11), but for large R it remains approximately constant <26>. This change in surface impedance in the throat region can cause undesirable coupling to the HE_{12} mode. This is clearly different from the case of the smooth wall conical horn where for a constant flare-angle a pure spherical mode can be maintained as the wave propagates down the horn. Therefore in the case of the corrugated horn some control of the change in surface impedance from throat to aperture, in order to minimise HE_{12} mode coupling, is desirable. This suggests some form of gradual change in slot depth from throat to aperture. Figure 10.19, curve A, shows the guide wavelength, λ_g, and slot depth profile as a function of radial

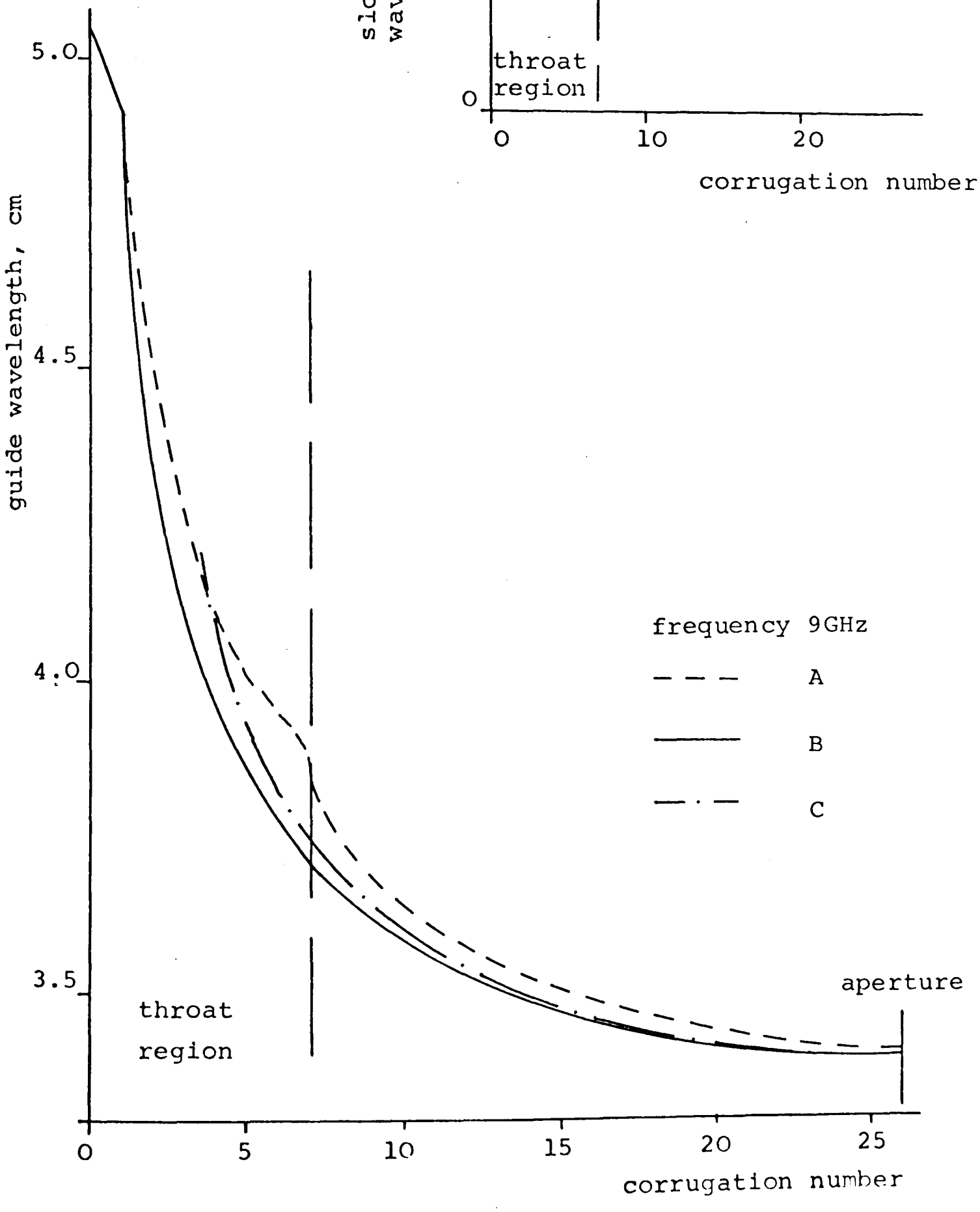

Fig. 10.19 Guide wavelength as a function of radial distance for several slot depth profiles.
Corrugated horn parameters as figure 10.5
See text for explanation of curves.

distance, for the corrugated horn of figure 10.5. The slight discontinuity in λ_g, and hence also in the surface impedance, at the boundary of the throat region suggests this to be the cause of the HE_{12} mode coupling in this particular horn. The lowest frequency for HE_{12} mode propagation in the throat region of this horn is 10.4GHz and this accounts for the measured peak cross-polar power, figure 10.6, being higher than the predicted value above this frequency. Any HE_{12} mode coupling below 10.4GHz will occur in the region where the guide wavelength changes smoothly down the horn, consequently resulting in a much lower coupling level. This is consistent with the good agreement obtained below 10.4GHz between the predicted results for the peak cross-polar power due purely to the HE_{11} mode and those measured, indicating negligible HE_{12} mode coupling.

Curve B of figure 10.19 shows the change in λ_g down the same horn, but possessing the linear slot depth profile shown inset to this figure. Comparison of these λ_g profiles is made with that obtained for a horn with transverse wavenumber constant and equal to that at the radiating aperture, curve C. For a narrow flare-angle horn the constant transverse wavenumber implies a constant surface impedance and consequently appears to represent the optimum guide wavelength profile for minimum HE_{12} mode coupling. The similarity between this curve and that obtained for the linear slot depth profile, curve B, is evident, indicating that this design would yield a lower

HE_{12} mode coupling. The deviation between these two λ_g profiles over the first few corrugations, required to produce a match for the input smooth wall waveguide mode, would not introduce any HE_{12} mode coupling as this mode remains cut-off below 12GHz in this region.

The requirement for low input V.S.W.R. and minimum HE_{12} mode coupling for corrugated horns has been considered here only qualitatively and therefore further experimental and theoretical research into these problems needs to be done in order to optimise these performance requirements.

10.6 CONCLUSIONS

The design curves for optimum cross-polar performance of corrugated waveguides suggest that a waveguide of diameter $\approx 2\lambda$ is the smallest that can exhibit a peak radiated cross-polar power of <-36dB over a 10% bandwidth. This value of feed cross-polar power producing an approximate overall cross-polar level of -40dB when used with a front-fed paraboloid reflector (see chapter 2). The co-polar beamwidth produced for this diameter rules out the use of corrugated waveguide feeds for front-fed parabolic reflectors of F/D <0.5. Improvements in the cross-polar performance of smaller diameter corrugated waveguide feeds will only follow if the undesirable effect of the plane metal flange can be reduced allowing the cross-polar null, predicted when no flange is present, to be practically achieved. However, for front-fed parabolic antennas with F/D's <0.35 corrugated waveguides

cannot achieve the large co-polar beamwidths required, other feeds such as wide flare angle corrugated horns and the 90^{o} corrugated horn <58> being much more suited to this application.

The radiation properties of corrugated waveguides and narrow flare-angle corrugated horns are much more suited as feeds for most practical sizes of dual reflector antenna. It has been shown in this chapter that if the power coupling level of higher order modes can be kept below about -35dB an acceptable feed cross-polarisation performance can be achieved if the *correct* slot depth at the radiating aperture is chosen. The optimum design curves presented in this chapter enable this choice of slot depth to be correctly made. For most practical feed aperture diameters required in this application the presence of the flange at the aperture does not introduce an unacceptably high cross-polarisation, and so methods of removing its effect are not generally required.

It has been shown that for long very narrow flare-angle corrugated horns, used for example as feeds for satellite earth stations, the frequency for minimum cross-polar power can be controlled over about a 10% bandwidth by adjusting the corrugation periodicity at the aperture, without the need for remaking the complete horn.

CHAPTER 11

CONCLUSIONS

In this final chapter the main conclusions resulting from the research are presented and a number of topics for further study discussed.

The review of the performance requirements for an antenna communications system carried out in chapter 2 concluded that the two principal applications for the corrugated waveguide were as a low attenuation feeder and a low cross-polarisation primary feed. Problems relating to these two applications have been studied in chapters 5 through 10 and a summary of the most significant results is given below.

The corrugated waveguide as an antenna feeder

The use of a flexible form of waveguide construction requires a knowledge of the degree of mode conversion resulting from a waveguide bend. This problem has been studied in chapter 5 and it was concluded that strict control over the minimum bend radii and maximum number of bends occurring along the waveguide run is required in order to achieve an acceptable level of mode conversion. If it is not practical to apply this constraint the use of a low insertion loss mode filter will be required.

Chapter 6 represents, as far as the author is aware, the first theoretical analysis of the problem of cross-

polar generation due to random ellipticity of the waveguide cross-section. Comparison of results with both smooth wall and corrugated circular waveguides showed the latter to be intrinsically less susceptible, both mechanically and electrically, to the generation of cross-polarisation by random ellipticity.

The development in chapter 7 of a negligible insertion loss mode filter is of great significance as it enables a relatively cheaply manufactured, poor tolerance, flexible corrugated waveguide to successfully operate as a single polarisation, low attenuation feeder. In addition, because the mode filter is an integral part of the waveguide structure it is possible to manufacture a corrugated waveguide that exhibits continual mode suppression. The main disadvantage of this design of mode filter is that it is fundamentally limited to the use of single linear polarisation.

In some antenna feeder applications flexibility and dual polarisation operation, coupled with a fairly low attenuation, are the prime requirements. The mono-mode corrugated waveguide, described in chapter 8, has been shown to be ideally suited to this application as it eliminates the many problems associated with overmoded operation. It has been found that the mono-mode corrugated waveguide exhibits an attenuation lower than any alternative flexible antenna feeder, but at the expense of a larger waveguide cross-section.

For a number of years the corrugated waveguide has been known to exhibit an attenuation advantage over currently available feeders, but the problems of mode conversion, waveguide generated cross-polarisation and fabrication have, to date, been the principal obstacles to its commercial exploitation. The results presented in this thesis have shown that the problems of mode conversion and cross-polarisation can be largely overcome by choosing the *type* of corrugated waveguide most suited to the particular application. This leads to the proposal of three principal types of corrugated waveguide feeder that could be commercially produced, each one exhibiting significant advantages over currently available feeders. A brief specification for these three waveguide types is presented in table 11.1, more detailed results can be found in the relevant chapters of the thesis.

The problem of fabricating the corrugated waveguide still remains to be completely solved. However a number of proposals concerning fabrication have been made throughout the thesis and these are summarised below.

Whilst the construction of rigid corrugated waveguide using the thermal contraction method (chapter 4) is suited to prototype manufacture it is totally unsuited to commercial production, mainly due to the problems of obtaining consistent pipe-iris contact over long waveguide lengths. Appendix 7.1 proposed a lightweight form of construction and initial measurements suggest that this structure may warrant further study. A method of fabrication

WAVEGUIDE TYPE	OPERATION	MAIN PERFORMANCE ADVANTAGES	MAIN APPLICATIONS
Rigid overmoded	Dual or single polarisation. High mechanical tolerances.	Very low attenuation.	Very low attenuation feeders for high towers.
Flexible overmoded	a) Dual polarisation with strict control on number of bends and minimum bend radii. Good mechanical tolerances. b) Single polarisation using short length of low insertion loss mode filter. Fairly good mechanical tolerances. c) Single polarisation. Waveguide construction including continual mode suppression. Fair-to-poor mechanical tolerances.	Considerably lower than any other flexible microwave waveguide and lower than overmoded TE^{o}_{11} mode waveguide.	Feeders for antenna communication systems of classes 2 and 3 (see table 2.2).
Mono-mode flexible	Dual polarisation.	Attenuation similar to overmoded TE^{o}_{11} and significantly lower than other single mode microwave waveguides.	Feeders for antenna communication systems of classes 2 and 3 (see table 2.2).

Table 11.1 Principal types of corrugated circular waveguide antenna feeder.

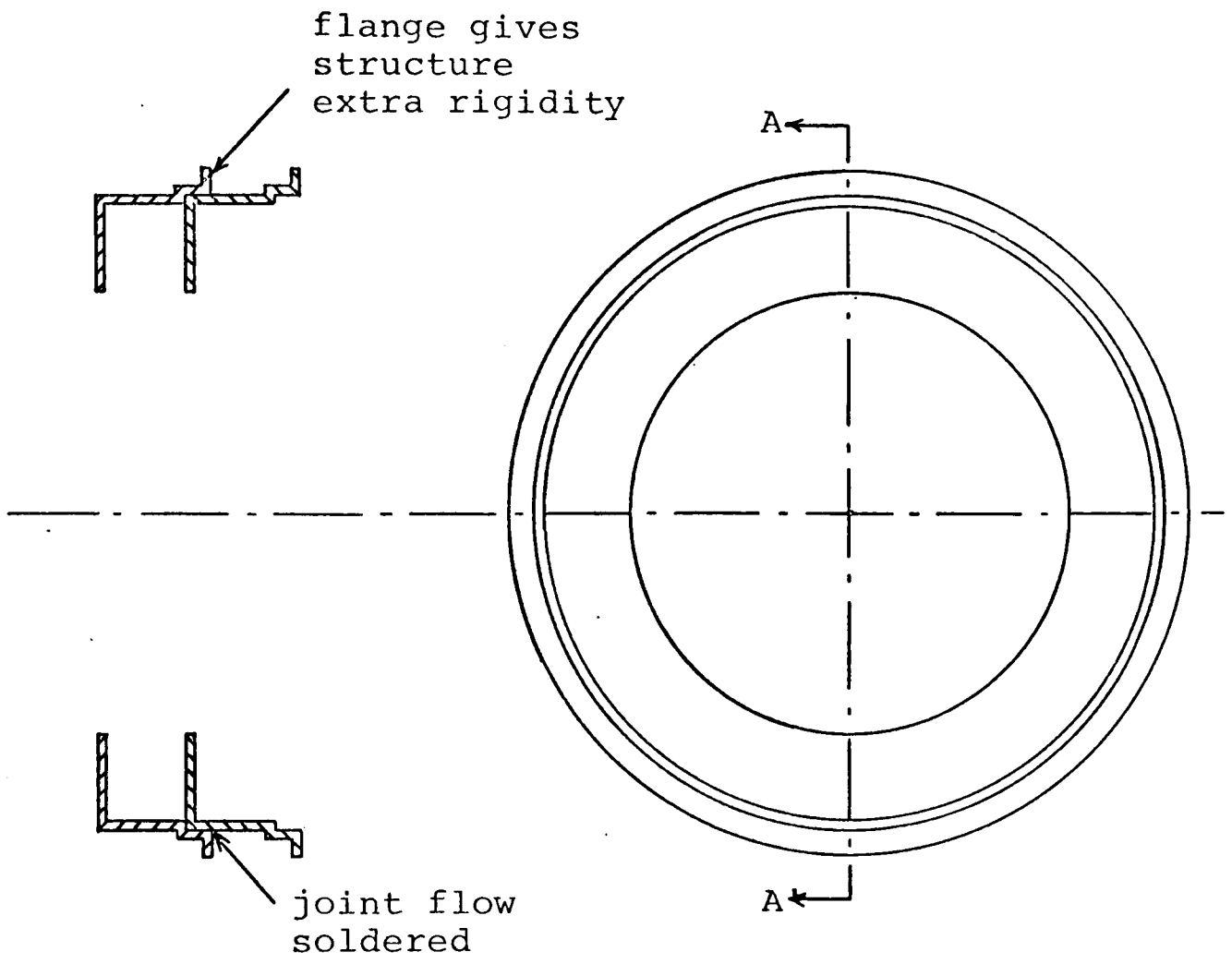

Section through AA'

Fig. 11.1 A possible method of construction for the rigid corrugated circular waveguide

similar to that of the sectional form of resonant cavity construction (chapter 4), but more suited to commercial production, has been proposed <59>, and is shown diagrammatically in figure 11.1. Each waveguide section is pressed from sheet metal and the sections are joined using a flow soldering process, the outer surface then being covered in a protective moulding of plastic or rubber.

For the fabrication of flexible corrugated waveguide a method employing two semi-circular shells welded together (figure 7.16) appears to be suitable, especially for the manufacture of continuous mode suppression waveguide. The fabrication of the mono-mode waveguide using this method may prove more difficult due to the deeper corrugations required. However, it may be possible to modify the method of construction shown in figure 11.1 to enable waveguide flexibility to be achieved.

If the corrugated waveguide feeder is commercially adopted it may be used in conjunction with a corrugated waveguide or horn primary feed as this eliminates the requirement to convert from the TE^{o}_{11} mode to the HE_{11} mode at the feed throat. This in turn allows the specified VSWR's for the remaining transitions and polarisers to be slightly relaxed whilst still meeting the overall specified system VSWR.

Corrugated circular waveguides and horns as primary feeds for reflector antennas

Although the cross-polar radiation from corrugated

circular waveguides and narrow flare-angle conical corrugated horns has been known to be low, to date, no reliable method of predicting the cross-polar pattern has been available. The results presented in chapters 9 and 10 have shown that by including the effects of space-harmonics and the inevitable waveguide flange the cross-polar radiation from corrugated waveguides and horns can be accurately predicted. The development of this more exact analysis is significant as it has enabled the optimum corrugation depth required to achieve minimum radiated cross-polar power to be predicted. This study has also shown that it is essential not to excite higher order modes, such as the HE_{12} mode, if a low level of cross-polarisation is to be achieved. Maximum allowable levels for the higher order modes to ensure that the cross-polar performance is not significantly degraded have been proposed in chapter 10.

As a result of this investigation it has been concluded that whilst corrugated waveguides and narrow flare-angle horns are well suited as primary feeds for dual reflector antennas, the beamwidths obtainable are generally insufficient for their use with front fed reflector antennas having F/D's < 0.35.

Future Work

This thesis essentially marks the conclusion of the research programme for the corrugated waveguide antenna feeder, future work being in the nature of development. Such a development programme would principally involve the

search for the best fabrication technique and the manufacture of practical lengths (of order 50 metres) of waveguide to allow field trials to be performed. The favourable results presented in this thesis certainly suggest that one or more of the waveguide types listed in table 11.1 should be taken into this development stage.

Future work on the cross-polarisation performance of corrugated circular waveguides and narrow flare-angle horns will probably lie in four main areas.

1) Further investigation into methods of reducing the undesirable effect of the finite flange on the cross-polar performance of small diameter corrugated waveguide feeds are required.

2) Experimental results presented in this thesis clearly showed the necessity for reducing both the HE_{12} mode coupling and the input VSWR of corrugated waveguide transitions and horns. Consequently the qualitative study of these effects presented in chapter 10 needs to be put on a more quantitative basis, both experimentally and theoretically.

3) By decreasing the rate at which the surface impedance presented by the corrugations changes with frequency the bandwidth over which the cross-polarisation minimum occurs would be increased. The *ring loaded* corrugated waveguide <60> has been shown to increase the bandwidth between the points where the surface admittance changes from

zero to infinity and so this technique may also enable the cross-polar bandwidth to be increased.

4) With the development in this thesis of an accurate model for predicting the cross-polar performance of corrugated waveguides and horns the possibility exists of using this model with reflector profile or multimode feed computer optimisation techniques to improve the overall cross-polar performance of dual or single reflector antennas. The advantage of such a technique to the design of space-craft antennas is self-evident.

To conclude, this thesis has shown that the corrugated waveguide or horn, when used as a feeder or primary radiator, can provide a significant performance advantage over currently available alternatives.

APPENDIX 4.1

RATIO OF TOTAL POWER LOSS TO WAVEGUIDE WALL POWER LOSS IN A CORRUGATED CIRCULAR WAVEGUIDE RESONANT CAVITY

If H_t represents the total transverse magnetic field of the waveguide mode then it can be shown <41> that the magnetic field tangential to the resonant cavity end plate is twice that for the travelling wave, i.e. $2H_t$. Therefore the total power loss, P_E, on <u>both</u> end plates of the resonant cavity is given by:

$$P_E = 2 \frac{R_s}{2} \int_{\text{end plate}} |2H_t|^2 ds$$

$$= 4 R_s \int_{\text{end plate}} |H_t|^2 ds \qquad \text{(i)}$$

where: $|H_t|^2 = |H_r|^2 + |H_\theta|^2$ and R_s is the surface resistivity of the metal end plates and is given by

$$R_s = \pi \sqrt{\frac{4\times10^{-7} \times \text{frequency}}{(\text{surface conductivity, s/m})}}$$

Equation (i) is evaluated by splitting the integration over the end plate into two regions, $r \leq r_1$, and $r_1 < r \leq r_o$, and substituting for the space-harmonic field components of the corrugated waveguide (appendix 5.1) in the inner region and slot region respectively, the fields being evaluated at z=0 (middle slot position).

Inner region $r \leq r_1$

$$P_E^I = \frac{4y_o^2 \pi R_s r_1^2}{(K_N r_1)^4} \left[\left(\bar{A}_N^2 r_1^2 + \bar{B}_N^2 (\beta_N r_1)^2 \right) \left(\tfrac{1}{2}\{ \pm (K_N r_1)^2 - n^2 \} \right.\right.$$

$$\left.\left. + \frac{(K_N r_1)^2}{2} \frac{J_n'^2(K_N r_1)}{J_n^2(K_N r_1)} + (K_N r_1) \frac{J_n'(K_N r_1)}{J_n(K_N r_1)} \right) + 2\bar{A}_N \bar{B}_N \bar{r}_1 (\beta_N r_1) n \right] \qquad \text{(ii)}$$

For n=0 modes equation (ii) is multiplied by a factor of 2 and for $K_N r_1$ real the + sign is taken.

Outer region $r_1 < r \leq r_o$

a) $\Gamma_m r_1$ real

$$P_E^o = \frac{4y_o^2 \pi R_s r_1^2}{(\Gamma_m r_1)^4} \left[c_m^2 \bar{r}_1^2 \left(\frac{2}{\pi^2} - \tfrac{1}{2}\{ (\Gamma_m r_1)^2 - n^2 \} S_n^{2D} - \frac{(\Gamma_m r_1)^2}{2} S_n^{2N} - \Gamma_m r_1 S_n^N S_n^D \right) \right.$$

$$+ d_m^2 (\eta_m r_1)^2 \left(\frac{2}{\pi^2} - \frac{-2n^2}{\pi^2 (\Gamma_m r_o)^2} - \tfrac{1}{2}\{ (\Gamma_m r_1)^2 - n^2 \} R_n^{2D} - \frac{(\Gamma_m r_1)^2}{2} R_n^{2N} - \Gamma_m r_1 R_n^N R_n^D \right)$$

$$\left. - 2c_m d_m n \bar{r}_1 (\eta_m r_1) S_n^D R_n^D \right] \qquad \text{(iii)}$$

b) $\Gamma_m r_1$ imaginary

$$P_E^o = \frac{4y_o^2 \pi R_s r_1^2}{(\Gamma_m r_1)^4} \left[c_m^2 \bar{r}_1^2 \left(\tfrac{1}{2} + \tfrac{1}{2}\{\Gamma_m^2 r_1^2 + n^2\} S_n^{2D} - \frac{(\Gamma_m r_1)^2}{2} S_n^{2N} - (\Gamma_m r_1) S_n^N S_n^D \right) \right.$$

$$+ d_m^2 (\eta_m r_1)^2 \left(-\tfrac{1}{2} - \frac{n^2}{2(\Gamma_m r_o)^2} + \tfrac{1}{2}\{\Gamma_m^2 r_1^2 + n^2\} R_n^{2D} - R_n^{2N} \frac{(\Gamma_m r_1)^2}{2} - (\Gamma_m r_1) R_n^N R_n^D \right)$$

$$\left. -2 c_m d_m n \bar{r}_1 (\eta_m r_1) S_n^D R_n^D \right] \qquad \text{(iv)}$$

where: $S_n^D, S_n^N, R_n^D, R_n^N$ are all evaluated at $r=r_1$ and for n=O modes equations (iii) and (iv) are multiplied by a factor of 2.

The power loss on the walls of a waveguide, length L, is given by:-

$$P_o(1 - 10^{-\frac{\alpha L}{10}}) \qquad \text{(v)}$$

where α is the attenuation coefficient in dB/m and P_o is the average power flow down the waveguide. The standing wave pattern of the field in a resonant cavity can be decomposed into two waves of equal amplitude travelling in opposite directions and consequently the waveguide wall loss of equation (v) is incurred twice. Therefore the total waveguide wall loss, P_W, in the resonant cavity is given by:

$$P_W = 2P_o(1 - 10^{-\frac{\alpha L}{10}})$$

The required ratio of total resonant cavity power loss to waveguide wall power loss is then given by

$$\frac{P_T}{P_W} = \frac{P_W + P_E}{P_W}$$

APPENDIX 5.1

SPACE HARMONIC FIELD COMPONENTS FOR THE CORRUGATED CIRCULAR WAVEGUIDE

For the Nth space harmonic the field components in the inner region of a corrugated circular waveguide are given by < 2 >:-

$$E_{zN} = A_N J_n(K_N r)\cos n\theta e^{-j\beta_N z}$$

$$H_{zN} = y_o B_N J_n(K_N r)\sin n\theta\ e^{-j\beta_N z}$$

$$E_{\theta N} = j\left[\frac{A_N n\beta_N r J_n(K_N r)}{(K_N r)^2} + \frac{B_N \bar{r} J_n'(K_N r)}{K_N r}\right]\sin n\theta e^{-j\beta_N z}$$

$$H_{\theta N} = -jy_o\left[\frac{A_N \bar{r} J_n'(K_N r)}{K_N r} + \frac{B_N \beta_N r\ n\ J_n(K_N r)}{(K_N r)^2}\right]\cos n\theta e^{-j\beta_N z}$$

$$H_{rN} = -jy_o\left[\frac{A_N \bar{r}\ n\ J_n(K_N r)}{(K_N r)^2} + \frac{B_N \beta_N r J_n'(K_N r)}{K_N r}\right]\sin n\theta e^{-j\beta_N z}$$

$$E_{rN} = -j\left[\frac{A_N \beta_N r J_n'(K_N r)}{K_N r} + \frac{B_N \bar{r}\ n\ J_n(K_N r)}{(K_N r)^2}\right]\cos n\theta e^{-j\beta_N z}$$

where $\bar{r}_1 = \frac{\omega r_1}{c}$; $y_o = \sqrt{\mu_o \varepsilon_o}$ and A_N, B_N are the space-harmonic coefficients and are normally used in their normalised form:

$$\bar{A}_N = A_N J_n(K_N r_1)$$
$$\bar{B}_N = B_N J_n(K_N r_1)$$

The field components for the m^{th} slot mode in the outer region of the waveguide, $r_1 < r < r_o$, are given by:-

$$E_{z_m} = \left[c_m S_n^D \cos\eta_m z \quad - j\, c_m' S_n^{D'} \sin\eta_m' z\right] \cos n\theta$$

$$H_{z_m} = y_o\left[-j d_m R_n^D \sin\eta_m z + d_m' R_n^{D'} \cos\eta_m' z\right] \sin n\theta$$

$$E_{\theta_m} = \left(\left[c_m n \frac{\eta_m r}{(\Gamma_m r)^2} S_n^D + d_m \frac{\bar{r}}{(\Gamma_m r)} R_n^N\right] \sin \eta_m z \right.$$

$$\left. + j\left[c_m' n \frac{\eta_m' r}{(\Gamma_m' r)^2} S_n^{D'} + d_m' \frac{\bar{r}}{(\Gamma_m' r)} R_n^{N'}\right] \cos \eta_m' z\right) \sin n\theta$$

$$H_{\theta_m} = y_o\left(-j\left[d_m n \frac{\eta_m r}{(\Gamma_m r)^2} R_n^D + \frac{c_m \bar{r}}{(\Gamma_m r)} S_n^N\right] \cos \eta_m z \right.$$

$$\left. - \left[d_m' n \frac{\eta_m' r}{(\Gamma_m' r)} R_n^{D'} + \frac{c_m' \bar{r}}{(\Gamma_m' r)} S_n^{N'}\right] \sin\eta_m' z\right) \cos n\theta$$

$$E_{r_m} = -\left(\left[c_m \frac{\eta_m r}{(\Gamma_m r)^2} S_n^N + d_m \frac{n\bar{r}}{(\Gamma_m r)} R_n^D\right] \sin \eta_m z \right.$$

$$\left. + j\left[c_m' \frac{\eta_m' r}{(\Gamma_m' r)^2} S_n^{N'} + d_m' \frac{n\bar{r}}{(\Gamma_m' r)} R_n^{D'}\right] \cos \eta_m' z\right) \cos n\theta$$

$$H_{r_m} = -y_o\left(j\left[c_m \frac{n\bar{r}}{(\Gamma_m r)^2} S_n^D + d_m \frac{\eta_m r}{(\Gamma_m r)} R_n^N\right] \cos \eta_m z \right.$$

$$\left. + \left[c_m' \frac{n\bar{r}}{(\Gamma_m' r)^2} S_n^{D'} + d_m' \frac{\eta_m' r}{(\Gamma_m' r)} R_n^{N'}\right] \sin \eta_m' z\right) \sin n\theta$$

where:-

c_m, c_m' are the coefficients of the E mode components,

d_m, d_m' are the coefficients of the H mode components,

and the factor $e^{-j\beta_o p\ell}$ (p an integer) has been omitted.

In the formulation presented above the waveguide geometry shown in figure 2.4 has been used. The symbols in the above equations have the following meanings:-

$$\beta_N = \beta_o + \frac{2\pi N}{\ell}$$

$$(K_N r)^2 = \bar{r}^2 - (\beta_N r)^2$$

$$\left.\begin{aligned} \eta_m r &= \frac{2m\pi r}{d} \\ \eta'_m r &= (2m-1)\,\frac{\pi r}{d} \end{aligned}\right\} \quad \text{longitudinal propagation coefficient in the slot}$$

$$\left.\begin{aligned} (\Gamma_m r)^2 &= \bar{r}^2 - (\eta_m r)^2 \\ (\Gamma'_m r)^2 &= \bar{r}^2 - (\eta'_m r)^2 \end{aligned}\right\} \quad \text{longitudinal wave number in the slot}$$

$$R_n^N = J'_n(\Gamma_m r)Y'_n(\Gamma_m r_o) - J'_n(\Gamma_m r_o)Y'_n(\Gamma_m r)$$

$$R_n^D = J_n(\Gamma_m r)Y'_n(\Gamma_m r_o) - J'_n(\Gamma_m r_o)Y_n(\Gamma_m r)$$

$$S_n^N = J'_n(\Gamma_m r)Y_n(\Gamma_m r_o) - J_n(\Gamma_m r_o)Y'_n(\Gamma_m r)$$

$$S_n^D = J_n(\Gamma_m r)Y_n(\Gamma_m r_o) - J_n(\Gamma_m r_o)Y_n(\Gamma_m r)$$

For $R_n^{N'}$, $R_n^{'D}$, $S_n^{N'}$, $S_n^{D'}$, $\Gamma'_m r$ replaces $\Gamma_m r$. When $K_N r$, $\Gamma_m r$ or $\Gamma'_m r$ are imaginary, $J_n(x)$ is replaced by $I_n(x)$ and $Y_n(x)$ by $K_n(x)$.

APPENDIX 5.2

MODE COUPLING DUE TO A WAVEGUIDE TILT

Defining the modal field in region 1 of figure 5.1 as $\underline{e}_n e^{-\gamma_n z}$, $\underline{h}_n e^{-\gamma_n z}$ where the modal vectors $\underline{e}_n$ and $\underline{h}_n$ satisfy the orthogonality definition between modes m and n :

$$\int_S \underline{e}_n \times \underline{h}_m^* . ds = \delta_{nm} \qquad \text{(unity power modes)}$$

The field at the aperture of waveguide 2, figure 5.1, is given by $\underline{e}_n e^{-\gamma_n x \delta\phi}$, $\underline{h}_n e^{-\gamma_n x \delta\phi}$ where the origin of the coordinate system is taken at the apex of the tilt. Representing x in terms of the waveguide coordinates r and θ, shown below, the aperture field of waveguide 2, $\underline{e}_{ap}$, is

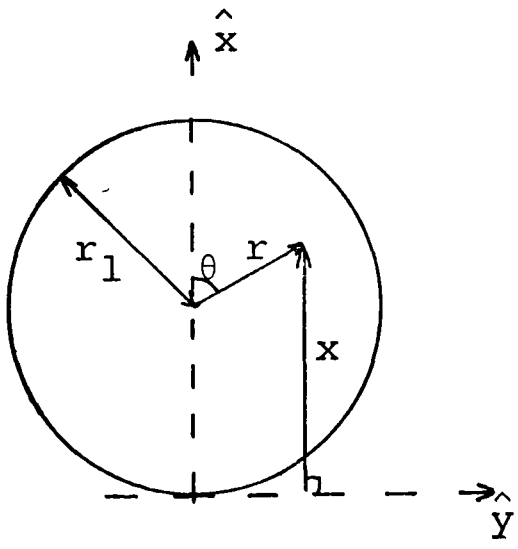

Waveguide cross-section geometry

given to first order by

$$\underline{e}_{ap} = \underline{e}_n \{ (1-\gamma_n r_1 \delta\phi) - \gamma_n r \cos\theta \delta\phi \} \qquad \text{(i)}$$

Expressing the aperture field, $\underline{e}_{ap} = \hat{\underline{x}} e_x + \hat{\underline{y}} e_y + \hat{\underline{z}} e_z$, in

terms of the coordinates of waveguide 2, ($\underline{x}'$,$\underline{y}'$,$\underline{z}'$), using the transformation shown in the figure below yields:

$$\hat{x} = \hat{x}' - \hat{z}'\delta\theta$$
$$\hat{y} = \hat{y}'$$
$$\hat{z} = \hat{z}' + \hat{x}'\delta\theta$$

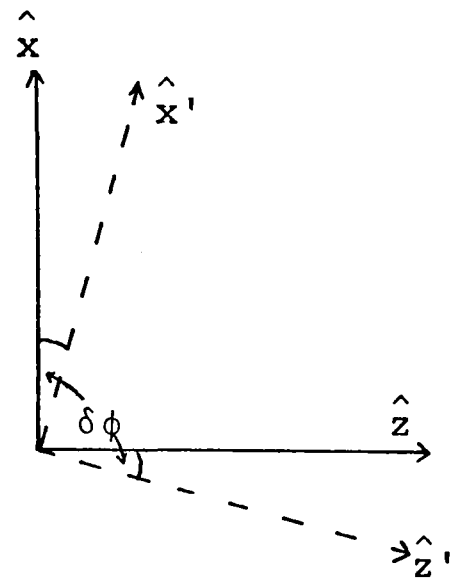

Coordinate transformation between waveguides 1 and 2

$$\underline{e}_{ap} = \underline{e}'_{ap} + \delta\phi(e_z\hat{\underline{x}}' + e_x\hat{\underline{z}}') \qquad \text{(ii)}$$

The coupling coefficient amplitude per degree of tilt, a_{mn}, for the coupled mode m in waveguide 2 (mode vectors e'_m and h'_m) is obtained by applying the orthogonality integral to the aperture field of equation (ii). Thus:

$$a_{mn}\delta\phi = \int_S \underline{e}_{ap} \times \underline{h}'_m . ds \qquad \text{(iii)}$$

where S is the waveguide cross-section. Evaluation of equation (iii) using equations (i) and (ii) and noting that the coupled mode differs from the incident mode ($m \neq n$) gives:

$$a_{mn}\delta\phi = \delta\phi\{-\gamma_n \int_S r\cos\theta \underline{e}'_n \times \underline{h}^{*}{}'_m . ds + \int_S e_{nz}\hat{\underline{x}}' \times \underline{h}^{*}{}'_m . ds\} \qquad \text{(iv)}$$

Expanding the cross-porudcts of this equation in terms of the field components of the modal vectors yields

$$a_{mn} = -\gamma_n \int_0^{r_1} \int_0^{2\pi} r\cos\theta\,(e'_{nr} h^{*'}_{m\theta} - e'_{n\theta} h^{*'}_{mr})\,r\,dr\,d\theta +$$

$$\int_0^{r_1} \int_0^{2\pi} e_{nz}\,(h^{*'}_{mr}\sin\theta + h^{*'}_{m\theta}\cos\theta)\,r\,dr\,d\theta \qquad \text{(v)}$$

for a waveguide tilt in the y=O plane. By a simple change in geometry it can be shown that for a waveguide tilt in the x=O plane

$$a_{mn} = -\gamma_n \int_0^{r_1} \int_0^{2\pi} r\sin\theta\,(e'_{nr} h^{*'}_{m\theta} - e'_{n\theta} h^{*'}_{mr})\,r\,dr\,d\theta -$$

$$\int_0^{r_1} \int_0^{2\pi} e_{nz}\,(h^{*'}_{mr}\cos\theta - h^{*'}_{m\theta}\sin\theta)\,r\,dr\,d\theta \qquad \text{(vi)}$$

Now expressing the mode field components in terms of their azimuthal dependence, for example mode n with azimuthal number n has:-

$$e'_{nz} = e_{nz}\cos n\theta, \qquad h'_{nz} = h_{nz}\sin n\theta,$$

$$e'_{n\theta} = e_{n\theta}\sin n\theta, \qquad h'_{n\theta} = h_{n\theta}\cos n\theta,$$

$$e'_{nr} = e_{nr}\cos n\theta, \qquad h'_{nr} = h_{nr}\sin n\theta \qquad \text{(vii)}$$

and equation (v) becomes:-

$$a_{mn} = -\gamma_n \int_0^{r_1} \int_0^{2\pi} r\cos\theta\,(e_{nr} h^{*}_{m\theta}\cos n\theta\cos m\theta - e_{n\theta} h^{*}_{mr}\sin n\theta\sin m\theta)\,r\,dr\,d\theta$$

$$+ \int_0^{r_1} \int_0^{2\pi} e_{nz}\,(h^{*}_{mr}\sin\theta\sin m\theta + h^{*}_{m\theta}\cos\theta\cos m\theta)\cos n\theta\,r\,dr\,d\theta \qquad \text{(viii)}$$

A similar expression is obtained for equation (vi).

The θ integrals of equation (viii) are zero unless $n-m=\pm 1$ and therefore only modes with azimuthal numbers differing by unity from that of the main mode are coupled due to a waveguide tilt. For the HE_{11} mode the coupled modes will have azimuthal numbers of 0 or 2. Evaluating the θ integrals of equations for a_{mn} in this case yield the following results.

For an E-plane bend with m=0:-

$$a_{mn} = -j\beta_n \pi \int_0^{r_1} r^2 e_{nr} h^*_{m\theta} dr + \pi \int_0^{r_1} r e_{nz} h^*_{m\theta} dr \qquad \text{(ix)}$$

the presence of only the $h_{m\theta}$ component implies that only E-type modes are coupled.

For an E-plane bend with m=2:-

$$a_{mn} = -j\beta_n \frac{\pi}{2} \int_0^{r_1} r^2 (e_{nr} h^*_{m\theta} - e_{n\theta} h^*_{mr}) dr + \frac{\pi}{2} \int_0^{r_1} r e_{nz} (h^*_{mr} + h^*_{m\theta}) dr \qquad \text{(x)}$$

for polarisation of mode m as equation (vii); for the orthogonal polarisation $a_{mn}=0$.

For an H-plane bend with m=0:-

$$a_{mn} = +j\beta_n \pi \int_0^{r_1} r^2 e_{n\theta} h^*_{mr} dr - \pi \int_0^{r_1} r e_{nz} h^*_{mr} dr \qquad \text{(xi)}$$

the presence of only the h_{mr} component implies that only H-type modes are coupled.

For an H-plane bend with m=2:-

$$a_{mn} = j\beta_n \frac{\pi}{2} \int_0^{r_1} r^2 (e_{nr} h^*_{m\theta} - e_{n\theta} h^*_{mr}) dr - \frac{\pi}{2} \int_0^{r_1} r e_{nz} (h^*_{mr} + h^*_{m\theta}) dr \qquad \text{(xii)}$$

for polarisation of mode m orthogonal to equation (vii); with polarisation equal to that of equation (vii) $a_{mn}=0$.

Evaluation of equations (ix) to (xii) for the corrugated waveguide is achieved by substituting for e_{nz}, h_{nz} etc., these being obtained from the space-harmonic field components in the inner region of the waveguide, appendix 5.1, via equation (vii).

APPENDIX 6.1

PERTURBATION ANALYSIS FOR THE CORRUGATED WAVEGUIDE

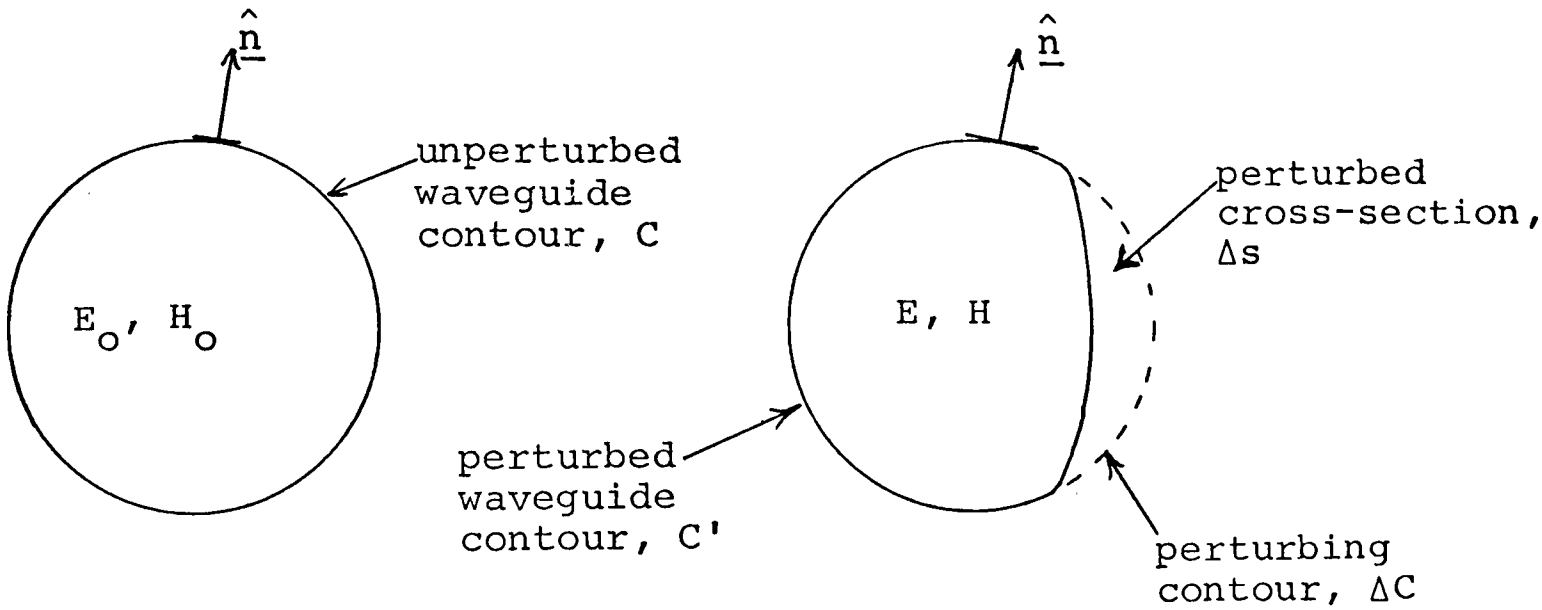

Express:-

unperturbed waveguide fields as $\underline{E}_o = \underline{E}_o(r,\theta)e^{-j\beta_o z}$

$\underline{H}_o = \underline{H}_o(r,\theta)e^{-j\beta_o z}$

perturbed waveguide fields as $\underline{E} = \underline{E}(r,\theta)e^{-j\beta_1 z}$

$\underline{H} = \underline{H}(r,\theta)e^{-j\beta_1 z}$

Application of Maxwells equations, integrating throughout the perturbed region, and applying the divergence theorem yields:-

$$\iint_{S'} (\underline{H}x\underline{E}_o^* + \underline{H}_o^* x\underline{E}).ds = 0$$

After some manipulation this yields

$$\delta\beta = \frac{j}{4P_o}\left[\oint_C (\underline{H}x\underline{E}_o^*).\hat{n}d\ell - \oint_{\Delta c} (\underline{H}x\underline{E}_o^*).\hat{n}d\ell + \oint_{c'} (\underline{H}_o^* x\underline{E}).\hat{n}d\ell\right] \quad (i)$$

where P_o is the power flow in the unperturbed waveguide.

For a waveguide with perfectly conducting boundaries, the 1st and 3rd terms of (i) are zero. The boundary conditions for the corrugated guide are:-

$E_{o\theta} = 0$ on C, the unperturbed waveguide boundary <26>

$E_{tangential} = 0 = E_{\xi}$ on C', the perturbed waveguide boundary.

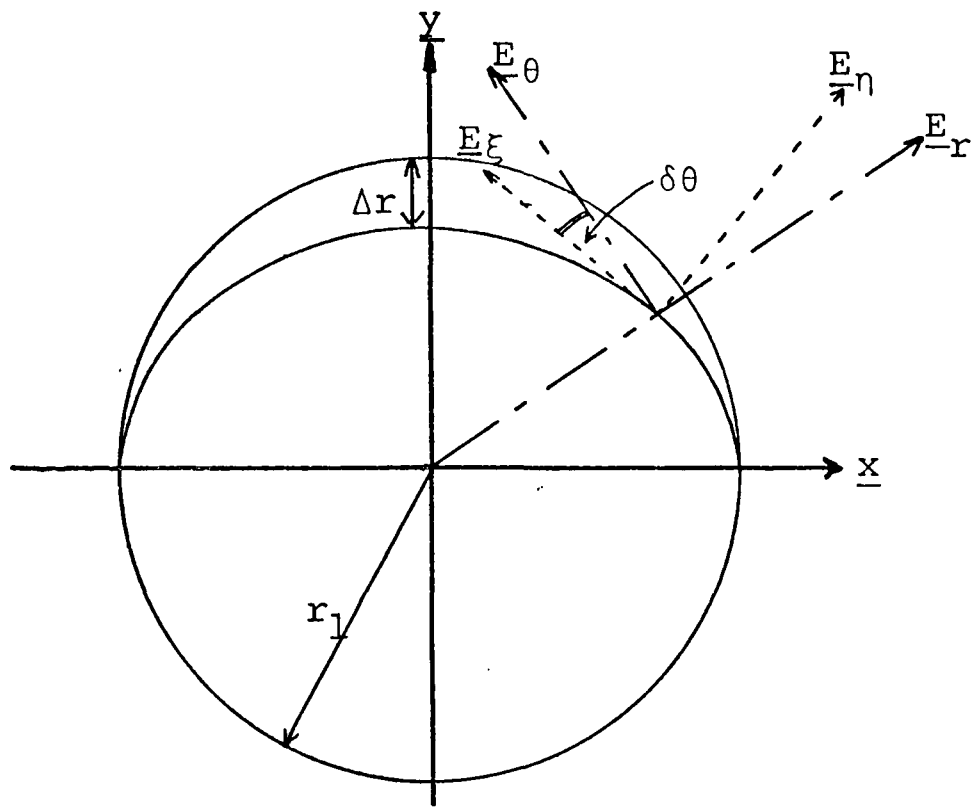

Expressing $\underline{E}_{\xi}$ in terms of $\underline{E}_{\theta}$, $\underline{E}_{r}$ and $\delta\theta$ yields:-

$$E_{o\theta} = 0 \text{ on } C$$

$$E_{\theta} - E_{r}\delta\theta = 0 \text{ on } C'$$

where

$$\delta\theta = \frac{\Delta r \sin 2\theta}{r_1}$$

Over the contour C, the unit normal, $\hat{\underline{n}}$, is given by $\hat{\underline{r}}$, and over the contour C' the unit normal is given by $\hat{\underline{n}} = \hat{r} + \hat{\underline{\theta}}\delta\theta$. After application of the boundary conditions and considerable manipulation equation (i) becomes:

$$\delta\beta = \frac{-j}{4P_o}\left[\oint_{\Delta C}(\underline{H}x\underline{E}^*_o).\hat{\underline{n}}d\ell + \oint_{\Delta c}(H^*_{o\theta}E_z)d\ell + \oint_{c'}(\delta\theta H^*_{or}E_z)d\ell\right.$$

$$\left. - \oint_{c}(H_\theta E^*_{oz}+H^*_{o\theta}E_z)d\ell\right] \qquad \text{(ii)}$$

Approximating the perturbed and unperturbed fields to be equal, and performing some tedious manipulation equation (ii) becomes, to first order in Δr,

$$\delta\beta = \frac{j\Delta r}{2P_o}\left[r_1\int_o^\pi (H_z\frac{\partial}{\partial r}E^*_\theta\Big|_{r=r_1})\sin^2\theta d\theta + \int_o^\pi (E^*_r H_z)\sin 2\theta d\theta\right]$$

Substitution of the corrugated waveguide field components yields

$$\delta\beta r_1 = \frac{-\Delta r\pi y_o\bar{B}}{16P_o}\left[A_1 - 2A_2\right]$$
even

where

$$A_1 = \left[\frac{(\bar{A}\beta r_1 - \bar{B}\bar{r}_1)}{Kr_1}\left(\frac{1}{Kr_1} - \frac{J_1'(Kr_1)}{J_1(Kr_1)}\right) + \bar{B}\bar{r}_1\right]$$

and $$A_2 = \left[\frac{\bar{A}(\beta r_1)}{Kr_1}\frac{J_1'(Kr_1)}{J_1(Kr_1)} + \frac{\bar{B}\bar{r}_1}{(Kr_1)^2}\right]$$

$$\delta\beta r_1 = \frac{-\Delta r\pi y_o\bar{B}}{16P_o}\left[3A_1 + 2A_2\right]$$
odd

$$(\delta\beta_{odd} - \delta\beta_{even})r_1 \equiv \Delta\beta r_1 = \frac{\Delta r\pi y_o\bar{B}}{8P_o}\left[A_1 - 2A_2\right]$$

where the corrugated waveguide field components are given in appendix 5.1.

APPENDIX 6.2

PERTURBATION FORMULAE FOR SMOOTH WALL WAVEGUIDE

From appendix 6.1 it can be shown that for a smooth wall waveguide

$$\delta\beta = \frac{-j}{4P_o} \oint_{\Delta C} (\underline{H} \times \underline{E}_o^*) . \hat{\underline{n}} d\ell$$

By applying Maxwells equations and the divergence theorem this can be expressed as:-

$$\delta\beta = \frac{-\omega}{4P_o} \iint_{\Delta s} (\mu |H_o|^2 + \varepsilon |E_o|^2) ds \qquad \text{(i)}$$

where H_o and E_o are the total magnetic and electric field magnitudes in the waveguide, and Δs is the perturbed cross-section surface. Applying the mode field components equation (i) becomes:-

For the TE_{1m} mode

$$\delta\beta_{even} = \frac{-\Delta r \; Kr_1^2 (Kr_1^2 - 3)}{4 \; \beta r_1 \; (Kr_1^2 - 1) r_1^2}$$

$$\delta\beta_{odd} = \frac{-\Delta r \; Kr_1^2 (3Kr_1^2 - 1)}{4 \; \beta r_1 \; (Kr_1^2 - 1) r_1^2}$$

giving:

$$\delta\beta_{odd} - \delta\beta_{even} \equiv \Delta\beta = \frac{\Delta r \; Kr_1^2 (Kr_1^2 + 1)}{2 \; \beta r_1 \; (Kr_1^2 - 1) r_1^2} = F\Delta r$$

where Kr_1 is the transverse wavenumber of the m^{th} mode.

For the TM_{1m} mode

$$\delta\beta_{even} = \frac{-\Delta r \; Kr_1^{\,2}}{4 \; \beta r_1 \; r_1^{\,2}}$$

$$\delta\beta_{odd} = \frac{-3\Delta r \; Kr_1^{\,2}}{4 \; \beta r_1 \; r_1^{\,2}}$$

giving:

$$\delta\beta_{odd} - \delta\beta_{even} \equiv \Delta\beta = \frac{\Delta r \; Kr_1^{\,2}}{2 \; \beta r_1 \; r_1^{\,2}} = F\Delta r$$

APPENDIX 6.3

THE CAVITY RESONANCE CONDITION

Consider the 4-port representation of a resonant cavity shown below

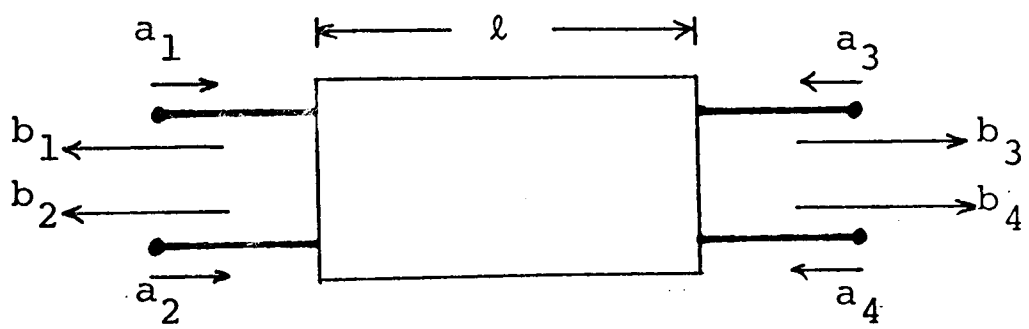

The transmission matrices are $\begin{bmatrix} b_1 \\ b_2 \end{bmatrix} = \underset{\sim}{B}\begin{bmatrix} a_3 \\ a_4 \end{bmatrix}$ and $\begin{bmatrix} b_3 \\ b_4 \end{bmatrix} = \underset{\sim}{A}\begin{bmatrix} a_1 \\ a_2 \end{bmatrix}$

The boundary conditions are $\begin{bmatrix} a_1 \\ a_2 \end{bmatrix} = -\begin{bmatrix} b_1 \\ b_2 \end{bmatrix}$ and $\begin{bmatrix} a_3 \\ a_4 \end{bmatrix} = -\begin{bmatrix} b_3 \\ b_4 \end{bmatrix}$

This yields $[\underset{\sim}{I} - \underset{\sim}{A}\,\underset{\sim}{B}]\begin{bmatrix} b_3 \\ b_4 \end{bmatrix} = 0$, and for a non-trivial solution the resonance condition is $|\underset{\sim}{I} - \underset{\sim}{A}\,\underset{\sim}{B}| = 0$ (i)

It is easily shown that $\underset{\sim}{A} \equiv \underset{\sim}{B}$ and from equation 6.2

$\underset{\sim}{A} = e^{-j\beta\ell}(\underset{\sim}{I} - j\underline{X})$ where

$$\underline{X} = \begin{bmatrix} \int_0^{\ell} (\delta\beta_e \cos^2\psi + \delta\beta_o \sin^2\psi)\,dz & \tfrac{1}{2}\int_0^{\ell} \sin 2\psi(\delta\beta_o - \delta\beta_e)\,dz \\ \tfrac{1}{2}\int_0^{\ell} \sin 2\psi(\delta\beta_o - \delta\beta_e)\,dz & \int_0^{\ell} (\delta\beta_e \sin^2\psi + \delta\beta_o \cos^2\psi)\,dz \end{bmatrix}.$$

To first order, the resonance condition, equation (i), becomes

$$\left|\underset{\sim}{I}(1-e^{-2j\beta\ell}) + \underset{\sim}{X}\,2je^{-2j\beta\ell}\right| = 0$$

Evaluation yields a quadratic equation in $\sin\beta\ell$ with solution

$$\sin\beta\ell = e^{-j\beta\ell(\beta' \mp \sqrt{\beta^{2}''})\ell} \qquad \text{(ii)}$$

where $\beta'\ell = \frac{1}{2}\int_{0}^{\ell}(\delta\beta_e+\delta\beta_o)dz$, the mean offset in propagation coefficient caused by ellipticity; and

$$(\beta''\ell)^2 = \tfrac{1}{4}\iint_{0}^{\ell}\Delta\beta(z_1)\Delta\beta(z_2)\left[\cos2\psi(z_1)\cos2\psi(z_2)+\sin2\psi(z_1)\sin2\psi(z_2)\right]dz_1dz_2$$

where $\Delta\beta(z) = \delta\beta_o(z)-\delta\beta_e(z)$ and $2\beta''$ is the difference in propagation coefficients between orthogonal polarisations.

Rearrangement of equation (ii) yields:

$$1 - e^{-2j\{(\beta-\beta')\pm\beta''\}\ell} = 0$$

Comparison of this equation with that for a perfectly circular waveguide,

$1 - e^{-2j\beta\ell} = 0$ having resonance condition $\beta\ell = n\pi$, yields the required resonance condition of

$$(\beta-\beta')\ell \pm \beta''\ell = n\pi \qquad \text{(iii)}$$

The *expected value* of $(\beta''\ell)^2$ is then given by:

$$E\{(\beta''\ell)^2\} = \tfrac{1}{4}\iint_{0}^{\ell}E\{\Delta\beta(z_1)\Delta\beta(z_2)\cos2\psi(z_1)\cos2\psi(z_2)\}dz_1dz_2$$

$$+ \tfrac{1}{4}\iint_{0}^{\ell}E\{\Delta\beta(z_1)\Delta\beta(z_2)\sin2\psi(z_1)\sin2\psi(z_2)\}dz_1dz_2$$

Using the result obtained in Appendix 6.5, this can be expressed as:

$$E\{(\beta'')^2\} = \frac{1}{2\ell^2}\int_{-\ell}^{+\ell}R_{\Delta}(\tau)(\ell-|\tau|)d\tau \qquad \text{(iv)}$$

Substituting for $R_{\Delta}(\tau)$ from appendix 6.5, equation (ix), the required expected value for the propagation coefficient spreading, $\Delta\beta_s$, is obtained as

$$\Delta\beta_s = 2\sqrt{E\{(\beta'')^2\}} = F(\sigma^2_{\Delta r}+\mu^2_{\Delta r})^{\frac{1}{2}}\sqrt{\frac{h}{\ell}} \qquad (v)$$

where h is the fixed correlation length. For the case where h is the average correlation length equation (v) is multiplied by $\sqrt{2}$.

APPENDIX 6.4

RELATIONSHIP BETWEEN THE FREQUENCY SPREADING AND PROPAGATION COEFFICIENT SPREADING IN AN ELLIPTICAL RESONANT CAVITY

Consider a cavity of length ℓ, for a small change in frequency, δf, β changes to β_c as:

$$\beta_c = \beta + \frac{\partial \beta}{\partial \omega} \delta \omega$$

or $$\beta_c = \beta + \frac{\delta \omega}{v_g}$$

where v_g is the group velocity and $\delta \omega = 2\pi \delta f$.

Let the split in propagation coefficient due to ellipticity be

$$\Delta \beta_s \text{ and let } \beta_e = (\beta - \beta') + \frac{\Delta \beta}{2}$$

$$\beta_o = (\beta - \beta') - \frac{\Delta \beta}{2}$$

If the resonant frequency of the perfectly circular waveguide is f_o, then the cavity resonance condition is

$$\beta \ell = n\pi \qquad \text{(i)}$$

For β_e to be resonant at length ℓ a change in frequency $\delta \omega_e$ is required such that

$$(\beta_e + \frac{\delta \omega_e}{v_g}) \ell = n\pi$$

or $$(\{\beta - \beta'\} + \frac{\Delta \beta_s}{2} + \frac{\delta \omega_e}{v_g}) \ell = n\pi$$

substitution of equation (i) yields: $\frac{\delta\omega_e}{v_g} = \beta' - \frac{\Delta\beta_s}{2}$

similarly for β_o $\frac{\delta\omega_o}{v_g} = \beta' + \frac{\Delta\beta_s}{2}$

The difference between the two frequency changes yields the required spreading Δf.

$$\Delta f = \frac{v_g \Delta\beta_s}{2\pi}$$

APPENDIX 6.5

STATISTICALLY AVERAGE VALUE FOR THE ORTHOGONALLY POLARISED POWER

From equation 6.5 the statistically average value for the orthogonally polarised power is given by

$$E\{b_y(\ell)b_y^*(\ell)\} = \frac{F^2 b_x^{\,2}(0)}{4} \int_0^{\ell}\int_0^{\ell} E\{\Delta(z_1)\Delta(z_2)\}dz_1 dz_2 \qquad \text{(i)}$$

where $\Delta(z) = \Delta r(z)\sin 2\psi(z)$. It can be shown <47> that for $\Delta(z)$ statistically stationary,

$$E\{\Delta(z_1)\Delta(z_2)\} = R_\Delta(z_2 - z_1) \equiv R_\Delta(\tau) \qquad \text{(ii)}$$

where $R_\Delta(\tau)$ is the autocorrelation function, given by

$$R_\Delta(\tau) = \int_{-\infty}^{+\infty}\int_{-\infty}^{+\infty} \Delta_1\Delta_2 p(\Delta_1)p(\Delta_2/\Delta_1;\tau)d\Delta_1 d\Delta_2 \qquad \text{(iii)}$$

with $p(\Delta_1)$ the probability density function for $\Delta(z)$ and $p(\Delta_2/\Delta_1;\tau)$ the probability density function for $\Delta(z_2)$ when $\Delta(z_1)$ has the value such that $\tau = z_2 - z_1$.

Substituting equation (ii) into equation (i) yields:

$$E\{b_y(\ell)b_y^*(\ell)\} = \frac{F^2 b_x^{\,2}(0)}{4} \int_0^{\ell}\int_0^{\ell} R_\Delta(z_2 - z_1)dz_1 dz_2 \qquad \text{(iv)}$$

The region of integration for this equation is shown below. The shaded area can be easily obtained as $(\ell - |\tau|)d\tau$

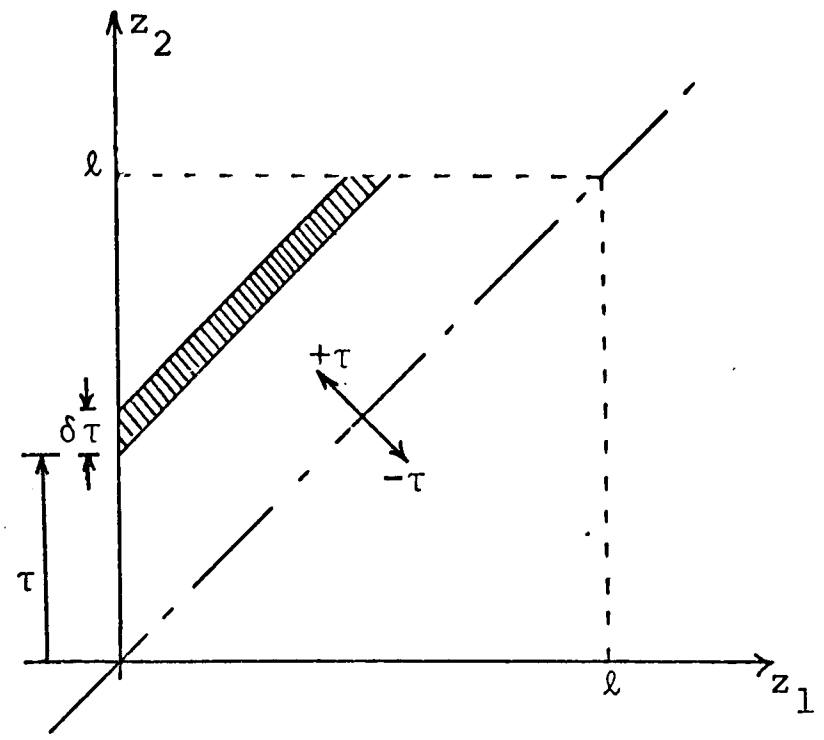

In the limit as $\delta\tau \to 0$ $R_\Delta(\tau)$ is constant over the shaded area, the contribution to the integral at τ is $R_\Delta(\tau)(\ell-|\tau|)d\tau$. The total area is found by integrating over all possible values of τ, yielding

$$\int_{0}^{\ell}\int_{0}^{\ell} R_\Delta(z_2-z_1)dz_1dz_2 = \int_{-\ell}^{+\ell} R_\Delta(\tau)(\ell-|\tau|)d\tau \qquad \text{(v)}$$

Thus equation (iv) becomes

$$E\{b_y(\ell)b_y^*(\ell)\} = \frac{F^2 b_x^{\,2}(0)}{4}\int_{-\ell}^{+\ell} R_\Delta(\tau)(\ell-|\tau|)d\tau \qquad \text{(vi)}$$

Now it is only possible to calculate $R_\Delta(\tau)$ for simple z dependences. One such simple assumption is that the waveguide ellipticity, $2\Delta r$, and orientation, ψ, are constant over a fixed length h (termed the correlation length), where $h << \ell$; this is shown diagramatically below.

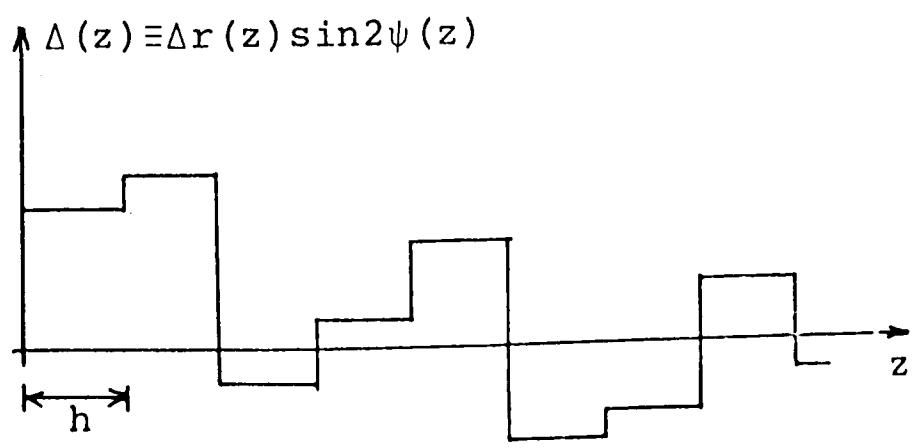

In this case it can be shown <46> that

$$R_\Delta(\tau) = (\sigma_\Delta^2+\mu_\Delta^2)\left(1 - \frac{|\tau|}{h}\right) + \mu_\Delta^2\frac{\tau}{h} \qquad |\tau| \leq h$$

$$= \mu_\Delta^2 \qquad |\tau| > h$$

where μ_Δ is the mean value of $\Delta(z)$ and σ_Δ is that standard deviation of $\Delta(z)$. However, in our case $\psi(z)$ is assumed to be random and so $\sin 2\psi(z)$ has zero mean value, consequently $\psi(z)$ also has zero mean value ($\mu_\Delta = 0$). Therefore $R_\Delta(\tau)$ becomes

$$R_\Delta(\tau) = \sigma_\Delta^2\left(1 - \frac{|\tau|}{h}\right) \qquad |\tau| \leq h \qquad \text{(vii)}$$

$$= 0 \qquad |\tau| > h$$

Now $\sigma_\Delta^2 = \int_{\text{all possible values}} \Delta^2 p(\Delta)\, d\Delta$

and substituting $\Delta = \Delta r \sin 2\psi$ gives

$$\sigma_\Delta^2 = \int_0^{\Delta r_{max}} \Delta r^2 \sin^2 2\psi\, p(\Delta r \sin 2\psi)\, d(\Delta r)\, d\psi$$

For ψ and Δr independent, the above equation becomes

$$\sigma_\Delta^2 = \int_0^{\Delta r_{max}} \Delta r^2 p(\Delta r)\, d(\Delta r) \int_0^{2\pi} \sin^2 2\psi\, p(\psi)\, d\psi \qquad \text{(viii)}$$

where $p(\Delta r)$ and $p(\psi)$ are the probability density functions for Δr and ψ respectively.

For ψ random, $p(\psi) = \frac{1}{2\pi}$ and noting that

$$\int_0^{\Delta r_{max}} \Delta r^2 p(\Delta r)\, d(\Delta r) = (\sigma_{\Delta r}^2+\mu_{\Delta r}^2)$$

equation (viii) becomes

$$\sigma_{\Delta}^{2} = \tfrac{1}{2}(\sigma_{\Delta r}^{2}+\mu_{\Delta r}^{2})$$

Thus the autocorrelation function, equation (vii), can be expressed as

$$R_{\Delta}(\tau) = \tfrac{1}{2}(\sigma_{\Delta r}^{2}+\mu_{\Delta r}^{2})\left(1 - \frac{|\tau|}{h}\right) \qquad |\tau| \leq h \qquad \text{(ix)}$$

$$= 0 \qquad |\tau| > h$$

Substituting equation (ix) into the expression for the expected orthogonal power, equation (vi), yields the required result.

$$E\{b_y(\ell)b_y^{*}(\ell)\} = \frac{F^2 b_x^{\,2}(0)}{8}(\sigma_{\Delta r}^{2}+\mu_{\Delta r}^{2})\ell h \qquad (\ell >> h)$$

A similar case, where the correlation length h is taken to be the *average* can be shown to yield <46> the following expression for the autocorrelation function

$$R_{\Delta}(\tau) = \tfrac{1}{2}\, e^{-\frac{|\tau|}{h}}(\sigma_{\Delta r}^{2}+\mu_{\Delta r}^{2})$$

This yields an expected orthogonal power of

$$E\{b_y(\ell)b_y^{*}(\ell)\} = \frac{F^2 b_x^{\,2}(0)}{4}(\sigma_{\Delta r}^{2}+\mu_{\Delta r}^{2})\ell h \qquad (\ell >> h)$$

APPENDIX 7.1

LIGHTWEIGHT FORM OF CONSTRUCTION FOR THE CORRUGATED CIRCULAR WAVEGUIDE

One disadvantage in the use of the corrugated waveguide as an antenna feeder is that it is much heavier than its smooth wall waveguide competitors. Experimental results described in chapter 7 indicated that slight perturbation of the base of the corrugations did not affect the low attenuation properties of the HE_{11} mode. Therefore, so long as good contact between the corrugation side wall and base can be achieved a rigid outer surface is not required. This leads to the possibility of replacing the outer metal pipe forming the corrugation base with metal foil, resulting in a structure very much lighter in weight.

The proposed form of construction consists of a metal frame or *cage* which contains the corrugation irises which are supported by a pair of longitudinal bars, figure i , the outer surface of the cage then being covered with aluminium foil. Resonant cavity measurements on this structure indicated an HE_{11} mode attenuation about twice the value obtained when a solid metal pipe formed the outer surface. This higher attenuation was caused by poor contact between the aluminium foil and both the metal irises and the waveguide flanges.

However, the results do suggest that if good contact between the foil and the cage could be obtained attenuation

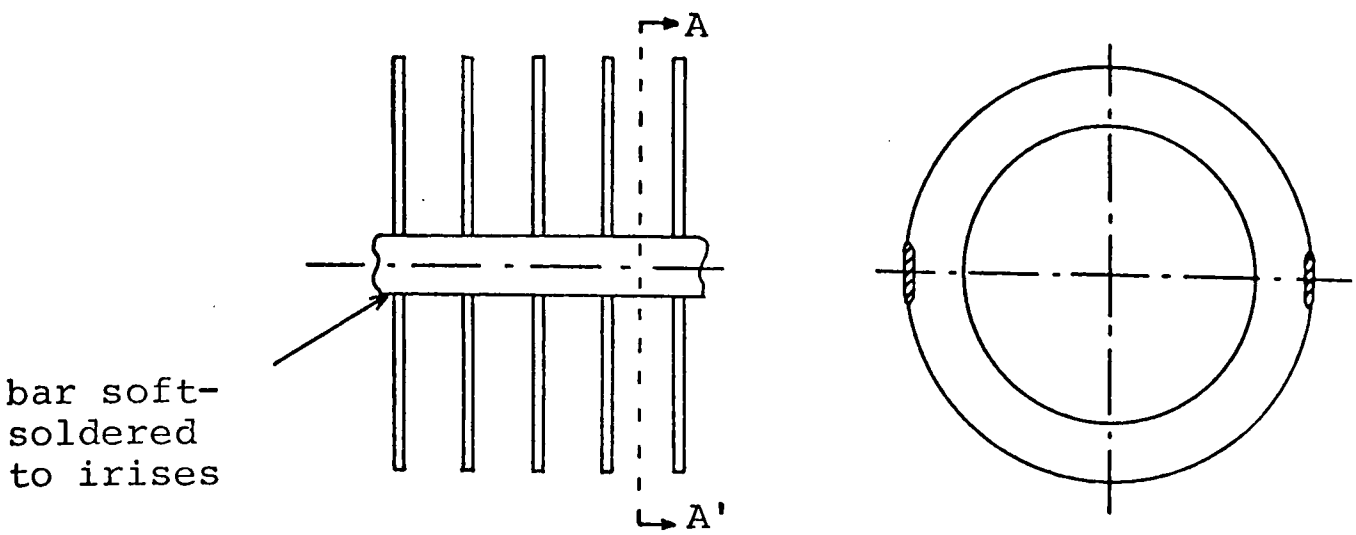

Fig. i The frame for the lightweight waveguide construction

values comparable with those achieved using the much heavier metal outer wall would be possible. A method of achieving this good contact would be to use some form of highly conducting bonding agent between the foil and the iris and then to cover the foil with a heat sensitive plastic shrink sleeving. When this sleeving is warmed it contracts in diameter tightly gripping the iris-foil joints together.

If commercial production of the corrugated waveguide was envisaged this form of lightweight construction would appear to warrant further investigation.

APPENDIX 9.1

KIRCHHOFF-HUYGENS FORMULAE FOR THE FAR-FIELD RADIATION FROM AN OPEN-ENDED CIRCULAR CORRUGATED WAVEGUIDE

This analysis includes space harmonics in the inner region and applies to any of the possible waveguide modes. The general expression for the radiation at a distant point P due to plane equiphase aperture, with fields E_t, H_t, forming part of a closed surface on which the remaining surface has zero field is given by <50>

$$\lim_{\frac{\omega}{c}R \to \infty} \underline{E}_p = \frac{-j\frac{\omega}{c}e^{-j\frac{\omega}{c}R}}{4\pi R} \underline{i}_R x \int_S \left((\underline{n}x\underline{E}_t - z_o \underline{i}_R x (\underline{n}x\underline{H}_t) \right) e^{j\frac{\omega}{c}\underline{r}\cdot\underline{i}_R} dS \quad (i)$$

where $\underline{n}$ is the unit normal to the aperture and $\underline{i}_R$ is the unit vector of $\underline{R}$. In the far-field it is not necessary to compute separately the magnetic field as it can be shown that:-

$$\lim_{\frac{\omega}{c}R \to \infty} \underline{H}_p = \frac{-\underline{E}_p x \underline{i}_R}{z_o} \quad (ii)$$

Taking the aperture field components as E_r, H_r, E_θ, H_θ the radiation at point P, using the coordinate system of figure 9.2, is given by:-

$$E_{p\theta} = \frac{-j\frac{\omega}{c}e^{-j\frac{\omega}{c}R}}{4\pi R} \int_0^{2\pi} \int_0^{r_1} \Big[-(E_r + z_o \cos\theta H_\theta)\cos(\phi-\theta) - (E_\theta - z_o \cos\theta H_r)\sin(\phi-\theta) \Big] e^{j\bar{r}\sin\theta\cos(\phi-\theta)} r\,dr\,d\theta \quad (iii)$$

$$E_{p\phi} = \frac{-j\frac{\omega}{c}e^{-j\frac{\omega}{c}R}}{4\pi R}\int_0^{2\pi}\int_0^{r_1}\Big[(E_r\cos\theta+z_oH_\theta)\sin(\phi-\theta)$$

$$-(E_\theta\cos\theta-z_oH_r)\cos(\phi-\theta)\Big]e^{j\bar{r}\sin\theta\cos(\phi-\theta)}\,r\,dr\,d\theta \quad \text{(iv)}$$

Substituting the expressions for the space harmonic field components of the corrugated waveguide given in appendix 5.1 leads to the required far-field radiation formulae. The resulting equations can be evaluated in closed form by making use of the following integral expressions:-

$$\int_0^{2\pi} e^{-jx\cos(\phi-\theta)}\begin{matrix}\cos\\ \sin\end{matrix}n\theta\,d\theta = 2\pi j^n\begin{matrix}\cos\\ \sin\end{matrix}n\phi J_n(x) \quad \text{(v)}$$

$$\int_0^{r_1} r\,J_{n+1}(\bar{r}\sin\theta)J_{n+1}(K_Nr)\,dr = \frac{-nJ_n(\bar{r}_1\sin\theta)J_n(K_Nr_1)}{K_N(\frac{\omega}{c})\sin\theta}$$

$$+\frac{J_n'(\bar{r}_1\sin\theta)K_Nr_1J_n(K_Nr_1)-J_n(\bar{r}_1\sin\theta)J_n'(K_Nr_1)\bar{r}_1\sin\theta}{K_N^2-(\frac{\omega}{c})^2\sin^2\theta} \quad \text{(vi)}$$

$$\int_0^{r_1} rJ_{n-1}(\bar{r}_1\sin\theta)J_{n-1}(K_Nr)\,dr = \frac{nJ_n(\bar{r}_1\sin\theta)J_n(K_Nr_1)}{K_N(\frac{\omega}{c})\sin\theta}$$

$$+\frac{J_n'(\bar{r}_1\sin\theta)K_Nr_1J_n(K_Nr_1)-J_n(\bar{r}_1\sin\theta)J_n'(K_Nr_1)\bar{r}_1\sin\theta}{K_N^2-(\frac{\omega}{c})^2\sin^2\theta} \quad \text{(vii)}$$

Equations (vi) and (vii) are the Lommel integrals.

The resulting closed-form expressions for equations (iii) and (iv) are given, after some manipulation, by:-

$$E^N_{p\theta} = \frac{-j^{n+1}\bar{r}_1 e^{-j\frac{\omega}{c}R}}{2K_N r_1 (\frac{R}{r_1})} \cos n\phi \left[\bar{A}_N (\beta_N r_1 + \bar{r}_1 \cos\theta) T(\theta) + \frac{\bar{B}_N (\bar{r}_1 + \beta_N r_1 \cos\theta) n J_n (\bar{r}_1 \sin\theta)}{(K_N r_1) \bar{r}_1 \sin\theta} \right] e^{-j\beta_N z} \quad \text{(viii)}$$

$$E^N_{p\phi} = \frac{j^{n+1}\bar{r}_1 e^{-j\frac{\omega}{c}R}}{2K_N r_1 (\frac{R}{r_1})} \sin n\phi \left[\frac{\bar{A}_N (\bar{r}_1 + \beta_N r_1 \cos\theta) n J_n (\bar{r}_1 \sin\theta)}{K_N r_1 \bar{r}_1 \sin\theta} + \bar{B}_N (\beta_N r_1 + \bar{r}_1 \cos\theta) T(\theta) \right] e^{-j\beta_N z} \quad \text{(ix)}$$

where:-

$$T(\theta) = \frac{J_n'(\bar{r}_1 \sin\theta) K_N r_1 J_n (K_N r_1) - J_n (\bar{r}_1 \sin\theta) J_n'(K_N r_1) \bar{r}_1 \sin\theta}{J_n (K_N r_1) \{ (K_N r_1)^2 - (\bar{r} \sin\theta)^2 \}} \quad \text{(x)}$$

Equations (viii) and (ix) give the far-field radiation pattern of an open-ended circular corrugated waveguide for each space harmonic, the total radiation pattern being obtained by summing each space harmonic contribution.

Thus:

$$E_{p\theta} = C_\theta(\theta) \cos n\phi \quad \text{(xi)}$$

$$E_{p\phi} = C_\phi(\theta) \sin n\phi \quad \text{(xii)}$$

where $C_\theta(\theta)$ and $C_\phi(\theta)$ are the pattern functions, given by $C_\theta(\theta) = \sum_{-N}^{+N} C^N_\theta(\theta) e^{-j\beta_N z}$ and $C_\phi(\theta) = \sum_{-N}^{+N} C^N_\phi(\theta) e^{-j\beta_N z}$

$C^N_\theta(\theta)$ and $C^N_\phi(\theta)$ being obtained from equations (viii) and (ix) respectively.

The limiting cases of these equations will now be considered.

As $\theta \to 0$ consider the term of (viii) within square brackets,

$$\text{for } n \neq 1 \qquad \frac{(\beta_N r_1 + \bar{r}_1)\bar{B}_N n}{K_N} \lim_{\theta \to 0} \left[\frac{J_n(\bar{r}_1 \sin\theta)}{\bar{r}_1 \sin\theta} \right]$$

$$\text{for } n = 1 \qquad \frac{(\beta_N r_1 + \bar{r}_1)}{K_N} \lim_{\theta \to 0} \left[\frac{J_1(\bar{r}_1 \sin\theta)\bar{B}_N}{\bar{r}_1 \sin\theta} + \bar{A}_N J_1'(\bar{r}_1 \sin\theta) \right]$$

Making use of the identities:-

$$J_1'(x) = J_o(x) - \frac{J_1(x)}{x}$$

$$\lim_{\theta \to 0} \left[\frac{J_n(x)}{x} \right] = \tfrac{1}{2} \qquad \text{for } n = 1$$

$$= 0 \qquad \text{for } n > 1$$

yields:-

$$\lim_{\theta \to 0} E^N_{p\theta} = \frac{\bar{r}_1 e^{-j\frac{\omega}{c}R} \cos\phi}{4(K_N r_1)^2 (\frac{R}{r_1})} (\beta_N r_1 + \bar{r}_1)(\bar{A}_N + \bar{B}_N) \qquad \text{for } n = 1$$

$$= 0 \qquad \text{for } n \neq 1 \qquad \text{(xii)}$$

Similarly,

$$\lim_{\theta \to 0} E^N_{p\phi} = \frac{-\bar{r}_1 e^{-j\frac{\omega}{c}R} \sin\phi}{4(K_N r_1)^2 (\frac{R}{r_1})} (\beta_N r_1 + \bar{r}_1)(\bar{A}_N + \bar{B}_N) \qquad \text{for } n = 1$$

$$= 0 \qquad \text{for } n \neq 1 \qquad \text{(xiii)}$$

Therefore for modes with non-unity azimuthal number the radiation pattern has a null on boresight.

Consider now the case of modes with zero azimuthal dependence. The H-type modes have $E_z = H_\theta = E_r = 0$ in equation (iii), and on evaluating the θ integral $E_{p\theta}$ is found to be identically zero. Similarly for E-type modes, where $H_z = E_\theta = H_r = 0$, $E_{p\phi}$ is identically zero. Thus the radiation pattern for H-type modes only have the $E_{p\phi}$ component whilst those for the E-type modes have only the $E_{p\theta}$ component.

APPENDIX 9.2

FOURIER INTEGRAL REPRESENTATION OF THE FAR-FIELD RADIATION FROM AN OPEN-ENDED CORRUGATED WAVEGUIDE

The problem will be restricted to that of a plane aperture at z = 0 consisting of a circular waveguide aperture plus an infinitely conducting plane. This method uses the concept that the electromagnetic field at the aperture can be represented as a superposition of propagating and evanescent plane waves. It can be shown that only the propagating waves will contribute to the energy received at infinity, the evanescent waves being localised around the radiating aperture.

The method is covered in some detail in reference 51 and will only be briefly described here.

According to the uniqueness theorem for electromagnetic fields, the field in the half space z > 0 is uniquely determined by a knowledge of either the tangential electric or magnetic field at z = 0, together with the radiation condition. Since in this case the tangential electric field, E_t, is zero everywhere over the plane z = 0, except on the aperture, it is more convenient to use the electric field. The distribution of the plane waves present in the region z > 0 are obtained by applying the double Fourier transform of the electric field in this region. It can be shown that the Fourier transform of this field has the form $\underline{f}(k_x,k_y)e^{-jk_z z}$ where $k_z^2 = (\omega/c)^2-k_x^2-k_y^2$;

$\underline{k} = k_x\underline{x}+k_y\underline{y}+k_z\underline{z}$ and k_x,k_y are the transform variables. Taking the inverse Fourier transform yields the electric field in the half space $z > 0$:-

$$E(R) = \frac{1}{4\pi^2}\int_{-\infty}^{+\infty}\int \underline{f}(k_x,k_y)e^{-j\underline{k}\cdot\underline{R}}dk_x dk_y \qquad (i)$$

This expression states that the field may be regarded as made up of a superposition of plane waves of the form $\underline{f}(k_x,k_y)e^{-j\underline{k}\cdot R}$, $\underline{f}(k_x,k_y)$ being obtained from the Fourier transform of the aperture field:-

$$f_x = \iint_{\text{aperture}} E_x e^{j(k_x\underline{x}+k_y\underline{y})}\,dxdy$$

$$f_y = \iint_{\text{aperture}} E_y e^{j(k_x\underline{x}+k_y\underline{y})}\,dxdy \qquad (ii)$$

It can also be shown that div $\underline{E}$ = 0 yields $\underline{k}.\underline{f} = 0$, which in turn yields

$$f_z = \frac{-\underline{k}_t\cdot\underline{f}_t}{k_z}$$

Equation (i) is evaluated for large R asymptotically using the method of stationary phase <51>. This uses the fact that when a slowly varying function of k_x,k_y is multiplied by a rapidly oscillating function $e^{-j\underline{k}\cdot\underline{R}}$ and integrated over k_x,k_y the main contribution to the integral comes from the stationary points of $\underline{k}.\underline{r}$, i.e. the stationary phase points. Applying this method and changing to spherical coordinates gives:-

$$\lim_{R\to\infty} E(R) = \frac{j\frac{\omega}{c}e^{-j\frac{\omega}{c}R}}{2\pi R}\left[\underline{\phi}(f_y\cos\phi-f_x\sin\phi)\cos\theta+\underline{\theta}(f_x\cos\phi+f_y\sin\phi)\right] \qquad (iii)$$

where $\underline{\phi}$ and $\underline{\theta}$ are the unit vectors of ϕ and θ. From this equation it is clear that the far-field radiation depends on the Fourier transform of the aperture field distribution f_x and f_y.

Changing equations (ii) to the r and θ coordinates of the waveguide yields:-

$$f_x = \int_0^{2\pi}\int_0^{r_1} (E_r\cos\theta - E_\theta\sin\theta)e^{j\bar{r}\sin\theta\cos(\phi-\theta)}\,r\,dr\,d\theta$$

$$f_y = \int_0^{2\pi}\int_0^{r_1} (E_r\sin\theta - E_\theta\cos\theta)e^{j\bar{r}\sin\theta\cos(\phi-\theta)}\,r\,dr\,d\theta \qquad \text{(iv)}$$

Substituting (iv) into (iii) yields:-

$$E_{p\theta} = \frac{j\frac{\omega}{c}e^{-j\frac{\omega}{c}R}}{2\pi R}\int_0^{2\pi}\int_0^{r_1}\{E_r\cos(\phi-\theta)+E_\theta\sin(\phi-\theta)\}e^{j\bar{r}\sin\theta\cos(\phi-\theta)}\,r\,dr\,d\theta \qquad \text{(v)}$$

$$E_{p\phi} = \frac{j\frac{\omega}{c}e^{-j\frac{\omega}{c}R}}{2\pi R}\int_0^{2\pi}\int_0^{r_1}\{-E_r\sin(\phi-\theta)+E_\theta\cos(\phi-\theta)\}\cos\theta e^{j\bar{r}\sin\theta\cos(\phi-\theta)}\,r\,dr\,d\theta \qquad \text{(vi)}$$

Substituting the expressions for the space harmonic field components of the corrugated waveguide given in appendix 5.1 in the above equations leads to the required far-field radiation formulae. As in the K.H. method the resulting equations can be evaluated in closed form by making use of equations (v) → (vii) of appendix 9.1. The resulting closed form expressions for equations (v) and (vi) are given, after some manipulation, by:-

$$E^N_{p\theta} = \frac{-j^{n+1}\bar{r}_1 e^{-j\frac{\omega}{c}R}\cos n\phi}{(K_N r_1)(\frac{R}{r_1})}\left[\bar{A}_N\beta_N r_1 T(\theta) + \frac{\bar{B}_N \bar{r}_1 n J_n(\bar{r}_1\sin\theta)}{(K_N r_1)\bar{r}_1\sin\theta}\right] \quad \text{(vii)}$$

$$E^N_{p\phi} = \frac{j^{n+1}\bar{r}_1 e^{-j\frac{\omega}{c}R}\cos\theta\sin n\phi}{(K_N r_1)(\frac{R}{r_1})}\left[\frac{\bar{A}_N\beta_N r_1 J_n(\bar{r}_1\sin\theta)n}{(K_N r_1)\bar{r}_1\sin\theta} + \bar{B}_N\bar{r}_1 T(\theta)\right] \quad \text{(viii)}$$

where $T(\theta)$, $\bar{A}_N$, $\bar{B}_N$ are defined as in equation (x) of appendix 9.1.

Thus the total far-field radiation pattern is given by:-

$$E_{p\theta} = C_\theta(\theta)\cos n\phi \quad \text{(ix)}$$

$$E_{p\phi} = C_\phi(\theta)\sin n\phi \quad \text{(x)}$$

where $C_\theta(\theta)$ and $C_\phi(\theta)$ are the pattern functions, given by

$$C_\theta(\theta) = \sum_{-N}^{+N} C^N_\theta(\theta)e^{-j\beta_N z} \quad \text{and} \quad C_\phi(\theta) = \sum_{-N}^{+N} C^N_\phi(\theta)e^{-j\beta_N z}$$

$C^N_\theta(\theta)$ and $C^N_\phi(\theta)$ being obtained from equations (vii) and (viii) respectively.

Considering the limiting cases for (vii) and (viii) as $\theta \to 0$, the term of (vii) within square brackets becomes:

for $n \neq 1$ $\quad \frac{\bar{B}_N n\bar{r}_1}{K_N r_1} \lim_{\theta\to 0}\left(\frac{J_n(\bar{r}_1\sin\theta)}{\bar{r}_1\sin\theta}\right)$

and for $n = 1$

$$\frac{1}{K_N r_1}\left[\bar{A}_N\beta_N r_1 J_1'(\bar{r}_1\sin\theta) + \frac{\bar{B}_N\bar{r}_1 J_n(\bar{r}_1\sin\theta)}{\bar{r}_1\sin\theta}\right]$$

making use of the identities given in equation (x) of appendix 9.1 yields:

$$\lim_{\theta \to 0} E^N_{p\theta} = \frac{\bar{r}_1 e^{-j\frac{\omega}{c}R} \cos\phi}{2(K_N r_1)^2 (\frac{R}{r_1})} \left[\bar{A}_N \beta_N r_1 + \bar{B}_N \bar{r}_1\right] \quad \text{for } n = 1$$

$$= 0 \qquad \text{for } n \neq 1 \qquad \text{(xi)}$$

Similarly:

$$\lim_{\theta \to 0} E^N_{p\phi} = \frac{\bar{r}_1 e^{-j\frac{\omega}{c}R} \sin\phi}{2(K_N r_1)^2 (\frac{R}{r_1})} \left[\bar{A}_N \beta_N r_1 + \bar{B}_N \bar{r}_1\right] \quad \text{for } n = 1$$

$$= 0 \qquad \text{for } n \neq 1 \qquad \text{(xii)}$$

Comparison of the F.T. far-field radiation pattern equations, (vii) and (viii), with those obtained using the K.H. analysis of appendix 9.1 (equations (viii) and (ix)) show great similarity. For the $E_{p\theta}$ component obtained using the K.H. analysis, replacement of $(\beta_N r_1 + \bar{r}_1 \cos\theta)$ by $2\beta_N r_1$, and $(\bar{r}_1 + \beta_N r_1 \cos\theta)$ by $2\bar{r}_1$, yields the F.T. formulation for $E_{p\theta}$. Similarly for the $E_{p\phi}$ component, replacement of $(\bar{r}_1 + \beta_N r_1 \cos\theta)$ by $2\beta_N r_1 \cos\theta$, and $(\beta_N r_1 + \bar{r}_1 \cos\theta)$ by $2\bar{r}_1 \cos\theta$ yields the F.T. formulation for $E_{p\phi}$.

APPENDIX 9.3

CORRUGATED CIRCULAR WAVEGUIDE APPROXIMATION TO A NARROW FLARE-ANGLE CORRUGATED CONICAL HORN

Using Clarricoats notation <26>, the characteristic equation for the spherical hybrid mode in a narrow flare-angle corrugated conical horn with a small half angle, θ_o, and a large normalised slant length, $\frac{\omega}{c}R$ (figure 9.11), is given by

$$\alpha\theta_o \frac{J_1'(\alpha\theta_o)}{J_1(\alpha\theta_o)} = -\sqrt{1 - \left[\frac{\alpha\theta_o}{\frac{\omega}{c}R\theta_o}\right]^2} \qquad \text{(i)}$$

where $\alpha = \sqrt{v(v+1)}$, v is the order of the Legendre function, and the Bessel function approximation to the Legendre function has been used. For small θ_o, $R\theta_o = r_1$ (figure 9.11), and equation (i) becomes

$$\alpha\theta_o \frac{J_1'(\alpha\theta_o)}{J_1(\alpha\theta_o)} = -\sqrt{1 - \left[\frac{\alpha\theta_o}{\frac{\omega}{c}r_1}\right]^2} \qquad \text{(ii)}$$

The characteristic equation for the corrugated circular waveguide, radius r_1, at the balanced hybrid condition is given by

$$(Kr_1) \frac{J_1'(Kr_1)}{J_1(Kr_1)} = -\sqrt{1 - \left(\frac{Kr_1}{\frac{\omega}{c}r_1}\right)^2} = -\left(\frac{\beta}{\frac{\omega}{c}}\right) \qquad \text{(iii)}$$

Equations (ii) and (iii) are identical when $\alpha\theta_o$ is equated to Kr_1.

The aperture electric fields defined over a spherical cap for the corrugated conical horn for small θ_o and large $\frac{\omega}{c}R$ are given by <26>

$$\underline{E}_\theta \propto \left[(\tfrac{\omega}{c}) \frac{J_1(\alpha\theta_o)}{r} + \tfrac{\omega}{c}\left(1 - \left[\frac{\alpha\theta_o}{\frac{\omega}{c}r_1}\right]^2\right) J_1'(\alpha\theta_o) \frac{\alpha\theta_o}{r} \right] \underline{\theta} e^{-j\frac{\omega}{c}R}$$

$$\underline{E}_\phi \propto \left[(\tfrac{\omega}{c}) \left[\frac{\alpha\theta_o}{r}\right] J_1'(\alpha\theta_o) + \tfrac{\omega}{c}\left(1 - \left[\frac{\alpha\theta_o}{\frac{\omega}{c}r_1}\right]^2\right) \frac{J_1(\alpha\theta_o)}{r} \right] \underline{\phi} e^{-j\frac{\omega}{c}R} \qquad \text{(iv)}$$

The transform from spherical coordinates (R,θ,ϕ) to cylindrical coordinates (r,ϕ,z) is given by:-

$$R = r \sin\theta + z \cos\theta$$

$$\underline{\theta} = \underline{r} \cos\theta - \underline{z} \sin\theta$$

$$\underline{\phi} = \underline{\phi}$$

When θ is in the range $0 \leq |\theta| \leq \theta_o$, and for small θ_o this becomes:

$$\underline{R} = \underline{z}$$

$$\underline{\theta} = \underline{r}$$

$$\underline{\phi} = \underline{\phi}$$

Therefore for small θ_o equations (iv) become

$$E_r \propto E_r' \, \underline{r} \, e^{-j\frac{\omega}{c}z}$$

$$E_\phi \propto E_\phi' \, \underline{\phi} \, e^{-j\frac{\omega}{c}z} \qquad \text{(v)}$$

Expressing the phase factor in terms cf the radial r component in the aperture, shown below, gives:

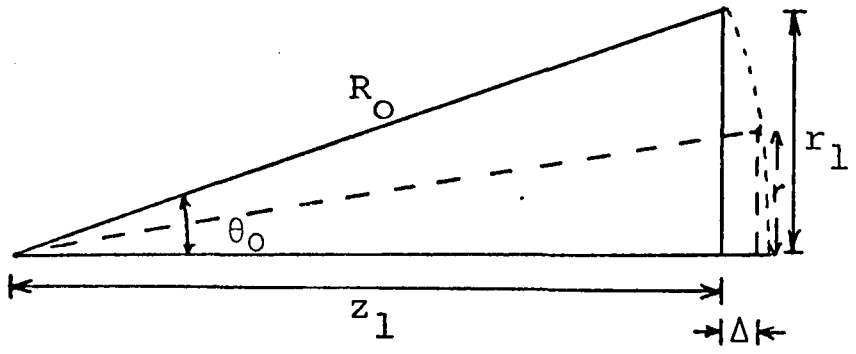

$$e^{-j\frac{\omega}{c}z} = e^{-j\frac{\omega}{c}(z_1+\Delta)}$$

By moving the phase reference to the plane aperture $z = z_1$, and expressing Δ in terms of r, the phase factor becomes

$$e^{-j\frac{\omega}{c}\left[1-\sqrt{1-(\frac{r}{R_o})^2}\right]} \equiv e^{j\Phi(r)} \qquad \text{(vi)}$$

Thus the aperture fields for the narrow flare-angle corrugated horn over a plane aperture are given by:

$$E_r \propto \left[(\frac{\omega}{c})\frac{J_1(\alpha\theta_o)}{r} + \frac{\omega}{c}\left[1-\left[\frac{\alpha\theta_o}{\frac{\omega}{c}r_1}\right]^2\right]J_1'(\alpha\theta_o)\frac{\alpha\theta_o}{r}\right]\underline{r}\, e^{j\Phi(r)} \qquad \text{(vii)}$$

$$E_\phi \propto \left[(\frac{\omega}{c})\left(\frac{\alpha\theta_o}{r}\right)J_1'(\alpha\theta_o) + \frac{\omega}{c}\left[1-\left[\frac{\alpha\theta_o}{\frac{\omega}{c}r_1}\right]^2\right]\frac{J_1(\alpha\theta_o)}{r}\right]\underline{\phi}\, e^{j\Phi(r)}$$

Comparison of equations (vii) with the aperture fields for the corrugated circular waveguide at the balanced hybrid condition shows them to be identical for $\acute{\alpha}\theta_o \equiv Kr_1$, except for the spherical phase factor $\Phi(r)$. Thus for a narrow flare-angle corrugated conical horn of large normalised slant length the aperture field can be approximated to that of a corrugated circular waveguide over a plane aperture, but with the addition of a spherical phase distribution. Whilst this result derived here is only strictly applicable at the balanced hybrid frequency it is reasonable to assume that it equally applies at other frequencies.

REFERENCES

1. CLARRICOATS, P.J.B. and SAHA, P.K.: 'Attenuation in corrugated circular waveguide', Electronics Letters, 6, No.12, June 1970, pp.370-2.

2. CHONG, S.L.: 'Corrugated circular waveguide for low attenuation transmission', Ph.D. thesis, Queen Mary College, University of London, Nov. 1974.

3. AL-HARIRI, A.M.B.: 'Low attenuation microwave waveguides', Ph.D. thesis, Queen Mary College, University of London, Oct. 1974.

4. KARBOWIAK, A.E.: 'Trunk waveguide communication', Chapman Hall, 1965.

5. CLARRICOATS, P.J.B., OLVER, A.D. and CHONG, S.L.: 'Attenuation in corrugated circular waveguides- Part I: Theory; Part II: Experiment', Proc. IEE, 122, No.11, Nov. 1975, pp.1173-86.

6. PAPIERNIK, A. and FRAY, C.: 'Low-loss open transmission line: The open ring line', Electronics Letters, 11, No.10, May 1975, pp.209-10.

7. BARLOW, H.M.: 'Dipole-mode propagation in hollow tubular waveguides', Proc. IEE, 121, No.7, July 1974, pp.537-40.

8. EVANS, B.G.: 'Satellite communication systems', IEE Microwave Summer School, Leeds, July 1975.

9. STAGG, L.J.: 'Microwave radio relay systems', ibid.

10. HALLIWELL, B.J.: 'Advanced communication systems', S.T.C. Monograph, Newnes Butterworths, 1974.

11. HILLS, M.T. and EVANS, B.G.: 'Telecommunications system design: Vol.1, Transmission systems', Allen and Unwin Ltd., 1973.

12. CUCCIU, C.L. et al: 'Microwave communications update - 1976', Microwave Systems News, 6, No.1, Feb./Mar. pp.20-53.

13. SOMMERS, D.J. et al: 'Beam waveguide feed with frequency re-use diplexer for satellite communication earth station', Microwave Journal, 18, No.11, Nov. 1975, p.51.

14. FOLDES, P.: 'Modification of feed systems for frequency re-use', Microwave Journal, 19, No.7, July 1976.

15. DUDZINSKY, S.J.: 'Atmospheric effects on terrestrial millimetre wave communications', Microwave Journal, 18, No.12, Dec. 1975, p.39.

16. HOGG, D.C. and CHU, T.S.: 'The role of rain in satellite communications', Proc. IEEE, 63, No.9, Sept. 1975, pp.1308-31.

17. THOMAS, B. MACA.: 'Cross-polarisation characteristics of axially symmetric reflectors', Electronics Letters, 12, No.9, April 1976, pp.218-9.

18. RIFAI, A.: 'Cross-polarisation in microwave reflector antennas', Ph.D. thesis, Queen Mary College, University of London, Oct. 1976.

19. MILLER, P.R.: 'Cross-polar characteristics of imperfect reflector antennas', Ph.D. thesis, Queen Mary College, University of London, Nov. 1976.

20. RUDGE, A.W.: 'Multiple-beam antennas: Offset reflectors with offset feeds', IEEE Trans. Antennas Propagation, AP23, No.3, May 1975, pp.317-22.

21. RUDGE, A.W. and ADATIA, N.A.: 'A new class of primary feed antennas for off-set parabolic reflector antennas', Second Symposium on Microwave Antennas, Queen Mary College. London, March 1976.

22. BRAIN, D.J.: 'Parametric study of the cross-polarisation efficiency of parabolic reflectors', Electronics Letters, 12, No.10, May 1976, pp.245-6.

23. PARINI, C.G., CLARRICOATS, P.J.B. and OLVER, A.D.: 'Cross-polar radiation from open-ended corrugated waveguides', Electronics Letters, 11, No.23, Nov. 1975, pp.567-8.

24. JACOBSEN, J.: 'European Space Agency plans and requirements for frequency re-use', IEE Colloquium on Antenna Systems for Frequency Re-use Applications, Feb. 1976.

25. MINNET, H.C. and THOMAS, B. MACA.: 'Fields in the image space of symmetrical focussing reflectors', Proc. IEE, 115, Oct. 1968, p.1419.

26. CLARRICOATS, P.J.B. and SAHA, P.K.: 'Propagation and radiation behaviour of corrugated feeds - Part I: The corrugated waveguide feed; Part II: The corrugated conical horn feed', Proc. IEE, 118, No.9, Sept. 1971, pp.1167-86.

27. POULTON, G.T.: 'The design of cassegrain antennas for high efficiency and low V.S.W.R.', Proc. 5th European Microwave Conference, Germany, Sept. 1975.

28. OLVER, A.D.: 'Evaluation of compact antenna range; Progress report No. 1', Queen Mary College, Electrical Engineering Department Technical Report, ADO/75/5.

29. OLVER, A.D.: 'Microwave anechoic chamber', ibid. Oct. 1975.

30. OLVER, A.D.: 'Design and evaluation of compact antenna ranges', Final Report of Ministry of Defence Agreement No. AT/2042/RL, Queen Mary College.

31. APPEL-HANSEN, J.: 'Reflectivity level of radio anechoic chamber', IEEE Trans. Antennas Propagation, AP21, July 1973, pp.490-8.

32. BUCKLEY, E.F.: 'Outline of evaluation procedures for microwave anechoic chambers', Microwave Journal, Aug. 1963.

33. LUDWIG, A.C.: 'The definition of cross-polarisation', IEEE Trans. Antennas Propagation, AP21, No.1, Jan. 1973.

34. KLINGER, Y.: 'The measurement of spurious modes in overmoded waveguides', Proc. IEE, 106B (supplement), 1959, pp.89-93.

35. ROBSON, P.N.: 'Overmoded rectangular waveguide', Millimetre and Sub-millimetre Waves, Editor F.A. Benson, Iliffe, 1969, Chap. 15.

36. OLVER, A.D.: 'Low attenuation waveguides',Queen Mary College Electrical Engineering Department Technical Report, ADO/73/1, Jan. 1973.

37. OLVER, A.D.: 'The manufacture of corrugated wave-guide by thermal contraction', ibid, ADO/73/9, Oct. 1973.

38. 'Microwave frequency synchroniser', Frequency Engineering Laboratories, Oct. 1967.

39. MORGAN, S.P.: 'Effect of surface roughness on eddy current losses at microwave frequencies', J. Appl. Physics, 20, 1949, pp.352-62.

40. BENSON, F.A.: 'Millimetre and Sub-millimetre Waves', Iliffe Books Ltd., London, 1969, Chapters 14 and 16.

41. MONTGOMERY, C.G. (Ed): 'Principles of microwave circuits', Dover Publications, New York, 1965, Chapt. 2.

42. POULTON, G.T.: 'Mode conversion due to a waveguide bend', Appen. 6 of Corrugated Circular Waveguides for Low Attenuation Transmission, Clarricoats, P.J.B. et al, Queen Mary College Electrical Engineering Department Technical Report, PJBC/ADO/72, Feb. 1972.

43. KING, A.P.: 'Dominant wave transmission characteristics of multimode round waveguide', Proc. IRE, 40, Aug. 1952, pp.966-9.

44. CHIRGWIN, B.H. and PLUMPTON, C.: 'A course of mathematics for scientists and engineers', Vol.2, (second edition), Pergamon Press, 1972.

45. HARRINGTON, R.F.: 'Time harmonic electromagnetic fields', McGraw Hill, 1961.

46. LATHI, B.P.: 'Random signals and communication theory', Intertext Books, London, 1968, Chapt. 3.

47. LEE, Y.W.: 'Statistical theory of communications', Wiley, 1960.

48. SLINN, K.R., Andrew Antenna Systems, private communication.

49. OLVER, A.D. et al: 'Experimental determination of attenuation in corrugated circular waveguides', Electronics Letters, 9, No.18, Sept. 1973, pp.424-6.

50. SILVER, S. (Ed.): 'Microwave antenna theory and design', M.I.T. Radiation Lab series, 12, McGraw Hill, 1949.

51. COLLIN, R.E. and ZUCKER, F.J.: 'Antenna theory: Part I', McGraw Hill, 1969.

52. HOCKHAM, G.A., 'Queen Mary College, private communication.

53. KNOP, C.M. and WEISENFORTH, H.J.: 'On the radiation from an open-ended corrugated pipe carrying the HE_{11} mode', IEEE Trans. Antennas Propagation, AP20, No.5, 1972, p.644.

54. ELLIOT, R.D.: 'SWEX in FORTRAN', Queen Mary College Electrical Engineering Department Technical Report, RDE/6/75.

55. AU, H.K.: 'Hybrid mode in corrugated conical horns with narrow flare-angle and arbitrary length', Electronics Letters, 6, No.24, Nov. 1970.

56. RUMSEY, V.H.: 'Horn antennas with uniform power patterns around their axis', IEEE Trans. Antennas Propagation, AP14, Sept. 1966, pp.656-8.

57. MINNETT, H.C. and THOMAS, B. MACA.: 'A method synthesising radiation patterns with axial symmetry', ibid, pp.654-6.

58. HOCKHAM, G.A.: 'Investigation of 90° corrugated horn', Electronics Letters, 12, No.8, April 1976, pp.199-200.

59. CHARLTON, T., Andrew Corporation, private communication.

60. TAKEICHI, Y. et al: 'The ring loaded corrugated waveguide', IEEE Trans. Microwave Theory Tech., MTT-19, No.12, Dec. 1971.

PUBLICATIONS

During the course of the research reported in this thesis, the following papers were published:

a) CLARRICOATS, P.J.B., OLVER, A.D. and PARINI, C.G.: 'Radiation method for the measurement of mode-conversion levels', Electronics Letters, 10, No.25/26, Dec. 1974.

b) CLARRICOATS, P.J.B., OLVER, A.D., PARINI, C.G. and POULTON, G.T.: 'Corrugated waveguide feeders for microwave antennas', Proc. 5th European Microwave Conference, Germany, Sept. 1975.

c) PARINI, C.G., CLARRICOATS, P.J.B. and OLVER, A.D.: 'Cross-polar radiation from open-ended corrugated waveguides', Electronics Letters, 11, No.23, Nov. 1975.

d) CLARRICOATS, P.J.B., OLVER, A.D. and PARINI, C.G.: 'Optimum design of corrugated feeds for low cross-polar radiation', Proc. 6th European Microwave Conference, Italy, Sept. 1976.